UNIVERSITY OF STRATHCLYDE

Department of Physics

Institute of Photonics

Neuromorphic Photonic Systems with Lasers

by

Joshua Robertson

Thesis presented in fulfilment of the requirement for the degree of Doctor of Philosophy

June 2022

Declaration of Authorship

This thesis is the result of the author's original research. It has been composed by the author and has not been previously submitted for examination which has led to the award of a degree.

Abstract

In this thesis we investigate the technology of Vertical Cavity Surface Emitting Lasers (VCSELs) as potential candidates for neuromorphic (brain-like) photonic computing hardware elements, towards the future realisation of ultrafast, energy-efficient and light-enabled information processing platforms. VCSELs are a type of semiconductor laser sources that not only exhibit numerous beneficial characteristics, such as low power requirements, compactness, low manufacturing costs and high modulation speeds, but also offer exciting prospects as photonic emulators of biological neurons. Hence, in this thesis we develop and study the behaviour of VCSEL-based artificial photonic neurons and reveal their capability to activate sub-nanosecond neuron-like optical spiking responses (3 orders of magnitude faster than state of the art electronic implementations of biological neurons). We further explore the control of the non-linear neuron-like dynamics in VCSELs before taking advantage of their ultrafast optical spiking signals to produce examples of spike-based photonic information processing systems.

First, we study the neuron-like excitable (spiking) dynamics exhibited by VCSELs under external optical injection. Both the activation and inhibition of 100 ps-long (GHz rates) spiking responses is demonstrated using both modulated optical injection and modulated bias current. These mechanisms are shown to elicit neuron-like optical spiking regimes, both controllably and consistently, in VCSELs. The similarities of the responses achieved in the analysed VCSEL neurons to neuronal models is then investigated, where we reveal further the underlying neuron-like behaviours (such as threshold-and-fire, and spiking refractory periods) in these photonic devices.

Second, we investigate the networking capability of the developed VCSEL neurons. By building experimental configurations of coupled VCSELs we demonstrate their ability to communicate optical spiking signals. Both the activation and inhibition of optical spikes is shown to be propagated in (1-to-1) feedforward architectures, revealing the output of an artificial VCSEL neuron is cascadable across layers in a network. Further we demonstrate the activation of two downstream VCSEL neurons

in a diverging (1-to-2) architecture and create a three layer (1-to-1-to-1) VCSEL network inspired by biological cell layers in the retina. The latter is achieved without signal manipulation between network layers, with the implementation of all optical signals using commercially-sourced VCSELs.

Finally, we discuss the successful application of VCSEL neurons in functional neuromorphic photonic information processing demonstrations. We achieved digital-to-spike conversion of return-to-zero (RZ) and non return-to-zero (NRZ) signals for the interfacing of spiking neuromorphic platforms with traditional digital technologies. We also explored the time-division multiplexing (TDM) of VCSEL inputs for the creation of a virtual converging (many-to-one) network architecture. Using this technique we revealed for the first time (experimentally) the neuronal integrate-and-fire behaviour of the VCSEL neuron. Exploiting this key neuronal behaviour, we implemented a single artificial VCSEL neuron as processing element, and demonstrated the coincidence detection of fast (sub-nanosecond) optical inputs with the firing of an optical spiking response. Further employing the integrate-and-fire capability, we demonstrated both 4-bit binary pattern recognition and image processing (edge-feature detection) tasks with a single VCSEL neuron. Moreover, we utilised the spike-based edge-feature detection of the VCSEL neuron (alongside a software implemented spiking neural network, SNN) to successfully classify digits from the MNIST handwritten digit database, achieving a high classification accuracy of 96.1%. Successful operation of different information processing tasks was therefore achieved with systems based on VCSEL neurons, that utilised both ultrafast (GHz rate) optical spiking representations and hardware-friendly (commercially-sourced) photonic components. We therefore believe VCSELs, with their exciting characteristic and highlighted neuronal behaviours, serve as excellent potential candidates for neuromorphic photonic implementations of novel ultrafast and efficient information processing systems for brain-inspired computing and light-enabled Artificial Intelligence (AI) hardware.

Acknowledgements

I would first like to extend my sincere gratitude to my primary (and long-time serving) supervisor, Dr. Antonio Hurtado. I thank him for both encouraging and challenging me to embark upon this PhD degree, and for always believing in my ability. I am also grateful for his enthusiasm, guidance, patience, and hard work over the years, and I look forward to further shared success (and pints!) in the future. I would also like to thank my second supervisor Prof. Michael Strain, he has always provided support, reassurance, and input into my studies.

Secondly, I want to thank all of my colleagues within the Institute of Photonics (IoP), past and present, for creating an exciting and excellent work environment. I particularly want to thank all the members of the Neuromorphic and Nanophotonic group. Thank you Dr. Dimitars Jevtics for first making me feel welcome and for training me up in the early days of the cleanroom (let's not forget passing up on the project). Thank you also to both Dr. Julián Bueno and Dr. Juan Arturo Alanis, I appreciate you sharing your knowledge, help and friendship with me over the years. Finally, thank you Matěj Hejda and (more recently) Dafydd Owen-Newns, you both are exemplar PhD candidates. I am grateful for all the time we spent working together and for the day-to-day encouragement we have shown each other. I also want to extend a special thanks to the administrative team at the IoP, Sharon Kelly and Lorraine Annand, your help over the years has been essential and I have always enjoyed the chatter. To all the friends I have made throughout my PhD studies, you (and the tea breaks) have helped make my experience all the more fun, thank you for everything from quick daily catch-ups to long drawn-out board games nights.

Finally, I want to thank all my family and friends. Thank you to both my parents, you have helped support me though my endless days of being a student, your encouragement has made this possible. Last but not least, thank you to my wife-to-be Kirsty for being there for me throughout this journey, for always encouraging me and for bringing me my evening tea with a smile.

List of Publications

1st Author Publications

- J. Robertson, J. Alanis, M. Hejda, and A. Hurtado, '*Photonic Synaptic System for MAC Operations by Interconnected Vertical Cavity Surface Emitting Lasers*', Opt. Mater. Express, vol. 12(4), pp. 1417-1426 (2022).

- J. Robertson, P. Kirkland, J.A. Alanis, M. Hejda, J. Bueno, G. Di Caterina and A. Hurtado, '*Ultrafast neuromorphic photonic image processing with a VCSEL neuron*', Sci. Rep., vol. 12(1), 4874 (2022).

- J. Robertson, Y. Zhang, M. Hejda, J. Bueno, S. Xiang and A. Hurtado, '*Image Edge Detection with a Photonic Spiking VCSEL-neuron*', Opt. Exp., 28(25), pp. 37526-37537 (2020).

- J. Robertson, M. Hejda, J. Bueno and A. Hurtado, '*Ultrafast optical Integration and Pattern Classification for Neuromorphic Photonics based on Spiking VCSEL Neurons*', Sci. Rep., 10(1), 6098 (2020).

- J. Robertson, E. Wade, Y. Kopp, J. Bueno and A. Hurtado, '*Toward Neuromorphic Photonic Networks of Ultrafast Spiking Laser Neurons*', IEEE J. Sel. Top. Quantum. Electron., 26(1), 7700715 (2019). (***Invited paper and issue front cover***)

- J. Robertson, E. Wade and A. Hurtado, '*Electrically-Controlled Neuron-like Spiking Regimes in Vertical-Cavity Surface Emitting Lasers*', IEEE J. Sel. Top. Quantum. Electron., 25(6), 5100307 (2019).

- J. Robertson, T. Ackemann, L.F. Lester and A. Hurtado, '*Externally-triggered activation and inhibition of optical pulsating regimes in quantum-dot mode-locked lasers*', Sci. Rep., 8(1), 12515 (2018).

- J. Robertson, T. Deng, J. Javaloyes, A. Hurtado, '*Controlled inhibition of spiking dynamics in VCSELs for neuromorphic photonics: theory and experiments*', Opt. Lett., 42(8), pp. 1560-1563 (2017).

Other Contributions

- J. A. Alanis, J. Robertson, M. Hejda, and A. Hurtado, '*Weight adjustable photonic synapse by nonlinear gain in a vertical cavity semiconductor optical amplifier*,' Appl. Phys. Lett., 119(20), 201104, (2021).

- J. Bueno, J. Robertson, M. Hejda, and A. Hurtado, '*Comprehensive Performance Analysis of a VCSEL-based Photonic Reservoir Computer*', IEEE Photonics Technology Letters, 33(16), pp. 920-923, (2021).

- M. Hejda, J. Robertson, J. Bueno, J. A. Alanis, and A. Hurtado, '*Neuromorphic encoding of image pixel data into rate-coded optical spike trains with a photonic VCSEL-neuron*,' APL Photonics, 6(6), 60802 (2021).

- Y. Zhang, J. Robertson, S. Xiang, M. Hejda, J. Bueno and A. Hurtado, '*All-optical neuromorphic binary convolution with a spiking VCSEL neuron for image gradient magnitudes*', OSA Photon. Res., 9(5), pp. B201-B209 (2021).

- D. Jevtics, M. Hejda, K. Peng, B. Guilhabert, J. Robertson, J. McPhillimy, H. Tan, C. Jagadish, M.B. Johnston, M. Strain, M. Dawson, and A. Hurtado, '*Heterogeneous integration of semiconductor nanowires in 2D and 3D nanophotonic systems*', Proc. SPIE 11680, Physics and Simulation of Optoelectronic Devices XXIX, 116800X, (2021).

- L.W. Smith, J.O. Batey, J.A. Alexander-Webber, Y. Fan, Y. Hsieh, S. Fung, D. Jevtics, J. Robertson, B. Guilhabert, M.J. Strain, M.D. Dawson, A. Hurtado, J.P. Griffiths, H.E. Beere, C. Jagadish, O.J. Burton, S. Hofmann, T. Chen, D.A. Ritchie, M. Kelly, H.J. Joyce, and C.G. Smith, '*High-Throughput Electrical Characterization of Nanomaterials from Room to Cryogenic Temperatures*', ACS Nano., 14(11), pp. 15293-15305 (2020).

- M. Hejda, J. Robertson, J. Bueno, A. Hurtado, '*Spike-based information encoding in vertical cavity surface emitting lasers for neuromorphic photonics*', IOP J. Physics: Photon, 2(4), 044001 (2020). (***Invited paper***)

• M. Dillane, J. Robertson, M. Peters, A. Hurtado, B. Kelleher, '*Neuromorphic Dynamics with optically injected quantum dot lasers*', European Physics Journal B, 92, 197 (2019).

• T. Deng, J. Robertson, Z. Wu, G. Xia, X. Lin, X. Tang, Z. Wang and A. Hurtado, '*Stable propagation of inhibited spiking dynamics in vertical-cavity surface-emitting lasers for neuromorphic photonic networks*', IEEE Access, 6, pp. 67951-67958 (2018).

• T. Deng, J. Robertson and A. Hurtado, '*Controlled propagation of spiking dynamics in vertical-cavity surface-emitting lasers: theory and experiments*', IEEE J. Sel. Top. Quantum. Electron., 23 (6), 1800408 (2017).

Contents

Chapter 1

Introduction

In this Chapter we will preface the reporting of results with the motivation behind this research (Chapter 1.1). Specifically, we will shed light on some of the reasons behind the desire for novel information processing architectures, including the draw backs of tradition processors and the arrival of the Artificial Intelligence (AI) revolution. We will then introduce the concept of neuromorphic information processing (Chapter 1.2), observe the biological systems that inspire the topic, and highlight how neuromorphic computing architectures are achieving information processing with electronic and photonic technologies. We will introduce semiconductor lasers (Chapter 1.3) and describe their operation, before focusing on vertical-cavity surface-emitting lasers (VCSELs) (Chapter 1.4) as the primary devices used in this PhD research project. Here, we will discuss the structure, properties and advantages of VCSELs. We will then discuss how the technique of optical injection (Chapter 1.5) can be used to produce numerous dynamical responses, including neuronal behaviours, in VCSELs. Finally, we will introduce the topic of VCSELs for neuromorphic computing (Chapter 1.6) and highlight the most recent reports on the use of these systems for ultrafast neuronal-like effects and information processing. A short outline of the thesis is given in Chapter 1.7.

1.1 Motivation

For decades digital electronics have powered the thriving advancement of information processing in our society. Following the first commercial microprocessor in 1971 [1], the precedent for central processing unit (CPU) development went as the doubling of transistor count, every two years. This observation, known as Moore's law [2], was used for decades to predict the progress

of digital processors with time. This law, however, now seems to be slowing with factors such as the breakdown of Dennard scaling [3] (the previous idea that power density remained constant when shrinking transistors) impeding the rapid development of new microchips. Fundamentally, it is now understood that the scaling of transistors in this fashion is limited by the energy consumption, dissipation, and joule heating of the components that make up electronic chips [4]. The ensuing struggle to maintain the pre-existing power efficiency growth rate (Koomey's law [5]) of the microprocessor has also impacted the overall growth of maximum clock speed. For this reason, we are witnessing a plateau in processor frequency and a shift to parallel-processing, multi-core designs [6], with the overall environment for creating new, fast and power efficient CPUs becoming increasingly challenging.

Alongside this plateau in the performance enhancement of digital processors, the way society uses and accesses data and information has significantly expanded over the past decade. The development and mass adoption of smart devices, that interconnect and share information (the so-called internet of things, IoT), as well as the big data problem (the challenge on how to process massive datasets) is putting extra pressure on the traditional digital computer processor. The ever-increasing demand for fast and highly efficient processing platforms has pushed digital electronics, and now having developed graphical processing units (GPUs) for higher computational throughput, electronics has laid the foundations for the AI [7]–[10].

AI, the ability of a computer to perform tasks that typically require human intelligence and discernment, is achieved by teaching computers to learn from data or experiences (machine learning) or by building artificial neural networks (ANNs) with structured algorithms that allow the computer to make decisions on its own (deep learning). Since its development, AI has worked its way into our daily lives, and now exists within our homes, hospitals, mobile devices, etc., thanks to its proven excellence at performing complex processing tasks (e.g. image processing [11], [12], language translation and speech recognition [13], even the strategy game Go [14]). The digital processor, based on the so-called Von-Neumann computing architecture, is, however, not well suited for deep learning. The Von Neumann bottleneck, the requirement to bus data from memory to the CPU, means that traditional digital processing architectures lack the parallelism to perform these complex tasks as

efficiently as brain-inspired (neuromorphic) ANNs. The AI revolution, big data and the plateauing of digital electronics, are all therefore responsible for pushing researchers in the direction of a novel processing paradigm, namely neuromorphic information processing.

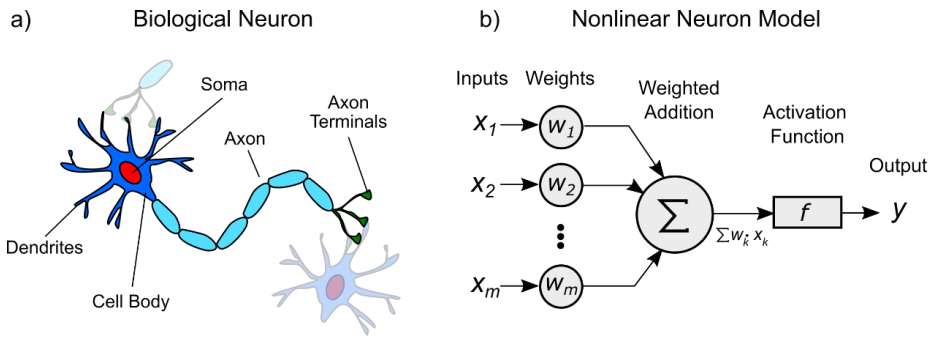

Figure 1.2.1 – a) Schematic of a biological neuron. b) Nonlinear model of a neuron, with inputs (x_1), weights (w_1), an adder, a non-linear activation function and an output (y).

1.2 Neuromorphic Information Processing

A new generation of non-Von Neumann computing architectures, called neuromorphic systems are seeing a research surge in an attempt to address the challenges posed by the AI revolution and big data. These neuromorphic computing architectures aim to decentralize dedicated processing units and create computers inspired by the processing systems observed in nature, namely neural networks. One of the most well-known and impressive neural networks in nature is that of the biological neurons in the brain. In the brain three essential elements are responsible for creating the efficient processing system, the neuron, the synapse, and the coding scheme. Biological neurons, are nerve cells that are known to communicate within the brain's neural networks using electrical graded action potentials, which appear in the form of spiking responses [15], or graded potentials, that appear as slower analog signals. The action potentials are typically generated via chemical processes and alter the voltage potential across the cell. Action potentials are passed to interconnected neurons through what are called synapses, where axon terminals of a neuron meet

the dendrites of another, allowing the generated electrical impulse to flow between neighbouring neurons (see Fig. 1.2.1 (a)). The action potentials created by neurons are a sparse coding scheme, digital in amplitude but analog in time, exhibiting both the expressiveness of an analog signal and the robustness of a digital signal [16]. Neuromorphic systems draw inspiration from these three elements, to create artificial spiking neurons and ANNs for use in information processing.

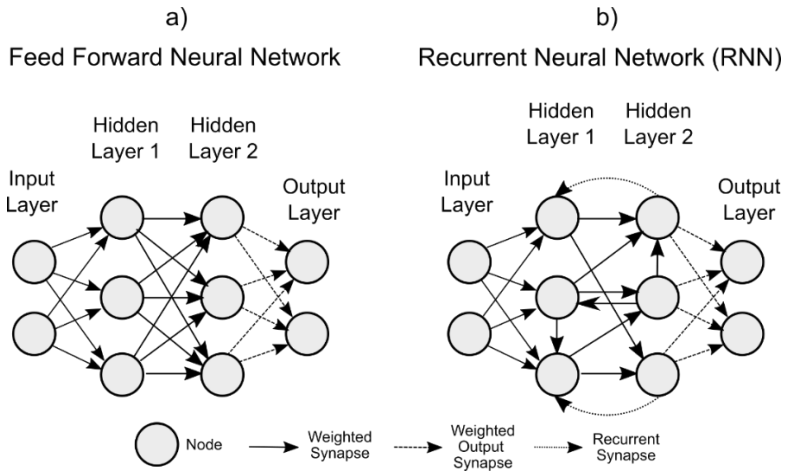

Figure 1.2.2 – Schematic of different Artificial Neural Network (ANN) architectures. a) A Feed-Forward Neural Network and a b) Recurrent Neural Network (RNN). Both architectures are comprised of three types of layers (input, hidden and output), each connected via weighted synaptic connections. Feed-forward networks pass information to the next layer. RNNs can pass information within a layer and backwards towards previous layers.

Initially, research into ANNs considered directly mimicking biological neural networks, but soon the field was reorientated to mimic the structure of neural networks with different neuronal models. ANNs were first proposed in 1943 [17] and ever since, a wide diversity of ANN models have been proposed, with and without spiking dynamics at the core of their operation [18]. One of the most typical ANN models is the so-called feed-forward neural network [19]. In this type of ANN structure (see Fig. 1.2.2 (a)), neurons (or nodes) are connected in layers, with neurons in one layer sequentially connected to neurons in the next layer. Within the ANN each connection has a strength called a weight, which controls how much one neuron influences another. The ANN has an input layer, one or more hidden layers, and an

output layer, with the number of neurons in each layer varying with the network application. The input layer introduces information into the ANN in the form of stimulations that trigger the dynamics of the system. The information is passed through the weighted connections in the hidden layer until it reaches the output layer, where the output of the system (in response to the incoming information) is encoded in the state of the nodes. Nodes within the hidden layers of ANNs do not always require to be fully connected, and connection architectures that pool neurons (the fan-in connection of many neurons to one) can be used to reduce the number of neurons in a layer [20]. Further, networks known as Recurrent Neural Networks (RNNs) can allow nodes within layers to interact and can even allow connections to be made to previous layers [21] (see Fig. 1.2.2 (b)).

ANNs come in a large variety of configurations, making it possible to implement numerous tasks. The highly parallel nature of ANNs spread computation across multiple nodes allowing complex problems, such as pattern (e.g. image and speech) recognition and decision making to be solved efficiently. However, with a diverse range of ANN parameters, such as weights, layer numbers, and node numbers, it can be difficult to find an optimal configuration for a specific task. The process of optimising an ANN configuration and minimising the error during processing tasks is called learning, and learning can be achieved by training the ANN [20]. During training the weighted connections within the ANN are configured to maximise the performance of the specified task, and training concludes when the observed error makes no notable improvement. If training does not provide sufficient performance, then the architecture and configuration of the ANN should be altered. The training of ANNs is very computationally expensive because the number of synaptic weights, which take positive and negative real values, far outnumber the nodes within a network. For example, in biological neural networks one cortical neuron can have up 1000 synaptic connections [22]. Training also often requires multiple cycles (or epochs) before the optimal network parameters are found, further intensifying the computational requirements. Due to these high computational requirements, although ANNs were initially simulated by IBM in 1955 [23], reports diminished until a more efficient back-propagation method of training neural networks was demonstrated [24].

Like biological neurons, nodes within ANNs perform specific functions. Fundamentally, the neuronal nodes apply a non-linear transformation, called an activation function, to the total summation (or integration) of all the weighted inputs coming from synapsed nodes (see Fig. 1.2.1 (b)) [25]. Different nonlinear transformations, such as Heaviside and sigmoid functions [26], have been used in ANNs but basic threshold-and-fire class models, such as the integrate-and-fire neuron model, describe well the behaviour of neurons in a network [27]. These neuronal models demonstrate the ability of a neuron to receive and combine inputs from multiple up stream neurons. An integrate-and-fire neuronal model will summate all weighted inputs that arrive over time and can appear leaky or perfect, meaning the integration decays or does not decay over time, respectively [28]. Leaky integration specifically, allows the neuronal model to hold short term memory, enabling the node to correlate inputs that arrive close in time. The integrated input contributions are subsequently subject to the activation function that acts as a thresholder, where it may or may not produce a dynamical response at the system's output, depending on the total input of the system. Successful dynamical responses then reset the system over a short refractory period, where the node (like cortical neurons in the brain) will not fire again.

The Leaky Integrate-and-Fire (LIF) neuronal model is one of the most typical models for spike-based ANNs, typically referred to as Spiking Neural Networks (SNNs). The LIF neuronal model can operate with the sparse all-or-nothing spike-based coding scheme and in doing so more closely emulates the spike-based networks of real biological neurons. SNNs produce and communicate information in a spiking representation that can be characterised by the firing rate (rate coding) or the timing of individual spikes (temporal coding) [16], [29]. There are benefits to representing information in this way, for instance; the sparse coding system only spends energy when activating a spike in the network, promising improvements to the power efficiency of computations in SNNs [30], [31]; spike information is not lost in dispersive networks due to pulse spreading as the information is contained in the timing of the spike; spikes can be regenerated by intermediate network nodes helping mitigate the accumulation of noise and lossy connections; a reduced number of nodes may be required by the network to perform certain tasks compared to other ANN

systems [32]–[34]. Spike-based approaches also promise improvements to the power efficiency of computations because they exploit the underlying physics of biological, analog electronic, and optoelectronic platforms.

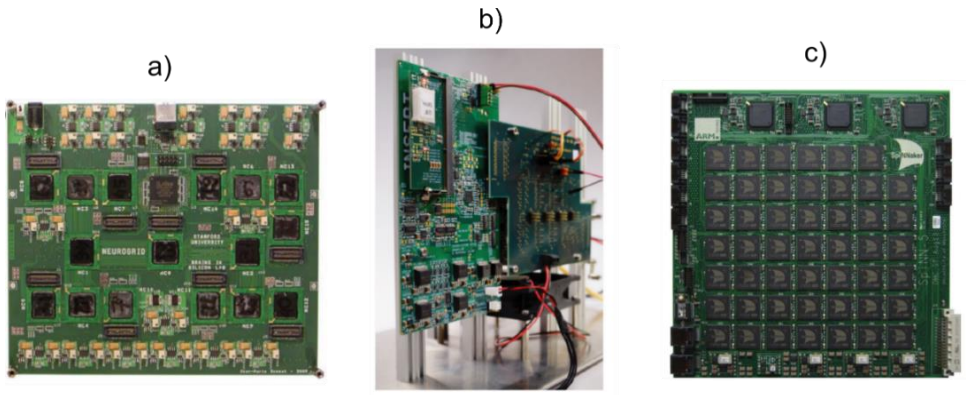

Figure 1.2.3 – Examples of electronic neuromorphic chips including the a) Neurogrid chip by Standford University (Image reproduced from [35]). b) BrainScaleS chip by University of Heidelberg (Image reproduced from [36]). c) The SpiNNaker project by the University of Manchester (Image reproduced from [37]).

Reports of electronic approaches to artificial neuromorphic computing systems first found interest several decades ago [38]. Since then, electronic technology has matured significantly and now there are several impressive electronic-based neuromorphic computing platforms in development. Some of the notable spiking neural network systems include; Neurogrid by Stanford University [35], [39], TrueNorth by IBM, as part of the SyNAPSE program [40], [41], HICANN and BrainScaleS systems by the University of Heidelberg [36], [42], Loihi by Intel [43], and SpiNNaker by the University of Manchester [37]. These spiking platforms apply electronics to realise networks of thousands of neurons and hundreds of thousands of synapses (see Fig. 1.2.3), with stackable architectures like SpiNNaker realising even larger million-neuron systems, well beyond what is achievable with alternative platforms. Typically, these spike-based systems realise neuromorphic operation with electronic spiking responses up to MHz speeds. For example, the recent Loihi system operates with an impressive 400 ns per timestep (2.5 MHz) [43], and the HICANN system utilises spiking refractory periods of 10 µs (0.1 MHz) [42]. Other systems,

such SpiNNaker, TrueNorth and Neurogrid operate with biologically realistic timescales of kHz (tens of millisecond speeds), making them highly valuable platforms for the investigation of how of biological neurons operate [39]. Further, neuromorphic electronic systems have implemented different neuronal computing principles including analog signalling and learning, and have shown great performance and efficiency when completing tasks of computer vision, speech processing and decision making. However, like the traditional microprocessor, cross talk, dissipation and joule heating place physical limitations on the speed, bandwidth and efficiency of the electronic platform [4].

An alternative to electronic-based implementations is a neuromorphic photonic platform. Photonics benefits from a wide range of light-enabled devices that have access to high communication bandwidths, low cross talk, high energy efficiency and high-speed optical signals. These characteristics align well with the goals of neuromorphic processing systems and help to remedy some of the limitations imposed on electronic-based platforms. Making a direct comparison between the energy efficiency of electronic neuromorphic systems and photonic neuromorphic systems is increasingly difficult task. Multiple approaches are taken on both platforms, and the platforms themselves are at different development stages. However, what can be said is that there is still gains to be made (in terms of energy efficiency) in photonics platform. Switching to photonics could provide benefits, inaccessible to electronics, such as low loss passive components for low cost computing operations. Further, photonic technology has access to optical techniques such as Wavelength-Division Multiplexing (WDM), where multiple signals can be can carried across the same communication channel using multiple wavelengths, to implement large network interconnects that introduce another dimension for processing in addition to space and time, also improving efficiency [44]. Further, maturing photonic technologies have also developed a growing tool kit of components for on-chip Photonic Integrated Circuits (PICs) [45]. For instance, PICs can make use of optical waveguides that are able to passively communicate analog signals with low latency and low electromagnetic interference. PICs therefore hold the potential to improve the footprint of neuromorphic photonic platforms, bringing the enhanced performance and efficiency to compact application-driven integrations.

A large benefit of utilising a photonic platform for neuromorphic processing is that photonics has many underlying physical processes analogous to biological neurons. In light-enabled platforms these physical processes can reach very high speeds (GHz-rates), >6 orders of magnitude faster than the timescales of biological neurons [46], and importantly, multiple orders of magnitude faster than the previously discussed electronic neuromorphic systems (MHz-rates). Since the early 2000's [47], reports of photonic systems for ultrafast artificial neuronal models and ANNs have slowly grown in popularity. In just the past decade however, the field has very rapidly expanded to the point where a plethora of photonic devices have been proposed for neuromorphic technology. Photonic crystal structures [48], [49], fibre lasers [50], [51], semiconductor optical amplifiers [52], [53] and optical modulators [54], [55] have all been demonstrated for their capability to create neuromorphic systems with varying degrees of inspiration on spiking and non-spiking neurons. Neuromorphic systems based on hybrid semiconductor-superconductor platforms have also been proposed as a means of scalable ANNs with low power density [56].

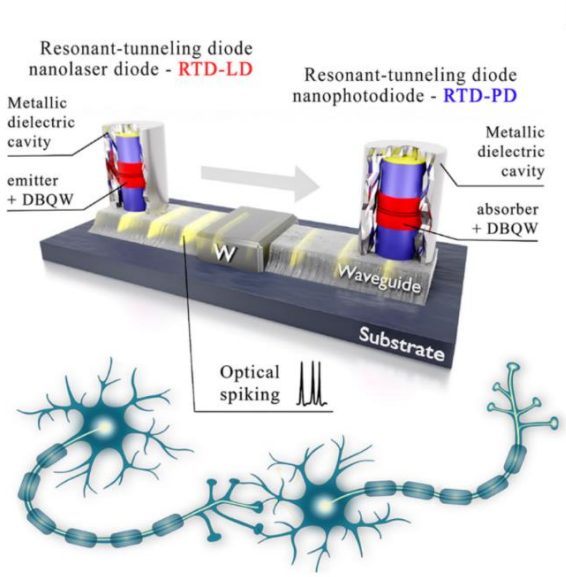

Figure 1.2.4 – Neuromorphic nanoscale optoelectronic Resonant Tunnelling Diode (RTD) circuit. RTD-laser diodes (LDs) and RTD-photodetectors (PDs) are used to interconnect two artificial spiking optoelectronic neurons. RTD-LDs can integrate signals and produce electrical excitable responses, subsequently generating optical spiking signals. RTD-PDs convert optical spiking signals to electrical inputs to the next artificial neuron. Figure reproduced from [57].

Resonant tunnelling diodes (RTDs) are another technology offering great promise for neuromorphic photonic computing [57]–[63]. RTDs are devices with embedded double barrier quantum wells (DBQW), which are realised with two thin layers of semiconductor material of narrow bandgap. When carriers are pumped with the energy matching the confinement energy of the double barrier structure, they can cross it, creating a current flow through the device. The correct pump energy represents a local maximum in the system, with changes in bias resulting in drops of current, forming the characteristic N shaped voltage-current relationship [58]. RTDs have shown the capability to operate as high frequency oscillators (up to THz rates) [58], [59] but also as neuromorphic spiking elements [57], [60]–[63]. RTDs have also been paired with semiconductor lasers (SLs) to create high-speed (sub-nanosecond) neuromorphic optoelectronic circuits [61], [62] with neuronal feedback connections also having been explored [63]. More recently, a nanoscale RTD-laser diode (LD) and RTD-photodetector (PD) system was proposed as a fast, spiking solution for ANNs (see Fig. 1.2.4) [57]. This theoretical work reports the temporal integration of high-speed inputs within an RTD and the subsequent generation of a (sub-nanosecond) spiking output, like that of a biological neuron, via an interconnected laser diode. The optical spiking signal is then collected by a PD and injected into the downstream neuron, realising an optoelectronic synaptic connection. In this report [57], pattern recognition and image edge detection were achieved with a single RTD-LD and supervised learning was also utilised to perform a high-speed pattern recognition task with a network of 5 RTD-based spiking nodes. These optoelectronic RTD circuits are therefore exciting nano-scale neuromorphic candidates, capable of neural network operation with fast optical spike-based signals.

One technology that has contributed substantially to the realisation of photonic neuromorphic systems is the semiconductor laser (SL). These devices, which will be discussed in more detail in Chapter 1.3, have created numerous reports of neuromorphic photonic systems thanks to their non-linear dynamical behaviours. Micro-disk lasers [64], micro-pillar lasers [65], micro-ring lasers [66], [67], quantum dot lasers [68]–[70], and distributed feedback lasers [71] to name a few, have all shown neuromorphic responses. Detailed reviews of the progress of semiconductor

lasers in neuromorphic photonics have been recently produced [46], [72]–[74], gathering key developments in this field. The neuromorphic applications of the vertical cavity-surface emitting laser (VCSEL) are particularly interesting and are hence the focus of this thesis. The uses of VCSELs in neuromorphic photonic systems will be firstly introduced in this thesis in Chapter 1.5-1.6.

Beyond SLs, additional research efforts have been made to accelerate information processing with photonic ANNs. Photonic neuromorphic accelerators, based on on-chip integrated micro-ring resonator weight banks [75], [76] and micro-ring modulators, have generated significant interest [77], [78]. The photonic ANN accelerator, shown in Fig. 1.2.5, weighs multiple wavelengths in parallel, via 4 in-series micro-ring resonators, before combining them in a balanced PD. The weight of each resonator is set via addressable heating controllers and the balanced PD enables the generation of positive and negative electrical signals. The PD signal is passed to a micro-ring modulator that integrates the contribution of each wavelength and regulates the intensity of a CW pump laser according to different configurable transfer functions, realising the operation principle of a neuron on-chip. This artificial (non-spiking) neuron has shown the possibility to operate with multiple fan-in connections and has demonstrated cascadability (the capability to trigger connected downstream neurons). This makes this approach suitable for integration into ANNs, built with multiple similar neurons, such as a proposed broadcast-and-weight architecture [79]. This system has been proposed for numerous computing tasks including image classification and model-predictive control, where the high-speed and highly-parallel nature of the photonic accelerator can overcome the bottlenecking experienced by digital processors [80]. Other neuromorphic photonic accelerators have also been reported towards the goal of achieving computer vision and image recognition [81]–[83]. These systems which are built using micro-ring resonators [81] and Phase Change Material (PCM) cells [82], [83], create photonic ANNs that apply the image processing technique convolution alongside machine learning to classify input images. The photonic accelerator system based on PCMs reported a high classification accuracy of 95.6% on the industry-standard MNIST hand-written digit image classification task. The high performance was paired with a very low power consumption per calculation, 17 fJ per multiply-and-accumulate (MAC)

operation, realising an efficient system that removes the bottleneck in machine learning tasks commonly found in applications such as live video processing and autonomous driving [83].

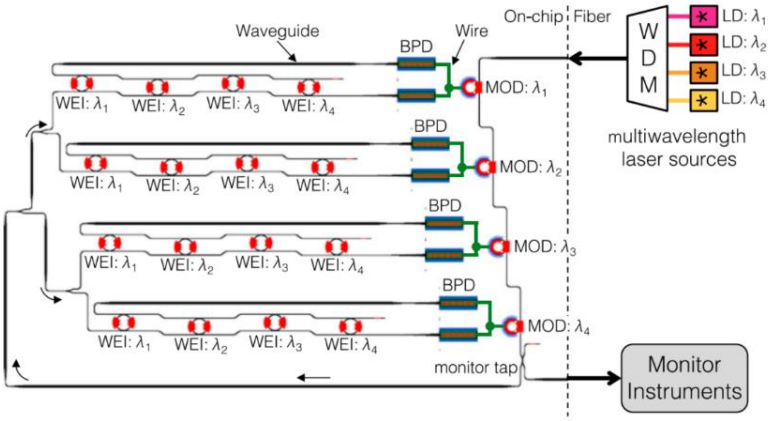

Figure 1.2.5 – A silicon photonic neuron. Micro-ring weight banks (WEI) and micro-ring modulators (MOD) are used in combination with balanced PDs (BPD) to create a broadcast-and-weight ANN. Multiple laser diodes (LD) are used as used as pumps sources. Green lines represent electrical connections. Figure reproduced from [77].

A very powerful neuromorphic processing technique, called reservoir computing (RC), has also found application on photonic platforms. RC, a technique directly related to RNNs, was first derived in the early 2000s as a means to reduce the costs of RNN training [84]–[86]. It was shown that successful performance could be achieved in RNNs by limiting the trained weights to those in the output layer [84]. In this configuration, nodes within the hidden layers of the network form what is called the reservoir. The nodes within the network are non-linear elements and the connections within the hidden layer are fixed. Any information that is injected into the reservoir is projected into a higher dimension where there is an increased chance of making the information linearly separable [84]. This makes reservoirs capable of performing tasks such as classification, where information that's difficult to distinguish can be separated by hyper planes in the reservoirs higher dimensional space. The concepts of echo state networks and liquid state machines both fall within the framework of RC [87], with extreme learning machines operating with a similar principle but without recurrent connections [88]. In photonics there have been reports of silicon photonic RC systems [89], and systems based on SLs with delayed optical

feedback [90], [91]. These systems have demonstrated impressive performance at numerous complex processing tasks including pattern recognition and image classification, time series prediction, and the post processing of signals received during communications [92]. The recent reports of photonic RC systems using VCSELs will be discussed in more detail in the upcoming Chapter 1.6.

Finally, neuromorphic SNNs, specifically software-implemented SNNs, have recently found application in a number of image processing tasks. Numerous reports detail the impressive performance of the software SNNs when combined with different photonic sensors [93]–[95]. The software SNNs have been combined with dynamic vision sensor cameras [93], neuromorphic vision sensors [94], and single photon avalanche detectors (SPADs) [95], that collect image information directly in a spiking representation. The hybrid sensor-software SNN is then used to directly perform convolution and pooling with the spiking input signals, to achieve different image classification tasks. Software SNNs have also shown lower energy requirements per operation than other ANNs. Latency in SNNs is low, due to only the active parts of the network requiring computation [96]. Overall, these reports of SNNs highlight the great potential of future experimental SNN realisations, which utilise the performance, energy efficiency and fast operation speeds of photonic technologies for neuromorphic processing systems.

In summary, neuromorphic computing systems, which take inspiration from biological neurons and neural networks, can therefore be implemented to realise complex computing tasks. The highly parallel nature of ANNs allows the computation to spread across the network removing the bottleneck that occurs in traditional digital processors. The field of photonics has additional advantages to offer when realising neuromorphic platforms, including high bandwidth, high efficiency and ultrafast speeds (multiple orders of magnitude faster the MHz timescales of electronic approaches [72]). A photonic platform that has shown great promise is that of SLs, which offer underlying nonlinear dynamical responses analogous to those found in biological neurons but at ultrafast speeds. In order to engineer future photonic ANNs, and unleash the computation power of neuromorphic systems, we look to creating artificial neurons with key-enabling VCSELs, as it will be discussed in detail in subsequent Chapters of this thesis.

1.3 Semiconductor Lasers

Lasers are a special type of light source that produce intense beams via the process of stimulated emission. The term LASER is an acronym of Light Amplification by Stimulated Emission of Radiation, and the focused beam of light emitted by lasers is characteristic. Laser beams are known for a number of useful properties including; directionality, they typically emit light in a single direction; coherence, the emitted waveforms have a constant or zero phase difference that does not change with time/space; near-monochromaticity, the wavelength of emitted light has a small linewidth [97].

The application of these light-emitting devices has undoubtably shaped the world around us, with a near endless list of disciplines benefiting from the technology. In industry, lasers are used for cutting, welding and cleaning. In medicine and cosmetics, they are used for tattoo removal, eye surgery, dermatological skin treatments, and imaging (through techniques such as tomography and microscopy [98]). Other applications, such as Light Detection and Ranging (LIDAR) use laser beams to scan landscapes, providing information on ranges for navigation, contributing massively to recent demonstrations of driverless vehicles [99]. Even in information technology they are responsible for optical storage, including the reading and writing of DVDs and Blu-rays. One field that has benefited significantly from the development of lasers is optical communications. The optical transmission of data through optical fibre has increased the speed of data transfer by multiple orders of magnitude, while enabling low loss, long distance connections [100]. Lasers are therefore utilised in many everyday technologies although it may not initially be obvious. One of the most common laser types, semiconductor lasers (SLs), are frequently found in optical communications and mobile technology thanks to their unique small compact structures, long lifetimes, and high efficiencies [101].

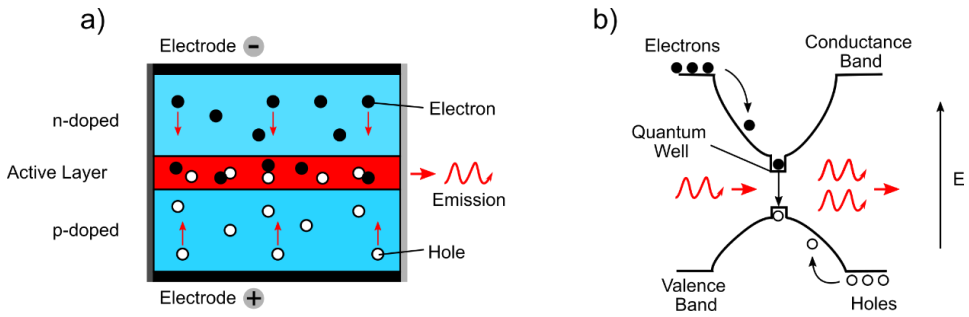

Figure 1.3.1 – (a) Schematic of a basic Semiconductor Laser. Electrons and holes from n- and p-doped semiconductor materials respectively, recombine to yield light emission. Light is confined between two reflective surfaces and extracted through one partially transparent mirror. (b) Energy band diagram of a Quantum Well (QW) laser undergoing stimulated emission. The QW's high refractive index difference improves emission efficiency.

SLs built using semiconductor materials, were first experimentally reported in 1962 [102], [103]. Since then, a large number of devices have been realised with different emission wavelengths, optical emission powers, polarisations and internal structures [104]. The operation principle of SLs is similar to that of forward-biased p-n junctions. Two doped semiconductor materials (one with n-donor and one with p-acceptor impurities) are sandwiched between two reflecting mirrors (see Fig. 1.3.1 (a)). Where the p and n-doped materials meet, is known as the active region. In the active region each semiconductor material has an associated band structure and band gap energy between the conductance and valence band. When a forward bias (approximately equal to the band gap energy) is applied to the material, electrons reach the conductance band where they can recombine with holes. Electron-hole recombination creates the emission of photons with energy approximately equal to the band gap energy. This process is called charged carrier radiative recombination and is the reason the frequency of laser light is generally dictated by the bandgap of the semiconductor material used to fabricate them. With electrons in the conduction band, stimulated emission can also occur, whereby an incoming photon of suitable energy stimulates the emission of another identical photon. Therefore, in order to achieve the lasing condition, the system must be pumped to population inversion, where more electrons exist in the conductance band than in the valence band. Here, during population inversion, the probability of radiative interactions (due to

stimulated emission) is higher than the probability of photon absorption. Therefore, the rate of stimulated emission overcomes the rate of optical losses, producing amplification and gain in the system (the lasing threshold) [105]. Pumping in SLs is typically achieved using an electrical current injection (as in p-n junctions) but can in some cases also be achieved by the optical absorption of light. The mirrors of the laser form a Fabry-Perot (FP) cavity with the gain section, allowing the light to be reflected and amplified repeatably. Light is extracted from the cavity by making one (or both) of the mirrors partially transparent. In semiconductor structures, the cavity mirrors are not always external and can instead be implemented using structures such as Distributed Bragg Reflectors (DBRs), a periodic structure of materials with alternating refractive indices that achieve high reflectivity through the interference of partial reflections.

Most modern SLs also feature additional heterostructures within the active region of the laser to help improve efficiency. One example is the widely adopted quantum well (QW) structure. In these QW SLs the active region consists of one of more layers of thin semiconductor material (thickness is smaller than the wavelength of the carriers), with a specific band gap. The thin QW layers impose quantum confinement on the carriers, restricting their motion within the plane of the film (see Fig 1.3.1 (b)). This improves the efficiency of QW structures allowing them to achieve lower threshold operation with a selectable frequency [106]. Stacking multiple QW layers at the peak of the laser standing wave can make use of resonant period gain to produce large amounts of optical gain. Various heterostructures that further confine the movement of free carriers in the active region, such as quantum wires and quantum dots (QDs), have also been realised [107], [108]. The selection of semiconductor material is also important as the gain depends on the α factor of the medium. The α factor, known as the linewidth enhancement factor, represents a coupling between the phase and gain of the light emitted by the laser. This arises from a carrier density-dependant refractive index and is responsible for the larger linewidth in SLs compared to other laser types. The α factor is therefore a non-linear effect which influences the dynamics produced by SLs under modulation and external optical injection [109].

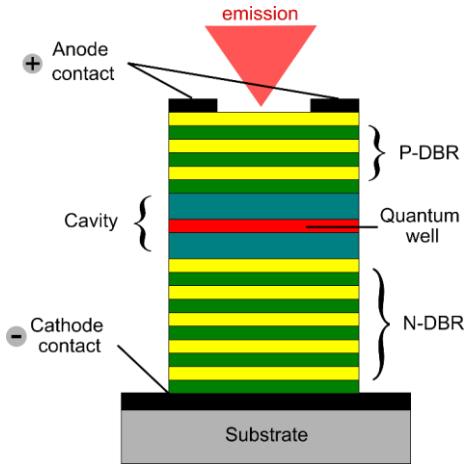

Figure 1.4.1 – A structure schematic of a vertical-cavity surface-emitting laser (VCSEL).

1.4 Vertical-Cavity Surface-Emitting Lasers (VCSELs)

SLs come in a variety of structures, but one in particular represents a growing section of SL research and application, the Vertical-Cavity Surface-Emitting Laser (VCSEL). VCSELs, known characteristically for their vertical light emission, are a design of SLs that have found a range of applications in-part thanks to their compact structure [110] and reduced manufacturing costs. VCSELs, are typically grown either using molecular-beam epitaxy (MBE) [111] or metal-organic chemical vapour deposition (MOCVD), and consist of two DBRs surrounding an active layer (see Fig. 1.4.1). The top and bottom DBRs (green and yellow layers in Fig. 1.4.1) are normally doped p- and n-type to assist in the movement of carriers. Typically, the top DBR features fewer alternating pairs to create a highly reflective, yet partially-transparent, mirror to maximise light emission vertically from the top surface of the device's stack structure. The active layer (red) within the cavity features the chosen heterostructure (frequently QWs) and the laser cavity is pumped electrically through positive and negative electrodes (black layers). The whole stacked structure sits on a substrate (grey) which is in contact with a heatsink for temperature measurement and control. The whole stacked structure is short and compact, with the cavity length measuring approximately one wavelength of the emitted light. The reflectivity of the DBR mirrors are therefore required to be very high (>99%) due to the small size of the

gain region [112]. The stacked structure is one of the benefits VCSELs have over conventional edge-emitting lasers. The vertical structure means both wafer-scale manufacturing and testing are possible before packaging, helping increase the yield and reduce the price of the laser production. Additionally, thanks to their short symmetrical cavities, VCSELs have a circular beam profile and inherently produce a single longitudinal mode, making them capable of highly efficient coupling to optical fibres and ideal for creating integrated 2D arrays of on-chip integrated laser sources. Compared to edge-emitting lasers, VCSELs also have low threshold currents and low power consumption [113], making them appealing in modern applications where power is restricted (e.g. mobile technology). Finally, unlike edge-emitting lasers, the vertical emission and small cavity of VCSELs also requires us to consider the spin state of electrons during carrier recombination. When up and down spin transitions occur, light with either left-circular or right-circular polarisation is created. Due to cavity anisotropies (the ability to exhibit different properties along different axis) VCSELs can support emission in two different linear polarisation modes. The two polarisation modes exist in the fundamental spatial mode of VCSELs and are orthogonal (in polarisation) to one another. Due to birefringence and dichroism, the two modes exhibit slightly detuned frequencies and different gain, typically producing linearly polarised light along one favoured axis [114]. The polarisation properties of VCSELs are therefore unique and are interesting to applications that can exploit the switching of the dominant polarisation mode.

The first demonstration of a VCSEL was made in 1979 [96], with low threshold operation reported as early as 1987 [115]. The first room temperature continuous wave (CW) operation was achieved in 1989 with GaAs VCSELs [116]. Since then, further design improvements have been made to enhance their low-threshold performance. Methods such as reducing the lateral dimension of the active layer [117] and introducing better carrier confinement have been used to reduce current required for lasing. Improved carrier confinement has been realised using a number of techniques [118], such as; the use of ring or circular electrodes to limit the current flow; proton bombardment to create insulating layers that limit the spread of current; and the implementation of transparent insulating layers via oxidised AlAs. Gain enhancement, via the improved overlap of the optical field with the gain region, has

also been implemented using oxidised AlAs layers. The oxidised layers create optical confinement via a lensing effect due to a difference in refractive index.

The design and production of GaAs VCSELs, mainly operating at 850 nm, is thus well established and has been widely adopted for short-range optical communications [119]. Long wavelength VCSELs (operating at the 1300 and 1550 nm wavelength windows), desirable for long distance single-mode fibre-optic communications, have however experienced a slower development. The lack of lattice-matched materials that provide high gain and sufficiently high-refractive index contrast for DBRs, have provided a design challenge. The first 1300 nm long wavelength VCSEL was demonstrated in 1993 [120], and now 1300 & 1550 nm VCSELs are commercially-available through companies such as RayCan [121], Vertilas GmbH [122], and Alight Technologies [123]. The commercially-sourced VCSELs featured in this work, are monolithic devices with an active layer of InGaAs QWs and InAlGaAs/InAlAs DBRs. These devices were reliability tested for optical communications and have long-term sustainability with room temperature lifetimes of 2×10^7 hours [121]. These devices are also desirable for optical communication because of their high modulation capability. The small compact volume of the VCSEL structure enables high modulation speeds to be reached while remaining at low bias currents, with a high power conversion efficiency and low power consumption. Numerous modulation techniques have been used to reach high data transmission speeds with VCSELs (see [124] for a review), but recently an energy-efficient, directly NRZ-modulated optical link, consisting of a ~30 GHz VCSEL was reported to achieve the high data transmission rate 80 Gbit/s [125]. With other complex multi-VCSEL modulation schemes reaching 224 Gbit/s [126], and some industrial companies adopting VCSELs for 5G datacentres, the technology is at the forefront of research into >100 Gbit/s data transmission. The challenge in creating VCSELs capable of high-speed modulation lies in improving optical confinement, improving the gain of the active layer and reducing heat generation.

1.5 Optical Injection in VCSELs

In SLs the use of optical signals goes beyond the optical pumping of cavities. The high gain and non-zero α factor mean changes in carrier density affect the SL's emitted light. The α factor couples light variations within the cavity to its phase, hence any light-induced intensity changes influence the carrier inversion and the subsequent output field of the laser, creating dynamical effects [127]. This makes SLs susceptible to light from different sources such as external lasers and even reflections of its own emission (optical feedback). When a SL is subject to optical injection, it is placed into a unidirectional scheme where light from a master laser (ML) is injected into the device's cavity, referred to as the slave laser. During optical injection the frequency of the injected light is set close to the resonant frequency of the slave laser, prompting the injected light to interact with the slave's lasing emission. Optical injection adds an additional degree of freedom, meaning various laser dynamics can be observed (see [127], [128] for reviews). A wide range of dynamics have been demonstrated theoretically and experimentally in SLs over the last decades, including stable and unstable injection locking [129], oscillations [130], instabilities and chaos [131], [132], and four wave mixing [133].

The technique of optical injection was demonstrated with SLs as early as 1975 [134] with subsequent reports [135], [136] demonstrating the technique as a means to stabilise single mode operation. Injecting light from one laser into another can transfer the frequency characteristics of the master to the slave, synchronising the emission wavelength and linewidth. This helps ensure single mode operation in the slave laser, reducing intensity noise [137], [138], and laser linewidth [139]. Enhanced modulation bandwidth has also been observed through optical injection [140] making it a topic of interest to optical communication applications. These improved conditions are achieved thanks to optical injection locking. During injection locking the frequency of the slave follows the frequency of the master (frequency-locking) given two conditions are satisfied; the detuning between the injected frequency and slave frequency is sufficiently small; and the injected power is sufficiently high. Due to the red shift of the cavity, caused by the α factor and the carrier density dependant refractive index, the range in which locking is achieved is typically asymmetrical

around the cavity resonance. If the system is operated out-with the required frequency and power parameter range, the lasers become unlocked, and non-linear dynamics can occur. Both theoretical and experimental SL studies into the effects of injection power and frequency detuning have been made using small perturbation analysis [141], [142]. In these reports, the dynamics of a slave SL are mapped out by testing the stability of each point (in parameter space) to small fluctuations in phase, carrier density, and electric field. In these maps, injection locking exists for regions in parameter space at or close to stable solutions. However, where no stationary solution exists, the laser system can exhibit non-linear behaviours (e.g. oscillations, chaos etc.). At the boundaries between injection locking and non-locking regions, there are fundamentally bifurcation points, where stable solutions change to unstable solutions. Within the region of optical injection both stable and unstable injection locking regions exist. In the unstable region, chaotic bifurcations can occur, disrupting the injection locking of the laser system, and along the boundary of the bifurcation, periodic oscillations can grow to chaotic dynamics [104].

Optical injection in VCSELs is particularly interesting given the unique attributes granted by their design (e.g. compact structure, vertical emission, telecom wavelength, etc.). However, performing optical injection in VCSELs does require an additional consideration beyond the power and frequency of the injected signal. Due to the anisotropies of the cavity, the polarisation of the light injected into the VCSEL must be considered. The light polarisation of the external injection can be selected to align with either the parallel or orthogonal polarisation modes supported by VCSELs, hence realising parallel- or orthogonally-polarised optical injection schemes. Additionally, due to the high reflectivity mirrors used to fabricate the VCSEL cavity, interference with reflections typically reduces the total detected output power. Optical injection in VCSELs was first investigated in 1993 with an orthogonally-polarised injection configuration [143]. In this report, the orthogonally-polarised optical injection matched the polarisation of the subsidiary (non-dominant) mode of the VCSEL. It was observed that optically-induced polarisation switching of the dominant VCSEL mode readily occurred, with minimum power requirements, when the injection frequency matched that of the orthogonally-polarised mode. Following the polarisation switch, the originally dominant output mode of the VCSEL was

supressed and the new, orthogonal, output mode was injection locked to the master laser. This revealed that polarisation of the injected light should coincide with that of the subsidiary mode, to achieve polarisation switching most efficiently. The injection locking of the orthogonal VCSEL mode was also found to be bistable with injection power. The system remained locked to the ML through reducing power levels, despite the optically-injected power being lower than the initial injection locking requirement. This hysteresis effect, surrounding injection locking and polarisation switching, is caused by the presence of two local stable points in parameter space, and has been reported in multiple VCSEL systems [144]–[146]. Parallel-polarised optical injection has also been investigated in VCSELs, with similar results achieving the injection locking and ultrawide hysteresis cycles of 473 GHz [147], [148]. It has also been demonstrated that in the case of multimode VCSELs, polarised optical injection can be used to select the dominant mode for improved long-distance optical communications [149]. The dynamical response of the multimode VCSEL was also found to depend strongly on the polarisation of both the injection and the individual mode. The polarisation switching effect, and the presence of bistable locking regimes, also makes VCSELs particularly interesting in applications involving the processing of digital (on-off) optical logic and optical memory [150].

Optical injection in VCSELs, like in other SLs, has also found application in the generation of diverse laser dynamical responses. There have been a large number of reports focusing on optical injection in VCSELs, providing small perturbation analysis and stability maps [151]–[157]. Specifically, experimental stability maps, which detail the dynamics produced by orthogonally-injected VCSELs operating at 850 nm [151] and 1550 nm [152]–[154], have been reported. Similarly, there have been a number of reported laser dynamics produced using parallel injection configurations [155]–[157]. In a report by A. Hurtado et al. [152], both orthogonal and parallel injection configurations are studied in a 1550 nm VCSEL. Initially, the injection frequency was swept around the resonant frequency of the parallel mode and dynamics such as period one oscillations, period doubling and chaos, were observed for various injection powers. Due to the parallel mode of the VCSEL being dominant, the observed results showed strong similarities to the dynamics observed in other SLs [127]. However, under orthogonal injection different dynamical regimes

appeared in the stability map (see Fig. 1.5.1). Regions of stable injection locking (SIL), period 1 oscillations (P1) and irregular/chaotic (CH) dynamics were all observed. Each dynamical regime could be observed using a single injection power (dotted line) and four different detuning values (black dots). Notably, the region of stable injection locking was found to be symmetric around the resonant frequency of the VCSEL. This is thought to be caused by the difference in power emitted by the two polarisation modes. Initially, the orthogonally polarised mode is suppressed until optical injection into the subsidiary VCSEL is performed. The large ratio of injection power to subsidiary orthogonally-polarised power, which is much larger than that of typical injection into the parallel VCSEL mode, is thought to be responsible for the change in behaviour. Polarisation switching (PS) behaviour was obtained across all injection locking conditions and for positive detuning values where period 1 oscillations were occurring (a behaviour also observed in 850 nm VCSELs [151]). Injecting into the subsidiary orthogonal VCSEL mode can create periodic dynamics due to the beating of the injected signal with the orthogonal VCSEL mode. Here the periodic oscillations occur at a frequency equal to the detuning of the injection.

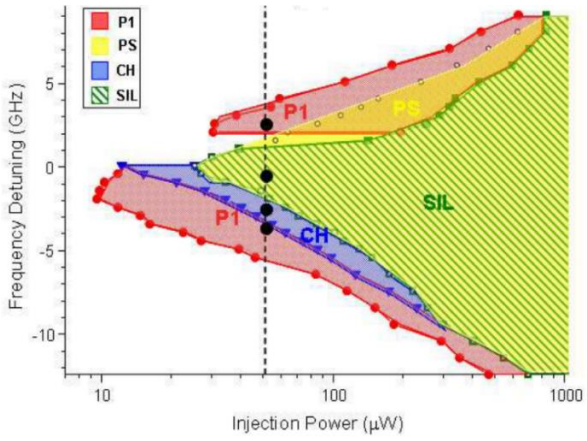

Figure 1.5.1 – Experimental stability map of a 1550 nm VCSEL device subject to orthogonally-polarised optical injection. The stability map shows the presence of stable injection locking (SIL), period 1 oscillations (P1), irregular and chaotic dynamics (CH), and polarisation switching (PS). Figure reproduced from [152].

Further, the total output dynamics observed by optically injected VCSELs are often the result of the interplay between both linear polarisation modes. A report by P. Perez et al. [158], explored the interplay of polarisation modes during the plotting of a stability map for an orthogonally-injected 1550 nm VCSEL. Two different bias current conditions were studied and the boundaries between distinct dynamical behaviours were identified. It was reported that one of the main differences between the negative and positive frequency detuning ranges, was the contribution from the two polarisation modes supported by the VCSEL. At positive frequency detunings, with increasing optical injection power, the orthogonal mode progressively dictated the dynamics of the VCSEL's total output. The orthogonal polarisation would provide periodic oscillations (period 1 & period doubling) while the parallel polarisation had a flat, weak contribution. At negative frequency detunings, both linear polarisation modes contributed to the total output dynamics. In some situations, both polarisations contributed oscillations, and in other cases, these would produce irregular dynamics. When both contributed to the total output, their dynamics were anti-correlated as the modes compete for dominant operation. The irregular dynamics observed were non-sinusoidal and pulse-like. These were produced near the injection locking boundary and displayed a broad frequency spectrum due to the dispersion in inter-pulse time. The inter-pulse time increased and broadened further when approaching locking due to the laser emitting more consistently at the orthogonal polarisation. VCSELs, subject to optical injection, are therefore well suited for the generation of a rich diversity of non-linear dynamical behaviours. Among these, VCSELs can access oscillations, irregular pulsating dynamics, chaos and injection locking; thus offering a plethora of diverse responses useful for numerous applications.

1.6 Neuromorphic computing with VCSELs

Novel photonic-based information processing platforms have a lot to gain from the potential implementation of novel architectures based upon VCSELs. As

discussed previously, VCSELs are excellent candidates for optical communication and networking, due to their possibility to operate at telecommunication wavelengths, their compact array-integrable structure, and efficient coupling to optical fibres. Importantly, their high efficiency, low power requirements and high-speed modulation capability makes them specifically appealing in modern day data processing applications where stringent energy and fast speed considerations are made. VCSELs have, however, received very important additional research thanks to their surprising capability to mimic the responses of biological neurons. Specifically, VCSEL-based systems have shown the means to generate non-linear responses, directly comparable to biological neurons, including the production of fast optical spikes. These optical spikes, similar to the neurons' electrical action potential, have been reported at ultrafast sub-nanosecond rates, multiple orders of magnitudes faster than the millisecond time scales of biological neurons [159], [160] and the microsecond timescales of recent electronic approaches [72]. Thanks to the initial interest in the non-linear dynamics of VCSELs subject to optical injection, a research-rich foundation for the generation of these neuromorphic responses exists. Therefore, we are now witnessing increasing amount of research into the potential realisation of spiking VCSELs for neuromorphic computing functionalities. In particular, VCSELs, like biological neurons, can exhibit excitability. A system is said to be excitable if a small perturbation, that forces the system away from a quiescent state, can result in a large excursion of the system before it returning to its original quiescent state. Excitability, like other types of non-linear dynamics, can be triggered in VCSELs when these devices are subject to optical injection and arises in the vicinity of bifurcation points in parameter space. Specifically, class 1 excitable pulses (spikes) can be generated by saddle-node bifurcations on a limit cycle (SNLC) or saddle-node bifurcations on an invariant cycle (SNIC) and is well described in numerous reports [18], [161], [162].

In 2010, A. Hurtado et al. [152] produced an experimental study on the dynamical behaviours of 1550 nm VCSELs subject to different types of linearly polarised optical injection. In [152], [158] a rich variety of non-linear dynamics were mapped in 1550 nm VCSELs across different optical injection powers and frequency detunings, including dynamics similar in appearance to excitable (neural-like) spikes.

The subsequent report by A. Hurtado et al. [163] then made the link between VCSEL dynamics and biological neurons, using linearly polarised modulated optical injection to build an artificial photonic spiking VCSEL neuron. In this demonstration, optical injection was made into the subsidiary polarisation mode of the VCSEL. An intensity modulator was used to generate short pulses that perturbed the system, triggering injection locking and polarisation switching. The polarisation-resolved output of the VCSEL revealed multiple types of excitable responses (both phasic and tonic spiking, see [18] for a review) could be made in response to the optical perturbation. The phasic spiking was produced as result of the system transitioning across the bifurcation point between the solitary and stable locking state. The phasic spikes appeared in both polarisations, at the onset of the perturbation in the orthogonal polarisation, and at the end of the perturbation (rebound spike) in the parallel polarisation. The oscillatory behaviour, resembling tonic spike firing, was produced in the orthogonal polarisation and increased in frequency as the strength of the perturbation increased. This was the first implementation of a dynamically-excited VCSEL neuron producing fast optical spiking at sub-nanosecond rates. This same optical injection method was later theorised in [164], to further explore neuron-like responses in long wavelength VCSELs. The theoretical results found that different excitable regimes existed around the injection locking boundary in both parallel- and orthogonal injection configurations. The numerical simulations showed that single, multiple, and burst excitable responses could be controllably triggered using optical perturbations.

Subsequently, the precise activation of excitable spiking responses in a telecom-wavelength VCSEL (at 1300 nm) was achieved experimentally in 2015 [160]. As theorised, by perturbing the bifurcation point at the injection locking boundary with short drops in injection power, the device transitioned through an excitable excursion, triggering a fast neuron-like spike. The emitted excitable responses were observed in the total output power of the VCSEL and were achieved with both parallel and orthogonal injection polarisations (see Fig. 1.6.1 [160]). The excitable responses produced were approximately 100 ps-long and highly consistent, yielding near identical responses across 100 consecutive perturbations. The precise control of the neuron-like excitability was also achieved through the manipulation of the

injected perturbation. Increasing the duration of the stimulation produced continuous tonic spiking with a controllable number of sub-nanosecond long spikes elicited. Similarly, variations in the strength of the stimulation revealed that an activation threshold existed within the system, where a response was only fired if the input signal (stimulus or perturbation) was sufficiently strong. The gating of excitable responses, also observed in biological neurons [15], is an exciting prospect for spike-based information processing, potentially enabling VCSELs to operate (like neurons) as optical threshold-and-fire elements. This report by A. Hurtado et al. [160] therefore demonstrated that excitable spikes could be activated with precise control in telecom-wavelength VCSELs upon the arrival of user-defined optical perturbations, enabling the further investigation of VCSELs as artificial spiking photonic neurons. The experimental technique applied in [160], forms the foundation for much of the research conducted in this thesis. The activation of ultrafast spiking dynamics, via modulated optical injection, is therefore discussed further in Chapter 3, alongside results collected from our existing VCSEL-based neuromorphic photonic systems.

Excitable pulses have also been observed in short-wavelength VCSELs (at the 980 nm wavelength window) subject to phase-modulated optical injection. Using a phase modulator, M. Turconi et al. [165] introduced 100 ps-long phase jumps of increasing amplitude and measured the response of the VCSEL. The report showed that low amplitude phase jumps produced no visible response, however like the activation threshold observed previously, increasing amplitudes triggered increasingly consistent excitable responses. This confirmed that like biological neurons the excitability present within VCSELs, here activated via phase modulation, have the activation threshold behaviour required for neuromorphic processing. Additionally, it was demonstrated in this report that modulation of the driving current of the VCSEL could trigger the excitable regime. The electrically-triggered spiking responses were found to be less reliable and longer (typically 1 ns in duration) than those produced by phase modulation, but nevertheless broadened the scope of methods for implementing controlled spiking in VCSEL neurons.

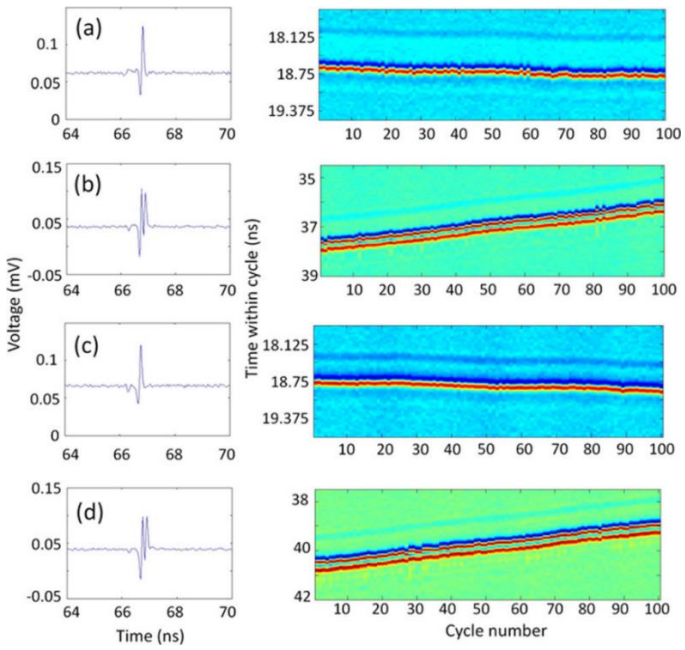

Figure 1.6.1 – Time series (left) and temporal maps (right) of a 1300-nm VCSEL neuron under (a)-(b) orthogonal and (c)-(d) parallel optical injection. The time series show (a) & (c) single and (b) & (d) bursts of excitable responses. The temporal maps reveal the consistency of 100 consecutive responses from the VCSEL neuron. The colour of the map is scaled to the amplitude of the associated timeseries. represents Figure reproduced from [160].

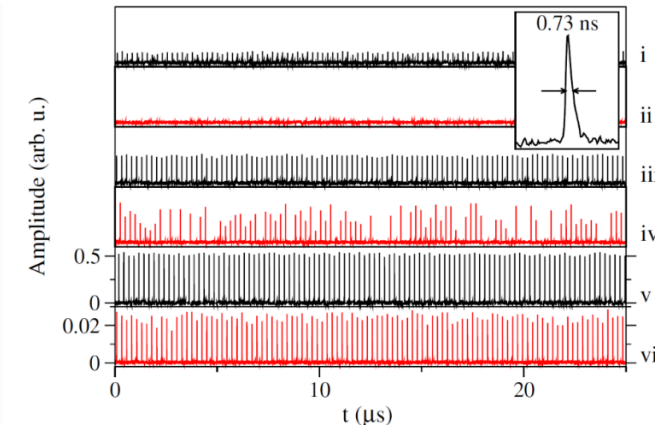

Figure 1.6.2 – Experimental time series of a 980 nm micropillar laser with an embedded saturable absorbing (SA) region subject to modulated optical pumping. Time series show the consistency of 100 excitable responses (red) to input pulses (black) of 0.4 (i,ii), 1.0 (iii,iv) and 1.78 (v,vi) input strength (scaled to the excitability threshold). The inset shows a 730 ps excitable response from the VCSEL-SA taken from series vi. Figure reproduced from [159].

More recently, phase modulated optical injection has been applied in the activation of excitable spikes in VCSEL memory systems, using optical feedback connections [166]. Further, resonant-and-fire and integrate-and-fire excitability mechanisms were released in VCSELs subject to phase modulation [167], towards the further mimicking of neuronal behaviour. In Chapter 3 of this thesis, we will also explore the possibility of controllable spiking in VCSELs via current modulation. This method of achieving neuron-like responses enables VCSELs to receive electrical inputs, expanding the potential methods of interconnecting VCSELs-neurons in larger neuromorphic systems.

Short-wavelength (980 nm) optically-pumped micropillar lasers with vertical light emission (with a similar structure to that typical of VCSELs) and containing an intracavity saturable absorber (SA) section have also been shown to exhibit excitability [159], [168]–[175]. From now onwards, we refer to these devices as VCSEL-SAs. In a first report by S. Barbay et al. [159], a 980 nm VCSEL-SA, optically pumped with 800 nm light, was demonstrated to produce self-pulsating dynamics when biased close to its lasing threshold. It was demonstrated that by operating the VCSEL-SA around 90% of its lasing threshold, and modulating the optical pumping with short pulses, fast 0.73 ns-long excitable pulses could be triggered at the VCSEL-SA's output. Here the system's cross from sub-threshold operation to the lasing state (influenced by the nonlinear effect provided by the SA section) represents a bifurcation in which excitability is produced. By altering the intensity of the optical pump, the existence of a spike activation threshold was again observed (see Fig. 1.6.2 [159]). At a low optical pump intensity, a stable non-lasing state was produced, however, further increasing the optical pump saw the consistency of the excitable response increase, confirming the neuronal threshold-and-fire behaviour in a VCSEL-SA with modulated pump current. Further, additional reports on the firing latency [168] and maximum frequency (refractoriness) [169] of the neuronal responses in VCSEL-SAs have appeared. Recently VCSEL-SAs have also demonstrated the exciting capability to temporally integrate multiple inputs towards the firing of excitable pulses (integrate-and-fire) [170], another highly desirable behaviour for the realisation of neuromorphic systems. Overall, the excitable

neuronal responses produced by VCSEL-SAs have been well described using the numerical Yamada model for a laser with a SA [171], [172]. Recently, a numerical investigation into the potential networking of evanescently coupled VCSEL-SAs has been reported [173]. In this work, a chain of spatially coupled VCSEL-SAs demonstrate that excitability can be passed into neighbouring devices, producing ~200 ps-long excitable responses. By simulating different architectures and exploiting the integration of multiple inputs, V. A. Pammi et al. [173] revealed networks of VCSEL-SAs can realise neuromorphic spiking logic and spike-pattern recognition circuits. Similarly, spiking memory systems created with VCSEL-SAs and optical feedback loops have been used to write, store and erase spike trains [174], [175], realising the neuronal behaviour of autaptic (self-feedback) neurons [176]. To date, these devices only allow operation under optical pumping schemes, and we are not aware of any reports of electrically-injected spiking VCSEL-SAs. This feature might ultimately limit the use of these micropillar-SA devices in future interconnected functional neuromorphic photonic systems. Hence, important research efforts remain to demonstrate photonic spiking neurons based upon electrically-injected VCSEL-SAs.

The use of excitability in VCSELs for neuromorphic applications has been thoroughly investigated theoretically in literature, via the Yamada [172] and Spin-flip models (SFM) [114]. Alongside the body of theoretical results presented in the previously discussed reports (modulated optical injection [160], [163]–[165] and modulated optical pumping [159], [168]–[170]) some groups have focused predominantly on the numerical investigation of VCSEL photonic spiking neurons. One of the first theoretical reports to describe the potential of VCSELs as artificial neurons for ultrafast computing, was made by M. A. Nahmias et at. [177]. This theoretical report revealed that by modulating the gain within the cavity of a VCSEL-SA (either optically or electrically), excitable responses could be generated at sub-nanosecond (sub-ns) rates. Furthermore, this report demonstrated that VCSEL-SA neurons could operate analogously to leaky integrate-and-fire (LIF) neurons. As demonstrated in Fig. 1.6.3, multiple inputs, insufficient to trigger the excitable response independently, can summate within a short integration period to reach the threshold requirement for spike activation. Alongside the theoretical LIF behaviour

of the VCSEL neuron, different networking architectures (such as mutual optical coupling and optical feedback arrangements) were also discussed. This report highlighted that VCSEL neurons are therefore theoretically capable of the basic spike processing model (LIF) which enables artificial neural networks to processing information. In Chapter 5 we explore experimentally the temporal integration of optical inputs in our VCSEL system and apply the neuronal behaviour to achieve initial reports of information processing.

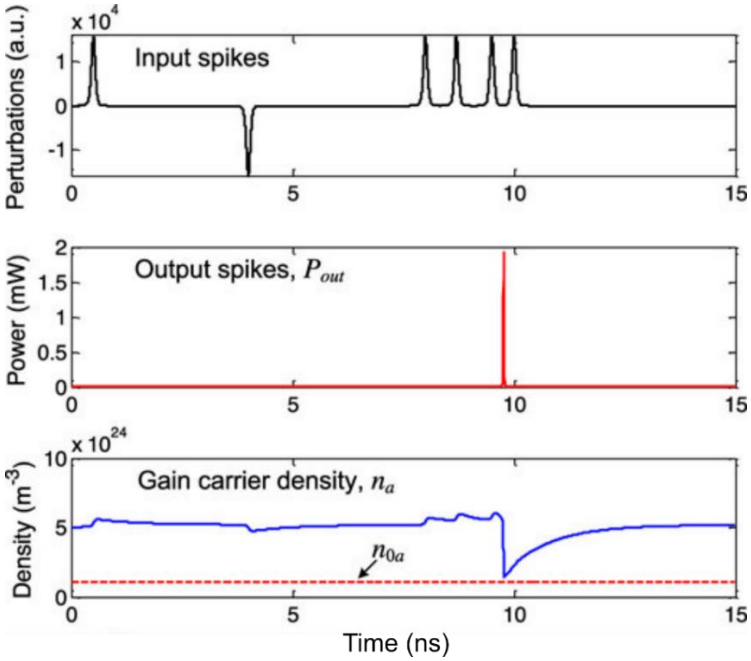

Figure 1.6.3 – Numerical simulation of a VCSEL-SA acting as a Leaky Integrate-and-Fire (LIF) photonic neuron. Inputs (top/black) are used to modulate the carrier concentration (bottom/blue). The output of the VCSEL-SA (middle/red) activates an excitable response when multiple inputs occur successively. Figure reproduced from [177]

Further theoretical reports have been made on the excitable behaviour linking VCSEL to biological neurons. In 2016 S. Xiang et al. [178] reported numerical results based on the SFM that replicated the experimental results of an earlier work by A. Hurtado et al. [163]. This report demonstrated that both phasic and tonic spike-like excitability could be observed from a VCSEL under linearly polarised optical injection, validating the earlier experimental findings. S. Xiang et al. later expanded

on this work by exploring similar cascadable spiking signals in multiple coupling configurations [179]. The use of polarisation mode competition in VCSEL-SAs has also been reported as a mechanism for spike inhibition [180]. A significant amount of theoretical work has since been produced by this group, and others, on the spike processing capabilities of VCSEL neurons. A wide variety of tasks ranging from spike-based convolution neural networks for image processing [181], spike information encoding [182]–[185], spike pattern recognition [186], [187], unsupervised learning via spike-timing dependant plasticity (STDP) [188]–[190], sudoku solvers [191], and spiking XOR gate implementations [192] have all been reported theoretically.

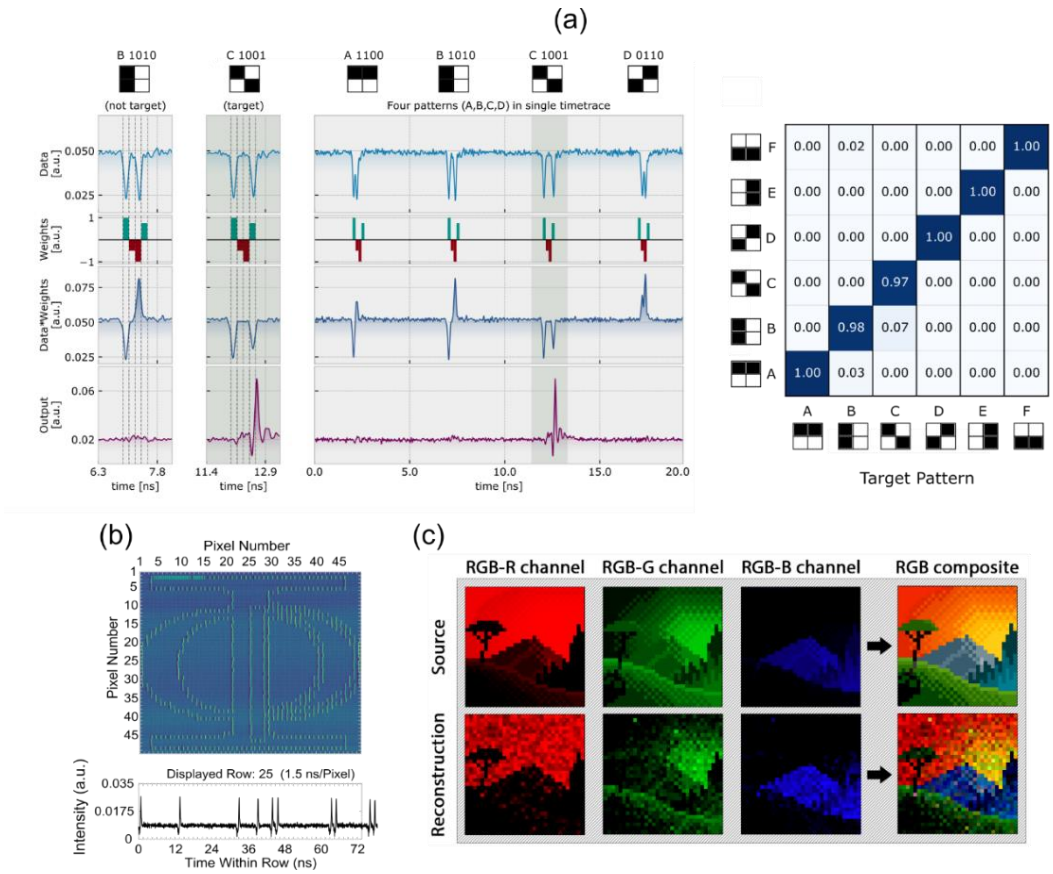

Figure 1.6.4 – VCSEL neuron-based neuromorphic processing demonstrations. Reports of (a) experimental 4-bit pattern recognition [193], and (b) spiking image edge detection [194] are expanded upon in this thesis (Chapter 5). (c) Fast spike rate encoding is used to represent a RGB image [195]. Three colour channels are encoded into spikes and recombined to recreate the source image. Figures reproduced from [193]–[195].

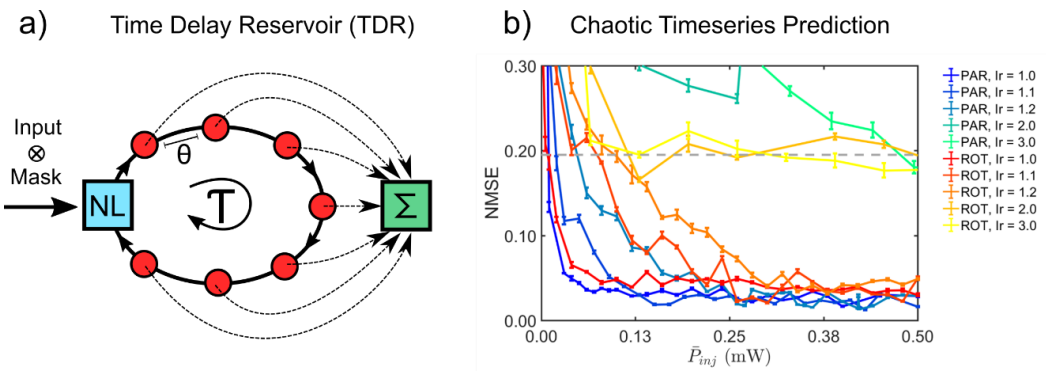

Figure 1.6.5 – (a) Schematic of a Time Delay Reservoir (TDR). A non-linear (NL) element with a T-long delay is sampled every θ to create a virtual network of nodes. (b) Performance of a VCSEL-based RC during a chaotic timeseries prediction task [205]. Two polarisation configurations were tested. Parallel-polarised optical injection and feedback produced the lowest normalised mean square error (NMSE) of 0.012. Figure reproduced from [205].

Only recently experimental reports of spiking VCSELs for neuromorphic processing have come to light. A large majority of the experimentally realised neuromorphic spiking VCSELs reported in literature [193], [194], [196]–[202], are generated through the research described in this thesis. These results, presented in Chapter 3-5 of this thesis, have produced reports of spiking VCSELs capable of spike activation/inhibition [196], [197], spike communication in feedforward networks [198], [199], retinal neural circuits [200], integrate-and-fire operation for pattern classification [193] (see Fig. 1.6.4 (a)), and convolution for image processing and classification [194], [201], [202] (see Fig. 1.6.4 (b)). Similarly, additional works on experimental VCSEL neurons by our group at Strathclyde, not directly included in this thesis, have demonstrated the ability to perform spike-based rate encoding. Hejda et al. [195], [203] demonstrated that experimental VCSEL neurons, like their biological counterparts, have a spike latency and inter-spike period dependant on the input signal. This has since been used to demonstrate precise spike-timing encoding for digital-to-spike conversion (at rates over 1 Gbps) [203] and for the fast rate-encoding of image colour information for spike-based image processing tasks [195] (see Fig. 1.6.4 (c)). Similarly, work from other groups have shown that spiking VCSEL neurons can be used to emulate pyramidal neurons for the realisations of XOR classification tasks [204]. These reports therefore make up some of the

experimental demonstrations of VCSEL neurons mimicking the spiking behaviour of biological neurons.

Beyond spike-based demonstrations of VCSEL neurons, compact, fast and energy efficient VCSELs (and the rich variety of non-linear dynamical behaviours they can display), have found additional important applications in non-spiking neuromorphic processing systems. Specifically, VCSELs have been used to create photonic reservoir computing (RC) systems. As discussed previously, reservoir computers are a specific type of RNNs which operate with a set of fixed network connections and non-linear nodes [206]. To date there have been demonstrations of two types of photonic RC systems based upon VCSELs, namely time-delayed reservoirs (TDRs) and spatio-temporal reservoirs (STRs). The former make use of a single VCSEL (as a non-linear element), optical injection, and an optical delay line, which continuously feeds information back into the VCSEL (see Fig. 1.6.5 (a)). A virtual network of nodes is then created by interpreting the output of the system at discrete times as the output of different nodes. Due to the fixed connections within the virtual neural network, the output weights of the system can be trained using known input values, allowing the system to be tasked with complex information processing problems, such as timeseries prediction and classification. The first VCSEL-based demonstration of a TDR with a VCSEL was made by Vatin et al. [207], [208]. These numerical [207] and experimental [208] reports showed that not only was reservoir computing possible with VCSELs but that because of the interplay of two orthogonal polarisations, the performance achieved could be enhanced. Specifically, in [208], it was shown that error-rate of a channel equalisation task and a chaos prediction task were below the state of the art at the time, due to the ability to use select feedback polarisation. In a more recent report by J. Bueno et al. [205], a full comprehensive study of how polarisation configurations (parallel or orthogonal) affected the performance of prediction (the benchmark Mackey-Glass) and classification (the channel equalisation) tasks. This report, which utilised an off-the-shelf commercial telecom-wavelength VCSEL, concluded that a parallel configuration provided the system with more memory and slightly better performance, helping again realise neuromorphic processing with competitive error rates (see Fig. 1.6.5 (b)). STRs based upon VCSELs, only very recently demonstrated experimentally, operate

similar to TDRs but instead of temporally multiplexing the virtual nodes, the nodes are spatially multiplexed across the surface of a Large Area-VCSEL (LA-VCSEL) [209]. Information is input into the system via a digital micromirror device (DMD) and a multimode fibre that project spatial patterns onto the top facet of the LA-VCSEL. The nodes of the network are therefore the spatially multiplexed positions on the devices surface which interact via carrier diffusion and optical diffraction. A near field image of the LA-VCSEL surface is reflected onto a second DMD where it is collected by a detector. In this VCSEL-based SDR the output weights are trained by altering the output collected by the DMD. A comprehensive analysis on the performance of the spatio-temporal reservoir under different consistency and dimensionality, as well as various optical injection conditions, was recently published by A. Skalli et al. [210]. VCSELs are therefore devices capable of producing powerful photonic reservoir computers. These demonstrations highlight the potential VCSELs have for high performance, high efficiency and high-speed neuromorphic processing functionalities.

Towards implementing artificial SNNs with VCSELs, we have recently demonstrated that VCSELs can act as photonic weighting synaptic elements. These results, achieved by myself as main author, have only been very recently reported and are therefore not fully discussed in this thesis. However, we deemed important to include the results here for completeness, in addition to the main body of results on spiking VCSEL neurons for neuromorphic photonic systems that are presented in subsequent Chapters of this thesis. Specifically, in this recent work we showed that VCSELs operating just below their lasing threshold current, acting therefore as vertical cavity semiconductor optical amplifiers (VCSOAs), can indeed operate as high-speed photonic weighting synaptic elements. Optical injection in 1550 nm VCSOAs was first shown experimentally to provide non-linear gain to injected signals [211]. Later a theoretical investigation, as part of a spike-timing dependent plasticity study [188], revealed that the gain could be provided to incoming optical pulses. However, only recently we demonstrated experimentally a VCSOA acting as a photonic weighting synapse [212].

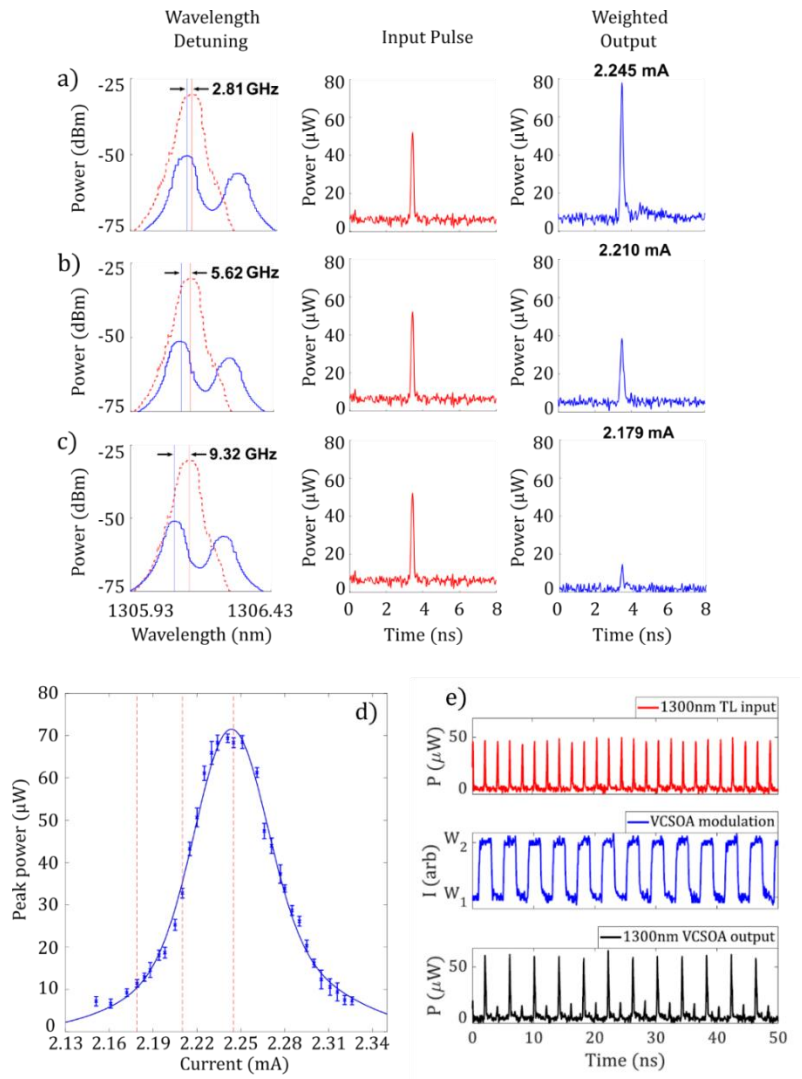

Figure 1.6.6 – Optical spectra of the injection (red) and VCSOA (blue) signals for various detuning frequencies of (a) -2.81 GHz, (b) -5.62 GHz, and (c) -9.32 GHz (corresponding to different VCSOA bias currents). Timeseries of the input pulse (red) and the weighted VCSOA output pulse (blue) are shown. The mean output optical pulse peak power is plotted against applied bias current for a (d) 1300 nm VCSEL, n = 6. The red vertical lines indicate cases (a)-(c). (e) High speed dynamic weighting is achieved by modulating the bias of the VCSOA. Figure reproduced from [212].

In this report, we exploited the non-linear gain profile to control the amplification of injected pulses via the VCSOA's bias current. By altering the driving current, the resonant frequency of the VCSOA was selected, and hence amplification was seen by the optical pulses. This effectively realised a large controllable weighting range.

As shown in Fig. 1.6.6, a bit precision of 11.6 was achieved (using in this case a 1300 nm VCSEL), making this photonic weighting approach comparable to weighting schemes based on micro-ring resonators [213] and phase change materials [214]. Very high-speed dynamic weighting was also achieved with these photonic synapses by modulating the driving current of the device (see Fig. 1.6.6 (e)). This realised a system where weights could be changed on the fly and output pulses customised at near GHz rates with faster rates expected for future optimised device designs.

Combinations of VCSEL-based photonic synapses have also been investigated for neural network operation [215]. In-series VCSOAs were shown to create a system capable of both input encoding and input weighting, and in-parallel VCSOA synapse were combined in a photodetector to realise fast multiply and accumulate (MAC) operations. These VCSEL-based photonic synapses are therefore suitable for the creation of neural networks capable of tasks such as convolution and image processing, with added benefit of potential amplification between network layers to counteract signal loss. Importantly, the power consumption of these adjustable photonic weighting systems is low, with operation achieved using μWs optical injection powers and small μAs bias current changes for weight tuneability.

The research into VCSEL-based optical neurons for computing has therefore revealed the potential of this exciting technology. VCSEL neurons have demonstrated excitable threshold-and-fire functionality and have theoretically been shown to operate as artificial LIF photonic neurons. This creates exciting possibilities for VCSEL-based spike-processing systems and SNNs capable of delivering complex light-enabled processing functionalities (e.g. image processing, computer vision, pattern recognition, etc.) using ultrafast neural-like spikes to operate. Further, the computational power of neural networks based upon (non-spiking) VCSELs has been realised through photonic RC systems, achieving state of the art performance with high speed and low power operation. For this reason, in this thesis we investigated VCSELs as high-prospect candidates for photonic neuromorphic systems.

1.7 Thesis Outline

In this thesis we provide an investigation of VCSELs as artificial photonic spiking neurons for use in future light-enabled neuromorphic information processing systems. In Chapter 2 we provide the experimental methods used in this work to achieve neuromorphic operation with spiking VCSELs neurons. Specifically, in Chapter 2 we introduce the equipment and experimental methods used, provide a characterisation of the VCSELs used in this work and introduce the numerical model utilised to simulate the neuronal-like responses that can be elicited in VCSELs. In Chapter 3 we provide results on the activation of neuronal responses in VCSELs, including spike activation, spike inhibition, and input thresholding, via external optical injection. In Chapter 4 we provide results on the interconnection of multiple VCSEL neurons in different network configurations. Specifically, we investigate the communication of dynamics between interconnected devices, devices in a 1-to-2 converging architecture, and explore a 3 VCSEL implementation of a biological retinal neural circuit. Finally, in Chapter 5 we report novel results that implement VCSEL neurons for functional information processing demonstrations. Specifically, we discuss how we can achieve the temporal integration of inputs with our VCSEL neurons and how we utilise this neuronal behaviour for information processing tasks. We experimentally realise systems of VCSEL neurons capable of tasks such as 4-bit pattern recognition and image processing functionalities (e.g. edge detection and classification) at ultrafast rates.

Chapter 2

Experimental Methods for the Investigation of Neuromorphic Photonic Systems

Neuromorphic computing systems were introduced in Chapter 1, where we discussed the benefits that can be achieved by emulating biological neurons for information processing. We introduced some of the platforms, both electronic and photonic, that have been used to emulate the computational features of biological neurons and highlighted semiconductor lasers as promising devices for photonic implementations of neuromorphic processing systems. Specifically, we introduced VCSELs as compact, high-speed and efficient devices for application in artificial neuronal models for neuromorphic photonic hardware. In this Chapter we will discuss the experimental equipment used during our investigation of VCSELs for neuromorphic photonic functionalities (Chapter 2.1). We will provide a characterisation of the VCSELs used in this work and will demonstrate the use of optical injection to excite a wide range of non-linear dynamics in VCSELs, including characteristic high-speed neural-like spiking responses (Chapter 2.2). Finally, we numerically investigate the dynamical operation of VCSELs for use in neuromorphic photonic implementations (Chapter 2.3).

2.1 Experimental Arrangements for Neuromorphic Photonic Implementations with Semiconductor Lasers

This Chapter describes the off-the-shelf telecom-wavelength fibre-optic components and various equipment used for the investigation of semiconductor lasers for neuromorphic photonic functionalities.

2.1.1 Laser Driving and Controls

The lasers predominantly used in the experimental work of this thesis are VCSELs. Specifically, we used commercially-sourced (RayCan Co., Ltd.) VCSELs operating at telecom wavelengths (1310 and 1550 nm). These were packaged (TO-56/TO-90) devices coupled with single-mode fibre pigtails of either FC/PC (physical contact) or FC/APC (angled physical contact) fibre connections. We discuss the characteristic of these lasers in Chapter 2.2. These packaged devices are electrically driven and temperature controlled using laser diode mounts (Thorlabs LDM21 and LDM90). These mounts, in addition to permitting the application of bias currents to drive the devices, also contain integrated thermal cooling elements and thermistors enabling precise temperature control and stabilisation. The mounts are connected to temperature controllers (Thorlabs TED200C), which monitor the temperature of the VCSELs and offer temperature control up to a range of 0 to 70 ºC. Bias currents are applied to the VCSELs through laser current drivers (Thorlabs LDC205C), providing maximum currents up to 100 mA. In this work our VCSELs are typically stabilised around room temperature (20 ºC or 293 K). However, temperature values may be subject to change when specific wavelength operation is required. The VCSELs of this work also have low lasing threshold current requirements, with a typical operating current of around 4 mA used during the experiments.

The LDM90 mounts also permitted the direct modulation of the bias current applied to the VCSELs. The mounts have an internal bias-tee that can modulate the laser current at up to 500 MHz through a 50 Ω SMA (Sub Miniature version A) connection. In combination with an arbitrary waveform generator (AWG) or pulse generator (PG), we can electrically modulate the applied bias current to encode information in the output power emission of the VCSELs under investigation. The simple schematic in Fig. 2.1.1 shows the equipment used to drive and control the VCSELs used during this work.

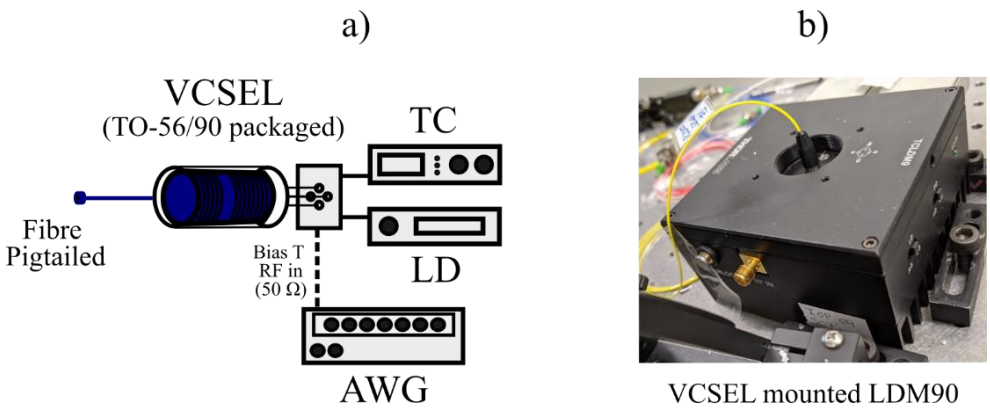

Figure 2.1.1 – (a) VCSEL control schematic. A 4-pin TO-56/90 packaged, fibre-pigtailed VCSEL is mounted in a LDM90 and controlled using a laser driver (LD) and a temperature controller (TC). The VCSEL's current can be modulated through a bias tee using an arbitrary waveform generator (AWG). (b) VCSEL installed in an LDM90 mount (with SMA modulation input visible).

2.1.2 Fibre Optic Components

The experimental setups used throughout this work are created using off-the-shelf fibre-optic telecommunication components. These are used to alter and redirect the light both produced by and injected into the VCSELs acting as artificial optical neurons. The VCSELs operate at the wavelengths of 1300 and 1550 nm, aligned with the O- and C- telecommunication bands. This grants us access to a large number of commercial fibre-optic telecom components for the simple implementation of a multiplicity of experimental systems (as shown in Fig. 2.1.2), including:

Fibre optic isolators (ISO) - Attenuate light (>40 dB) in a single direction by exploiting faraday rotation in combination with a half waveplate and birefringent beam displacers. Isolators prevent backward reflections within our system, helping protect sensitive equipment and reduce the effect of unwanted feedback.

Optical couplers and splitters - Combine multiple paths or split a single path of light with a specified coupling ratio. Multiple optical fibres are fused and tapered to create different varieties including 1x2 port splitters/combiners, 2x2 port couplers and larger 1xM tree couplers. Both 3 port splitters and 4 port couplers are used (50:50

and 90:10 coupling ratios) to create our VCSEL networks and perform simultaneous analysis with multiple pieces of equipment.

Variable optical attenuators (VOA) - Controllably attenuate (1.5-50 dB) the optical power passing through them. A tuning element can variably deviate the beam path, altering the coupling efficiency to the output fibre. VOAs are used to control the optical injection and feedback power within our system and protect sensitive equipment from high optical powers.

Polarisation controllers (PC) – Controllably tune the polarisation of light within the fibre optic system. Stress induced birefringence is used to create fractional waveplates ($\lambda/4$, $\lambda/2$, $\lambda/4$) out of loops of single mode fibre. Altering the rotation of the fibre loops influences the polarisation of the output light. Here, the polarisation of injection and feedback are selected using these components, allowing different polarisation configurations to be investigated. Polarisation controllers also help to improve coupling efficiency into polarisation dependent components and equipment.

Optical circulators (CIRC) – Restricts the light flow to a single direction through the 3-port component. Light input at Port 1 sees output at Port 2. Light input at Port 2 sees output at Port 3. Light input at Port 3 sees large attenuation (50 dB). These devices operate like an isolator, making use of faraday rotation and birefringence to deviate the beam path. However, upon input at Port 2 the output is not neglected but collected at output Port 3. Circulators are used to simultaneously inject and collect light from the VCSEL devices in our systems.

The fibre optic cables used in this work to connect the multiplicity of optical components used, as well as the VCSELs under investigation, were predominantly single-mode fibres (SMF) and are non-polarisation maintaining (non-PM).

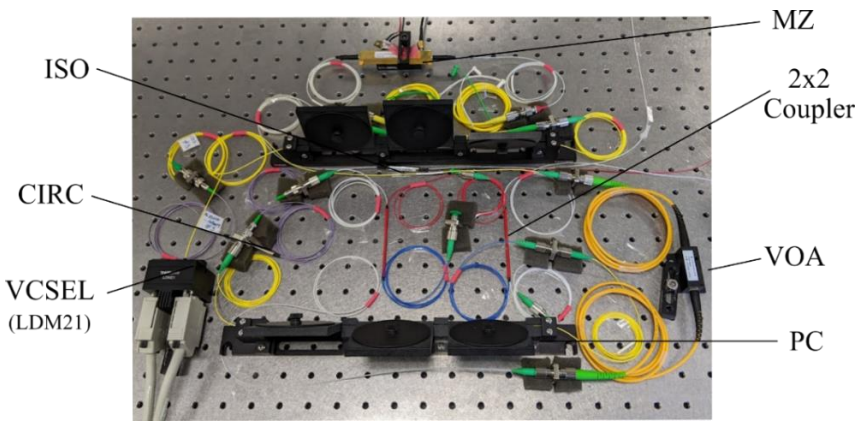

Figure 2.1.2 – Picture of one of the experimental setups used in this work including multiple fibre optic components, such as optical couplers, isolators (ISO) and circulators (CIRC), polarisation controllers (PC), variable optical attenuators (VOA) and a LDM21-mounted VCSEL. A Mach Zehnder (MZ) intensity modulator is also shown.

2.1.3 Optical Injection and Laser Modulation

Throughout our work we regularly use a technique called optical injection. This technique takes an optical signal and introduces it to an existing laser cavity. The injected optical signal can be created by another semiconductor laser source. The technique of optical injection was initially implemented to control the frequency and stabilise the output of the slave laser subject to injection [129], [137]. The laser source creating the injection signal is therefore called the master laser (ML). During optical injection an effect called injection locking can occur given the correct injection parameters (optical power, frequency & polarisation). During injection locking the frequency of the slave laser switches to that of the master and output oscillations become damped. However, under different operating conditions, optical injection can lead to a wide range of non-linear dynamics in the response of the slave laser, including neural-like spiking responses [127], [128], [152], [158]. Optical injection is therefore instrumental in this work to the creation of neuron-like dynamics in VCSELs for neuromorphic photonic functionalities.

The experimental setup created to investigate the effects of optical injection in VCSELs is shown in Fig. 2.1.3. The optical injection line consists of an external tuneable laser (TL), an optical isolator (ISO), a variable optical attenuator (VOA), a

Mach Zehnder (MZ) intensity modulator (driven by a power source, PS, and an AWG), two polarisation controllers (PCs), a 50/50 coupler, a power meter (PM), and an optical circulator (CIRC). These components, some of which are previously described, allow us to introduce a unidirectional optical signal into our slave laser with control over its optical injection power (via the VOA) and polarisation (using the PCs).

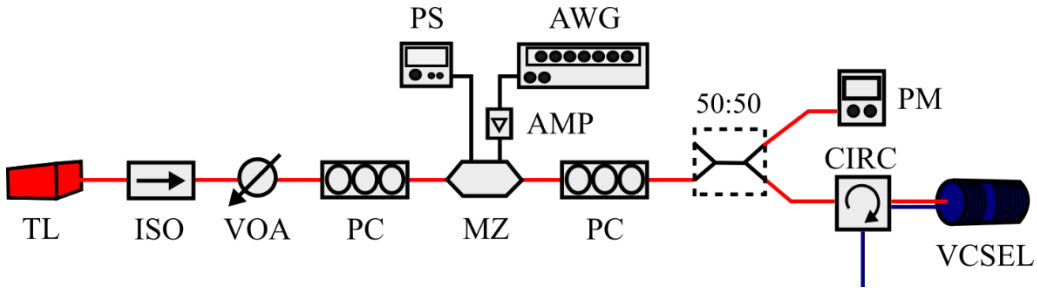

Figure 2.1.3 – Setup used to perform the modulated optical injection of a VCSEL.

As shown in Fig. 2.1.3, a number of components are required to create an optical injection line, however the most important component is the master laser source. In this work we use two master TLs, one at 1300 nm and one at 1550 nm:

Santec TSL-210V – Tuneable Laser (TL), >10 mW output power, 1260-1360 nm wavelength range, < 0.001 nm resolution.

Santec WSL-110 – Tuneable Laser (TL), 15 dBm output power, 1527-1567 nm wavelength range, 100 MHz resolution.

These widely TL systems offer wavelength tuning ranges of 100 and 40 nm, respectively, with fine tuning capabilities and high resolution. This permits to accurately select the wavelength at which we inject optical signals into the VCSELs under investigation. We operate VCSELs at both the 1300 and 1550 nm wavelength windows. Additionally, the TLs have moderately high optical power outputs, allowing us to investigate a large range of optical injection powers and overcome any power losses in the setup.

MZ intensity modulators are used throughout this work to grant us the capability to encode injection light with input perturbations (stimuli) or data. MZ modulators are based on interferometers with one arm containing Pockels cells. Pockels cells are non-linear crystals that exhibit the Pockels effect, whereby their refractive index is altered by changing the strength of the electric field across it. The changing refractive index creates a phase difference in the arms of the interferometer, hence when they are recombined the intensity of the output signal is influenced. In this work we use two commercially-sourced Lithium Niobate ($LiNbO_3$) MZ intensity modulators, **JDS-Uniphase 10 Gb/s integrated amplitude modulator and Thorlabs LN81S-FC 10 Gb/s intensity modulator**. These modulators feature low half-wave voltages (voltage required to create a phase change of π) of 6 V and operate in the wavelength range of 1525 to 1605 nm. Both feature a DC bias input, an RF electrical input and optical fibre connections. The DC bias permits the configuration of the modulator's output intensity. The RF input is then used to introduce the desired input perturbations or data. The RF signal is added to the DC bias voltage inside the modulator, altering the intensity of the output at up to a rate of 10 Gb/s. In these modulators the optical fibre connections are polarisation maintaining, meaning a polarisation controller is required to correctly align signals for efficient modulation.

To create the electrical signals used for modulation we employ a high bandwidth AWG:

Keysight M8190A – 12 bit, 12 GSa/s, Dual Channel, 5 GHz bandwidth AWG.

This AWG generates customisable electrical signals at a maximum sample rate of 12 GSa/s. This AWG therefore easily produces short pulses (100 ps width) and can incorporate fast bursts of up to 6 pulses within a short 1 ns period. Signals are either designed using the AWG software interface or are created in programming software, such as MatLab, and uploaded directly to the AWG. The AWG featured two channels which could be driven at the same time, enabling us to use two modulators simultaneously to create to different modulated optical injection paths. The maximum output voltage of the AWG was rated at 1.5 V therefore to incorporate it effectively with our modulators, we required the use of a high bandwidth electrical amplifier (AMP):

Minicircuits ZX60-14012L-S+ – 10 dBm amplification, 300 kHz – 14 GHz bandwidth electrical amplifier. The electrical amplifier helps increase the amplitude of the electrical signal granting a larger range of intensity modulation. The amplifier also inverts the signal; however, this can be compensated by the AWG or the DC bias of the modulator.

The DC bias of the modulator was provided by a variable power supply (PS):

RS PRO Bench Power Supply IPS 603 – 20 V, 10 A, 200 W output. The PS delivers an output from 0 to 20 V, allowing us to sufficiently control the bias point of the modulators. Typically, the bias point of our modulator is set near minimum phase difference such that we have a high injection power. Using positive voltage RF inputs, we push the modulators to larger phase differences and encode the optical injection with drops in intensity.

These components therefore make up the optical injection line used throughout this work to introduce signals into the VCSELs. We perform optical injection into both 1300 and 1550 nm devices, meaning that at times the MZ intensity modulators are operated out with their specified wavelength ranges, causing additional optical power losses, however, thanks to the high power output of the TL sources, these losses are overcome.

2.1.4 Detection and Analysis

Here we discuss the different equipment used to measure the optical and dynamical properties of the VCSELs used in the experiments.

Average Optical Power

Average optical power measurements were made with a Thorlabs PM20C fibre optic power meter (PM). This instrument uses an InGaAs sensor which converted optical power into voltage and provided power measurement based on the user-defined wavelength. The device had a wavelength range of 800-1700 nm. The power meter provided a power measurement in the range of 1 nW to 20 mW at a sample rate of 10 Hz. The sample rate of the instrument is slow compared to the near GHz spiking

rates used in this work hence this power measurement is considered an average measurement. This device was typically connected to the 50/50 coupler in the optical injection line to measure the average injection optical power entering the VCSELs.

Spectral Analysis and Polarisation Setting

The monitoring and measurement of the wavelength properties of the VCSELs in this work was performed using an Anritsu MS9710C optical spectrum analyser (OSA). This system had a wavelength range of 600 to 1750 nm, at a resolution of 0.05 nm and an optical sensitivity of -90 dBm. This system was used to capture the optical spectra plotted throughout this work and was directly connected to the output of the system via an optical fibre input terminal.

This system was also regularly used to provide a measurement of injection frequency detuning between the TL's light and the VCSEL(s) under investigation. By comparing the peak emission wavelength of the VCSEL to the wavelength peak of the injected laser light from the TL, a direct measurement of frequency detuning could be made by the instrument.

The polarisation of optical injection and optical feedback light was routinely selected by measuring the optical spectra of the slave VCSEL. Using the OSA, the two orthogonal polarisations supported by the VCSELs were clearly observable (see spectra in Chapter 2.2). When optically injecting light into one of two linear polarisation modes (referred to from now onwards as the parallel and orthogonal polarisation modes), variations in the polarisation of the incoming injected light would cause a change in their output powers.

When injecting light into one of the linear polarisation modes of a VCSEL, the output power of the slave VCSEL mode could be affected in one of two ways; If variations in injection polarisation resulted in an overall higher spectral power, then the slave VCSEL mode and the injection light had matching polarisation states; If changes in injection polarisation decreased the output spectral power of the slave mode, then the slave VCSEL mode and the injection light had perpendicular polarisation states.

This is caused by the same birefringence and anisotropy effects responsible for the splitting of polarisation modes in VCSELs [114]. This method was applied to set the

light polarisation used for optical injection and optical feedback experiments. In this work, the polarisation of the injected light was typically set to match that of the slave VCSEL's polarisation mode. This condition would help improve the coupling of optical injection into the VCSEL cavity and reduce the power requirements for dynamical behaviours such as injection locking.

Temporal Intensity Dynamics in VCSELs

Measurement of the time-dependent dynamical output of VCSELs was performed using two pieces of equipment namely, a high-speed amplified photodetector (PD), and a high-bandwidth real time oscilloscope. A Thorlabs PDA8GS PD was used to convert the collected optical outputs from the VCSELs into electrical currents. This system featured an InGaAs PIN photodiode and a transimpedance amplifier making it compatible with low light level signals. The PD had a bandwidth of 9.5 GHz and a wavelength range of 750-1650 nm, making it compatible with the VCSELs' operating wavelengths whilst also allowing the measurement of their fast optical output signals. The electrical signals generated by the PD were connected via SMA cables to a high-speed real-time oscilloscope for analysis. The results presented in this work were collected using one of two real-time oscilloscopes available for use in our laboratory (Agilent or Rohde & Schwarz).

Agilent Infiniium DSO81304B – 40 GSa/s sample rate with 13 GHz bandwidth.

Rohde & Schwarz RTP – 40 GSa/s sample rate with 16 GHz bandwidth. An additional memory upgrade for the capture of longer timeseries was used.

The Agilent Infiniium oscilloscope was used to capture most of the early work presented in this thesis. This oscilloscope features a large sample rate; however, the internal memory of the oscilloscope was limited, restricting the length of the timeseries the device could capture. The R&S RTP oscilloscope was a more recent acquisition and has therefore been used to capture the latest results presented in this work. This device featured a higher bandwidth and a significantly larger memory, allowing for the capture of longer timeseries across multiple channels. Once captured by the oscilloscope the timeseries were saved into (.bin) files and were analysed using bespoke MatLab scripts. Experimental results were plotted as a function of intensity

I (arbitrary units) versus time t (ns), to show the fast nature of the dynamical responses of the system. This presentation of captured waveforms is the standard format for figures throughout this work.

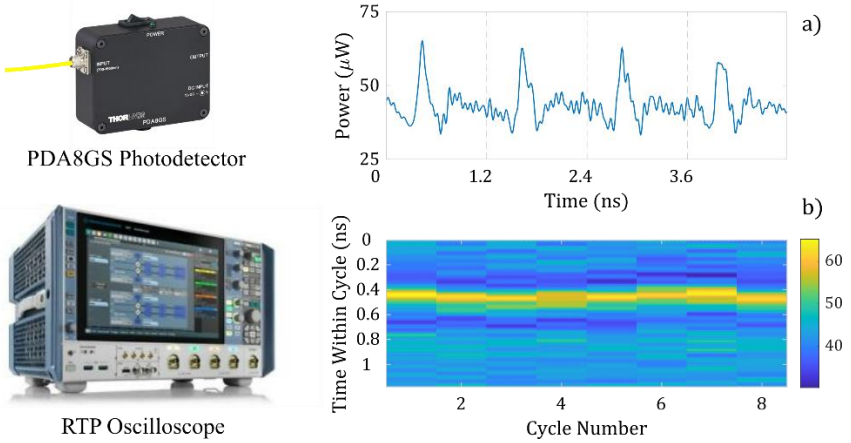

Figure 2.1.4 – Images of the PD and oscilloscope used to measure temporal dynamics and an example of a time series measurements. (a) Example timeseries plots a noisy pulsating signal and (b) the corresponding temporal map. The timeseries plots the output of the system measured by the oscilloscope. The temporal map is configured to plot 1.2 ns segments of timeseries (a) as colourmaps. The colour of the map is scaled to the amplitude of the associated timeseries. Yellow colour indicates intensity (power) maxima and dark blue indicates intensity (power) minima. Cycle number 1 therefore corresponds to the first 1.2 ns shown in (a). A total of 8 cycles appear in the temporal map, providing information on the full recorded signal, beyond the scope of the results shown in the timeseries.

Alongside the plotting of timeseries, 2D temporal maps are also used throughout this work. Temporal maps allow us to observe the evolution of the dynamical response across timescales much wider than those possible in typical timeseries plots. These temporal maps reveal the evolution, arising patterns and consistency of the measured dynamical responses via a 2D representation using colour mapping [216]. In these temporal maps, the intensity of the systems' response is represented with colour, where yellow and dark blue pixels indicate maximum and minimum values of intensity respectively. The attached colour bar represents the linear relationship between the temporal map and the power measurement made at the photodetector.

Time on the y-axis plots segments of timeseries within a repeating period or cycle, dictated by a selected time folding parameter (usually referred by τ). The cycle or fold number is then plotted on the x-axis with one pixel width representing a single cycle. An example of a timeseries and its corresponding temporal map is plotted in Fig. 2.1.4.

The folding parameter is often selected to match the frequency of the response as shown in Fig. 2.1.4. This forms a yellow line indicating the same behaviour is occurring in each segment and that the system response is frequent. The timing of responses can also be more easily seen in this representation. The line formed by temporal maps may drift if repeated over a large number of cycles. This effect is caused by the folding parameter being an integer value, meaning that the frequency of the responses may not be perfectly matched, and excess/insufficient samples may be included in each repeating cycle.

2.2 VCSEL Characterisation and Dynamics

Here we present a description of the characterisation measurements performed on the VCSELs used in this work and provide exemplar measurements from a number of the devices used during experiments. Alongside the characterisation measurements, we provide some examples of non-linear laser dynamical responses produced by VCSELs under external optical injection.

We experimentally use multiple batches of VCSELs, commercially-sourced from RayCan Co., Ltd. These VCSELs are TO-56/TO-90 packaged, fibre pigtailed laser diodes. These monolithic devices feature an InGaAs QW active layer and InAlGaAs/InAlAs DBRs. Single transverse-mode devices were selected for use throughout this work with light emission at typical O- (1300 nm) and C-Band (1550 nm) telecom wavelengths. A report on similar RayCan VCSEL devices showcased that the commercial devices were highly reliable for room temperature optical communications operation [121].

2.2.1 Characterisation Measurements

In this work, we aim to investigate VCSELs as key-enabling photonic platforms for neuromorphic photonic functionalities. However, prior to performing experiments with these VCSELs it is required to characterise some basic laser parameters.

The first laser parameter we measure is the VCSELs' threshold current. This marks the onset of lasing operation, where stimulated emission dominates over spontaneous emission and the losses within the cavity are overcome [105]. Upon exceeding the lasing threshold current, the light within the cavity experiences gain and the optical output power of the laser (a VCSEL in our case) grows substantially. To make a measurement of the threshold current we read the output power of the fibre-pigtailed VCSELs while increasing the applied bias current. In Fig. 2.2.1 we show the lasing threshold current characterisation for two different VCSELs, one with emission at 1300 nm and the other at 1550 nm. Both experiments were performed with the VCSELs' temperature stabilised at 293 K. The light-current (LI) curves of each device plot the emitted optical output power of the VCSEL versus the applied electrical bias current. We can see in both Fig. 2.2.1 (a) & (b) that after exceeding 2.96 mA (1300 nm VCSEL, left plot) and 1.20 mA (1550 nm VCSEL, right plot) of current, respectively, the output powers of the VCSELs grow in a linear fashion. In these devices the linear region of the curve indicates steady-state lasing, corresponding to a continuous wave (CW) laser output. The threshold current, as well as the maximum optical output power of VCSELs, may vary from one device to another, as seen in Fig. 2.2.1. In Fig. 2.2.2 we characterise a different 1300 nm VCSEL also used during this PhD project. For this case, we plot the measured LI curves for laser operation at three different set laser temperatures, namely 290.5 K, 293 K and 295.5 K.

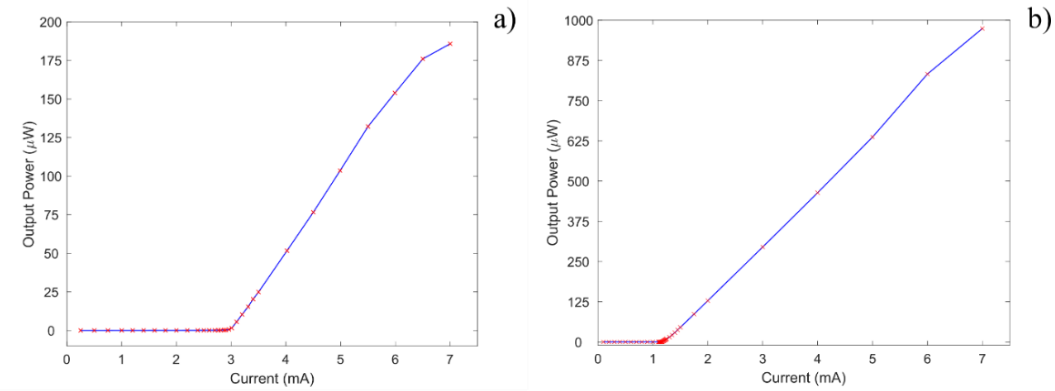

Figure 2.2.1 – Light-Current (LI) curves for a 1300 (a) and a 1550 nm (b) VCSEL measured at 293 K. The threshold currents were equal to 2.96 (a) and 1.20 mA (b), respectively.

Output power measurements were taken around the threshold current of the VCSEL for bias currents up to 1 mA at each temperature. The results show that as the temperature of the laser is increased, the laser threshold increases from 0.80 mA to 0.819 mA and 0.83 mA respectively. In this case a temperature change of 5 K results in 0.03 mA rise in laser threshold current for this particular device. Increasing the initially low temperature of the laser cavity generates more intrinsic losses within the cavity. As the threshold of the laser occurs when losses are overcome, an increase of losses results in a higher lasing threshold.

Another parameter that can be measured from the LI curve is the slope efficiency of a laser. This helps provide an understanding of the losses within the laser cavity and highlights how well a laser is converting input power (electrical pumping) to output power (light emission). In electrically driven lasers this is given in Watts/Amp. The output of a laser is typically linear after threshold, therefore, by measuring the slope of a linear fit we can determine the slope efficiency of the VCSEL. Measuring the slope of the lines in Fig. 2.2.2, we find an average slope efficiency of 96.06 ± 0.94 μW/mA. This value allows us to estimate the output optical power for a specific applied bias current and would permit us to compare the efficiency of this device to other VCSELs used for experimentation. Similarly, significant changes to the slope efficiency of a laser over time could indicate ageing issues and potential degradation. Typically, the slope efficiency of a laser decreases at higher input power values (bias

currents) due to increasing losses due to non-radiative processes that convert input energy to heat. This is responsible for the reduction in slope seen in Fig. 2.2.1 (a) & (b).

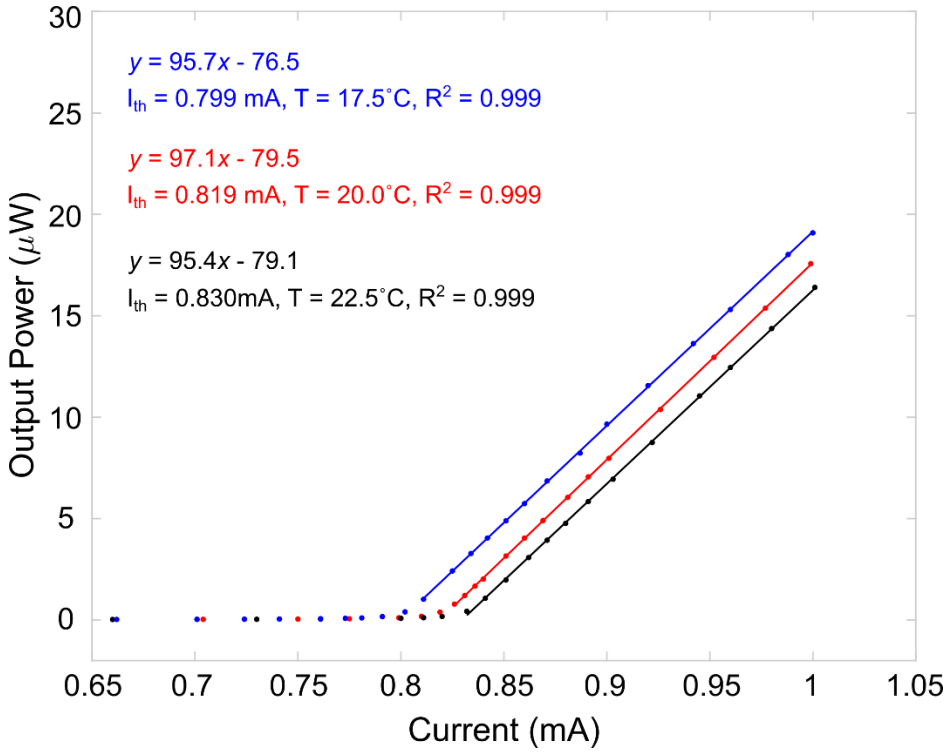

Figure 2.2.2 – Light-Current (LI) curves for a 1300 nm VCSEL at three operating temperatures (blue) 290.5, (red) 293 and (black) 295.5 K. A linear fit of each LI curve was made. Increasing the temperature of the VCSEL produces a higher lasing threshold.

Another typically performed characterisation measurement is that of the VCSELs lasing spectra. Captured using the optical spectrum analyser (OSA), the lasing spectrum provides a measurement of a laser's output wavelength/frequency as well as specific spectral features (e.g. single/multi-mode emission, linewidth, etc.). The optical spectra of the 1300 and 1550 nm VCSELs investigated in Fig. 2.2.1 are also provided below in Fig. 2.2.3. Six spectra were taken for each device at increasing increments of 1 mA. The spectra show the two single mode VCSELs operating at 293 K. In Fig. 2.2.3 (a) the 1300 nm device displays two peaks in wavelength at all pump currents. These two peaks correspond to the two orthogonal polarisations of the fundamental transverse (spatial) mode of the device. A characteristic of VCSELs

is that two linear (and orthogonal) polarisation modes arise due to the design and vertical emission of the laser. Cavity anisotropies (birefringence and dichroism) influence opposite spin transitions differently, separating wavelengths, while exposing each to varying levels of gain, finally creating two orthogonal linear polarisation modes [114]. Throughout this work we will refer to these modes as the parallel (λ_y) and orthogonal (λ_x) polarisation modes. In most of the VCSELs used in our experiments, as is the case in Fig. 2.2.3 (a) we find that the parallel (λ_y) polarisation is dominant above threshold as it experiences higher gain. However, as shown in Fig. 2.2.3 (b) this is not always the case, as the orthogonal (λ_x) polarisation can also be dominant at all pump currents. All the VCSELs selected in this work favoured a single linear polarisation mode above threshold (side mode suppression ratios of 28 and 33 dBm at 3.0 mA for the cases in Fig. 2.2.3). Polarisation switching, where the dominant polarisation mode changes with applied bias current, was also observed in some of the VCSELs utilised. In both cases the 1300 and 1550 nm devices demonstrate the characteristic red-shift with increasing bias current. The latter leads to small increases in temperature that effect the refractive index of the medium altering the output wavelength of the laser. Using this effect, the wavelength of the VCSELs could be tuned (in the order of a few nm) by controlling the device's operating temperature.

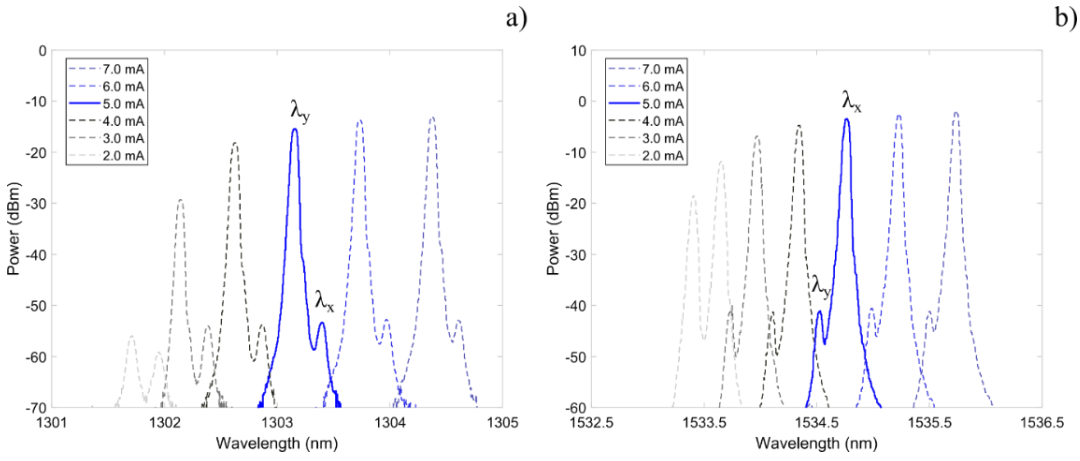

Figure 2.2.3 – Optical spectra of (a) a 1300 and (b) a 1550 nm VCSEL. The spectra were taken at 293 K with 1 mA bias current increments. Both plots (a) & (b) correspond to the devices in Fig. 2.2.1.

The separation between the two linear and orthogonally polarisation modes supported by the VCSELs can also be measured from their spectra. Mode separations of approx. 43 GHz and 31 GHz were measured in the 1300 nm and 1550 nm cases respectively. The separation between polarisation modes can change across different devices with values ranging from 25 to 50 GHz.

2.2.2 Nonlinear Dynamics in VCSELs subject to Optical Injection

As previously discussed in Chapters 1.5 & 2.1.3, we utilise optical injection to produce different non-linear laser dynamics in VCSELs. Specifically, we focus on achieving neuron-like excitable spiking responses at ultrafast rates for neuromorphic photonic processing functionalities. However, a wide range of additional nonlinear dynamical responses can be triggered in VCSELs under external optical injection. In this Chapter, whilst we do not provide an in-depth study into the dynamical behaviour of VCSELs, we highlight some of the non-linear behaviours that can be observed when polarised optical injection is performed.

Optical injection, initially seen as a tool to stabilise the light emission of a laser, is known to create a rich variety of non-linear dynamics in SLs. These include responses such as periodic oscillations [130], chaos [131], [132] and excitability [152], [158], that can be specifically targeted by controlling the operation conditions of the ML (e.g. optical power, light polarisation, frequency/wavelength). Control over the optical injection conditions is therefore key to the production of the nonlinear dynamics in VCSELs that will be used in this work to demonstrate neuromorphic processing functionalities.

When performing optical injection, external light is input into the slave laser through one of its partially reflecting cavity mirrors. The increased number of photons within the cavity alters the refractive index, creating a red shift in cavity wavelength. When light from a ML with a frequency close to that of the slave laser is injected, the gain profile of the latter is altered such that its emission peak shifts to the frequency of the

master. The two lasers can become injection locked and the frequency of the slave laser will oscillate at that of the master. The output power of the laser is stabilised, and the spectral linewidth can be enhanced during stable injection locking operation [137]–[139]. Injection locking is achieved at a specific range of frequency detuning between the ML and slave laser, and typically the higher the injection optical power the larger the detuning range over which injection locking can be achieved. Due to the red shift of the cavity the locking range is typically asymmetrical around the cavity resonance. At the boundaries of injection locking bifurcations form in parameter space that give rise to a variety of non-linear dynamical behaviours in the output of the slave laser. By targeting the injection parameters surrounding these bifurcations we can explore the regions of non-linear dynamical responses available to the VCSELs used during this project.

In the single (transverse) mode VCSELs used in this work, two linear (orthogonally polarised) modes are supported. Figs. 2.2.4 (a) & (b) show how external optical injection can affect the spectral response of the slave VCSEL. In this experiment, a 1300 nm VCSEL with dominant emission in its parallel-polarised mode (Fig. 2.2.4 (a)) receives optical injection near its (heavily suppressed) orthogonal polarisation mode (red arrow). For the case investigated in Fig. 2.2.4 the optical injection was made with an optical input power of 127 μW at a frequency detuning of -5.64 GHz (between the ML's peak and the resonance frequency of the subsidiary (λ_x) orthogonally-polarised mode). The optically injected light was polarisation matched to that of the VCSEL's orthogonal (λ_x) mode, hence referred to as orthogonally-polarised optical injection. The optical spectrum in Fig. 2.2.4 (b) shows that under these conditions, polarisation switching occurs in the VCSEL. Here the dominant polarisation mode of the VCSEL changes from parallel (λ_y) to orthogonal (λ_x), and the output power of the λ_y mode is attenuated (but not completely suppressed). The VCSEL is now yielding emission in both polarisations and the spectral properties of the VCSEL have undergone change. To fully understand the influence of the optical injection we must however also consider the temporal dynamics at the output of the VCSEL.

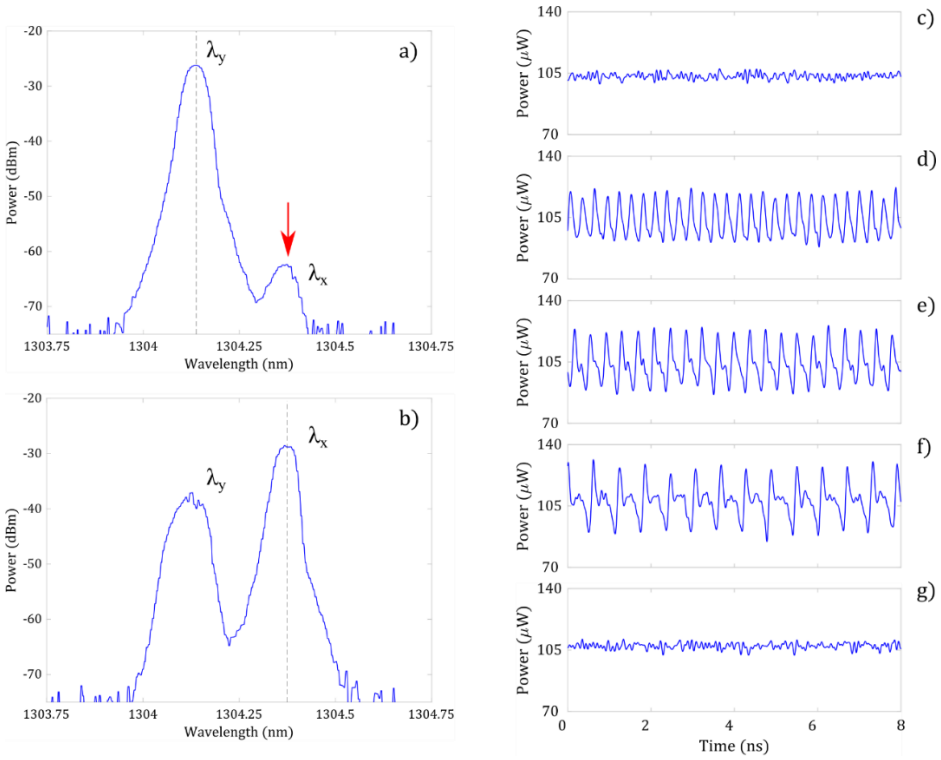

Figure 2.2.4 – (a)-(b) Effect of optical injection on the spectral response of a 1300 nm VCSEL. Wavelength spectra were taken (a) before and (b) during orthogonally-polarised optical injection. The optical injection occurred Δf = -5.64 GHz from λ_x (red arrow) with an injection power of 127 μW. (c)-(g) Temporal dynamics of a 1300 nm VCSEL subject to orthogonally-polarised optical injection with increasing levels of injection power: (c) no injection, (d) 20.9 μW, (e) 40.1 μW (f) 53.5 μW and (g) 59.8 μW.

In a second experiment, the temporal laser dynamics at the output of a similar 1300 nm VCSEL, subject to orthogonally-polarised optical injection, were observed (see Fig 2.2.4 (c)-(g)). Here, the slave VCSEL was subject to increasing levels of injection power at a fixed frequency detuning of Δf = -3.62 GHz. The orthogonally-polarised optical injection was increased until a switch of the dominant (polarisation) mode occurred and injection locking was achieved. Figs 2.2.4 (c)-(g) reveal the temporal measurements made at the output of the VCSEL. Initially, under no optical injection (Fig. 2.2.4 (c)) the slave laser outputs a steady state response with emission in its main parallel polarised mode. The output of the laser was stable with a low intensity noise, commonly associated with quantum noise, noisy pump sources and small thermal fluctuations. When the injection power was increased to 20.9 μW (Fig. 2.2.4

(d)) the VCSEL produced a periodic oscillation. Periodic signals (period 1, period 2 and multiperiodic signals) are the result of bifurcation points in the form of limit cycles or in some cases the beating of the injected signal with the slave laser. Increasing the optical power to 40.1 μW produced a lower frequency periodic signal (Fig. 2.2.4 (e)), before an increase to 53.5 μW produced continuous spiking responses (Fig. 2.2.4 (f)). The spiking responses featured drops in intensity, followed by sharp rises, and finally a return to a stable level. Finally, increasing injection power to 59.8 μW (Fig. 2.2.4 (g)) injection locked the system, producing a stable steady state output, as well as polarisation switching as now the VCSEL's emission was in the orthogonal polarisation mode. The injection of light into the cavity increased the output power of the slave laser, giving the injection locked signal a higher output intensity that the steady state signal under no injection. Optical bistability, associated with this injection locking response, was also observed with the VCSEL unlocking the ML's injection at a power lower than the initial requirement. This effect was observed during the injection locking of multiple tested VCSELs and occurred more prominently at higher bias currents.

Under these optical injection parameters this 1300 nm VCSEL produced periodic oscillations, spiking and injection locking. However, under alternative injection parameters, it was possible to achieve regimes of period doubling and chaos. Importantly, the regimes of non-linear behaviour produced by the VCSEL were accessed by varying the injection power. The same effect, however, was observed when altering frequency detuning. Therefore, in order to identify regimes of non-linear dynamics we experimentally explored variations of both injection power and frequency detuning. This way we could identify key spiking regimes that could potentially be utilised to produce neuron-like optical responses in VCSELs. More specifically, to begin a search for spiking dynamics in a VCSEL device the bias current was set to ~2 times the threshold current value. Injection would then made into the subsidiary mode of the VCSEL with a low frequency detuning of -2 GHz. The injection power would then be scanned until polarisation switching and locking was achieved. If no spiking responses were observed the frequency detuning would be increased incrementally (with further power scans) until -10 GHz. Again, if no neuron-like responses were observed, injection would be switched to the alternative

polarisation mode of the VCSEL. The same procedure would then be repeated in search of spiking responses. Finally, if both polarisation modes failed to trigger neuron-like spikes, an alternative higher bias current was tested and the procedure was repeated. The mapping of non-linear dynamics was not performed in full, rather only regimes and devices of interest were recorded.

It is also noted that optical injection could be made into the VCSEL's main parallel polarisation (λ_y) mode with a parallel-polarised optical injection configuration. That scheme could also be applied to trigger an injection locking behaviour as well as a wide range of nonlinear dynamics.

2.3 Spin-Flip Model (SFM) for VCSEL analysis

In this work we use a modified version of the so-called spin-flip model (SFM) to theoretically simulate the dynamical behaviour of VCSELs. The main focus is to analyse theoretically the neural-like dynamical regimes that can be triggered in VCSELs and their potential for neuromorphic photonic processing functionalities. The SFM, firstly proposed by San Miguel et al. [114], provides an accurate description of the nonlinear behaviours that can arise in the two orthogonally-polarised modes supported by a VCSEL.

VCSELs have a cavity whose thickness is much smaller than the typical dimensions of edge-emitting semiconductor lasers, and VCSELs specifically have circular (or elliptical) apertures with vertical light emission from the substrate's surface. As a result of their particular design, to investigate the emission properties of VCSELs numerically we are required to consider electron spin states, specifically the difference between up and down spin transitions in the valence and conductance bands. In the lowest momentum state of the conductance band there are total angular momentum values of $J_z = \pm 1/2$. In the valence band there are both heavy-hole states and light hole states that correspond to angular momentum values of $J_z = \pm 3/2$ and $J_z = \pm 1/2$ respectively. In bulk quantum well devices the higher energy heavy hole band produces transitions with $\Delta J_z = \pm 1$ and lower energy light hole states can be

neglected. The VCSEL model therefore has two transitions from the conductance band to the heavy hole band that produce right-circularly polarized ($J_z = -1/2 \rightarrow J_z = -3/2$) and left-circularly polarised ($J_z = +1/2 \rightarrow J_z = +3/2$) light. With two opposite spins, the model considers both the carrier population inversion between each spin as well as the total carrier inversion between conductance and valance bands. The model also considers the mixing of populations with opposite spins in the decay rate γ_s for spin-flip relaxation processes (spin flip rate). The SFM for the analysis of VCSEL emission also includes cavity anisotropies that give rise to birefringence and circular dichroism. Birefringence causes frequency splitting of the polarised light due to differing refractive indices experienced while travelling through the medium. This produces two linear orthogonally-polarised modes in the fundamental spatial mode of VCSELs (as seen in the spectra shown in Fig. 2.2.1). The dichroism effect then also subjects the two light polarisations to different absorption and gain ratios. This is responsible for the creation of a dominant linear polarisation mode and allows the model to predict VCSEL behaviours like polarisation switching, where the dominant polarisation mode of the device can change under different operating conditions.

In this work we use a modified version of the SFM that includes additional terms that accounts for the external injection of an optical signal. These are based on modification made in [217]. The modified rate equations are shown below in Eq. 2.3.1-2.3.3:

$$\begin{aligned}\frac{\mathrm{d}E_{x,y}}{\mathrm{d}t} = &-(k \pm \gamma_a)E_{x,y} - i(k\alpha \pm \gamma_p)E_{x,y} \\ &+k(1+i\alpha)(NE_{x,y} \pm inE_{x,y}) \\ &+k_{inj}E_{inj}(t)e^{i\Delta\omega_x t} + F_{x,y}\end{aligned} \tag{Eq. 2.3.1}$$

$$\begin{aligned}\frac{\mathrm{d}N}{\mathrm{d}t} = &-\gamma_N[N(1+|E_x|^2+|E_y|^2) - \mu \\ &+in(E_yE_x^* - E_xE_y^*)]\end{aligned} \tag{Eq. 2.3.2}$$

$$\frac{\mathrm{d}n}{\mathrm{d}t} = -\gamma_s n - \gamma_N[n(|E_x|^2 + |E_y|^2) + iN(E_y E_x^* - E_x E_y^*)]$$

(Eq. 2.3.3)

Here, we again name the two linear orthogonally polarised modes in the VCSEL as the orthogonal and parallel modes. These modes are represented by the subscript x (orthogonally-polarised) and y (parallel-polarised) respectively. The field amplitudes of the subsidiary and solitary modes are represented by E_x and E_y. N is the total carrier inversion between conduction and valence bands and n is the carrier inversion difference between spins of opposite polarity. γ_a is the linear dichroism rate, γ_p is the birefringence rate, γ_N is the decay rate of the carrier inversion and γ_s is the spin-flip rate. k and k_{inj} are the field and injected field decay rates, α is the linewidth enhancement rate and μ is the normalised pump current (μ=1 represents the VCSEL's threshold pump level). E_{inj} represents the optically injected signal and is dimensionless variable that controls the injection strength. The angular frequency detuning between the externally injected signal and the VCSEL's resonance is defined as $\Delta\omega_x = \omega_{inj} - \omega_0$, where the central frequency $\omega_0 = (\omega_x + \omega_y)/2$ lies between the frequencies of the subsidiary $\omega_x = \omega_0 + \alpha\gamma_a - \gamma_p$ and the solitary mode $\omega_y = \omega_0 + \gamma_p - \alpha\gamma_a$. $\Delta f_x = f_{inj} - f_x$ is the frequency detuning between the injected field and the subsidiary mode, hence $\Delta\omega_x = 2\pi\Delta f_x + \alpha\gamma_a - \gamma_p$. The spontaneous emission noise terms F_x and F_y are calculated according to Eq. 2.3.4-2.3.5.

$$F_x = \sqrt{\frac{\beta_{sp}\gamma_n}{2}}(\sqrt{N+n}\xi_1 + \sqrt{N-n}\xi_2)$$

(Eq. 2.3.4)

$$F_y = -i\sqrt{\frac{\beta_{sp}\gamma_n}{2}}(\sqrt{N+n}\xi_1 - \sqrt{N-n}\xi_2)$$

(Eq. 2.3.5)

where β_{sp} represents the spontaneous emission strength and $\xi_{1,2}$ represent two independent Gaussian white noise terms of zero mean and a unit variance.

The model and its equations were reproduced using programming language MatLab, where they were solved using the fourth order Runge-Kutta method. A consistent set of parameters were used to model the VCSELs used in this project work across a number of theoretical experiments: $\gamma_a = 2\text{n}s^{-1}$, $\gamma_p = 128\text{n}s^{-1}$, $\gamma_N = 0.5\text{n}s^{-1}$, $\gamma_s = 110\text{n}s^{-1}$, $\alpha = 2$, $E_{inj} = 0.12$, $k = 185\text{n}s^{-1}$, $k_{inj} = 125\text{n}s^{-1}$ and $\beta_{sp} = 10^{-5}$.

Using this modified SFM we were able to recreate the behaviours observed experimentally in our photonic VCSEL neurons. This allows us to validate the experimental findings and confirm the neuromorphic dynamical responses and spike processing functionalities achieved with the VCSELs used in this work.

Chapter 3

Controllable Neuromorphic Spiking Dynamics in VCSELs

In Chapter 1 we introduced neuromorphic systems and highlighted the benefits of using photonic technologies for their implementation. We also discussed the potentials of SLs for neuromorphic photonic functionalities and introduced the devices we focused on in this work, VCSELs. In Chapter 2 we detailed the experimental arrangements used throughout this work. We also discussed how the injection of external optical signals influences the laser dynamics in VCSELs and revealed how we measure and present results. In this Chapter, we demonstrate how to controllably produce neuromorphic spiking dynamics in VCSELs via the external optical injection of modulated signals. Specifically, we investigate the controllable activation (Chapter 3.1) and inhibition (Chapter 3.2) of fast optical spiking dynamics via pathways such as pulsed optical injection and bias current modulation. We also investigate the thresholding of VCSEL neurons, plotting the activation function of spiking responses, and discuss the refractory period of the spiking dynamics (Chapter 3.3) in the investigated VCSEL-based artificial optical neurons.

In this chapter we will discuss experimental results that have produced journal publications. The following articles therefore relate to the forthcoming discussion:

[193] J. Robertson, M. Hejda, J. Bueno, and A. Hurtado, "Ultrafast optical integration and pattern classification for neuromorphic photonics based on spiking VCSEL neurons," *Sci. Rep.*, vol. 10, no. 1, p. 6098, Dec. 2020, doi: 10.1038/s41598-020-62945-5.

[196] J. Robertson, E. Wade, and A. Hurtado, "Electrically Controlled Neuron-Like Spiking Regimes in Vertical-Cavity Surface-Emitting Lasers at Ultrafast Rates," *IEEE J. Sel. Top. Quantum Electron.*, vol. 25, no. 6, 2019, doi: 10.1109/JSTQE.2019.2899040.

[197] J. Robertson, T. Deng, J. Javaloyes, and A. Hurtado, "Controlled inhibition of spiking dynamics in VCSELs for neuromorphic photonics: Theory and experiments," *Opt. Lett.*, vol. 42, no. 8, pp. 1560–1563, 2017, doi: 10.1364/OL.42.001560.

[200] J. Robertson, E. Wade, Y. Kopp, J. Bueno, and A. Hurtado, "Towards Neuromorphic Photonic Networks of Ultrafast Spiking Laser Neurons," *IEEE J. Sel. Top. Quantum Electron.*, 2019, doi: 10.1109/JSTQE.2019.2931215.

3.1 Spike Activation

The activation of spiking action potentials is a characteristic feature of biological neurons and is the means by which neurons communicate information within cortical neural networks. The spiking dynamics observed by biological neurons have a typical duration of 3-5 ms and are governed by the release of ions upon neuron stimulation [218]. When a neuron is subject to a depolarising stimulation (the reduction of negative charge in the cell) sodium and potassium ion channels open, creating an immediate influx of sodium ions that reinforce the membrane depolarisation. During the continued depolarisation of the neuron, the membrane potential switches from negative to positive, reaching a peak potential value where sodium ion channels close. The delayed release of potassium ions then rapidly counteracts the depolarisation, repolarising (increasing negative charge) the membrane potential towards the resting potential. The rapid repolarisation results in an undershoot of the rest potential before the neuron finally hyperpolarises and recovers (see Fig. 3.1.1) [218], [219].

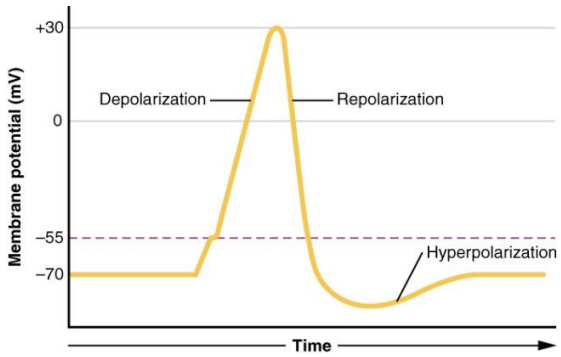

Figure 3.1.1 – Diagram of a neuron's action potential. When a strong stimulus, exceeding the neuron's threshold (dotted line) arrives, ion channels open and the neuron depolarises. The membrane potential reaches a maximum and repolarisation begins. The membrane potential undershoots the rest potential and hyperpolarises. The action potential is complete when the membrane potential resets to its rest value. Figure reproduced from [219].

This mechanism creates the characteristic electric action potentials observed in biological neurons. However, not every input stimulus will activate the neuron. Neurons have a characteristic membrane threshold potential which sets a requirement on the strength of input stimuli such that only super-threshold inputs trigger spiking responses. Therefore, the contribution of multiple inputs, integrated by the neuron, must surpass the difference between the rest and threshold potentials to activate a spike. The action potential response of neurons is an all-or-nothing signal which indicates the firing condition of the neuron was met by the inputs of the system. Neurons are known, however, to store information in the precise timing of spiking responses and have been observed operating with analog input signals for additional processing capability [220]–[224].

In this Chapter we aim to produce neuronal spiking behaviour using the dynamical responses obtained in VCSELs. Specifically, we capitalise on the excitable dynamics that can be obtained in VCSELs under suitable operating conditions. Excitable dynamics can be accessed in different ways, two possible mechanisms are neural excitability with short perturbations, or the transition from rest to a periodic spiking activity. In each of these mechanisms we exploit what are known as bifurcation points in dynamical systems. Bifurcation points represent the boundary between two qualitatively similar behaviours in parameter space. A specific bifurcation known as a saddle-node on a limit cycle (SNLC) or saddle node on an invariant circle (SNIC) can be responsible for the creation of class 1 excitable spikes [161]. In the case of a SNLC, a repeller-node (an unstable fixed point in phase space where the solution of the system is real and positive) and an attractor-node (stable fixed point with a real and negative solution) exist at an arbitrary small distance from each other on a limit cycle in phase space. These two fixed point solutions represent the threshold (saddle/repeller, θ^{+}) point and the rest point (attractor, θ^{-}) of the system, respectively (see Fig. 3.1.2). The system produces excitability when the rest solution is perturbed (neural excitability) or moved (transition of behaviour) such that the two fixed points combine and annihilate. Annihilation causes the solution to undergo a large 2π phase excursion as it is sent through the limit cycle of the system, after which the solution returns to the initial rest point. The stimuli must be sufficient such that the attractor

solution meets the repeller (threshold) and annihilates, otherwise the system will decay back to its rest point. Given the 2π excursion occurs fast enough, the SNLC bifurcation will produce spiking action potentials [72], [161], [162]. The further from the threshold the system is successfully perturbed, the shorter the orbit of the excursion and the faster the spiking rate [72]. If the parameters of the system are altered such that the fixed solutions continuously annihilate, then repetitive continuous spiking can be produced by the dynamical system. The spiking dynamics produced by SNLC bifurcations are ideal for modelling biological neurons as they contain the desired threshold and fire mechanism but also allow for the integration of input stimuli.

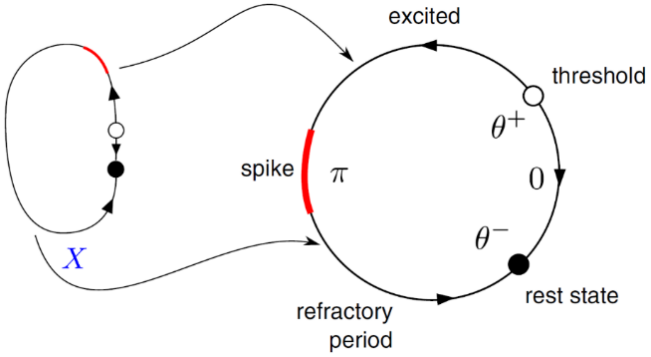

Figure 3.1.2 – Mechanism for Class 1 neural excitability. A SNLC bifurcation (*X)* is mapped onto a 1-dimensional invariant cycle. The system has two stable solutions, the rest (θ-) and threshold (θ^+) states. Any sub-threshold perturbation will fail to make the stable points annihilate, causing the system to return to its rest state. Super-threshold perturbations send the system through a larger trajectory where from 0 to π a spike is excited, and from π to 0 (2π total) the system is returned to its rest state. Figure reproduced from [72].

The bifurcation point we investigate for neuronal-like excitability in VCSELs is that of the optical injection locking boundary. As discussed previously in Chapter 2.2.2, under optical injection several dynamical behaviours exist, and during optical injection locking, the system crosses the locking boundary to a stable dynamical state [151]–[157]. In this first demonstration of the achievement of controllable excitable spikes in VCSELs, we utilise the amplitude modulation of optical injection to perturb

the system (around the locking boundary) with short drops in injection power. The detailed schematic shown in Fig. 3.1.3 reveals the experimental arrangement used for the investigation of controllable spiking responses in VCSELs under modulated optical injection. This experimental setup features consistently throughout our work and is most commonly used when controlling the activation and inhibition of fast optical spiking dynamics in VCSEL neurons.

This experimental arrangement takes customisable inputs (from a 12 GSa/s arbitrary waveform generator - AWG) and encodes them in the intensity of an external tuneable laser (TL). To achieve this, the pulsed electrical outputs from an AWG are amplified (10 dB) and passed into a 10 GHz Mach Zehnder (MZ) optical intensity modulator. The modulator converts the electrical pulses into variations of optical intensity according to the selected modulation curve. The light from the tuneable laser passes through an optical isolator (ISO), preventing unwanted feedback from reaching the source, and the light continues through a variable optical attenuator (VOA), controlling the total optical injection power. Before the injection light enters the MZ modulator the light polarisation is altered to optimise it and thus reduce power losses in the system. Following the encoding of optical pulses, the polarisation of the injection is again tuned to match the target polarisation mode of the VCSEL. Using a 50:50 beam splitter the optical power incident of the VCSEL is measured by a fibre-optic power meter (PM). An optical circulator is used to simultaneously direct the injection into the VCSEL and collect its output. Using an optical spectrum analyser (OSA) the wavelength of the device can be analysed. By converting the optical signal to an electrical signal (via a 9.5 GHz amplified photodetector - PD) a fast 16 GHz real-time oscilloscope can provide the temporal analysis of the VCSEL output. In this arrangement the off-the-shelf VCSELs are temperature stabilised to avoid wavelength drift. This setup allows us to inject customisable pulse trains into the VCSEL and capture the subsequent temporal response of the laser in real time.

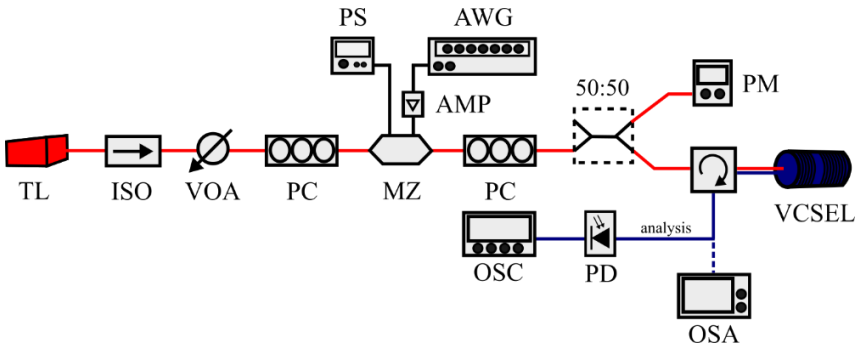

Figure 3.1.3 – Experimental setup for the controllable activation and inhibition of spiking dynamics in a VCSEL neuron. Light from a tuneable laser source is encoded with optical pulses before injection into the VCSEL neuron. The latter's output is collected by a photodetector and analysed using a real-time oscilloscope. Experimental components include: TL – tuneable master laser, ISO – optical isolator, VOA – variable optical attenuator, PC - polarisation controller, MZ – Mach Zehnder intensity modulator, PS – power supply, AWG - arbitrary waveform generator, AMP – electrical amplifier, PM – power meter, OSA – optical spectrum analyser, PD - photodetector, OSC – oscilloscope.

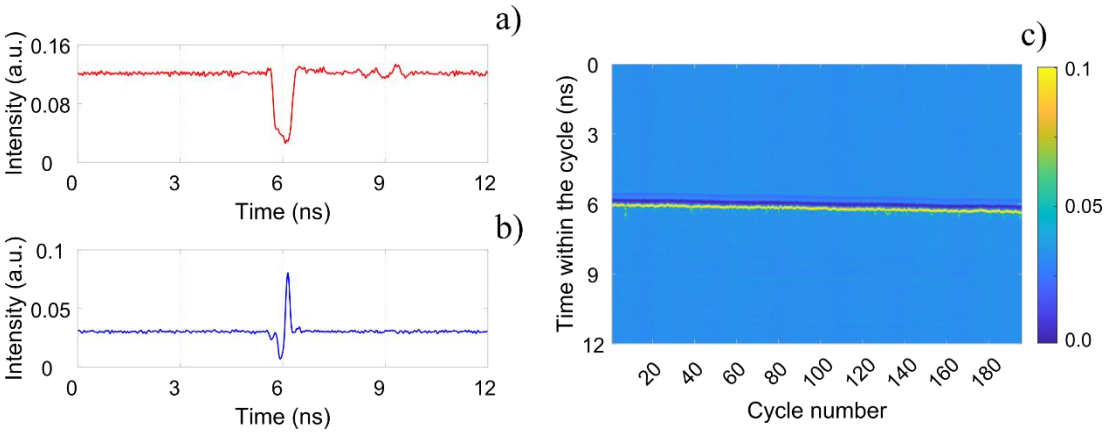

Figure 3.1.4 – Controllable activation of a single optical spike. A 0.64 ns-long pulse is encoded in the optical intensity of the VCSEL's optical injection (a). The incoming optical pulse breaks the injection locking condition by briefly reducing injection power, forcing the system to enter a regime of fast excitable spiking dynamics (b). Plotting 200 consecutive optical pulses, the temporal map (c) reveals a consistent and repeatable spiking response from the VCSEL neuron. Experimental parameters: I = 2.2 mA, T = 300 K, external orthogonal (XP) mode injection with Δf = -10.3 GHz and P_{inj}= 270 μW. Figure reproduced from [200].

To perform the controllable activation of neuromorphic optical spiking dynamics in VCSELs we inject pulses (stimuli) into the device. In the simplest case (shown in Fig. 3.1.4 (a)), the input injected into the VCSEL neuron is a negative pulse, with a high intensity baseline and a short low intensity drop. Initially, the input provides a high level of optical injection power such that optical injection locking is achieved between the slave VCSEL and the master TL. Optically injection locking the VCSEL shifts its laser cavity resonance to that of the master laser and stabilises the temporal dynamics at the device's output (as seen initially in Fig. 3.1.4 (b)). However, when the negative drop, which has a lower optical injection power than the initial baseline level, enters the VCSEL neuron, the operation point of the laser system in parameter space is altered. Given a sufficiently lower optical injection power than before, the system is forced out of the stable injection locking state and thrown to the other side of the bifurcation point. As VCSELs are capable of displaying excitability, a strong perturbation, and the resulting change of system parameters (frequency detuning, injection power and bias current), can trigger spiking responses at the device's output (as shown in Fig. 3.1.4 (b)). Following the activation of a spiking event and the removal of the negative input, the system quickly recovers to a stable output as the high injection power restores the initial optical injection locking condition. Exploiting this injection locking-unlocking transition creates a controllable mechanism for the achievement of fast spiking responses with good signal-to-noise ratio. Further, here the spiking dynamics produced by the VCSEL have widths of approximately 100 ps (full width half maximum - FWHM) and trigger at nanosecond inter-spike intervals. This makes these spiking dynamics 3 orders of magnitude faster than spiking observed in recent electronic neuromorphic systems (μs-timescales). The power requirement for neuronal spike activation in VCSEL is also relatively low, with only a driving current of a few mA's and μW levels of optical injection power necessary.

By testing the response of the VCSEL to 200 consecutive input pulses and plotting the results in a temporal map (Fig. 3.1.4 (c)), we can observe the consistency of the triggered optical spikes. The plotted temporal map shows the evolution of time on the y-axis, the intensity of the measured signal in the colour map and each

consecutive result on the x-axis. In the colour map blue pixels indicate the low intensity drops and yellow pixels indicate the high intensity peaks. The temporal map forms a line of yellow pixels indicating the response from each consecutive input is the same. This means the system is highly consistent and that the VCSEL reliably triggers a spiking response upon the injection of a short negative pulse.

Short input pulses (<1 ns-long) can therefore consistently perturb the laser system and trigger a single spiking response from the VCSEL, so next we investigated the effect of extending the input pulse duration (t_d). Again, we first optically injection locked the slave VCSEL to the tuneable master laser's light, and then injected negative optical pulses of increasing temporal duration t_d = 2.06, 2.91 and 4.52 ns as shown in Fig. 3.1.5, to trigger different spiking responses in the device.

Fig. 3.1.5 (a) shows the 2.06 ns long input pulse (red) injected into the VCSEL neuron and the spiking response from the system (blue). With an initial optical injection power of 237 μW the system produces a stable output, where the VCSEL is injection locked to the tuneable master laser light. When the negative pulse enters the VCSEL we see that a single spiking dynamic is activated. Upon increasing the duration of the optical input pulse, t_d = 2.91 ns (Fig, 3.1.5 (b)) and 4.52 ns (Fig, 3.1.5 (c)), we find that an increasing number of spiking events are activated. Here the change of injection parameters (optical pulse duration) forces the system out of the injection locked state for an extended period, resulting in the continuous activation of the bifurcation point. This therefore results in the constant activation of spiking dynamics. Upon testing the response to multiple consecutive inputs, we again found that the number of activated spiking dynamics was highly consistent. The number of spike activations produced by the system can therefore be controlled using the duration of negative input pulses. Modulated optical injection therefore grants a simple and effective method of triggering fast (sub-ns) optical spiking responses with a controllable number of spike events.

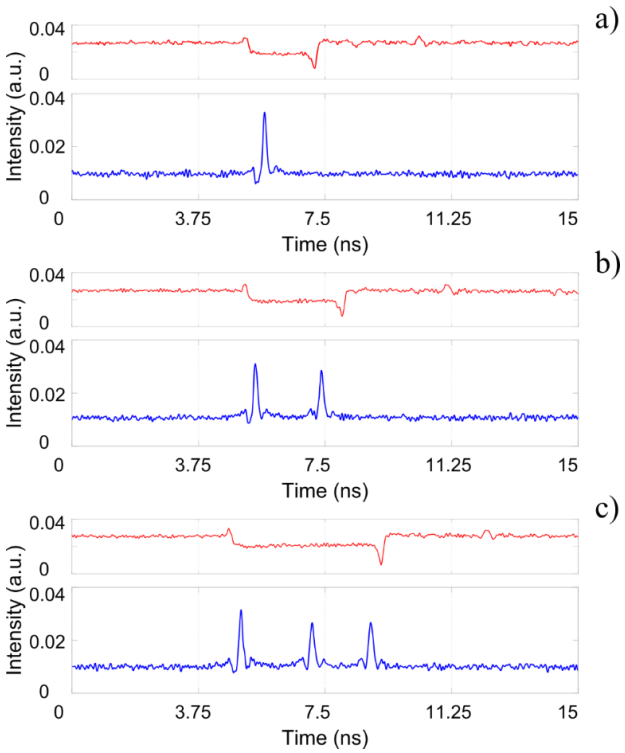

Figure 3.1.5 – Controllable activation of tonic spiking responses in a VCSEL under modulated optical injection inputs. Optical pulses of increasing temporal duration, 2.06 ns (a), 2.91 ns (b) and 4.52 ns (c) were injected into the VCSEL neuron (red), and its temporal response was recorded (blue). Experimental parameters: I = 3.6 mA, T = 298 K, external orthogonal (XP) mode injection with Δf = -5.65 GHz and P_{inj}= 237 μW. Figure reproduced from [200].

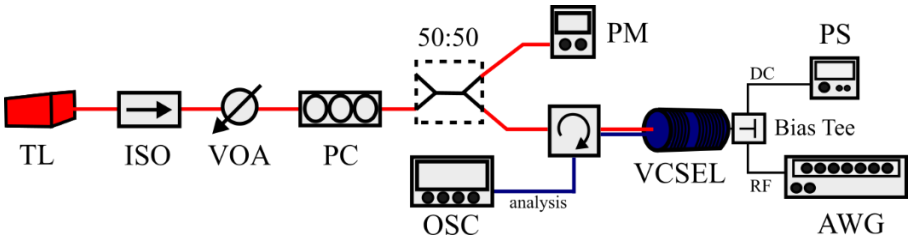

Figure 3.1.6 – Experimental setup for electrically-controlled optical spike activation in a VCSEL neuron. An external optical signal is used to injection-lock the VCSEL neuron before the device's bias current is modulated via a bias tee. The radio frequency (RF) component of an AWG electrical pulse is combined with DC voltage to create a controllable bias modulation. For every 50 mV of RF electrical pulse the VCSEL bias was increased by 1 mA. Experimental components are the same as in Figs. 3.1.3-3.1.5.

The controllable nature of the spiking dynamics produced by the VCSEL is exciting for the potential implementation of a VCSEL-based neuromorphic photonic system. The results of Fig. 3.1.5 show directly the achievement of tonic spiking behaviour analogous to that observed in biological neurons. Tonic spiking is the continuous activation of spiking responses in neurons upon extended temporal stimulation [18]. The activation of continuous spiking responses (of consistent amplitude) is also an indicator that the spiking behaviour produced the system is class 1 excitability. Class 1 excitability is the product of a SNLC bifurcation, further reinforcing the appropriateness of this mechanism for emulating the different functionalities observed in biological neurons. This promising result indicates that modulated optical injection, in tandem with off-the-shelf VCSELs operating at key telecom wavelengths (1310 and 1550 nm), may hold great prospects for future processing systems based on the ultrafast emulation of neurons.

In our investigation into optical spiking VCSEL neurons and the controllable activation of spiking dynamics we explored options other than the modulation of optical injection. We created an experimental system (shown in Fig. 3.1.6) that introduced electrical pulses in the bias current of the VCSEL, subject to constant optical injection. We used a bias tee to summate components from an RF and a DC input, producing a time-varying bias current in which we could apply fast electrical input pulses to the VCSEL.

A continuous light signal from a tuneable master laser was sent into the VCSEL, initially injection locking it to the external injection. This was achieved using an injection power of 252 μW and a frequency detuning of Δf = -5.65 GHz from the Orthogonal (XP) mode of the device. The DC bias of the VCSEL was set to 6.0 mA before positive RF pulses, (shown in Fig. 3.1.5 (a)) modulated the bias current applied to the device. The bias tee produced a change of 1 mA per 50 mV of RF signal amplitude. The RF input was set as a square-wave pulse with a duration of 1.07 ns and an amplitude of 186 mV which temporally increased the VCSEL bias current by 3.72 mA. The recorded temporal output of the VCSEL is plotted in Figs. 3.1.5 (b) & (c).

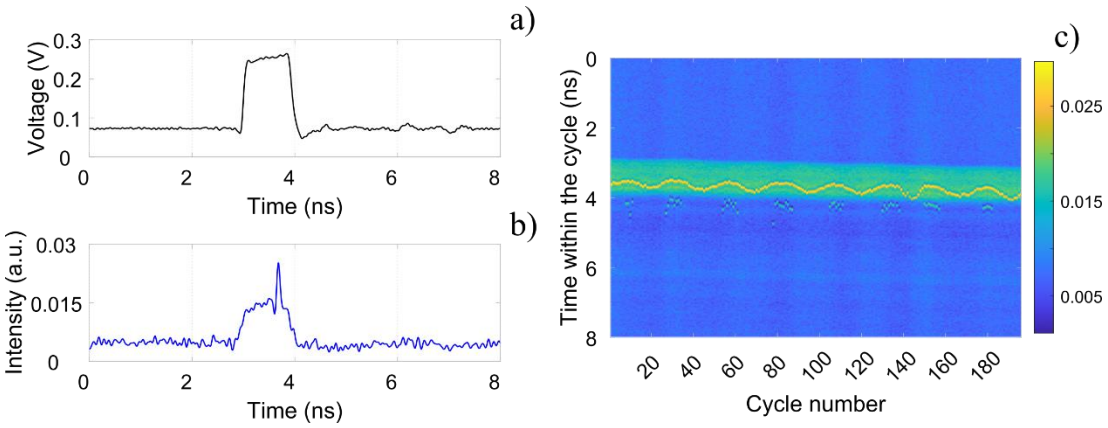

Figure 3.1.7 – Electrically activated optical spikes in a VCSEL neuron. An electrical pulse of duration 1.07 ns and amplitude 186 mV was fed into the bias tee connected to the device (a). The electrical pulse is converted into a 3.72 mA bias modulation, breaking the injection locking conditions, and placing the VCSEL in a regime of spiking dynamics (b). The temporal map of the measured VCSEL response indicates that 1 spike is consistently activated by all 200 incoming electrical pulses (c). Experimental conditions: I = 6.0 mA, T = 293 K, external orthogonal (XP) mode injection with Δf = -5.65 GHz and P_{inj}= 252 μW. Results previously published in [196].

Initially the VCSEL produces a stable output as the system is optically injection locked to the master laser. When the rising edge of the RF input enters the bias tee (at 3 ns in Figs. 3.1.7 (a)-(c)) we see that the output signal of the VCSEL increases. This is caused by the jump in VCSEL bias current which in turn produces more output power and a larger measurement on the photodetector. During the 1.07 ns-long pulse we see that the VCSEL triggers a fast optical spike. The injection locking condition is again broken during exposure to this input pulse. When the bias current in increased the resonant wavelength of the VCSEL is altered, increasing the peak wavelength of the XP and YP modes of the device. However, because the injection wavelength is stable, the frequency detuning Δf is temporally increased and the conditions for injection locking altered. The electrical perturbation therefore forces the bifurcation point in the system to trigger spiking responses. The consistency of the activated spike is plotted in the temporal map of Fig. 3.1.7 (c), which shows the arrival of 200 consecutive RF input pulses. The results show that a single spiking dynamic is consistently activated within the 1.07 ns pulse, and that a second spike is

intermittently triggered towards the end of the RF input. This indicated that the pulse duration may be too short for consistent 2 spike activation so extended pulse durations of 1.34 ns, 1.9 ns and 2.35 ns were tested (see Figs. 3.1.8 (a)-(c)).

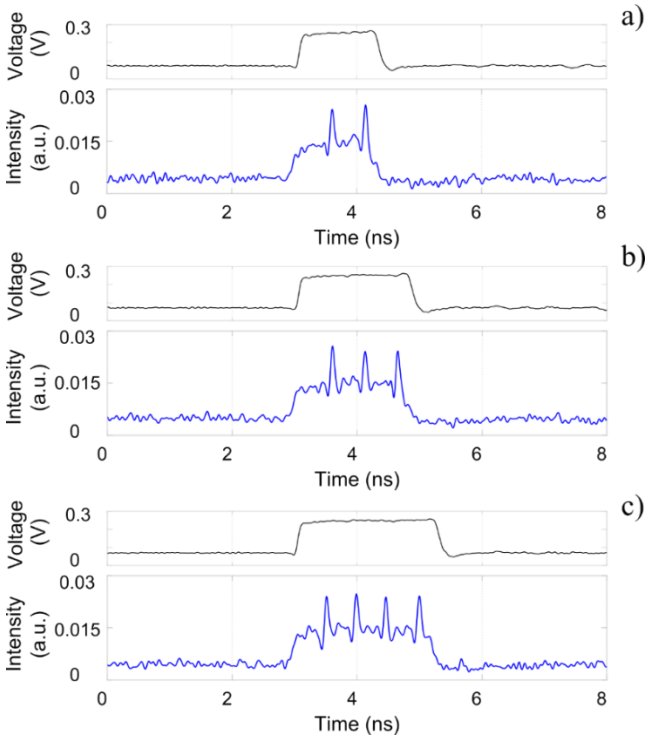

Figure 3.1.8 – Tonic spike activation with electrical bias modulation. Pulses of increasing duration, 1.34 ns (a), 1.90 ns (b) and 2.35 ns (c) (in red) modulate the bias current of the VCSEL neuron. The bias modulation interrupts the injection locking behaviour producing trains of 2, 3 and 4 pulses at the output of the VCSEL (in blue). Experimental parameters are identical to those in Fig. 3.1.7. Results previously published in [196].

The extended RF input pulses successfully produced 2, 3 and 4 optical spike activations, with fast (100 ps-long) durations and sub-nanosecond inter-spike intervals. The number of optical spikes activated remained consistent across all 200 consecutive RF input pulses. As seen in the temporal map of Fig. 3.1.7 (c) a slow variation in the activation time of the spike can be observed. This variation is present within the entire temporal map, with the shade of blue fluctuating across all 200 cycles. This indicates that during this measurement the output power of the VCSEL was fluctuating hence the experimental parameters, (the temperature or applied bias current) were not completely stable. The fluctuation of bias or temperature would

alter the position of the system around the bifurcation point, hence the spike activation time (and the activation of a second spike) varies across the 200 cycles. Given improvements to experimental stability we would expect the dampening of fluctuations in spike activation time. The results shown here for electrically-triggered spiking dynamics have been reported in [196].

Overall, this method of electrically-controlled optical spike activation can also reproduce the tonic spiking behaviour of biological neurons, activating spiking continuously for the whole duration of an input stimulus. This method of spike activation has exciting opportunities to enable the network interconnectivity of VCSEL neurons through electrical connections, granting additional freedom to the operation wavelength of coupled devices.

3.2 Spike Inhibition

The controlled activation of excitatory spiking dynamics is key to the functionality of neuromorphic systems. However, the ability to controllably inhibit and suppress spiking responses is also crucial to the smooth operation of biological neural networks. In biological neurons, inhibition is used to stop or slow the firing of excitatory neurons, keeping the data traffic within the network under control and allowing the network to function efficiently [225]. Similarly, inhibitory responses are also important in learning rules based on spike-timing dependant plasticity (STDP) [53], [226] and for effective input integration. In this demonstration we again show that both optical and electrical modulation can be used to inhibit a spiking VCSEL neuron for a controllable duration of time.

To realise inhibition in our photonic VCSEL neurons via optical modulation, we again utilise the experimental setup shown in Fig. 3.1.3. As in the activation of spiking dynamics (Chapter 3.1), we use modulated optical injection to induce transitions from parameters that produced continuous spiking responses to parameters that produced injection locking. Unlike the previous demonstrations we achieve inhibition by initially positioning our system in a regime of continuous

spiking dynamics. For this a low injection power of 33.56 µW and a frequency detuning of Δf = -2.83 GHz from the XP mode of the VCSEL were used. Under these experimental conditions the VCSEL produced continuous spiking dynamics with sub-nanosecond inter-spike intervals. Positive input pulses were then introduced into the optical injection, causing the optical injection power to increase for a configurable temporal duration. A 4.33 ns input optical pulse and the corresponding output of the VCSEL neuron are shown in Fig. 3.2.1 (a)-(c).

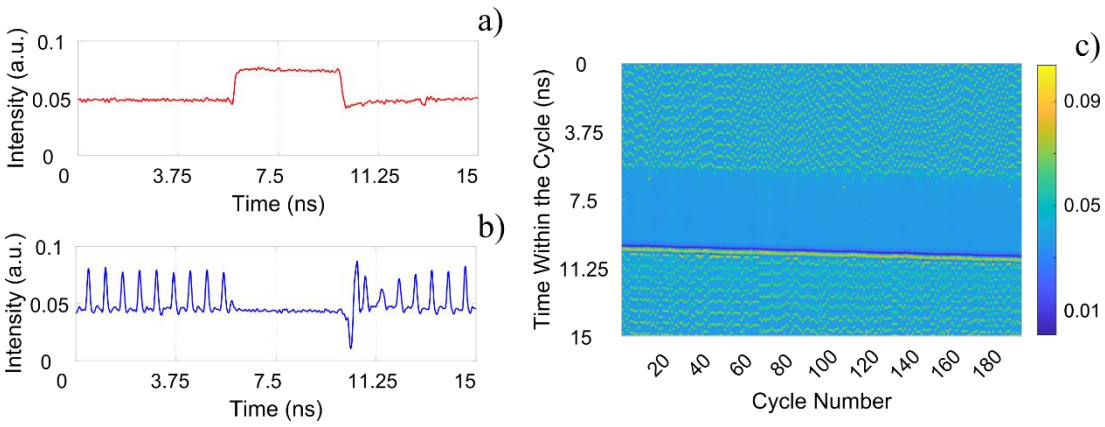

Figure 3.2.1 – Spike inhibition in a VCSEL neuron via optical modulation. A positive optical pulse of duration 4.33 ns was encoded into the optical signal injected into the VCSEL neuron (a), producing an inhibition window in the spiking output (b). The temporal map of the VCSEL neuron's response reveals optical spikes are consistently inhibited for the temporal duration of each of the 200 consecutive optical pulses injected into the system (c). Experimental conditions: I = 3.0 mA, T = 293 K, external orthogonal (XP) mode injection with Δf = -2.83 GHz and P_{inj}= 33.56 µW. Results previously published in [197].

The VCSEL neuron's output shows the continuous firing of optical spikes until the rising edge of the input pulse enters the device. The incoming pulse increases the optical input power such that the VCSEL becomes optically injection locked, altering the resonant wavelength, and suppressing the optical spiking responses. The window of inhibition is achieved for the entire duration of the input pulse. The response of the VCSEL neuron is plotted for 200 consecutive inputs in Fig. 3.2.1 (c). Here the temporal map shows clearly that spiking dynamics are consistently suppressed during

the inhibition window and that the unlocking transition consistently recovers the optical spiking.

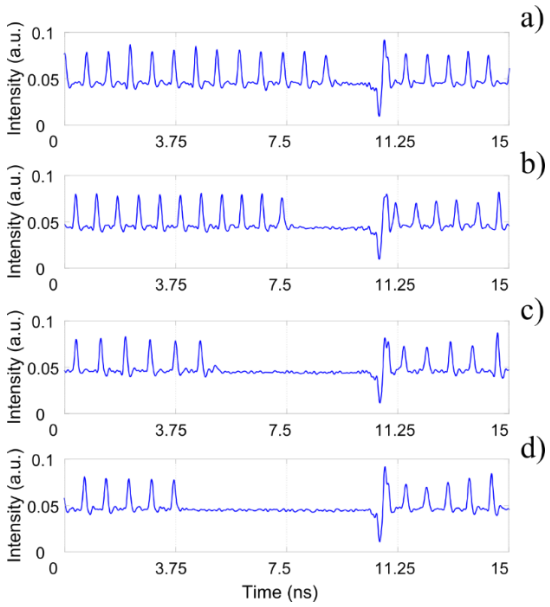

Figure 3.2.2 – Controlled spike inhibition is obtained with a VCSEL neuron. Positive optical input pulses of increasing duration of 1.89 (a), 3.30 (b) 5.30 (c) and 6.70 ns (d) were used. Positive optical pulsed inputs injection-lock the VCSEL neuron, suppressing the production of continuous spike trains. Experimental parameters are the same as those used in Fig. 3.2.1. Results previously published in [197].

To further test the controllability of the spike inhibition response of the VCSEL neuron, we injected optical pulses of various temporal durations (1.89, 3.30, 5.30 and 6.70 ns) into the spiking VCSEL neuron (Figs. 3.2.2 (a)-(d)). The temporal outputs measured in Figs. 3.2.2 (a)-(c) show that as the duration of the optical input pulse is increased, the length of the inhibition window is also increased, thus giving a simple mechanism for controllable optical spiking inhibition. The configurable length of the spiking inhibition window revealed no detrimental effect on the consistency of the suppression as spiking dynamics were effectively removed in multiple consecutive inputs.

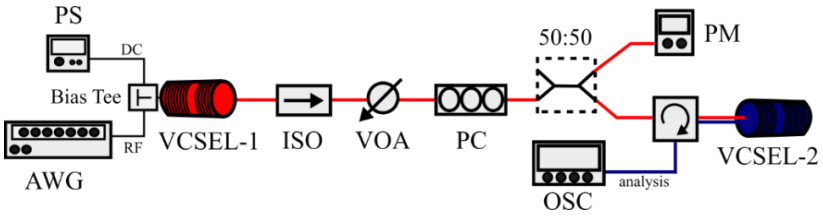

Figure 3.2.3 – Experimental setup for electrically-controlled spike inhibition. An external electrical signal is used to modulate the bias of a master VCSEL (VCSEL-1). VCSEL-1's signal is injected into the slave VCSEL neuron (VCSEL-2), producing continuous spiking dynamics. When the electrical input pulse arrives at VCSEL-1, the output power is increased, injection locking VCSEL-2 and suppressing spiking dynamics. Experimental components are as previously described.

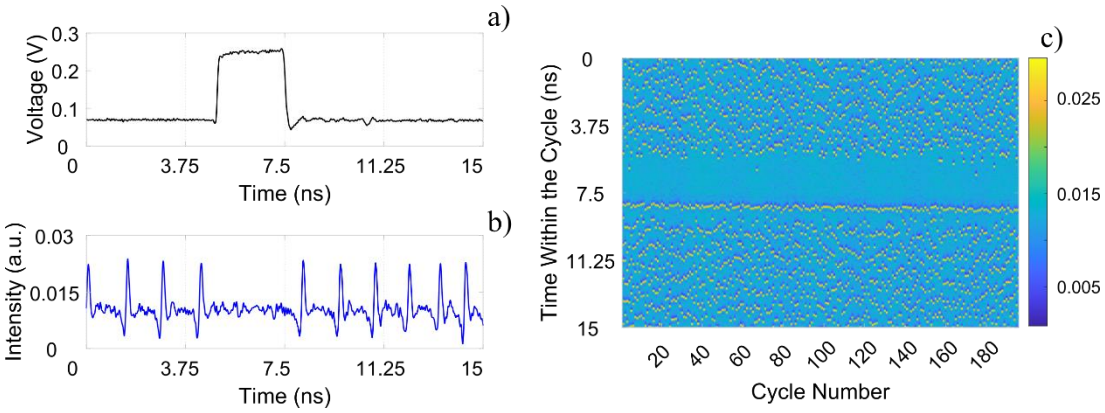

Figure 3.2.4 – Spike inhibition via electrically-controlled bias modulation in a VCSEL neuron. A positive pulse of 2.66 ns (a) modulates the bias current of the master VCSEL. The modulated optical signal is injected into the slave VCSEL neuron producing continuous spike trains. When positive pulses enter the slave VCSEL neuron the spiking responses are inhibited as the device enters the injection locking regime (b). A temporal map, measured across 200 consecutive input pulses, shows the consistency of the spike inhibition response (c). Experimental conditions: I_{master} (I_{slave}) = 4.16 mA (4.06 mA), T_{master} (T_{slave}) = 293 K (294 K), external orthogonal (XP) mode injection with Δf= -2.83 GHz and P_{inj}= 42 μW. Results previously published in [200].

The results show the consistent triggering of a large spike at the removal of the inhibition. This rebound spike, is produced when the parameters of the system are close to the locking/unlocking boundary of the VCSEL neuron. The constant

injection parameters of the system are important to the spike firing rate observed at the output of the VCSEL. The closer the parameters are to the bifurcation point (here the locking/unlocking boundary) the slower the spiking rate [197]. Here the injection parameters initially position the system far from the locking boundary, hence the continuous spiking responses from the VCSEL are fast. The rebound spike is the result of the system firing close to the bifurcation point as the input pulse is removed, hence appearing as a slower, larger spike. These result are consistent with the experimental and theoretical results we previously reported in [197].

We have therefore demonstrated that optical modulation can be used to exploit a bifurcation in our VCSEL neuron to achieve spike inhibition like that observed in biological neurons. Additionally, we can also demonstrate a pathway to controllable inhibition via the injection of electrically-modulated signals into a VCSEL neuron. The experimental setup used to realise electrically-controlled spike inhibition with a VCSEL neuron is shown in Fig. 3.2.3.

Electrical signals are introduced to a master VCSEL (VCSEL-1) via the RF port of an electrical bias tee. The electrical input modulates the bias current of the master VCSEL producing a higher VCSEL output power during the positive input pulse. VCSEL-1 is then injected into a slave VCSEL neuron (VCSEL-2) using an optical attenuator and polarisation controller to configure the injection power and polarisation. The injection of VCSEL-1 is made into the orthogonal mode of VCSEL-2 with a frequency detuning of Δf = -2.83 GHz and an injection power of 42 μW. Under these conditions VCSEL-2 produces a continuously spiking output. The electrical input used to modulate VCSEL-1 is shown in Fig. 3.2.4 (a) and the resultant VCSEL-2 output is plotted in Figs. 3.2.4 (b) & (c).

Electrical pulses of 2.66 ns temporal length were used to modulate the light output of the master VCSEL (VCSEL-1) with pulse amplitudes of 160 mV producing a temporary bias current increase of 3.2 mA (Fig. 3.2.4 (a)) in VCSEL-1. As shown in Fig. 3.2.4 (b) in the absence of an input pulse, VCSEL-2 produced fast continuous spiking dynamics. Upon the injection of an input pulse from VCSEL-1 into VCSEL-2, the system remained quiescent and did not trigger a fast spiking response. Here the increased injection power, associated with the increased electrical bias across

VCSEL-1, injection-locked VCSEL-2 to the signal from VCSEL-1, pulling the system out of the excitable spiking regime. The temporal map of 200 consecutive inputs (plotted in Fig. 3.2.4 (c)) shows that the mechanism for spiking inhibition is consistent and that for the duration of the input pulse a window of stable, non-spiking dynamics is produced. After the removal of the input pulse, the system recovers and returns to the original spiking regime in a highly consistent way as can be seen clearly in Fig. 3.2.4 (c).

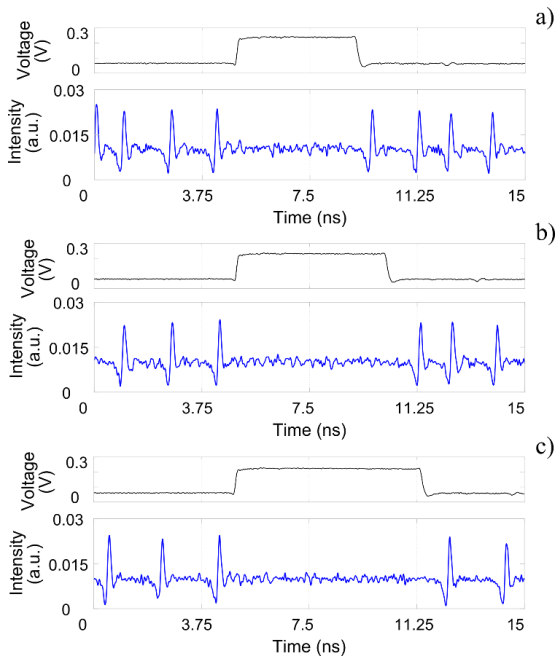

Figure 3.2.5 – Electrically-controlled spike inhibition with extended duration in a VCSEL neuron. Time series from the electrically modulated master VCSEL (top plots, in black) and the subsequent inhibition of spiking responses obtained from the VCSEL neuron (bottom plots, in blue). Electrical pulse duration was increased from 4.29 ns (a) to 5.35 ns (b) and 6.61 ns (c). Experimental conditions are identical to those used in Fig. 3.2.4. Results previously published in [200].

The controllability of the electrically triggered spiking inhibition behaviour was also tested for various input pulse durations. Electrical pulse durations of 4.29, 5.35 and 6.61 ns were all used to modulate the bias of VCSEL-1. The electrical inputs and the subsequent output of VCSEL-2 is plotted in Fig. 3.2.5. The VCSEL-2 outputs measured in Fig. 3.2.5 (a)-(c) show that as the input pulse duration is increased, the

duration of the spiking inhibition window is also increased. The length of positive electrical inputs can therefore be used to control the number of spiking events inhibited at the output of VCSEL-2. As in the case of Fig. 3.2.4, the inhibition of spiking dynamics was consistent across all consecutive inputs and was not influenced by the duration of the inhibition window. Electrical bias modulation can therefore be used to controllably inhibit fast sub-nanosecond neuromorphic spiking dynamics in VCSELs operating at key telecom wavelengths.

Overall, we have demonstrated that spike inhibition is possible with off-the-shelf VCSELs, acting as artificial optical spiking neurons. This is achieved both via the injection of optically- or electrically-modulated signals into a VCSEL neuron. These techniques allow us to silence the tonic firing of neuromorphic spiking dynamics in VCSEL neurons. Photonic VCSEL neuron systems therefore have the capability to apply inhibition alongside excitable spiking dynamics to emulate the functionality of biological neurons.

3.3 Neuromorphic Properties of Spiking Dynamics

We have shown in Chapters 3.1 & 3.2, that neuron-like spiking dynamics can be controllably activated and inhibited in VCSEL neurons via both optical and electrical modulation. However, equally crucial to the functionality of the neuron is its ability to integrate incoming stimuli (inputs) and threshold input contributions (in the soma of the cell). Without the ability to threshold input contributions the neuron would fire for all inputs and not be capable of its decision-making functionality, meaning thresholding is key to neural processing and neuromorphic devices [32]. Thresholding enforces a requirement on the activation of the neuron, making it such that the inputs must have sufficient energy/potential before the neuron will trigger the firing of spiking responses [218], [219]. In this Chapter we investigate further the neuromorphic spiking dynamics of VCSEL neurons, specifically, the existence of an activation threshold and the inter-spike interval of the spikes triggered in our devices.

We previously demonstrated that 100 ps-long spiking responses could be controllably obtained from a VCSEL neuron subject to modulated optical injection. Using the same experimental setup (Fig. 3.1.3) we now investigate the effect of varying the input perturbation's (negative pulses) amplitude (strength) on the spiking responses of the system. By varying the strength of the injected inputs, we can determine the existence of a neuronal activation threshold for spike firing in VCSEL neurons. In this experiment the VCSEL neuron was injection locked with an optical signal of 164.8 μW from the tuneable master laser. This was injected into the orthogonal (XP) polarisation mode of the VCSEL with a frequency detuning of $\Delta f = -6.71$ GHz. The input used to test the system for a spike activation threshold, was made up of 7 negative pulses of increasing amplitude. The input amplitudes were configured to 0.4, 0.5, 0.6, 0.7, 0.8, 0.9 and 1.0 times the maximum range of the AWG in our experimental setup. Once encoded into the optical injection, the largest amplitude input (1.0 times the max range) produced a power drop of 59.8 μW. The input pulses were generated with 100 ps temporal widths and 2 ns time separations between them. The input-encoded optical injection and the response of the VCSEL neuron are shown in Figs. 3.3.1 (a) & (b) respectively.

When the first input pulse, corresponding to a small power drop of 24 μW (0.4 x 59.8), entered the VCSEL neuron, the system failed to trigger a neuron-like spiking response. Further increasing the input amplitude to 0.5 and 0.6 x 59.8 μW, similarly failed to activate a response from the VCSEL neuron. However, when an input amplitude of 41.9 μW (0.7 x 59.8) entered the VCSEL neuron, the system responded as previously observed, activating a fast spiking response (Fig. 3.3.1 (b)). When the input amplitude was increased further to 0.8, 0.9 and 1.0 x 59.8 μW, the system continued to activate neuronal spiking responses. Plotting the results of 653 consecutive input sequences in a temporal map (Fig. 3.3.2 (a)), we gain additional information about the activation of spiking dynamics in the VCSEL neuron. The temporal map reveals that the consistency of the spiking response decreases with the strength of the input. The efficiency curve plotted in Fig. 3.3.2 (b) better illustrates the spike activation efficiency against input strength.

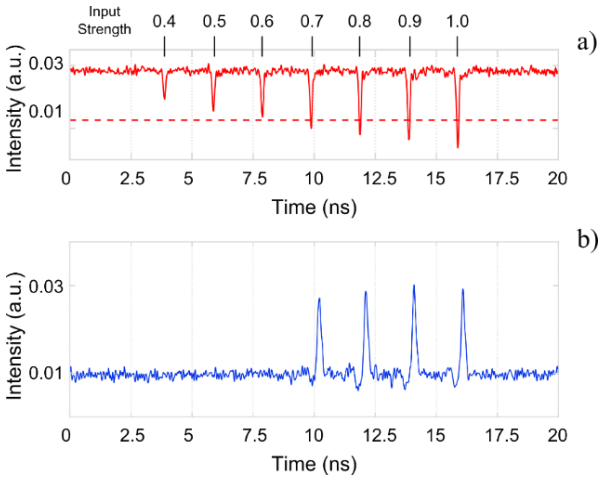

Figure 3.3.1 – Spike activation in the VCSEL neuron with varying input perturbation amplitudes (strength). Time series showing the externally injected optical signal with 7 (100 ps) pulses of increasing intensity (a), and the corresponding VCSEL neuron response (b). Input pulses correspond to drop amplitudes of 0.4-1.0 x 59.8 μW. The red dotted line represents the system's spike activation threshold. Experimental conditions: I = 5.0 mA, T = 293 K, external orthogonal (XP) mode injection with Δf = -6.71 GHz and P_{inj}= 164.8 μW. Figure reproduce from [193].

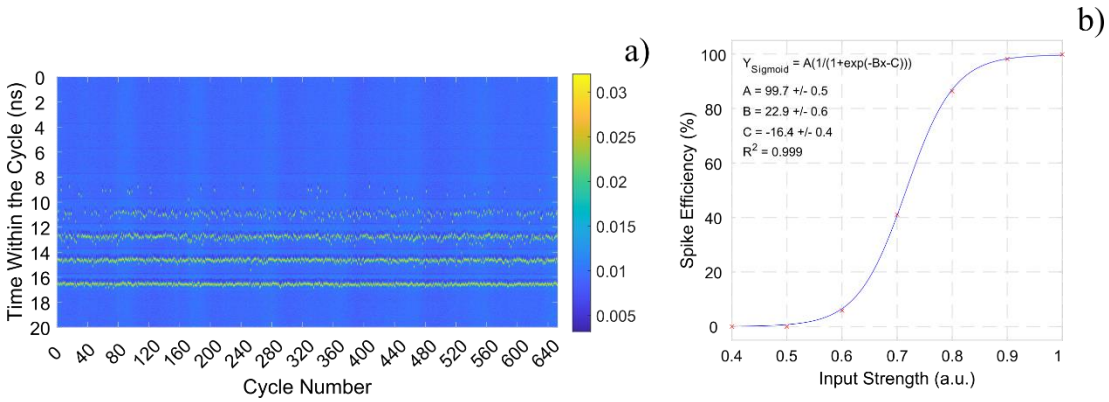

Figure 3.3.2 – Temporal map and spike efficiency curve for optical spike activation. The temporal map plots the response of the VCSEL neuron to 653 consecutive input sequences (a). The activation efficiency of spiking responses is plotted for the increasing values of input strength (b). The results plotted in (a) and (b) correspond to the time series of Fig. 3.3.1. Experimental conditions are identical to those used in Fig. 3.3.1. Figure reproduced from [193].

We see that for the strongest input pulse the spike efficiency is 100%, meaning every input activated a spiking response. This is expected as the strongest pulse reduces the injection power most significantly, effectively perturbing the system, annihilating the bifurcation solutions, and sending the system through the limit cycle generating a spike. The spike efficiency drops to 41% when the 0.7 strength input pulses enter the VCSEL neuron. Reducing the input amplitude produces smaller injection power drops, resulting in less consistent activation of the system, until smaller power drops (0.4-0.6 in this demonstration) fail to successfully cross the locking boundary. In our system, this mechanism creates a non-linear activation threshold like those in biological neurons. A sufficient input pulse amplitude and hence injection power drop are required to break down the injection locking condition and achieve the activation of neuromorphic spikes.

To further confirm the existence of a spike activation threshold in VCSEL neurons, we also analysed the effect of input perturbation amplitude for the case of electrically triggered spiking responses. Using the experimental setup shown in Fig. 3.1.4, we injected positive electrical inputs of increasing amplitude into the bias current of the VCSEL neuron. Each electrical input was used to modulate the bias of the device with amplitudes of 59.1, 91.1, 122.9, 166.3 and 206.3 mV producing 1.18, 1.82, 2.46, 3.33 and 4.13 mA changes in bias respectively (Figs. 3.3.3 (a)-(e)). Input pulses were configured to have 0.65 ns long pulse widths and optical injection locking was achieved with an external optical signal. The blue plots of Figs. 3.3.3 (a)-(e) show the VCSEL neuron's response to each electrical input. These results are adapted from our publication on electrically trigger spiking dynamics in VCSELs [196].

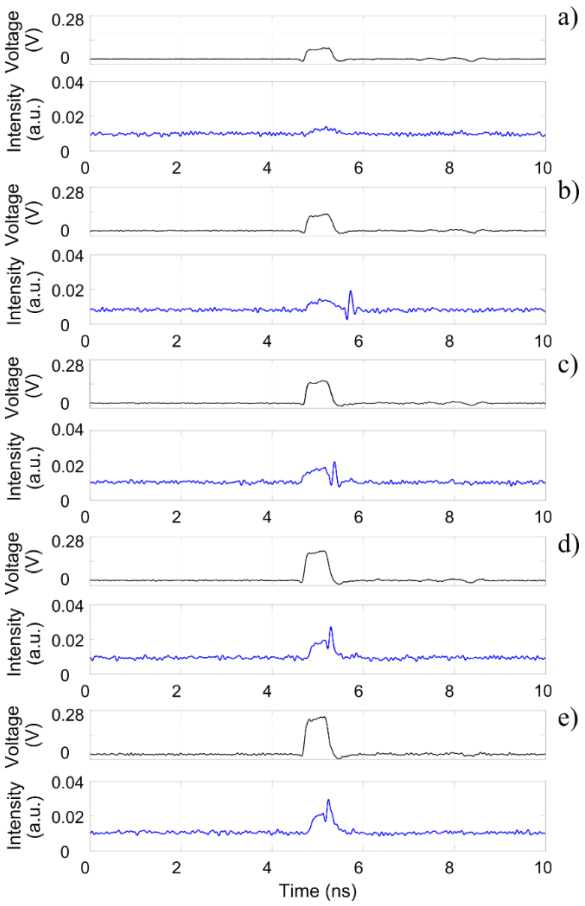

Figure 3.3.3 – Electrically triggered spike activation with varying input amplitude (strength). Time series showing the electrical signals used to modulate the VCSEL bias (top - in black), and the corresponding VCSEL neuron response (bottom - in blue). Electrical input amplitudes of 59.1 (a), 91.1 (b), 122.9 (c), 166.3 (d) and 206.3 mV (e) were injected into the bias tee. Experimental conditions: I = 6.0 mA, T = 293 K, external orthogonal (XP) mode injection with Δf = -5.65 GHz and P_{inj}= 210 μW. Results previously published in [196].

In Fig. 3.3.3 we observe spiking responses from all input amplitudes greater than 91.1 mV, with only the smallest amplitude pulse (51.1 mV) failing to activate the device. As in our previous electrical activation demonstration, the increase in VCSEL bias creates a step in observed output intensity. A temporal map created using 40 measurements of each input pulse and the corresponding spike efficiency (for 200 consecutive measurements of each input) are also plotted in Figs. 3.3.4 (a) & (b). In the temporal maps we can see that the spike efficiency for the two smallest inputs is low (0 and 12.2%). However, when the electrical pulse amplitude is increased to

122.9, 166.3 and 206.3 mV the spike efficiency increases to 90.8, 100 and 100% respectively. This non-linear rise in spike efficiency again indicates the presence of an activation threshold in our VCSEL neuron. In a similar mechanism to that of the optical modulation technique, here increasing the bias alters the frequency detuning between optical injection and the resonant mode of the laser. When input pulse amplitudes are insufficient the system remains comfortably locked to the external optical signal. Only when a large enough bias modulation is produced by electrical inputs do spiking responses appear consistently.

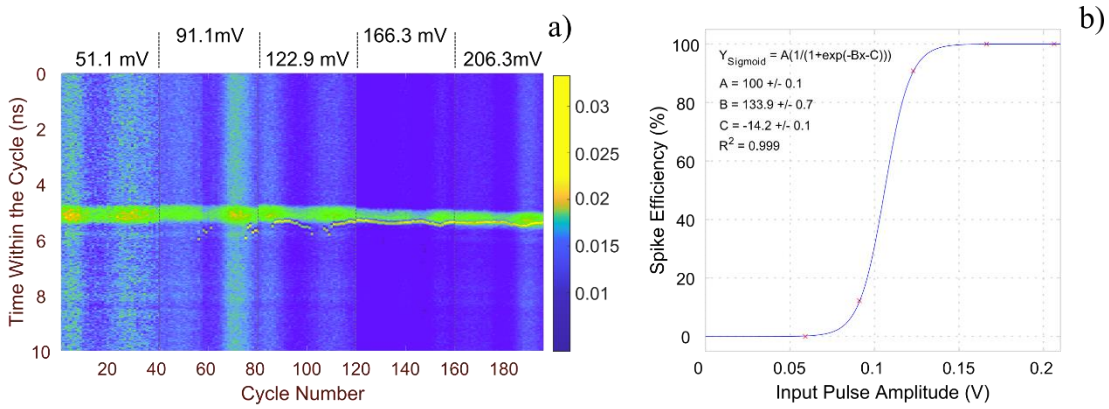

Figure 3.3.4 – Temporal map and spike efficiency curve for electrically-controlled spike activation in a VCSEL neuron. The temporal map combines 40 consecutive responses to each of the 5 input pulses shown previously in Fig. 3.3.3. In total the temporal map (a) and the corresponding spike efficiency curve (b) sample a total of 200 consecutive input sequences. The spike efficiency curve reveals a non-linear spike activation threshold. Experimental conditions are identical to those used in Fig. 3.3.3. Results reported in [196].

From the results of Figs. 3.3.1-3.3.4 we can therefore deduce that our VCSEL neuron has a non-linear activation threshold like that of a biological neuron. While doing so we have also identified the two key experimental parameters that govern the thresholding behaviour, injection power (P_{inj}) and frequency detuning (Δf). The mechanism for activating spiking dynamics in our photonic VCSEL neuron is the perturbation of the system around a bifurcation present at the injection locking boundary. Therefore, the threshold for spike activation is dependent on the position of the system in dynamical space. If the system is positioned closer to the locking/unlocking boundary, then the amplitude (strength) of the inputs required to

trigger spikes are lower than those when positioned further from the locking/unlocking boundary. We can therefore reposition our system (using injection power and frequency detuning) to select the desired spike activation threshold. We also note here the existence of a threshold with regards to the spiking inhibition mechanism discussed in Chapter 3.2, and have shown in a previous report that sufficient input pulse strength is required to efficiently lock and inhibit spiking responses [197].

The time series plots of Figs. 3.3.3 (c)-(e) and the temporal map of Fig. 3.3.4 (a) indicate that the strength of the input perturbation (stimulus) may also have an effect on the latency of the spiking response by the VCSEL neuron. In these cases, we observe lower latency in the activation of spikes when the amplitude of the input perturbation is high and a larger latency when low. The latency of the spike therefore contains information of the input perturbation (stimulus) that was used to activate the spike event in the VCSEL neuron. This storing of information in the latency of spikes has been observed in biological neurons. For example, in the neurons of the visual cortex the latency of spikes was shown to be shorter when processing higher contrast ratios [223] and when handling auditory signals, neurons have been shown to store the directionality of sound in spike latency [224]. The input-dependant spike latency is therefore another neuronal behaviour exhibited by VCSEL neurons allowing the storage of additional input information in the spiking outputs.

In biological neurons the maximum spike firing rate for two consecutive input stimuli is governed by what is called the refractory period. Specifically, the absolute refractory period is the time after a first stimulation (yielding a spiking event) that a second action potential cannot be fired by a second stimulation, irrespective of the latter's input strength. Following the absolute refractory period, the potential of the neuron begins to recover, returning to its rest potential after a given time. That time between the absolute refractory period and the neuron's full recovery is called the relative refractory period, whereby the neuron can be forced to elicit an action potential given a stronger than normal stimulation [218], [219]. By investigating the refractory period within our VCSEL neuron we can therefore determine the minimum inter-spike interval possible with consecutive input perturbations in our system. Absolute and relative refractory periods have been observed in diverse laser-

based neuromorphic models and highlight the fast operation speed of different photonic platforms [169], [177], [227].

We have investigated the refractory period for the VCSEL neurons of this work. Using modulated optical injection and the experimental arrangement reported in Fig. 3.1.3, we generated pairs of input pulses (perturbations) with increasing temporal separation for their injection into a VCSEL neuron. The input pulses (perturbations) were configured to have super-threshold strength and pulse widths of 0.3 ns. External optical injection was made into the VCSEL's Orthogonal (XP) mode with a detuning of Δf = -6.35 GHz and an injection power of P_{inj} = 185 μW. The response of the VCSEL neuron to incoming input pulse pairs is plotted in Fig. 3.3.5.

The time series for the case of input pairs with 0.66, 1.03 and 1.21 ns separation are shown in Figs 3.3.5 (a)-(c). In this experiment the input separation was measured from the rising edge of the initial pulse to the rising edge of the second pulse. In the case of the 0.66 ns-separated input perturbations, we find that a single spiking response is triggered by the VCSEL neuron, resulting in a zero second-spike firing efficiency, as shown in the curve of Fig. 3.3.5 (d). This indicates that for this case the system is not capable of firing a second response and that this input separation falls within the absolute refractory period of the VCSEL neuron. The input pulse here attempts to perturb the system before the recovery of sufficient carriers in the device, resulting in no response from the system. Growing the input separation to 0.93 ns results in an increase in the firing efficiency of a second spike by the VCSEL neuron. This indicates that the system in now capable of activating a spiking response, however, the response in not consistent as a second spike is only triggered for 39.7% of the 232 consecutive measurements. Looking at the efficiency curve in Fig. 3.3.5 (d), we can conclude that the tested VCSEL neuron had an absolute refractory period of 0.84 ns. The spiking response for the input pair separated by 1.02 ns is plotted in Fig. 3.3.5 (b), showing that indeed two spiking responses are fired by the VCSEL neuron. The spike efficiency curve reveals that the triggering of the second spike is consistent across all 232 consecutive inputs. However, the second response from the VCSEL neuron does not produce a complete spiking orbit, with the shape differing from that of the initial response. The opening drop of intensity, clearly visible in the initial response, and the overall spike amplitude are not consistent with the spike

triggered earlier in the sequence. This indicates that the excursion used to produce the intensity spike was altered because the system did not fully recover before the arrival of the second input. Despite activating a consistent response, this means the 1.02 ns input pair fall within the relative refractory period of the VCSEL neuron. It is not until pulse separations of 1.14 ns or higher are used that the relative refractory period is overcome, and consecutive spiking responses are produced by the VCSEL neuron in response to two consecutive input perturbations. An example of consistent consecutive spikes for a 1.21 ns input pair is given Fig. 3.3.5 (c).

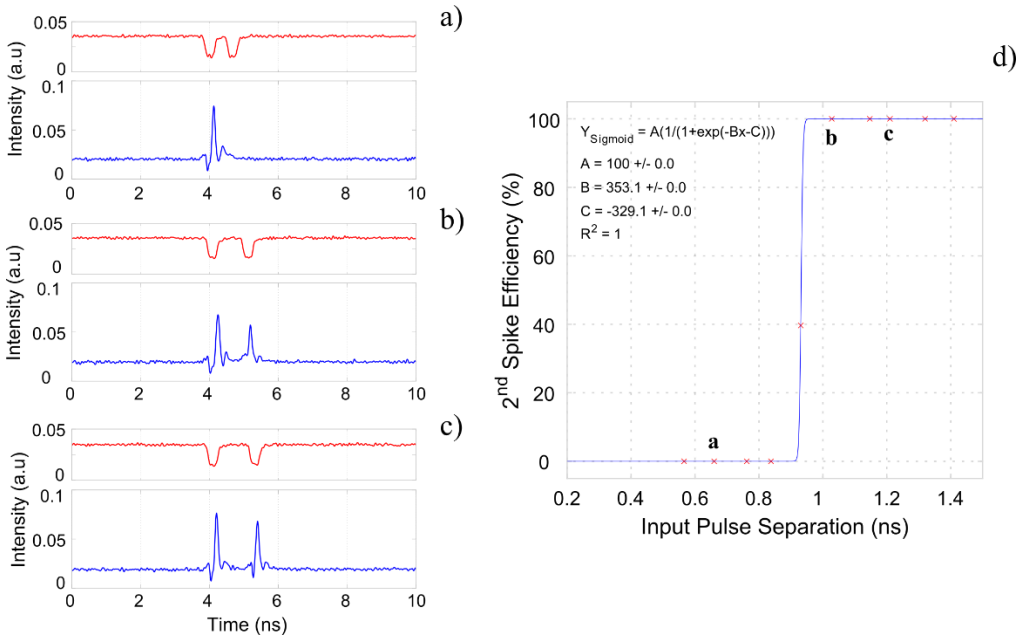

Figure 3.3.5 – Refractory period analysis of a VCSEL neuron under external optical injection. Pairs of input pulses of increasing temporal separation are injected into the VCSEL neuron (top, in red) and its spiking response is measured (bottom, in blue). Time series show the VCSEL neuron response for input pulse pair separations of 0.66 (a), 1.02 (b) and 1.21 ns (c). The second spike firing efficiency versus perturbations temporal separation is plotted for 232 consecutive measurements (d). Experimental conditions: I = 5.0 mA, T = 293 K, external orthogonal (XP) mode injection with Δf = -6.35 GHz and P_{inj} = 185 μW.

Overall, the absolute refractory period of the measured VCSEL neuron was found to be 0.84 ns, and the relative refractory period was found to be 1.14 ns. This means

that our VCSEL neuron can operate reliably with inter-spike intervals above 1.14 ns but can be made to operate at sub-nanosecond rates under the injection of strong input perturbations. Whilst in Fig. 3.3.5 a specific VCSEL neuron was tested, we also observed similar refractory periods for multiple other VCSEL devices, with the VCSEL neuron in [203], reporting a refractory period of 1.08 ns. The presence of both absolute and relative refractory periods is therefore another key feature shared by our VCSEL neurons and biological ones. The inter-spike interval observed in this work indicates that VCSEL devices are suitable for GHz operation which could realise spike-based processing in neuromorphic systems at rates multiple orders of magnitude faster than electronic implementations of neurons. The carrier dynamics of the presented VCSELs are believed to be responsible for the minimum 1 ns inter-spike interval. There are reports in literature of VCSEL devices producing pulse trains at 10 GHz rates (with pulse widths of 11.5 ps) using gain switching [228], and it has been shown that relaxation oscillations in gain switched VCSELs can reach 71 GHz [229], due to the high concentration of carriers in the active region. These results offer promise for the realisation of further inter-spike interval enhancement in VCSELs (bringing it below the 1 ns frontier) with additional design, optimisation and fabrication stages.

In conclusion, the results in this chapter have demonstrated that VCSEL neurons are capable of delivering controllable and reproducible spiking dynamics, analogous to those observed in biological neurons, but at ultrafast speed rates. Exploiting a bifurcation point around the injection locking/unlocking boundary in the VCSELs investigated we can perturb our system with input signals (stimuli); hence achieving (neural-like) excitability behaviour that triggers class 1 excitable spiking dynamics at very high speeds. We demonstrated that fast perturbations (down to sub-ns durations) introduced through the use optical and electrical modulation can stimulate a VCSEL neuron making it produce fast spiking responses with ~ 100 ps pulse widths and nanosecond rates. We revealed the number of spiking responses can also be controlled by the duration of the injected pulse, corresponding to the behaviour of tonic spiking in biological neurons. Similarly, the inhibition of spiking dynamics with optically and electrically modulated signals was demonstrated experimentally. Exploiting injection locking, we also showed continuous spiking neurons could be

silenced for a controllable duration, hence realising the same functionality of inhibitory biological neurons. Exploring further the neuronal properties of our artificial photonic spiking VCSEL neurons we showed that the excitability (and inhibitory) mechanisms were governed by input thresholds. Like biological neurons, our photonic VCSEL neurons require a specific input strength before the activation/inhibition of spikes can be achieved. We demonstrated this was true for both optical and electrical excitation and discussed that the threshold can be controlled by varying the position of the system in parameter space. The investigation into input thresholding for spike activation subsequently led to results that showed VCSEL neurons can encode information of the input in the precise timing of spikes. We demonstrated that with increasingly strong inputs the activation delay of spiking dynamics was reduced. This feature corresponds to a rate encoding functionality observed in biological neurons, promoting our VCSEL neurons from devices that can receive only binary inputs to those that can operate with analog signals. Finally, we measured the refractory period of our VCSEL neuron (the minimum inter-spike interval) when subject to two consecutive stimuli. The absolute refractory period was found to be 0.84 ns and the relative refractory period was found to be 1.14 ns, enabling our VCSEL neuron to operate at GHz rates provided strong input pulses are used. This imposes a theoretical limit on the speed of our VCSEL neurons in the same way that is observed in other spiking systems, but at speeds 3 orders of magnitude faster than some electronic approaches [72]. VCSEL neurons therefore possess multiple controllable and accessible neuromorphic functionalities in-line with those observed in biological neurons, making them excellent candidates for artificial photonic spiking neurons for future light-enabled neuromorphic processing platforms for ultrafast brain-inspired computing and AI functionalities.

Chapter 4

Towards the Implementation of Networks of Artificial Photonic Neurons

In Chapter 1 we discussed the reasoning behind the increasing demand for neuromorphic systems and have discussed the laser dynamics within VCSELs devices that allow us to achieve spiking signals. In Chapter 3 we demonstrated how we can experimentally implement VCSEL neurons and how we controllably activate and inhibit fast spiking responses. Here in Chapter 4, we investigate the capability of photonic spiking VCSEL neurons to communicate in network architectures. Applying the controllable neuromorphic functionalities achieved so far, we study the propagation of spiking signals between interconnected VCSEL neurons. Specifically, we investigate the propagation of controllable spike (activation and inhibition) signals in feedforward configurations where the output of one device is fed to the input of another (Chapter 4.1). We also investigate the propagation of spiking signals in a diverging architecture where 1 VCSEL neuron feeds 2 downstream VCSEL neurons in a 1-into-2 network arrangement (Chapter 4.2). Finally, we demonstrate a photonic experimental incorporation of a biological retinal neural circuit that communicates via both spiking and non-spiking signals in a 3-VCSEL feedforward interconnected arrangement (Chapter 4.3).

In this chapter we will discuss experimental results that have produced journal publications. The following articles therefore relate to the forthcoming discussion:

[198] T. Deng, J. Robertson, and A. Hurtado, "Controlled Propagation of Spiking Dynamics in Vertical-Cavity Surface-Emitting Lasers: Towards Neuromorphic Photonic Networks," *IEEE J. Sel. Top. Quantum Electron.*, vol. 23, no. 6, 2017, doi: 10.1109/JSTQE.2017.2685140.

[199] T. Deng *et al.*, "Stable Propagation of Inhibited Spiking Dynamics in Vertical-Cavity Surface-Emitting Lasers for Neuromorphic Photonic Networks," *IEEE Access*, vol. 6, 2018, doi: 10.1109/ACCESS.2018.2878940.

[200] J. Robertson, E. Wade, Y. Kopp, J. Bueno, and A. Hurtado, "Towards Neuromorphic Photonic Networks of Ultrafast Spiking Laser Neurons," *IEEE J. Sel. Top. Quantum Electron.*, 2019, doi: 10.1109/JSTQE.2019.2931215.

4.1 Feedforward (1-to-1)

In this Chapter, we describe the first and simplest implementation of multiple networked artificial photonic VCSEL neurons, the feedforward configuration. In this network implementation we investigate the propagation of optical neuromorphic signals, spiking and inhibitory, from the output of a primary VCSEL neuron, into a secondary one (1-to-1). Integral to the function of biological neural networks, cascadability, the process of passing excitable spiking potentials from one neuron to another in sequence, is achieved through synaptic connections. Inter-neuron connections are made by the axon terminals to that of the dendritic tree of neighbouring neurons, or in some cases to that of its own dendritic tree (autapse/self-feedback) [176]. Biological neurons in the brain have thousands of connections to neighbouring neurons, creating vast interconnected networks with massive parallelism. This massive interconnectivity and parallelism is in-part responsible for the high processing performance of neural networks compared to traditional Von Neumann computing architectures [230]. Hence, without interconnectivity and the cascadability of neuronal signals, neural networks, and their impressive processing capabilities, breakdown.

In the simplest case, a network of multiple nodes can be realised using two individual neurons. In this configuration, information or inputs can flow from the first neuron to the second in what we call a feedforward arrangement. In a network of two excitatory neurons, the system can be deemed cascadable if the output of the first neuron provides a sufficiently strong (super-threshold) input, capable of successfully activating the second networked neuron. In this 1-to-1 feedforward arrangement, only one input is incident on the second neuron, hence if the input is not strong, then the second neuron sees no influence from the first and cascadability is not achieved. If cascadability in a 1-to-1 feedforward architecture is achieved then the system can

incorporate additional neuron layers downstream, with the confidence that any postsynaptic neuron can feel the influence of the presynaptic input given appropriate weighting. In more complex fan-in architectures, multiple inputs can integrate together towards the activation of a single neuron. This reduces the reliance of a single input to meet the requirement for network cascadability as many can contribute to the activation and continued propagation of information in the network.

The requirement for cascadability in networks such as the simple feedforward system can be extended directly to the development of artificial neural networks, where the successful inter-neuron transmission of inputs and information is key. There have been investigations into the network coupling of different photonic devices including semiconductor ring lasers [66], micro-ring lasers [231], micro-disk lasers [232], and micro-pillar lasers [173]. However, VCSELs have provided some truly encouraging results regarding the cascadability and networking of multiple devices [179], [233]. It was shown that using similar (commercially-sourced) VCSELs to the ones used in our reports, with analogous wavelength, lasing threshold and polarisation mode separation, the conditions for cascadability were met when using polarised optical injection to perform all-optical-inversion functionality [233]. It was determined that the polarisation switching in VCSELs, the physical effect used to realise the inversion operation, was cascadable when performed at high bias where the devices' output power exceeded the input power required for switching. This result draws a number of parallels to the work we present here in Chapter 4, from the devices used in each system to the optical injection-induced polarisation switching mechanism, giving us confidence that cascadability is possible in our VCSEL-based approach to photonic neuronal models. Similarly, recent numerical investigations into coupled VCSEL topologies (see [179] for instance) have found that a number of coupling topologies, with various polarisation mode coupling configurations, enabled the communication of phasic spiking dynamics between VCSELs. The cascadable spiking signals were achieved for different coupling strengths, injection stimuli and frequency detuning conditions, indicating a promisingly flexible parameter space for achievable spike-based network communication with VCSEL-based photonic neuronal models. For this reason, we investigate the propagation of the controllable neuronal signals (spiking and inhibitory) in VCSEL neurons when connected in a 1-

to-1 feedforward network. The experimental setup used to implement the feedforward network is shown in Fig. 4.1.1. The results plotted in the following Chapter are adapted from our reports in literature [198]–[200].

The experimental setup is an extension of that used in Chapter 3 to controllably activate neuronal spiking in VCSEL neurons. Amplitude-modulated optical injection is incorporated as before using an external Tuneable Laser (TL) source and a Mach-Zehnder (MZ) optical modulator. The power of the modulated optical injection is controlled using Variable Optical Attenuators (VOAs) and the polarisation of the incident light signals are controlled using Polarisation Controllers (PCs) upon entry to the MZ and a 50:50 coupler. An optical circulator is used to inject the externally modulated signal into the first VCSEL neuron (VCSEL-1). The optical circulator collects the output of VCSEL-1 before passing it through to the second device (VCSEL-2). The polarisation and the optical power of the propagated light was again controlled using a PC and a VOA. The outputs of VCSEL-1 and VCSEL-2 were captured via the analysis lines using a real-time oscilloscope.

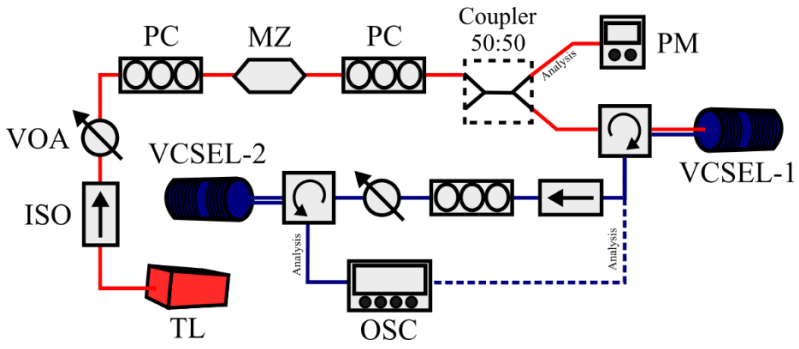

Figure 4.1.1 – Experimental setup for feedforward (1-to-1) propagation of spiking signals in a network of two serial VCSEL neurons. VCSEL-1 is subject to polarised optical injection (red path) from a TL. VCSEL-1's output is reinjected into VCSEL-2. Experimental components as described previously; TL – tuneable master laser, ISO – optical isolator, VOA – variable optical attenuator, PC- polarisation controller, MZ – Mach Zehnder intensity modulator, PM – power meter, OSC – oscilloscope.

Two commercially-sourced fibre-coupled 1300 nm VCSELs were used in this experiment. Both devices, VCSEL-1 and VCSEL-2 exhibited Parallel (YP) polarisation mode dominant emission and were selected for their similar emission wavelengths and threshold currents. Both VCSEL-1 and 2 were operated at I = 1.5 mA (~2.5 times the threshold current). The temperature of each device was set in order to better match their emission wavelengths and create a frequency detuning of Δf = -3.55 GHz between the two VCSELs. The polarisation of the external TL injection was set to match that of VCSEL-1's Orthogonal (XP) mode with a frequency detuning of Δf = -3.55 GHz. The propagated (transmitted) light from VCSEL-1 had its polarisation set to match that of VCSEL-2's subsidiary Orthogonal (XP) mode. Both devices had demonstrated excitable regimes of dynamics under the optical injection of orthogonally (XP-orientated) polarised light.

The controlled activation of excitable spiking dynamics, as described in Chapter 3, was performed in VCSEL-1 before the injection of VCSEL-1's output was made directly into VCSEL-2. Figure 4.1.2 shows the measured VCSEL responses when a single input pulse of duration t_d = 0.61 ns, is injected into VCSEL-1. Fig. 4.1.2 (a) plots the optical injection incident on the first VCSEL neuron (VCSEL-1). Initially, the high optical input power, P_{inj} = 102 μW, successfully injection locks the Orthogonal polarisation mode of VCSEL-1 to the external light signal from the TL. This results in the production of a stable output during the first ~5 ns of VCSEL-1's output (Fig. 4.1.2 (b)). When the short (t_d = 0.61 ns) input enters the first VCSEL at ~ 7 ns, the system responds by activating a single ~100 ps-long excitable spiking response. This response, analogous to those observed in biological neurons, is the result of the injection locking/unlocking transition, as discussed previously (Chapter 3). After the removal of the input pulse the system returns to a stable output as the higher optical power injection locks VCSEL-1 once again.

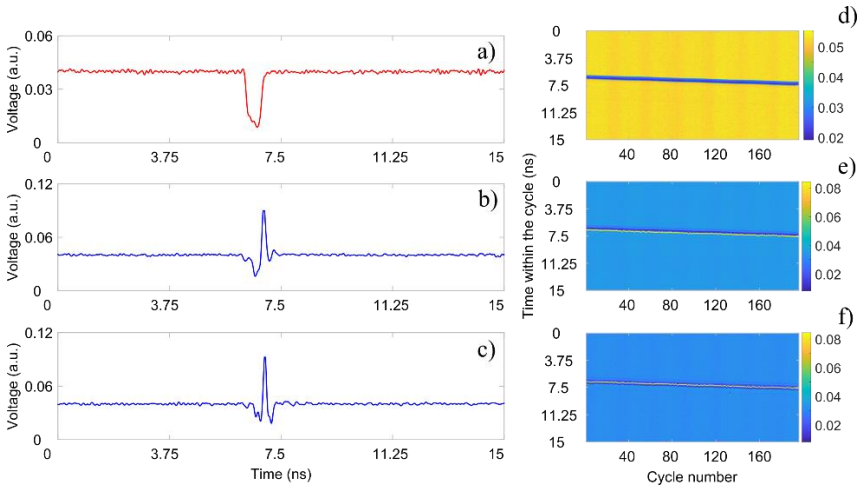

Figure 4.1.2 – Spike propagation in a feedforward (1-to-1) network of VCSEL neurons. Time series show the encoded optical injection (a negative pulse, t_d = 0.61 ns) incident on the first VCSEL (VCSEL-1) (a) and the measured spiking response (b). The spiking response, upon the injection of (b), is measured at the output of the second VCSEL neuron (VCSEL-2) (c). Temporal maps (d)-(f) show the consistency of responses for the results in (a)-(c). Optical inputs are cycled 180 times consecutively. Yellow lines indicate the consistent activation of spikes. Parameters of VCSEL-1 (VCSEL-2): I = 1.5 mA (1.35 mA), T = 298 K (292K), external orthogonal (XP) mode injection into VCSEL-1 with Δf = -3.55 GHz and P_{inj}= 102 μW, VCSEL-1 and VCSEL-2 were separated by $\Delta f_{V1\text{-}V2}$ = -3.55 GHz with $P_{V1\text{-}V2}$= 56.2 μW. Results previously published in [200].

The output of VCSEL-1 is then injected into the second VCSEL neuron (VCSEL-2) that responds according to Fig. 4.1.2 (c). The constant injection level propagating from VCSEL-1, measured to have an average power of $P_{V1\text{-}V2}$ = 56.2 μW, enters VCSEL-2 and successfully injection locks the Orthogonal (XP) polarisation mode. This generates the stable output initially observed from VCSEL-2. The arrival of the spike generated by VCSEL-1, in response to the external input, now produces a locking/unlocking transition in VCSEL-2, activating an excitable optical spiking response. The activation of a spike in VCSEL-2 indicates the successful transmission of information in the network formed by the two VCSEL neurons. A time delay of ~ 62 ns was measured between the spiking output of VCSEL-1 and VCSEL-2. This delay, created by the additional optical path traversed during signal propagation corresponds to the length of optical fibre used in the experiment. Controlling the

length of optical fibre alters the arrival time of inputs incident on VCSEL-2, a feature desirable in more complex network configurations. Figure 4.1.2 and following feedforward results have been adjusted to display results from each VCSEL on the same timescale. Temporal maps, indicating the consistency of excitable responses to 180 consecutive inputs are shown in Figs. 4.1.2 (d)-(f). The formation of straight lines in these maps indicate that the same response is triggered from each of the 180 cycles measured. In Figs. 4.1.2 (e) & (f) straight lines can be observed. This demonstrates the response from VCSEL-1 to the external input is consistent and that the propagation of spiking from VCSEL-1 to VCSEL-2 is also consistent. The feedforward network of VCSEL neurons is therefore capable of cascading an excitable response via direct optical injection of the previous layer's output.

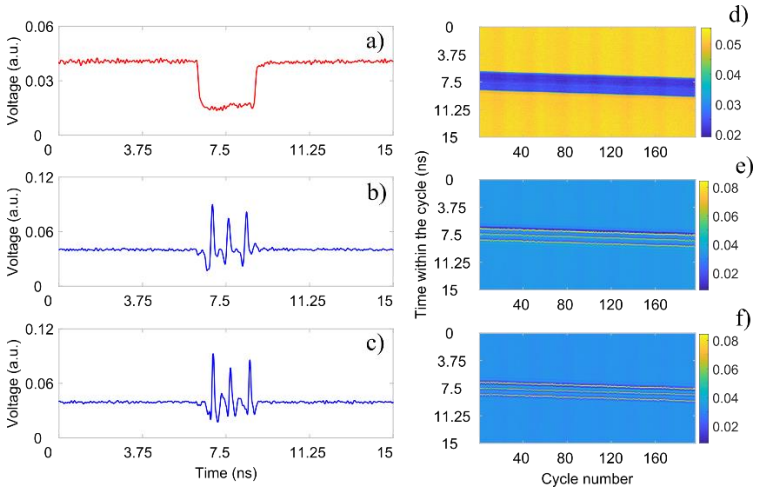

Figure 4.1.3 – Spike propagation in a feedforward (1-to-1) configuration of VCSEL neurons with extended input perturbation temporal duration (t_d). Time series show the encoded optical injection (a negative pulse, t_d = 2.74 ns) incident on the first VCSEL (VCSEL-1) (a), the measured spiking responses of VCSEL-1 (b), and the second VCSEL neuron (VCSEL-2) (c). Temporal maps (d)-(f) show the consistency of responses corresponding to results (a)-(c). Experimental parameters are identical to those used previously in Fig. 4.1.2. Results published in [200].

To further investigate the system, we tested the propagation of excitable signals generated by external inputs with increasing pulse duration (t_d). The response of

VCSEL-1 and VCSEL-2 to an external pulse of duration t_d = 2.74 ns is shown in Fig. 4.1.3, with the results of a larger parameter study shown in Fig. 4.1.4.

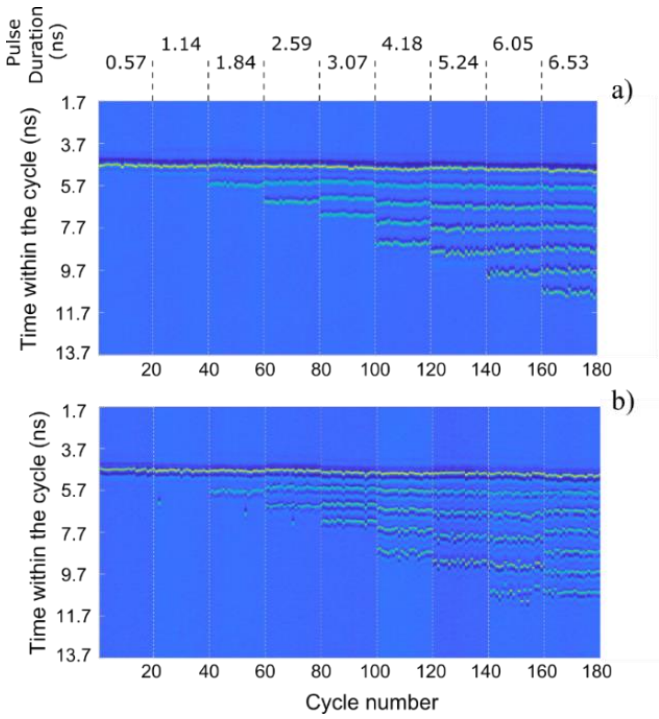

Figure 4.1.4 – Multi-spike propagation in a feedforward (1-to-1) network of VCSEL neurons with varying perturbation times (t_d). Temporal maps merging 20 cycles of 9 input durations (t_d) from 0.57 to 6.53 ns, show the consistency of responses from VCSEL-1 (a) and VCSEL-2 (b). Deviations of the colour from the blue background indicate a change in amplitude. Yellow/green pixels represent the peak amplitude of a spiking response. Parameters of VCSEL-1 (VCSEL-2): I = 1.5 mA (1.5 mA), T = 300 K (292K), external orthogonal (XP) mode injection into VCSEL-1 with Δf = -3.89 GHz and P_{inj}= 89.71 μW, VCSEL-1 and VCSEL-2 were separated by Δf = -3.89 GHz with P_{inj}= 34.19 μW.

As anticipated, upon the injection of a larger duration input perturbation (Fig. 4.1.3 (a)), VCSEL-1 (Fig. 4.1.3 (b)) shows the activation of a train of excitable spiking dynamics. For the input pulse used, this train is formed of 3 fast ~100 ps spikes. When injected into VCSEL-2 the system responds by triggering a similar train of 3 spikes (Fig. 4.1.3 (c)). The temporal maps (Fig. 4.1.3 (d)-(f)) indicate that the multi-spiking response from VCSEL-1 and the propagation to VCSEL-2 are highly

consistent over 180 cycles. In Fig. 4.1.4 the temporal maps of nine increasing pulse widths, t_d = 0.57 to 6.53 ns, are combined showing 20 cycles in each segment. The measured responses of VCSEL-1 (Fig. 4.1.4 (a)) show an increasing number of spike activations as the pulse width grows, with the largest train activating 7 spikes in total. The temporal maps reveal that the activated trains consistently contain the same number of spikes. Figure 4.1.4 (b) reveals the response of VCSEL-2 to the transmitted spiking signals. The responses of VCSEL-2 reveal overall that the multi-spike patterns are propagated successfully, with the same number of spikes being produced at the output of the system as measured at VCSEL-1. The consistency of the spike trains in VCSEL-2 is very high, with only a small number of unexpected activations appearing at short input durations. Similarly, the activation delay of spikes in the 6.05 ns case seems to be larger than that of VCSEL-1. These discrepancies indicate that the excitable regimes in each device may follow slightly different timescales but are still consistent enough to produce the same number of spiking responses. In any case, the system demonstrates that two networked VCSEL neurons can successfully transmit various excitable spiking signals from one device to another.

We have also investigated theoretically this 1-to-1 feedforward network of VCSEL neurons, to validate our experimental findings on the propagation of excitable spiking signals in this configuration [198]. The theoretical model, based on the Spin Flip Model (SFM) of a VCSEL subject to optical injection, was used to generate the theoretical output of VCSEL-1 before it was passed again into the model to predict the output of VCSEL-2. The theoretical results are reported in detail in [195]. These show excellent agreement with the experimental measurements. The theoretical results show that by increasing the input pulse duration, the network can propagate diverse patterns of multiple sub-ns optical spikes between VCSEL neurons. For instance, for a modelled input pulse duration of 6.8 ns seven excitable spikes are generated and propagated, as in the experiments shown in Fig. 4.1.4.

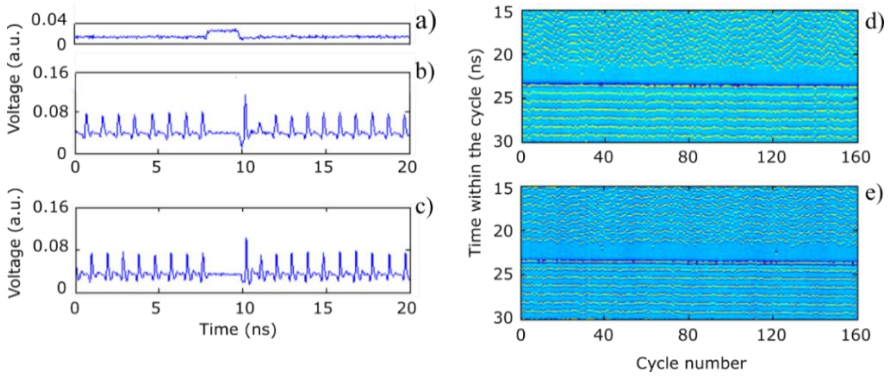

Figure 4.1.5 – Inhibition spike propagation in a feedforward (1-to-1) network of VCSEL neurons. Time series show the encoded optical injection (a positive pulse, t_d = 2.0 ns) incident on VCSEL-1 (a) and the spike-inhibiting response at its output (b). The second response, upon the injection of (b), is measured at the output of VCSEL-2 (c). Temporal maps (d) & (e) show the consistency of responses corresponding to results (b) & (c). Optical inputs are cycled 140 times consecutively. The colour of the map is scaled to the amplitude of the associated timeseries. Stable blue windows of invariant behaviour indicate the consistent suppression of spiking dynamics. Experimental parameters of VCSEL-1 (VCSEL-2): I = 1.5 mA (1.5 mA), T = 300 K (292K), external orthogonal (XP) mode injection into VCSEL-1 with Δf = -3.68 GHz and P_{inj}= 28.56 μW, VCSEL-1 and VCSEL-2 were separated by Δf_{V1-V2} = -2.79 GHz with P_{V1-V2}= 60.11 μW. Figure reproduced from [234].

Excitable neuronal signals are only one of many types of signals propagated in networks of biological neurons. As well as producing excitable spiking signals, biological neurons are capable of firing spike-inhibitory signals [18], [161]. We therefore investigated the propagation of spike inhibiting signals in our neuromorphic 1-to-1 feedforward network of VCSEL neurons. As demonstrated previously in Chapter 3, we can produce spike inhibition using the same experimental arrangement as that used to controllably activate excitable dynamics. For this reason, we can use the experimental arrangement shown in Fig. 4.1.1, to propagate spike inhibitory signals between two VCSEL neurons. The same two VCSELs were used to demonstrate spike inhibition propagation. The principal distinction between the cases of spike activation and inhibition is the shape and power level of the external optical input signal used. The shape of the injected input pulse is the inverse of the activation case (positive pulses are now used), allowing the external injection to increase input

power for a short duration. By positioning the system in a continuous spiking regime with an injection power lower than that required for optical injection locking, the input pulse can trigger an unlocking/locking transition, creating a stable window of suppressed spiking dynamics. When the pulse is removed the continuous spiking is resumed. This is demonstrated in Fig. 4.1.5 where spiking inhibition is achieved experimentally in VCSEL-1. The results shown in Figs. 4.1.5 & 4.1.6 are adapted from our published report [199].

The amplitude modulated optical injection incident on VCSEL-1 is shown in Fig. 4.1.5 (a). The positive input pulse has a duration of t_d = 2.0 ns and an injection power of 28.56 μW. Initially, as shown in Fig. 4.1.5 (b), the low injection level positions the system in a state of continuous spiking. Upon the injection of the positive pulse, the external optical injection locks the orthogonal polarisation mode of VCSEL-1, producing a stable window of spike inhibition. When the input pulse is removed, VCSEL-1 triggers once again continuous spiking responses. The output of VCSEL-1 is injected directly into the second VCSEL neuron (VCSEL-2). The response at the output of VCSEL-2 is shown in Figure 4.1.5 (c). Here the system is operating in a continuous spiking regime, induced by the injection of VCSEL-1. When the inhibition window enters VCSEL-2, the increased output power of VCSEL-1 (induced by the injection of the optical pulse) is sufficient to injection lock the orthogonal polarisation mode of VCSEL-2, suppressing the continuous tonic spiking output. The propagation of a spike inhibiting signal is therefore demonstrated in the feedforward system. Temporal maps in Fig. 4.1.5 (d) & (e) show the consistency of the VCSEL responses, where the window of inhibition is represented by a constant blue gap in spiking. The maps indicate very high consistency, over 160 repetitions of the input pulse. Similar to the propagation of excitable spikes, we can use increasing pulse width (t_d) inputs to investigate how the propagation of inhibition changes. The time series and temporal maps in Fig. 4.1.6 show the results of the parameter study where pulse duration was increased from 0 to 5.8 ns.

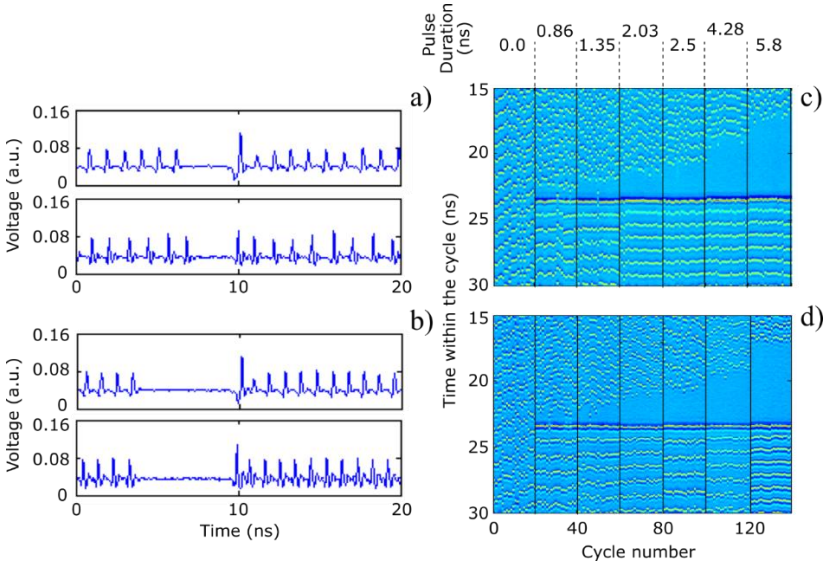

Figure 4.1.6 – Inhibition propagation in a feedforward (1-to-1) configuration of VCSEL neurons with varying input temporal duration (t_d). Time series show the output of VCSEL-1 (top) and VCSEL-2 (bottom) for inhibition inputs with durations t_d = 2.5 ns (a) and 5.8 ns (b). Temporal maps combining 20 cycles of 7 various input durations (t_d) from 0 to 5.8 ns, show the consistency of spike suppression at the output of VCSEL-1 (c) and VCSEL-2 (d). Experimental Parameters are identical to those of Fig. 4.1.5. The colour of the map is scaled to the amplitude of the associated timeseries. Figure reproduced from [234].

The time series for the cases of input pulse widths of 2.5 ns and 5.8 ns are plotted in Fig. 4.1.6 (a) & (b), respectively. These plots demonstrate the number of spikes suppressed by the input pulse increases as the input pulse (perturbation) grows. The propagation of the spike inhibitory signal is effectively passed from VCSEL-1 to VCSEL-2 with the latter suppressing the same number of spikes at its output. The temporal maps in Fig. 4.1.6 (c) & (d) combine seven pulse widths, each showing 20 cycles of inputs. These maps as expected also indicate that the effective window of spike suppression increases with input pulse width. Both the input pulse and transmitted signal are highly consistent with little to no unexpected responses. Similar to the case of excitatory spiking propagation, the inter-spike interval of the continuous spiking dynamics may indicate slightly different dynamical timescale in the two VCSEL neurons. However, overall the simple system demonstrates that inhibitory signals can transmitted in a feedforward network of VCSEL neurons.

Theoretical simulations have also been produced and are reported in [199]. The theoretical results showed excellent agreement with the experimental mechanism of spike inhibition and predicted, as found experimentally, the increasing suppression window with increasing input pulse duration. Additionally, the simulation demonstrated that the propagation of the spike-inhibiting signals could be performed with highly consistent VCSEL neuron responses.

VCSEL neurons have demonstrated their ability for network connectivity, initially in a 1-to-1 feedforward architecture formed of two nodes. They have shown the capability to communicate both controllable excitable and inhibitory spiking signals at speeds much faster than biological neural networks. These results indicate the output of VCSEL neurons are directly cascadable to other VCSEL neurons without the requirement for further signal amplification or modulation. This makes VCSEL neurons more desirable for investigation into larger, more complex network configurations as modulation may only be required at the input layer of the network. The application of these devices in functional circuits will require further investigation, however, these initial results offer great potential for brain-inspired photonic neural networks that combine both excitatory and inhibitory functionalities towards novel neuromorphic computing.

4.2 Diverging Architecture

In this Chapter we build upon the demonstration of the 1-to-1 feedforward network investigated in Chapter 4.1, and advance towards fan-out networks. A fan-out network, referred to here as a diverging architecture, is a network where the number of postsynaptic neurons in the secondary layer is more than that of the presynaptic neurons in the initial layer. This fan-out architecture can exist over a number of layers, allowing a single neuron activation to cascade to many. In biology, a good example of a fan-out (diverging) neural network is that of motor neurons in muscles [15]. Upon the activation of a single neuron, thousands of downstream connections can be activated making the muscle contract. Diverging neurons

however, do not necessitate the existence of a purely divergent network architecture. In fact, the divergence of a single neuron within a larger network of many neurons can be a measure of how many downstream synaptic connections are made. The higher divergence of an individual neuron in a network layer the more connectivity, and the higher the flow of information to the next layer. This means that within almost any network architecture, diverging connections are always made in the case of one individual neuron to many. Without diverging connections, neurons would not be able to create synapses to multiple neurons or share information effectively with others in large networks, making complex tasks such as classification impossible.

As expected, the existence of diverging connections in artificial neural networks, that target biological inspired systems for their impressive processing capabilities, is also key. Therefore, building upon the experimental implementation of a (1-to-1) feedforward VCSEL neuron system, we investigated the possibility of divergence with this photonic-based platform. The experimental setup used in the 1-to-1 demonstration was expanded to include an additional downstream VCSEL neuron (VCSEL-3), as shown in Fig. 4.2.1.

In this experimental system the output of one VCSEL neuron (VCSEL-1) is split and cascaded into two VCSEL neurons (VCSEL-2 and VCSEL-3) in a 1-to-2 fan-out network. As demonstrated previously throughout our work, light from an external tuneable laser is intensity modulated using a MZ modulator to create a time varying optical injection. This optically-modulated signal is injected into VCSEL-1 by means of fibre-optic components that allow for control of injection polarisation, optical power and frequency detuning. The external optical signal is set to injection lock VCSEL-1 and activate controllably spikes (see Chapter 3). The output of VCSEL-1 is collected and split into two paths using a 50:50 optical coupler. Each branch of the coupler is injected to an individual downstream VCSEL neuron via further optical polarisation and power controls. The outputs of VCSEL-2 and VCSEL-3 were captured using 9 GHz photodetectors and analysed with a 13 GHz oscilloscope. The three VCSEL neurons were chosen such that their peak emission wavelengths had similar values and each displayed Parallel (YP) mode dominant free-running operation. The emission wavelengths of the devices were fully matched by adjusting the temperature and bias current of each device individually. Polarisation-matched

optical injection was made into the Orthogonal (XP) mode of VCSEL-1, inducing a polarisation switch during injection locking. The bias current of VCSEL-1 was set to 2.2 mA and under optical injection provided an output power (after splitting) of $P_{V1\text{-}V2}$ = 84 μW and $P_{V1\text{-}V3}$ = 82.7 μW, for the injection of each downstream VCSEL respectively. The fed-forward signals were used to injection lock the orthogonal (XP) modes of VCSEL-2 and VCSEL-3, with XP mode-matched polarisation to maximise the signal coupling into each device.

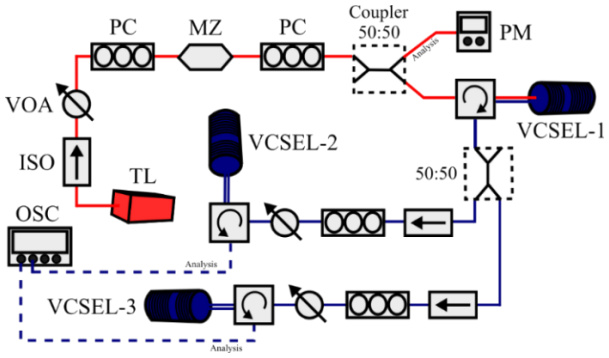

Figure 4.2.1 – Experimental setup for feedforward (1-to-2) spike propagation in a diverging network of VCSEL neurons. VCSEL-1 is subject to polarised optical injection (red path) from a tuneable laser. The output of VCSEL-1 is split using a 50:50 coupler with each path (depicted both with blue lines) subsequently injected VCSEL-2 or VCSEL-3. Experimental components as described previously; TL – tuneable master laser, ISO – optical isolator, VOA – variable optical attenuator, PC- polarisation controller, MZ – Mach Zehnder intensity modulator, PM – power meter, OSC – oscilloscope.

To test the activation and propagation of fast optical spikes in this fan-out VCSEL neuron network, pulses (perturbations) of varying temporal durations (t_d) were injected into VCSEL-1. The response of VCSEL-1 to a negative optical pulse of t_d = 0.61 ns is shown in Fig. 4.2.2 (a). Upon the injection of the optical pulse at ~6.0 ns, VCSEL-1 responds by eliciting a fast optical spike. The time series of Fig. 4.2.2 (a) was captured right at the output of VCSEL-1. The spiking signal from VCSEL-1 was then split into 2 via the optical coupler and injected into both downstream VCSEL neurons. The responses of VCSEL-2 and 3 are shown in Figs. 4.2.2 (b) & (c). In the output of both VCSELs we observe the activation of a single optical spike at ~6 ns. As before in the (1-to-1) feedforward network, a delay of ~62 ns exists between the

activation of spiking in VCSEL-1 and the activation in the downstream VCSELs. This delay has been compensated for during the plotting of figures to improve readability. The presence of spiking dynamics in each networked VCSEL indicates that the spiking from VCSEL-1, even after splitting, holds enough influence to cross the activation threshold of the devices and trigger a locking/unlocking transition.

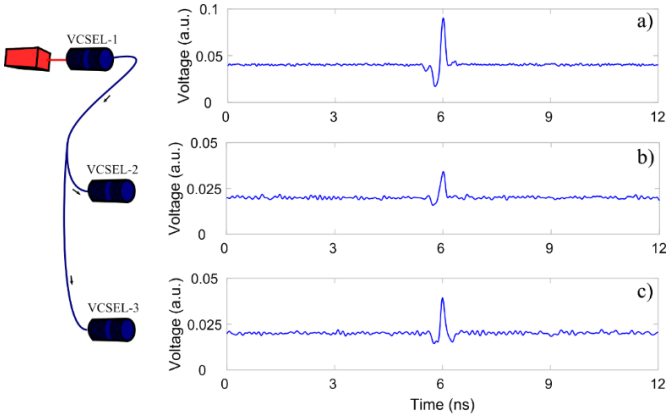

Figure 4.2.2 – Single spike propagation in a feedforward (1-to-2) diverging VCSEL neuron network. Time series show the response of the first VCSEL neuron (VCSEL-1) (a) upon the injection of an optical input pulse (t_d = 0.61 ns). The subsequent responses of VCSEL-2 (b) and VCSEL-3 (c) are captured upon the injection of the signal seen in (a). Experimental parameters, VCSEL-1: I = 2.2 mA, T = 301 K, external orthogonal (XP) mode injection into VCSEL-1 with Δf = -10.27 GHz and P_{inj}= 270 μW. VCSEL-2: I = 1.76 mA, T = 287 K and $P_{V1\text{-}V2}$= 84 μW. VCSEL-3: I = 1.0 mA, T = 296 K and $P_{V1\text{-}V3}$= 82.7 μW.

The spiking dynamics of the downstream VCSEL neurons do however, appear different to that of VCSEL-1. In Figs. 4.2.2 (b) & (c) the spikes are less defined and produce less distinctive drops. These differences are caused by the varying operation conditions of devices. Both VCSEL-2 and VCSEL-3 are driven with bias currents lower than that of VCSEL-1. The bias currents were specifically selected to best match emission wavelengths as previously stated, but they were also selected to allow for easy locking to the propagated VCSEL-1 signal. For this reason, the dynamical regimes accessed by each device are different, producing differing phase excursions and hence spike shapes. Additionally, due to the reduced bias currents, VCSEL-2 and

VCSEL-3 produce less output optical power than that observed from VCSEL-1. This reduces the signal detected by the photodetectors and decreases the overall amplitude of the recorded spikes. These result in time series that have features less distinguishable from noise level. The downstream VCSELs (VCSEL-2 and 3) indicate that a single optical spike can be cascaded through the network successfully. The temporal duration of the initial pulse was increased to next test the propagation of tonic or burst spiking in the diverging architecture. The results for four different pulse durations were recorded demonstrating that larger trains of pulses can also be communicated in a diverging architecture. The pulse duration was increased through 0.64 ns, 1.29 ns, 1.58 ns and 2.51 ns, producing pulse trains of one, two, three and four spikes respectively.

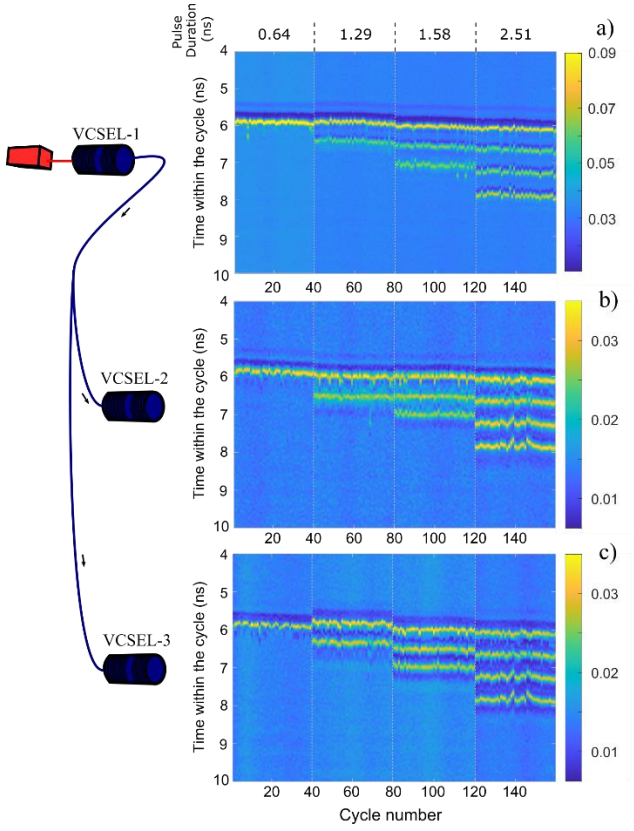

Figure 4.2.3 – Temporal maps showing multi-spike propagation in a feedforward (1-to-2) diverging configuration with varying input duration (t_d). Temporal maps, that combine 40 cycles of 4 various input durations (t_d), show the consistency of spiking dynamics measured

at the output of VCSEL-1 (a), VCSEL-2 (b) and VCSEL-3 (c). The temporal maps display data from the previously plotted Figures (Figs. 4.2.2 and 4.2.3).

In Fig. 4.2.3 the temporal maps of this 4-input pulse duration study are shown. Each map shows the response of VCSEL-1 (Fig. 4.2.3 (a)), VCSEL-2 (Fig. 4.2.3 (b)) and VCSEL-3 (Fig. 4.2.3 (c)) when subject to the four input pulse durations configured. A total of 40 consecutive cycles are shown for each input pulse, however the original temporal maps indicate consistency across the entire measurement length (196 cycles). The temporal maps for the response of each device shows a high consistency in the number of spikes activated and demonstrate that for every spike elicited in VCSEL-1, we successfully trigger one in VCSEL-2 and 3. We see excellent correlation between the plots of Figs. 4.2.3 (b) & (c) with even small features, such as short delays in spike activation, mirrored in the response of both devices. These small changes, that likely originate from the spike timings of the VCSEL-1 signal, indicate that both downstream VCSELs are receiving near-identical inputs from the first layer of the network. This means that a single input can be spilt and transmitted successfully in our photonic network without the loss of the important spike-timing information, a feature key to the operation of biological networks. Overall the temporal maps of the three VCSEL neurons show that the neuromorphic responses to both input pulses and input spikes are reliable and repeatable over a high number of cycles.

The VCSEL neuron demonstration provided here showcases the successful propagation of neuromorphic dynamics in a diverging (1-to-2) network architecture. The propagation of both single excitable spikes and trains of excitable spikes was performed with high levels of consistency across a number of experimental repetitions. The results demonstrated a single presynaptic VCSEL neuron can drive two postsynaptic VCSEL neurons using simple benchtop fibre optic components, while preserving key neuronal spike timing information. Diverging connections can be found within most networks and are directly responsible for the connectivity of a network. This demonstration further inspires the application of these VCSEL-based neuromorphic elements in more complex network architectures.

4.3 Retinal Neuronal Circuitry Emulation with Artificial Optical Neurons

In this Chapter we continue to advance our exploration of networked systems of VCSEL neurons with the experimental demonstration of a basic real-life biological neuron circuit in the human retina, a first step towards biological inspired photonic spike processing systems. In this first demonstration, we capitalise on the optical activation and propagation of fast neural-like signals in interconnected VCSEL neurons. Similar to the (1-to-1) feedforward network of Chapter 4.1, we emulate now a more complex three node (1-to-1-to-1) feedforward neural circuit found in the retina. This seemingly random application of our photonic system is in fact logical as there is an extensive scientific understanding of the neuronal circuits within the retina [235]–[237], and a number of electronic emulations of retinal circuitry have been reported in literature [238]–[242].

In the retina, light energy is converted into spiking potentials and the conversion is made by three principal neuronal layers. These are made up of different types of cells including photoreceptors, Bipolar Cells (BCs) and Retinal Ganglion Cells (RGCs) [15]. The photoreceptors are the cells in the initial neuronal layer that absorb light and generate the initial electrical or chemical signals. There are different types of photoreceptors, namely rods and cones, which react to different light conditions. Rods are responsible for highly sensitive vision at night and cones are responsible for daylight and colour vision. Rods and cones synapse with the BCs in the second cell layer of the retina. BCs, which are non-spiking neurons, yield graded potentials of varying intensities in response to photoreceptor signals produced by changing external lighting conditions. A single BC can receive input from hundreds of photoreceptors and multiple BCs converge on a single retinal ganglion cell. RGCs are the second neuron in the retinal circuit and form the final neuronal layer in our network. The RGC is the largest neuron in the retina and fires spiking signals in

response to inputs from BCs. The spiking RGC outputs are passed to the brain, via the optic nerve, for further image processing.

Different types of BCs and RGCs have been reported, two of which are known as ON- and OFF-type cells [235]–[237]. The ON- and OFF-neuronal circuits produce spiking signals via two different mechanisms. In light stimulus, photoreceptors are hyperpolarised, reducing glutamate, and in turn excite ON-type BCs and RGCs, creating circuits that elicit spiking signals. However, in light stimulus, OFF-type BCs are instead inhibited by reducing glutamate, reducing the excitatory responses of the RGC. In the dark, the opposite mechanisms are triggered, with increasing glutamate exciting the firing of the OFF-RGCs and inhibiting ON-type RGCs. These mechanisms are demonstrated in Figs. 4.3.1 (a) & (b). The ON- and OFF-type circuits produce activated and inhibited spiking signals as shown at the output of the retinal circuits. In the retinal neural networks, a large number of such neuronal circuits exist in parallel, allowing the network to converge and pre-process incoming visual information before passing it to the visual cortex of the brain.

With our photonic network will look to create a three layer system inspired by an ON-type circuit, subject to both increasing and decreasing light stimulus, using VCSEL neurons connected in series (see Fig. 4.3.1 (c)) [200]. In our photonic retinal-inspired circuits, two VCSEL neurons are used to produce the responses of the BC-(BC-VCSEL) and RCG-inspired (RGC-VCSEL) neurons. The BC-VCSEL is operated such that it reproduces the graded potentials of a BC neuron and RGC-VCSEL is operated such that it reproduces the spiking response of a RGC neuron. VCSEL devices can produce a rich variety of dynamics including neuromorphic spiking signals as demonstrates previously in Chapter 2, but they also have capability to produce non-spiking responses. For instance, when subject to polarised optical injection, polarisation switching can occur, creating square switches in the output intensity of polarisation-resolved signals [217], [243]. Similarly, optical injection can be used to influence the total output power of a VCSEL. This creates an avenue to injection-controlled output modulation, where fluctuations in injection power can create small changes in VCSEL output intensity. Using this technique, it is possible to create BC graded potentials with a VCSEL neuron, delivering the ultrafast

emulation of both spiking and non-spiking neurons with the same artificial photonic neuron.

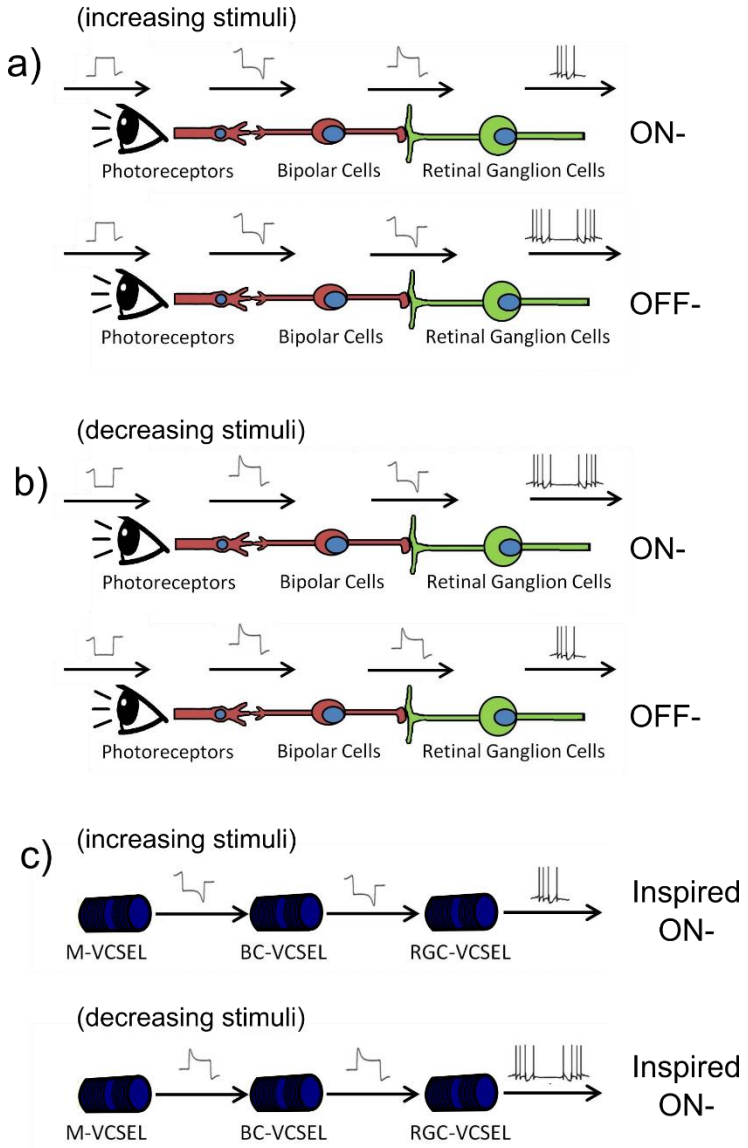

Figure 4.3.1 – Schematics of the retinal neural circuits emulated with interconnected VCSEL neurons. The circuits are formed by two types of neurons connected in series: Bipolar Cells (BC), connected to photoreceptors in the eye, and Retinal Ganglion Cells (RGC) receiving inputs from BCs. These neurons are of two different types, ON and OFF. The signal conversion performed by photoreceptors, BCs and RGCs, in both the ON and OFF circuits, are shown for increasing light stimulus (a) and decreasing light stimulus (b). The interconnected feedforward VCSEL network used to create an ON-inspired circuit shown (c) for both increasing and decreasing light stimuli. The ON-inspired circuits are made up of an M-VCSEL: Master VCSEL (VCSEL-1) showing a photoreceptor response, a BC-VCSEL:

Bipolar Cell VCSEL (VCSEL-2), and an RGC-VCSEL: Retinal Ganglion Cell VCSEL (VCSEL-3). Results taken from [200].

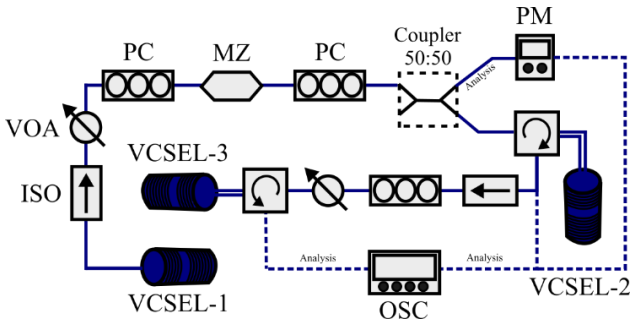

Figure 4.3.2 – Experimental setup for the ON-type-inspired retinal circuit with networked VCSEL neurons arranged in a feedforward (1-to-1-to-1) configuration. The output of VCSEL-1 (M-VCSEL) is optically encoded with input pulses (similar to those of photoreceptor cells) and subsequently injected into the second VCSEL neuron (VCSEL-2, BC-VCSEL). This creates a graded potential at the output of VCSEL-2 which is then injected into VCSEL-3 (RGC-VCSEL). Experimental components as described previously; ISO – optical isolator, VOA – variable optical attenuator, PC- polarisation controller, MZ – Mach Zehnder intensity modulator, PM – power meter, OSC – oscilloscope.

The experimental setup used to implement the three VCSEL (1-to-1-to-1) feedforward retinal-inspired neural circuit is shown in Fig. 4.3.2. Three VCSELs of similar peak wavelength (1536.5 nm) and orthogonal XP-mode dominant operation were selected for the network nodes. Light from a master VCSEL (M-VCSEL/VCSEL-1) was passed through an optical intensity modulator (MZ) and encoded with input pulses of opposite signs according to the response of the photoreceptor cells in increased and decreased light stimuli. In ON-type circuits with increasing stimuli, photoreceptor outputs take the form of short (hyperpolarising) power drops. In ON-type circuits with decreasing stimuli, photoreceptor outputs take the form of short (depolarising) power raises. As in previous studies, the temporal durations (t_d) and input strengths were controlled during the experiments. This arrangement allowed M-VCSEL to emulate the response of photoreceptors in the ON-type-inspired circuits. Optical polarisation controllers and variable optical

attenuators were used to control the polarisation and injection power produced by M-VCSEL. The encoded output of the M-VCSEL was optically injected into the second VCSEL (BC-VCSEL/VCSEL-2) via an optical circulator where the light from M-VCSEL was used to injection lock BC-VCSEL. The output of BC-VCSEL was again collected by the optical circulator and injected into the third VCSEL (RGC-VCSEL/VCSEL-3), via a polarisation controller and a variable optical attenuator. Depending on the retinal-inspired neural circuit (increasing or decreasing light stimuli), the RGC-VCSEL was (was not) injection locked to BC-VCSEL, producing both excitable (and inhibited) spiking signals. The output of each VCSEL was analysed using a fast (13 GHz) real-time oscilloscope, allowing the analysis of the propagated signals in each layer of the network. The wavelength, and hence the injection frequency detuning of each VCSEL neuron in the network was set using the bias current and operating temperature.

In the first experiment we investigated the ON-type-inspired retinal neural circuit with the three cascaded VCSEL neurons. Figure 4.3.3 plots the time series captured at the output of (i) M-VCSEL, (ii) BC-VCSEL and (iii) RGC-VCSEL. The duration of the input pulse encoded in M-VCSEL's signal was increased with t_d equal to (a) 0.85 ns, (b) 2.79 ns and (c) 4.90 ns, across three experimental runs. This was used to test the non-spiking and spiking responses of the BC- and RGC-VCSELs to increasing stimuli lengths. In Fig. 4.3.3 (a)(i), the M-VCSEL signal with a 0.85 ns-long power drop input is shown. This signal was injected into BC-VCSEL with an injection power of P_{BC-M} = 70.35 μW at a frequency detuning of Δf_{BC-M} = -2.3 GHz, locking BC-VCSEL's output and producing the time series shown in Fig. 4.3.3 (a)(ii). The BC-VCSEL output shows an initially stable intensity, indicating the successful injection locking of the device. At ~ 15 ns the input pulse enters BC-VCSEL, however, the system remains injection locked, producing a stable output with an overall lower output level. The injection conditions here were selected such that the input pulse did not cross the activation threshold of the BC-VCSEL, instead creating a small non-spiking graded potential at the output. This non-spiking signal was then propagated into the RGC-VCSEL producing the time series shown in Fig 4.3.3 (a) (iii).

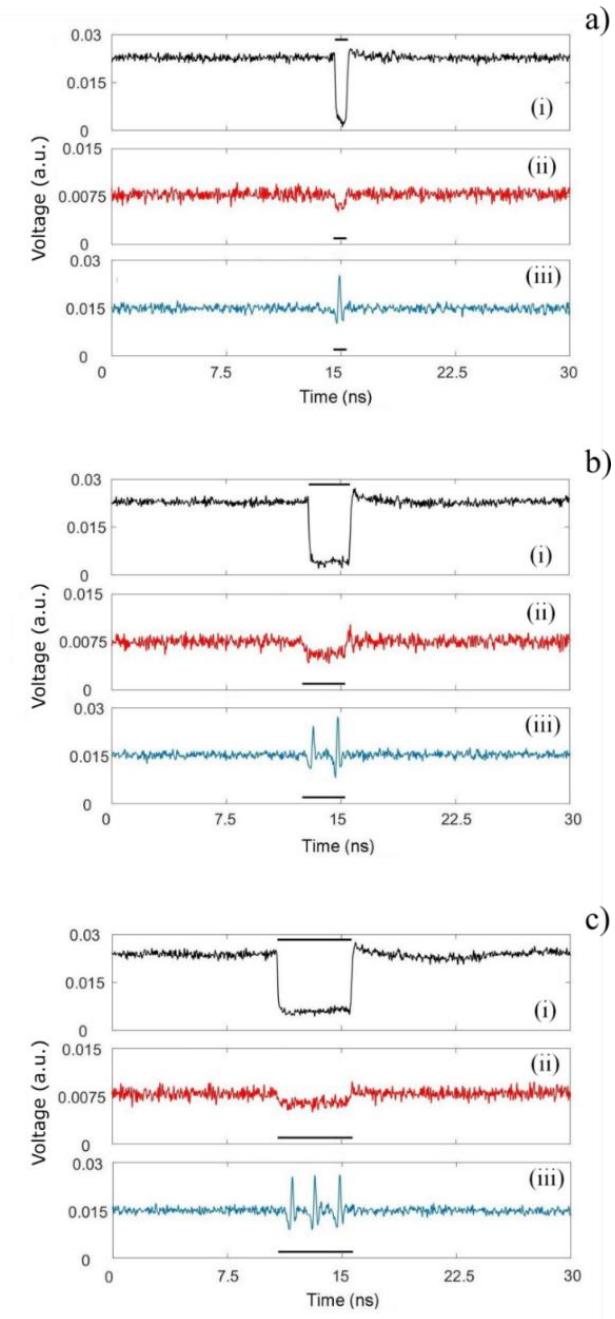

Figure 4.3.3 – ON-type-inspired retinal circuit with three connected VCSEL neurons, when subject to increasing light stimuli. Input pulses of various length (a) t_d = 0.85 (b) 2.79 and (c) 4.9 ns were optical encoded into the light of the M-VCSEL (VCSEL-1) (i). Upon injection of this input signal into the BC-VCSEL (VCSEL-2) a graded potential is generated (ii). The response of the RGC-VCSEL (VCSEL-3) to the graded potential is plotted in (iii). Experimental parameters, VCSEL-1: I = 4.64 mA, T = 298 K, P_{BC-M} = 70.35 μW and Δf_{BC-M} = -2.3 GHz. VCSEL-2: I = 4.38 mA, T = 290 K, P_{RGC-BC} = 28.8 μW and Δf_{RGC-BC} = -2.53 GHz. VCSEL-3: I = 3.7 mA, T = 300 K. Figure reproduced from [200].

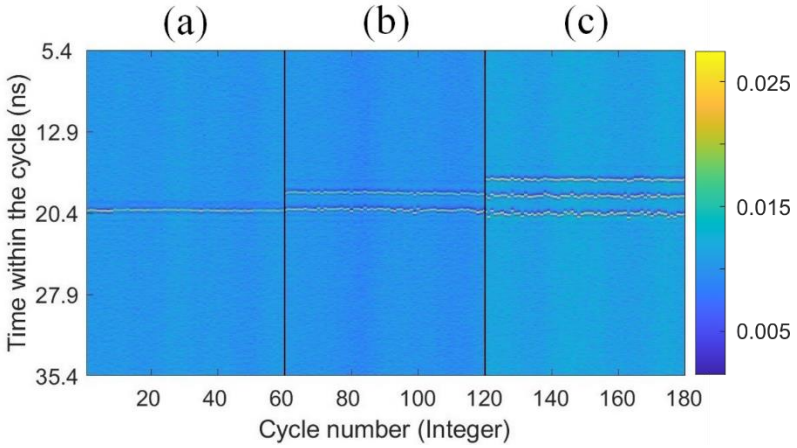

Figure 4.3.4 – Temporal maps showing the consistency of the RCG-VCSEL response in the ON-type-inspired circuit (with increasing light stimuli) when M-VCSEL inputs are varied from (a) t_d = 0.85 ns (b) t_d = 2.79 ns and (c) t_d = 4.9 ns. The temporal maps combine 60 cycles of each various input duration. The temporal maps display data from the previously plotted Figure. 4.3.3. Figure reproduced from [200].

Here, an injection power of $P_{RGC\text{-}BC}$ = 28.8 μW and a frequency detuning of $\Delta f_{RGC\text{-}BC}$ = -2.53 GHz was used to lock the RGC-VCSEL to the BC-VCSEL. The plotted time series shows again an initially stable output, consistent with injection locking. However, at ~15 ns, upon the injection of the small graded potential, the RGC-VCSEL elicits a single sub-nanosecond spike. After the 0.85 ns input, the system returns to injection locking producing again a stable output. The RGC-VCSEL therefore converts the non-spiking input from the BC-VCSEL into a spiking signal. The results for the increasing input durations can be seen in Figs. 4.3.3 (b) & (c).

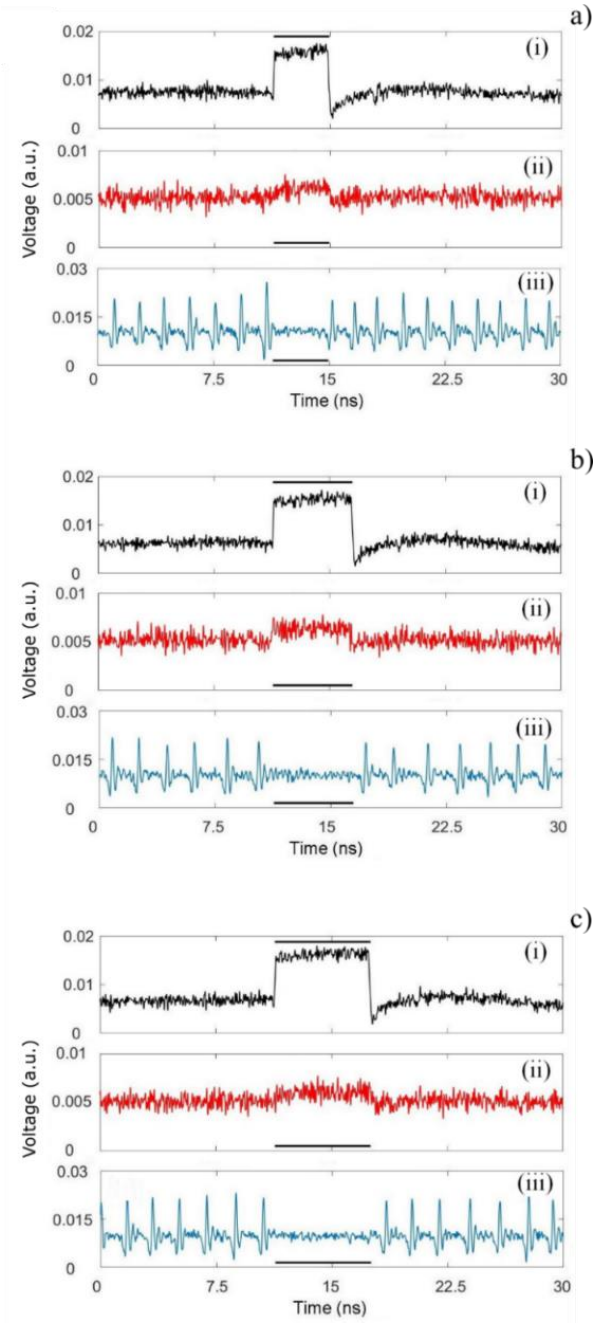

Figure 4.3.5 – ON-type-inspired retinal circuit with three connected VCSEL neurons, when subject to decreasing light stimuli. Input pulses of various length (a) t_d = 3.60 (b) 5.18 and (c) 6.22 ns were optical encoded into the light of the M-VCSEL (VCSEL-1) (i). Upon injection of this input signal into the BC-VCSEL (VCSEL-2) a graded potential in generated (ii). The response of the RGC-VCSEL (VCSEL-3) to the graded potential in plotted in (iii). Experimental parameters, VCSEL-1: I = 4.61 mA, T = 298 K, P_{BC-M} = 57.5 μW and Δf_{BC-M} = -4.81 GHz. VCSEL-2: I = 4.30 mA, T = 290 K, P_{RGC-BC} = 8.8 μW and Δf_{RGC-BC} = -4.81 GHz. VCSEL-3: I = 3.72 mA, T = 300 K. Figure reproduced from [200].

In both cases the BC-VCSEL responds with a small negative graded potential for the entire duration of the input pulse. These graded potentials in turn trigger an increasing number of spiking responses from the RGC-VCSEL with the total number of yielded spikes increasing from two to three. The time series shown in Fig. 4.3.3 have been aligned to improve figure readability. The response of the RGC-VCSEL to the increasing input duration is shown further in the temporal maps of Fig. 4.3.4. Three temporal maps are combined, each showing 60 consecutive cycles for the input pulses of t_d = (a) 0.85 ns, (b) 2.79 ns and (c) 4.9 ns. The 60 cycle segments were taken from temporal maps originally showing 196 consecutive cycles (the entire length of the captured measurement). Each of the maps show excellent consistency across the entire measurement with the same spiking pattern (1-, 2- or 3-spikes) being produced at the output.

In the second experimental demonstration of the three VCSEL (1-to-1-to-1) feedforward network, an ON-type-inspired retinal circuit with decreasing light stimulus was created. Similar to the previous experiment, the time series captured at the output of each VCSEL is plotted for increasing input durations (t_d) of (Fig 4.3.5 (a)) 3.60 ns, (Fig.4.3.5 (b)) 5.18 ns and (Fig. 4.3.5 (c)) 6.22 ns. Each plot shows the time series of the (i) M-VCSEL, (ii) BC-VCSEL and (iii) RGC-VCSEL.

The (i) time traces in Figs. 4.3.5 (a)-(c) show the three input pulses encoded in the intensity of M-VCSEL's output. These signals were then injected into the BC-VCSEL with an injection power of P_{BC-M} = 57.5 μW at a frequency detuning of Δf_{BC-M} = -4.81 GHz from the dominant Orthogonal (XP) mode. The injection conditions were again selected to injection lock BC-VCSEL to M-VCSEL. The resulting BC-VCSEL outputs, shown in (ii) of Fig. 4.3.5 (a)-(c), initially have a steady output consistent with injection locking. At ~11 ns the input pulse is injected into BC-VCSEL, and a positive graded potential is generated with injection locking remaining intact. Here the input pulse in M-VCSEL's injection is positive pushing the system further from the activation threshold, increasing the injection power and hence the output power of BC-VCSEL. The graded potential produced in BC-VCSEL is then injected into RGC-VCSEL with an input power and frequency detuning of P_{RGC-BC} =

8.8 μW and $\Delta f_{RGC\text{-}BC}$ = -4.81 GHz. Injection was made such that upon the incidence of a photoreceptor signal (M-VCSEL), spiking dynamics produced an inhibited RGC response. This was achieved by positioning the system below the injection locking level in a regime of continuous spiking, where the positive graded potentials could be used to injection lock RGC-VCSEL. RGCs do not operate as continuously firing neurons, however, for demonstrative purposes the ON-type inspired circuit has the RCG-VCSEL spiking constantly to better demonstrate the inhibition. The output of the RGC-VCSEL is shown in the (iii) plots of Fig. 4.3.5 (a)-(c). Here, we see the system is in a continuous (tonic) spiking regime until the arrival of the graded potential (at ~11 ns). The graded potential then successfully injection locks the system, inhibiting the spiking with a stable output. In each of the cases presented the system locks for the entire duration of the graded potential before returning to tonic spike firing. The 3-VCSEL system is therefore capable of creating an ON-type-inspired retinal neural circuit using fast cascaded non-spiking and tonic (sub-nanosecond) spiking signals. The consistency of each result is presented in the temporal maps of Fig. 4.3.6. As in Fig. 4.3.4, segments of 60 cycles are taken from consistency plots of 196 cycles and combined into a single figure, showing the results for input durations of (a) 3.60 ns, (b) 5.18 ns and (c) 6.22 ns. The maps again show high consistency regarding the inhibition of spiking with almost complete suppression for the entire duration of the input pulses.

The three VCSEL networks therefore successfully demonstrate ON-type-inspired retinal neural circuits. We note here that in both cases the BC-VCSEL produced the opposite response to that of true BCs in the ON-type circuit. While this is the case, the VCSEL network was able to operate with the photoreceptor responses producing the desired RGC response for the ON-type circuit. Considering the differing mechanisms underlying laser dynamics and biological cells, we claim only the successful demonstration of a ON-type inspired circuit. In both experimental demonstrations of the ON-type circuits the system showcased the controllability and reproducibility of the spiking and non-spiking signals accessible to VCSEL neurons. These BC/RGC signals were produced at fast sub-nanosecond/nanosecond timescales making them over 6 orders of magnitude faster than their biological counterparts. Furthermore, these demonstrations showcase the capability of

networked VCSEL neurons to propagate and communicate different spiking/non-spiking signals in a feedforward architecture. Interestingly, we show here non-spiking signals being generated and propagated within the VCSEL network but also demonstrate their use to directly influence and activate spiking signals in the final layer without additional signal manipulation. The three VCSEL neurons used in this study were selected from a batch of commercially-sourced VCSELs. For this reason, additional wavelength tuning had to be conducted, resulting in the devices having differing operating parameters. Despite this the system showed the three layers of VCSEL neurons were capable of cascading signals in feedforward architecture with only polarisation, attenuation and frequency detuning control. The ease of experimental implementation could therefore be improved by using optimised VCSEL designs, grown for the purpose of network connectivity.

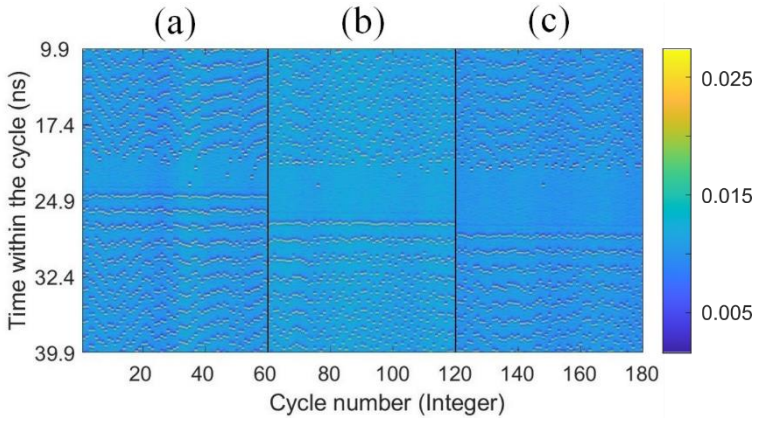

Figure 4.3.6 – Temporal maps showing the consistency of the RCG-VCSEL response in the ON-type circuit (subject to decreasing light stimuli) when M-VCSEL inputs are varied from (a) t_d = 3.60 ns (b) t_d = 5.18 ns and (c) t_d = 6.22 ns. The temporal maps combine 60 cycles of each various input duration. The temporal maps display data from the previously plotted Figure. 4.3.5. Figure reproduced from [200].

In this experiment, no external tuneable laser (TL) source was used. The decision to utilise a VCSEL in the input layer was made to test the possibility of an all-VCSEL network. This has a number of advantages, for example; VCSELs are relatively inexpensive compared to more costly TL units, VCSELs have significantly smaller

footprint than TLs helping reduce the size of the experimental system as a whole, VCSEL devices produce a smaller range of output power with a higher wall plug efficiency compared to TL units, etc. However, the use of VCSELs brings its own set of challenges. Devices with the appropriate output power, threshold current, peak wavelength and dominant polarisation mode need to be utilised. Additionally, we found the inherent optical power loss, caused by the experimental intensity modulators, posed a more significant issue with VCSELs than the TL unit due to the decreased power availability. Despite these drawbacks, the implementation of an all-VCSEL neuromorphic spiking network marks an important milestone for the development of our brain-inspired photonic systems, showing progression to a more VCSEL-dependent execution.

Overall, the experimental demonstrations of retinal neural circuits in ON-type-inspired configurations were achieved using 3 cascaded VCSEL neurons in a (1-to-1-to-1) feedforward architecture. This highlights the suitability of VCSELs as neuromorphic devices capable of real-life biological neuron emulation. Additionally, this demonstration has revealed that an all-VCSEL system can sustain the required power levels for cascadability in feedforward architectures, increasing VCSEL neuron prospects as reliable devices for potential implementations of network functionality in the future.

In conclusion, the results in this chapter have investigated experimentally the application of VCSEL neurons in interconnected network architectures. Specifically, we have shown the communication of optical spike activations/inhibitions in a (1-to-1) feedforward configuration, revealing the capability of one VCSEL neuron to pass information to another one in a subsequent network layer. Next, we demonstrated the propagation of optical spiking signals in a diverging (1-to-2) feedforward configuration. Here, with the successful activation of both downstream devices, we revealed that a single VCSEL neuron can feed information into multiple downstream network nodes, facilitating in the future the additional neural connections required for complex configurations and network processing capability. Finally, we demonstrated the emulation of a real biological retinal neural circuit using 3 interconnected VCSELs. In this demonstration, both non-spiking and spiking signals were used to successfully reproduce the signals two of ON-type-inspired circuits of

BCs and RGCs in a (1-to-1-to-1) feedforward network. This demonstration revealed that non-spiking signals can also be propagated between VCSELs and that they can be used to activate neuronal spiking further downstream in the network. Additionally, we have shown an all-VCSEL approach to network implementation, revealing that network cascadability can still be achieved with a VCSEL realised input layer. Such all-VCSEL networks have the potential to be created without the expense and footprint of larger tuneable laser sources, increasing the prospect and appeal of VCSEL neurons as networked devices for future neuromorphic systems. These promising results highlight that VCSELs have the capability to operate in interconnected architectures as networks of neuron-emulating devices, capable of generating and communicating spike activating, spike inhibiting and non-spiking signals at sub-nanosecond speeds. We have seen that in simple network configurations these devices can cascade signals without additional signal manipulation and that VCSELs can inject information into the network, simplifying the hardware requirements for a basic neuromorphic network implementation. The experimental investigation of fan-in configurations remains of significant interest to neuromorphic networks of VCSELs as it will contribute to the realisation of functional decision-making circuits where multiple neuron inputs arrive on a single VCSEL neuron. This will be realised experimentally using time-division multiplexing techniques in Chapter 5 to demonstrate and use further the neuromorphic properties of VCSEL-based photonic neuronal models.

Chapter 5

Functional Neuro-inspired Photonic Circuits and Demonstrations

In Chapter 1 we introduced the concept of neuromorphic information processing and have since described methods of achieving neural-like spiking with VCSELs in Chapter 3. In Chapter 4 we described how it is possible to combine artificial photonic VCSEL neurons in order to implement network configurations capable of spike propagation. We also demonstrated the photonic emulation of basic neuronal circuits within the retina using interconnected VCSEL neurons. In this Chapter (Chapter 5) we will draw upon each of the functionalities realised within our VCSEL neuron and apply them to achieve neuro-inspired photonic circuits capable of functional processing demonstrations. We will discuss utilising our VCSEL neuron for the generation of fast optical spiking signals via Digital-to-Spike (DTS) format conversion (Chapter 5.1). We will demonstrate the creation of photonic spiking memories through the use of single and mutually-coupled VCSEL neurons in feedback configurations (Chapter 5.2). We will also exploit the temporal integration of fast input perturbations to realise photonic AND/OR spiking logic operations (Chapter 5.3) and perform a supervised pattern recognition task (Chapter 5.4). Finally, we will apply VCSEL neurons to the field of image processing where multiple techniques are used to implement image convolution with our photonic VCSEL neurons to achieve image edge detection and (in tandem with software-implemented SNNs) image classification (Chapter 5.5).

In this chapter we will discuss experimental results that have produced journal publications. The following articles therefore relate to the forthcoming discussion:

[193] J. Robertson, M. Hejda, J. Bueno, and A. Hurtado, "Ultrafast optical integration and pattern classification for neuromorphic photonics based on spiking VCSEL neurons," *Sci. Rep.*, vol. 10, no. 1, p. 6098, Dec. 2020, doi: 10.1038/s41598-020-62945-5.

[194] J. Robertson, Y. Zhang, M. Hejda, J. Bueno, S. Xiang, and A. Hurtado, "Image edge detection with a photonic spiking VCSEL-neuron," *Opt. Express*, vol. 28, no. 25, pp. 37526–37537, Dec. 2020, doi: 10.1364/OE.408747.

[200] J. Robertson, E. Wade, Y. Kopp, J. Bueno, and A. Hurtado, "Towards Neuromorphic Photonic Networks of Ultrafast Spiking Laser Neurons," *IEEE J. Sel. Top. Quantum Electron.*, 2019, doi: 10.1109/JSTQE.2019.2931215.

[201] Y. Zhang, J. Robertson, S. Xiang, M. Hejda, J. Bueno, and A. Hurtado, "All-optical neuromorphic binary convolution with a spiking VCSEL neuron for image gradient magnitudes," *Photon. Res.*, vol. 9, no. 5, pp. B201–B209, 2021, doi: 10.1364/PRJ.412141.

[202] J. Robertson *et al.*, "Ultrafast neuromorphic photonic image processing with a VCSEL neuron," *Sci. Rep.*, vol. 12, no. 1, p. 4874, Dec. 2022, doi: 10.1038/s41598-022-08703-1.

5.1 Digital-to-Spike Format Conversion

In this first demonstration of a functional neuro-inspired photonic circuit we introduce Digital-to-Spike (DTS) format conversion. Neuromorphic photonic systems, as described in Chapter 1, make use of pulses of light (spikes) that are digital in amplitude but analog in the temporal domain. Biological neural networks are known to encode information in the precise timing of these spikes when communicating between neurons in the network [221], [222]. However, traditional computer processors and telecom networks mostly operate with digital binary format signals. Hence, it is key for future neuromorphic photonic processing systems to implement DTS format conversion to successfully interface with digital computing and telecommunication platforms.

A commonly used information encoding format in digital systems is Non-Return-to-Zero (NRZ). This features two signal levels, one for each bit value (1 & 0), but requires clock synchronisation as sequential bits can maintain a constant signal level. The clocking requirement of NRZ clashes with the asynchronistic format of spiking signals; hence conversion is required for the information to pass into neuromorphic systems. Another commonly used binary encoding format is Return-to-Zero (RZ). This features signal pulses (RZ unipolar), or both signal pulses and drops (RZ

bipolar), that return to zero between each bit. This removes the requirement of a clocking signal and helps to avoid bit slips. The removed requirement of clocking and its on-off keying (pulse-like) nature means that RZ unipolar signals share a commonality with spiking signals where information is carried in the activation of a pulse or spike. In essence the conversion of NRZ to RZ unipolar should therefore provide the required format change to operate with neuromorphic systems given RZ unipolar encoding can be achieved at the appropriate bit rate.

The conversion of binary data from NRZ to RZ format has been proposed and realised in literature using photonic systems that exploit the behaviour of semiconductor optical amplifiers (SOAs) to produce trains of pulses [244], [245]. Photonic DTS conversion, where spike activations, as opposed to square pulses, are triggered via an excitability mechanism has been recently reported. A graphene excitable laser (GEL) has demonstrated the conversion of binary NRZ signals into spike trains [246]. When perturbed electrically the GEL, containing a gain and saturable absorber section, converted NRZ input signals to spike trains at a modelled bit rate of 10 Gb/s and an experimental bit rate of 40 Kb/s. The subsequent spiking signal required no clock synchronisation making it an appropriate format for neuromorphic systems that operate using optical spiking signals.

We utilise excitability in VCSEL neurons to perform DTS format conversion, where each triggered spike represents the presence of a bit with value ‘1’. To demonstrate the DTS conversion capability of VCSEL neurons we perform optical injection with an external signal, intensity modulated by digital binary patterns. Using the setup described in Chapter 2 (Fig. 2.1.3) we generate electrical NRZ, bipolar RZ and unipolar RZ signals. Incoming 8-bit NRZ and RZ binary signals, representative of ASCII characters that form the word ‘IPC19’ (acronym of the IEEE International Photonics Conf. 2019, where these results were presented), were generated at 1 ns/bit (1 Gb/s) for NRZ and 2 ns/bit (0.5 Gb/s) for RZ, and optically-injected into the VCSEL neuron. Experimental results demonstrating DTS format conversion with the VCSEL neuron are shown in Fig. 5.1.1.

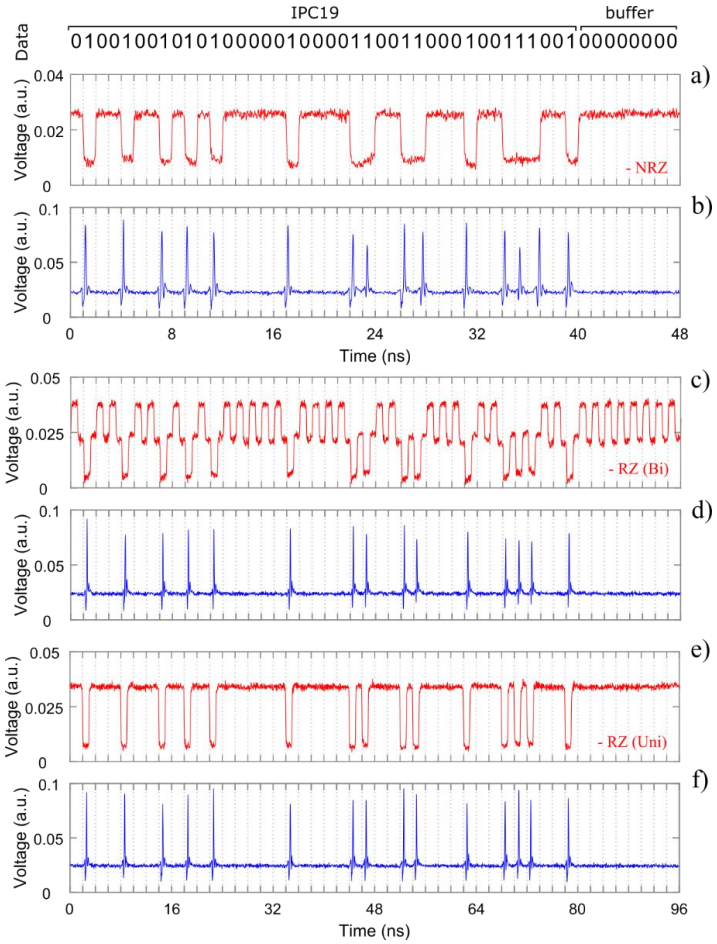

Figure 5.1.1 – DTS conversion with a photonic VCSEL neuron. (a) NRZ-, (c) Bipolar RZ-, (e) Unipolar RZ-encoded optical injection and (b,d,f) the spiking VCSEL neuron response. Experimentally obtained using the optical injection setup (Fig. 2.1.3). Experimental parameters: I = 5.0 mA, T = 293 K, Orthogonal (XP) mode injection, (a-b) Δf = -8.47 GHz, P_{inj}= 252 μW, (c-d), Δf = -4.61 GHz, P_{inj}= 230.6 μW, (e-f) Δf = -6.35 GHz, P_{inj} = 243.5 μW.

Fig. 5.1.1 (a) shows the 48 ns long NRZ binary input corresponding to the five 8-bit ASCII characters and an 8-bit buffer. When in a 0-bit state the NRZ input injection locks the system producing a stable output as shown in Fig. 5.1.1 (b). However, when in a 1-bit state the injection locking is disrupted and the VCSEL neuron falls into the excitable spiking regime. When consecutive 1-bits enter the VCSEL neuron at bit numbers 22, 26 and 34, the device remains out with injection locking and fires tonic (continuous) spikes. The encoding rate of 1 Gb/s was selected such that the number of 1-bit triggers matched the number of spikes activated. This was achieved by

matching the bit length to that of the refractory period of the VCSEL neuron (approx. 1 ns). In the VCSEL neuron response we successfully activate all required responses. The VCSEL neuron utilised in this work can therefore achieve the DTS conversion of NRZ signals at approximately 1 Gb/s, however this upper limit is dependent on the system's refractory period.

In Fig. 5.1.1 (c)-(d) we demonstrate the DTS conversion of a bipolar RZ binary signal. This binary signal has three states and resets to the middle state at the end of every input bit. We inject a signal encoded at 2 ns per bit (0.5 Gb/s) and set the '0' and reset states at powers above the injection locking condition. Therefore, we expect only the 1-bit state to cross the activation threshold of the VCSEL neuron and trigger spiking responses. As demonstrated in Fig. 5.1.1 (d), we successfully achieve the activation of spiking dynamics for each 1-bit. After the successful triggering of a spike the injection locking condition is restored during the RZ reset. This means spikes triggered by 1-bit inputs are more consistent in amplitude and spike timing than tonic activations in the NRZ case. Additionally, here at half the encoding rate (0.5 Gb/s), we reliably achieve activations as we allow 2 ns between bits, a much longer time that the refractory time of the VCSEL neuron. In Fig. 5.1.1 (e)-(f) we demonstrate the similar case of a unipolar RZ binary signal. This signal has 2 states and resets to the 0-bit state at the end of each bit. This signal was generated again at 0.5 Gb/s, with the 0-bit state set above the injection locking threshold and the 1-bit state in the excitable spiking regime. These results show again the successful activation of spike events for every input 1-bit. Similar to the previous results, the RZ nature of the input helps to increase the consistency of the response amplitude and timing, and the 0.5 Gb/s encoding rate is handled reliably by the VCSEL neuron. In the case of RZ binary signals the upper encoding limit is dictated by the refractory period of the excitable dynamics, however DTS conversion can be achieved at slower rates due to the non-requirement of clocking.

Comparing Fig. 5.1.1 (e)-(f) we can see that both the unipolar RZ and the VCSEL neuron's spike-conversion are equivalent as pulses are simply replaced by excitable spiking dynamics. Despite this similarity, the secondary conversion of the signal from the electrical domain to the optical domain is also occurring within our DTS conversion system. This system therefore demonstrates that the conversion of

different electrical digital binary formats into optical spiking signals can be achieved, in the devices tested, at up to 1 Gb/s (25 times faster than the experimental GEL demonstration [246]). The maximum spike conversion rate is ultimately dictated by the refractory period of the accessed dynamics and hence could be improved in other VCSELs through specialised device design and fabrication stages. Overall the implementation of DTS conversion systems like this is required to bridge the gap between photonic neuromorphic systems attempting to integrate with conventional digital devices. This system in particular allows an off-the-shelf VCSEL to perform that function while offering a platform wavelength-compatible with communication networks as well as other neuromorphic systems of VCSEL neurons.

5.2 Spiking Photonic Memory

In this Chapter we introduce a discussion of photonic spiking memory in VCSEL neurons through the use of optical feedback connections in functional neuro-inspired architectures. We explore two system architectures that demonstrate both self-feedback connections in a single VCSEL neuron and mutual coupling connections in a 2 VCSEL neuron system.

In biological neural networks, natural autaptic (self-feedback) neuron connections, which were once thought to be uncommon, are now understood to be commonly widespread. These self-feedback connections have been found to occur in many parts of the brain (cerebellum [247], neocortex [248], hippocampus [176], etc.) yet, their function in the nervous system is still not fully understood. Research into autaptic neuron connections has shown that they can provide self-control in neurons, helping the neuron maintain persistent activity [249] and increase spike-timing precision [250]. Similarly, in groups of neurons it was found that autapses can create the synchronisation of action potentials [251], a role important for the processing function of the brain, as well as trigger inhibitory and excitatory postsynaptic currents that effect the activation of subsequent potentials [176], [252]. The role of autaptic

connections in biological neurons is therefore thought to be similar to that of self-feedback systems observed in other fields, where they are used to stabilise signals, regulate behaviour [253] or create memory in a system allowing past events to influence the present [254].

In general, self-feedback connections are implemented when the output of a system is redirected back into the system. In photonics, as lasers are susceptible to optical pumping and optical injection, they are too susceptible to feedback of their own generated light. The reinjection or feedback of light in semiconductor lasers has shown in some cases to lead to the reduction of laser linewidth, when low power phase-matched optical feedback is introduced [255], [256]. When introducing high levels of feedback, external cavity modes are created that inject oscillations into the system increasing the linewidth of the laser while producing rich intensity dynamics, such as chaos and low frequency fluctuations, at the output [257], [258]. For this reason, interest in semiconductor laser feedback architectures has led to their application in numerous research fields including frequency stabilisation [259], secure communication [260] and random bit generation [261]. Similarly, the high dimensionality produced by semiconductor laser feedback systems makes them extremely useful for information processing systems, such as time delay reservoir computers. The latter use delayed feedback cycles to produce multiple interconnected virtual nodes in an artificial neural network [206]. Similar to biological autapses, the feedback delay in these systems is crucial for creating additional memory, helping reservoir computers perform different complex learning tasks [262]. Self-feedback architectures with different neuromorphic photonic systems have also been recently investigated to explore autaptic neuron-inspired functionalities [174], [175], [189], [263]. Semiconductor micropillar lasers with saturable absorbers have reported the storage of pulse trains and long-term pulse interactions in memory using feedback loops [174], [175]. Optical self-feedback loops have also been suggested in theory to implement unsupervised learning via spike timing dependent plasticity (STDP), with vertical-cavity semiconductor optical amplifiers (VCSOAs) in photonic spiking neural networks [189]. In this technique, the spiking output of a networked VCSEL is fed back and combined with its own input signal to derive the appropriate input weighting by consideration of precise

spike timing. Feedback connections in general however, are not required to be implemented by single delay lines or loops but can in fact be implemented by networks of multiple devices. Examples include demonstrations of mutually coupled excitable devices, where excitable dynamics can become self-sustained in the memory of the system [264] and reservoir computing systems with 2 mutually delay-coupled semiconductor devices [265]. In this Chapter we report on both feedback architectures to investigate and compare the memory functionality of our VCSEL neurons.

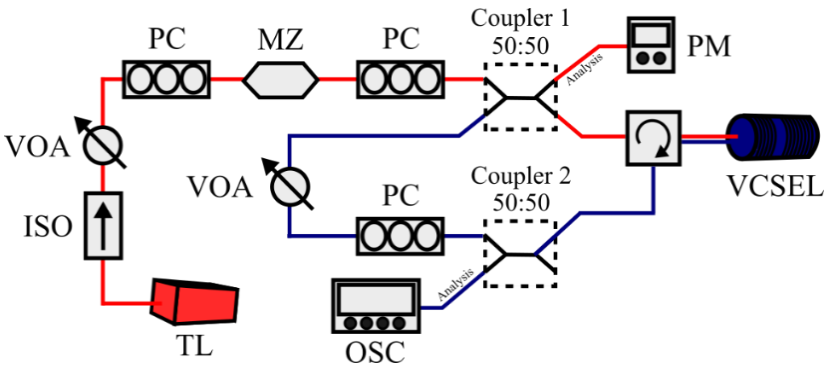

Figure 5.2.1 – Setup to study a self-feedback photonic VCSEL neuron. A VCSEL is subject to both polarised optical injection (red path) and feedback (blue path) via a fibre-optic feedback loop. TL – tuneable master laser, ISO – optical isolator, VOA – variable optical attenuator, PC- polarisation controller, MZ – Mach Zehnder modulator, PM – power meter, OSC – oscilloscope.

The first of the cases studied, namely optical self-feedback in a VCSEL neuron, is implemented by splitting the output of a VCSEL neuron and recombining it into the optical injection line. The complete experimental arrangement is shown in Fig. 5.2.1. Light from a tuneable master laser is encoded with intensity modulations from a MZ-modulator before being split 50:50 by a 4-port fibre optical coupler (Coupler 1). One output port of Coupler 1 is used for the analysis of injection and the second is passed to the VCSEL neuron via an optical circulator. The final output of the optical circulator is again split using a second coupler (Coupler 2) to create a feedback line and a VCSEL-output analysis port. The optical feedback line, which includes both a

variable optical attenuator and a polarisation controller, is connected to the input port of Coupler 1, for its reinjection into the VCSEL neuron. Using the analysis ports of Couplers 1 and 2 the injection signal and the VCSEL neuron output can be collected and analysed with a real-time oscilloscope. The polarisation controller and optical attenuator present in the feedback line allow for the control of key feedback parameters, namely the feedback light polarisation and optical power.

Using the experimental arrangement shown in Fig. 5.2.1 we injected a modulated optical signal into a VCSEL neuron subject to optical self-feedback. The feedback delay time (τ) was 142.1 ns. The feedback polarisation was set to match that of the optical injection (orthogonal XP polarised). An optical injection power of 29 μW was used at a frequency detuning of -2.53 GHz (injection locking the VCSEL neuron to the external signal), along with 10.4 μW (35.9%) of optical feedback. Spike-activating perturbations (input pulses) of 0.6 ns duration were injected into the system at a repetition rate of 1.5 MHz. The output of the VCSEL is plotted in Fig. 5.2.2.

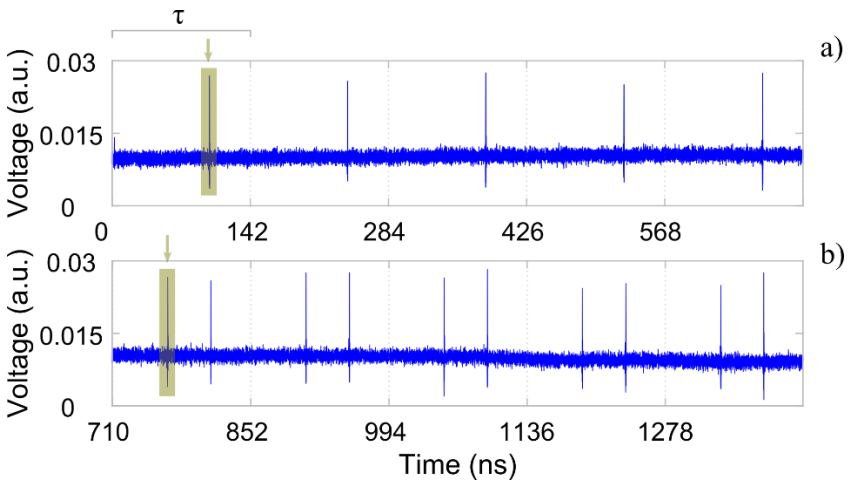

Figure 5.2.2 – 15 cycles of spike encoded memory in a self-feedback VCSEL neuron. Input perturbations are used to write spike events in τ-long (142.1 ns) memory cycles. Memory cycles 1-5 (a) and 6-10 (b) are part of a single continous measurement. Controlled spike ativations are highlighted in green at 100 ns and 766 ns. Experimental parameters: I = 5.3 mA, T = 293K, Orthogonal (XP) mode injection, Δf = -2.53 GHz, Orthogonal (XP) polarised feedback. Figure reproduced from [200].

Each plot provided in Fig. 5.2.2 (a)-(b), shows the VCSEL neuron output for five consequtive memory cycles of 142.1 ns duration. In the first τ-long memory cycle of each plot, we highlight in green, the activations of new spike events caused by the injection of external perturbations. In Fig. 5.2.2 (a) we see that the externally triggered 1-spike sequence stored in the first memory cycle is fed back through the feedback delay line, where after 142.1 ns, it is regenerated in the form of a second identical sequence. In the same fashion the 1-spike sequence is stored and regenerated in a total of 5 memory cycles indicating that externally-generated perturbations can successfully write spikes within the memory of the VCSEL neuron. In Fig. 5.2.2 (b) the second external perturbation arrives at 766 ns writing an additional spike in the memory cycle. As before this 2-spike sequence is sucessfully stored and regenerated in memory cycles 6-10. The writing of additional spikes is therefore possible without the disruption of prevously stored dynamics.

Fast sub-nanosecond spiking responses can therefore be written into the memory of a VCSEL neuron using this controllable technique. The fundamental capacity of the memory cycles will be ultimately limited by the refractory period of the VCSEL neuron. The maximum potential spike capacity of memory cycles in this system is therefore given simply by Eq. 5.2.1.

$$N_{cap} = \frac{1}{T_{refr}} * \tau \qquad \text{(Eq. 5.2.1)}$$

Where N_{cap} is the maximum spike capacity in a memory cycle created by a system with a set feedback delay τ and a spiking refractory period T_{refr}. In the VCSEL neuron we have limited control over the refractory period of our devices, therefore, in order to control the capacity of memory we need to vary the length of the delay τ. With spike capacity proportional to delay, should we require more memory capacity, we could look at increasing the length of the memory cycles (τ).

When encoding the memory cycles if a spike is written within T_{refr} of one already stored in memory then we can experience the re-writing of the spike. If an external perturbation arrives within T_{refr} but before the stored spike, the stored spike is erased and the newly activated spike is stored in memory. However, if the external perturbation arrives after the stored spike, the external perturbation will fail to

activate a new spike as the system has not recovered from the previous excitation. Further investigation into the full capability of the system to write, re-write and erase spiking within memory would be of interest for memory functionality in VCSEL neurons. However, further testing is not provided in this work due to experimental limitations at the time of reporting (previously no access to an AWG). Work performed by other groups exploring self-feedback architectures in micropillar lasers [174], [175] and VCSELs [263] have shown promising results regarding the erasing of memories using external perturbations to influence carrier dynamics, suppressing individual pulses within the feedback memory. A similar method in our experimental arrangement would grant us the ability to fully control the spike memory within our VCSEL-based neuromorphic system.

Overall this single VCSEL neuron with a self-feedback connection demonstrates the ability to controllably write and store mulitple spikes in repeating memory cycles. In this work these memory cycles have demonstrated to exist for up to 7 μs. However, we believe with improvements to experimental stability and noise performance, longer durations could be achieved [175]. With increased stability, additional testing could be completed to investigate and identify pulse interactions within memory over large cycles numbers [174]. The storage capacity of the system is determined by the length of the delay line and the refractory period of the activated dynamics.

In the second feedback architecture studied in this thesis we utilise two mutually-coupled VCSEL neurons to create a networked feedback loop. In this system architecture the output of each VCSEL neuron is injected into the other, as shown in Fig. 5.2.3. No external tuneable source is used for optical injection in this experimental arrangement and no optical modulation is performed. Light from each VCSEL is passed through an optical circulator to a coupler where 50% of the signal is taken for analysis and 50% is transmitted to a polarisation controller and optical attenuator for injection into the neighbouring device. The VCSEL neurons used in the experiment were selected such that they had consistent characteristics. In particular, they each demonstrated orthgonal (XP) mode dominant free-running operation, similar operating wavelengths and dynamical regimes under external optical injection. The bias current and operating temperature of the devices were

adjusted to create a frequency detuning of Δf = -2.03 GHz between the devices and the injection polarisation was set to orthogonally-polarised light to improve the coupling between the dominant polarisation modes of the two VCSELs.

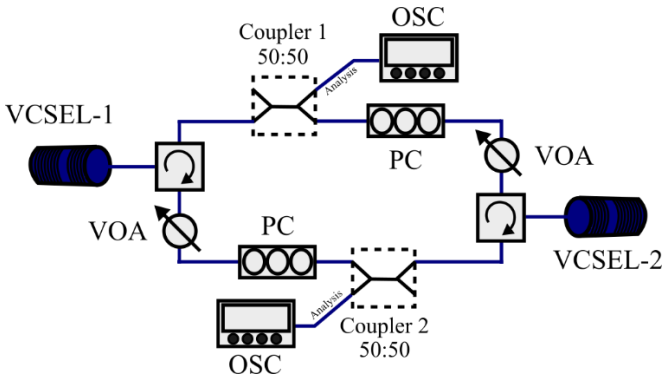

Figure 5.2.3 – Experimental arrangement for mutually-coupled VCSEL neurons. Each VCSEL neuron is subject to polarised optical injection from the neighbouring device. Fibre optical components create a coupling delay of 108.5 ns for a total feedback delay of τ = 217 ns. VOA – variable optical attenuator, PC- polarisation controller, OSC – oscilloscope.

Each branch of the optical feedback loop contributes a measured coupling delay of 108.5 ns to the signals between the two neighbouring VCSEL neurons. This coupling delay is equivalent to half the feedback time (τ = 217 ns) experienced by each device. The system was brought into injection locking with VCSEL-1 (I = 6.05 mA, T = 294 K) producing an output power of 111.7 μW and VCSEL-2 (I = 6.17 mA, T = 291 K) producing an output power of 72.3 μW. Though initially injection locked to each other, the experimental parameters were selected to be close to the unlocking boundary of the devices such that noise could trigger random transitions, producing internally triggered spiking patterns. This mechanism granted us the ability to elicit random spike sequences within the feedback loop without the use of external modulated optical injection. Once generated, the noise-induced spike sequence is then stored in the mutually coupled devices as shown in Fig. 5.2.4.

The elicited noise-induced 11-spike sequence is shown first in the output of VCSEL-1 (Fig. 5.2.4 (a), red). The random 11-spike sequence has a distinct gap between the first and second spike allowing for easy identification in the measured time series. After the coupling delay of 108.5 ns the 11-spike sequence enters VCSEL-2,

producing the successful regeneration shown in Fig. 5.2.4 (b). The reduction in spiking amplitude from VCSEL-1 to VCSEL-2 can be attributed to the reduction in device output power as well as varying optical component efficiencies. After a second coupling delay of 108.5 ns the spiking sequence is re-injected into VCSEL-1, where again we see the successful regeneration of the spiking signal. The spiking signal is stored within the τ-long memory cycle and remains written in the memory of each device for the entire duration of the captured time series (60 memory cycles/ 13 μs). The length of the memory cycle, as in the previous experiment, is dictated by the feedback delay τ. Hence we highlight that the noise-induced spike sequence shown in Fig. 5.2.4, can be replaced by any sequence of spikes. up to the maximum capacity $N_{cap,}$ as calculated in Eq. 5.2.1.

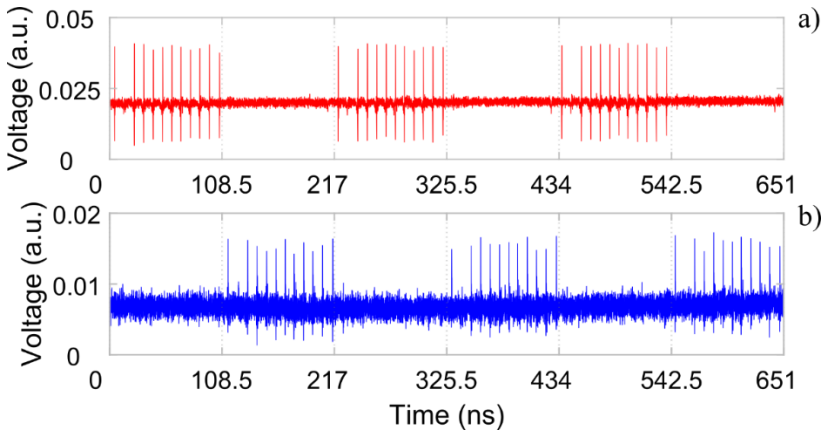

Figure 5.2.4 – 3 cycles of a noise-induced 11-spike sequence in mutually-coupled VCSEL neurons. The noise-induced spiking sequences appear in τ-long (217 ns) memory cycles with a coupling delay of τ/2 (108.5 ns) between devices. The time traces of VCSEL-1 (a, red), and VCSEL-2 (b, blue) were recorded using Coupler 1 & 2 repectively. Experimental parameters VCSEL-1 (VCSEL-2): I = 6.05 (6.17) mA, T = 294 (291) K, XP mode injection, Δf = -2.53 GHz. Figure reproduced from [200].

Overall both VCSEL neuron feedback architectures generate great promise for neuromorphic spiking photonic memory systems. We have demonstrated that single VCSEL neurons, subject to self-feedback, can write excitable spikes into memory through the use of optical modulation, creating sequences of fast spiking patterns that

regenerate in τ-long cycles. This architecture opens a pathway to neuron-like, regenerative spiking memory using only a single VCSEL neuron and a delayed feedback line. In the second experimental study, two VCSEL neurons in a mutual-coupling configuration demonstrated the formation of self stablising τ-long memories. This performance indicates that this feedback architecture would be well suited to implementing the storage of spikes for applications in in-memory processing systems.

Finally, the VCSEL neuron architectures studied in this work make a good case for application in neuromorphic information procesing systems where memory requires creation as each approach can be formed with simple hardware friendly components. The components used in both experimental arrangements are commercial avaliable and telecom-compatible allowing an affordable pathway to neuromorphic systems that demonstrate memory functionality at GHz rates.

5.3 Photonic Spiking Logic Operations

We discuss now the application of spiking VCSEL neurons for decision making logic operations and reveal their key input integration behaviour. We consider a single approach that enables both AND and OR logic operation with mulitple input signals coincident on a single VCSEL neuron.

Biological neurons operating in neural networks are subject to multiple inputs from neighbouring neurons via their dendrtic tree forming synapses. Each synaptic connection made from one neuron to another has an associated weight which controls the strength of the connection. Once weighted inputs enter the neuron, their contribution is summated and temporally integrated in the soma (cell body). The integrated inputs contribute to the build-up of a membrane potential within the neuron that is governed by what is known as an activation function. Neuron firing is only achieved when the threshold membrane potential is exceeded by the integrated inputs [15], [219]. In VCSEL neurons, as shown in Chapter 3.3, analogous thresholding and spike activation functionality is achieved. Similarly, in Chapter 4.1

we demonstrated the communication of spikes in neighbouring neurons. However until now, only single inputs were incident on a VCSEL neuron. In order to sucessfully emulate biological neurons, we need our system to incorporate the contribution of multiple inputs to the firing of a single VCSEL neuron. The leaky integrate-and-fire (LIF) neuronal model describes this behaviour [27], [28], [266].

The LIF neuronal model can be described using a simple neuron surrounded by a cell membrane, and a set of equations for theory of electricity, as shown in Fig. 5.3.1(a). The momentary value of the membrane potential, V, in the absence of any external injection current, I, has a potential equal to its rest value, V_{rest}. When an external current pulse, $I(t)$, is introduced to the neuron the additional electric charge, q, is passed to the cell membrane, which functions as a capacitor with capacity C. The cell membrane however, is not a perfect insulator, leading to the leaking of charge characterised by a leak resistence, R. The LIF model therefore represents the entire neuron as a capacitor and a resistor in parallel, driven by a current. The law of current conservation can be used to split the driving current into a resistive current, I_R, and a capacitive current, I_C, as shown below in Eq. 5.3.1.

$$I(t) = I_R + I_C \qquad \text{(Eq. 5.3.1)}$$

The resisitve current, I_R, is calculated using Ohm's law where the voltage across the resistor is given by $V_R = V - V_{rest}$. The capacitive current, I_C, is calculated from the definition of capacity, $q = VC$, with $I_C = \frac{dq}{dt}$, giving Eq. 5.3.2.

$$I(t) = \frac{V(t) - V_{rest}}{R} + C\frac{dV}{dt} \qquad \text{(Eq. 5.3.2)}$$

Multiplying through by R and using $RC = \tau_m$ to introduce the membrane time constant, τ_m, we arrive at Eq 5.3.3, the equation of a leaky integratory.

$$\tau_m \frac{dV}{dt} = -[V(t) - V_{rest}] + RI(t) \qquad \text{(Eq. 5.3.3)}$$

We are able to observe the solution to this equation and the leaky nature of the integrator when we assume the membrane potential takes an initial value of $V(t_0) = V_{rest} + \Delta V$ at $t = 0$. We then remove the current input at $t > 0$, making

$I(t) = 0$. In the absence of the current input, for $t > t_0$, the membrane potential decays according to Eq 5.3.4.

$$[V(t) - V_{rest}] = \Delta V e^{\left(-\frac{t-t_0}{\tau_m}\right)} \qquad \text{(Eq. 5.3.4)}$$

The solution decribes an exponential membrane potential decay according to the membrane time constant τ_m. The solution to the differential equation can be validated by performing the derivative of each side of Eq. 5.3.4 when $t > t_0$. Physically, this solution means that when we remove inputs, the membrane potential will always approach the rest potential. The system is therefore inherently leaky, however, because the decay of the membrane potential is not instantaneous, multiple inputs are able to influence the overall membrane potential given they occur within a short temporal window.

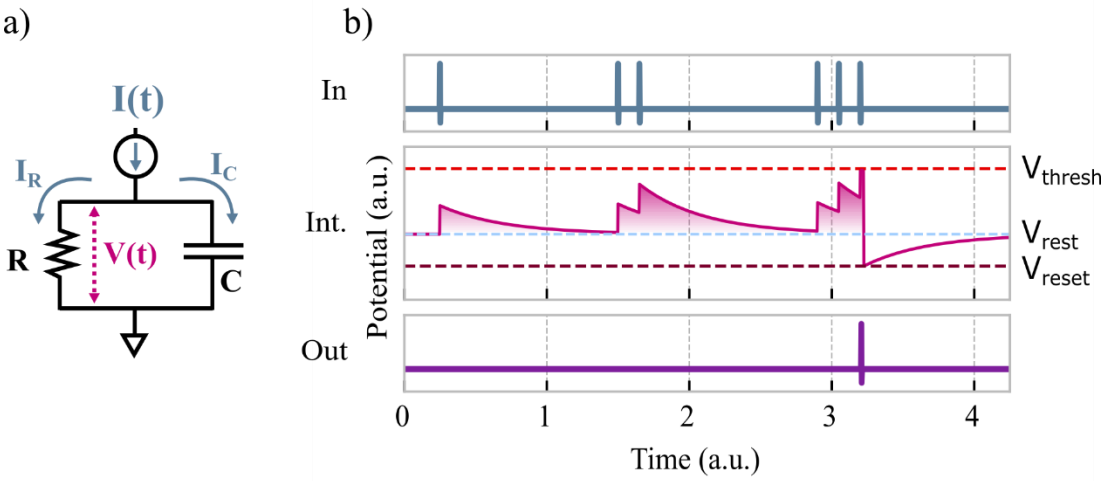

Figure 5.3.1. – Electrical circuit description of a neuron in a passive cell membrane (a). Idealistic depiction of the LIF neuronal model (b). Inputs injected into the artificial neuronal model (In) are integrated (Int.), with a time constant decay, towards a threshold potential (red dotted line). When the threshold is exceeded, the system fires a spike (Out) and the potential reaches the reset value (dark red) before returning to its resting potential (light blue).

This temporal window, here referred to as the integration window, allows multiple inputs occuring in a quick succession to summate towards the triggering of a single neuron activation. Inputs arriving within the temporal window arrive before the membrane potential depletes to its rest value, enhancing their contribution towards

the threhsold potential V_{thresh}. These effects together build the LIF model of a simple neuron. A depiction of an idealistic LIF neuron model is given in Fig. 5.3.1(b).

In the example given in Fig. 5.3.1(b), we can see that a singlet and doublet of input pulses, incident on the LIF neuron, sucessfully integrate together. Despite the succesful integration, the weighting of the inputs and the leaky nature of the system reduce their overall contribution to the potential. Their final contribution is not significant enough to cross the threshold potential and no response is observed at the output of the system. A triplet of input pulses in quick succession is required to produce a potential greather than V_{thresh} after integration, and trigger a response at the output of the neuron.

In our VCSEL neuron system we implement a similar test to investigate its ability to integate multiple input perturbations entering at different and controlled time-instants to analyse their ability to trigger spike firing events (upon exceeding the VCSEL neuron's activation threshold). The experimental arrangement used for this study was the same as that described in Fig. 3.1.3. Figure. 5.3.2 plots the results showcasing the response of the VCSEL neuron to different incoming temporal perturbation patterns, including the injection of fast singlet, doublet and triplet bursts of input perturbations.

Figs. 5.3.2 (a) & (b) show four sets of input injection perturbations incident on the VCSEL neuron and the resultant output of the system. The rising edge of each set of perturbations is separated by 2.0 ns and each pulse has a width of 100 ps. Pulses within the doublet and triplet bursts were configured with a peak to peak separation of ~160 ps, giving the doublet and triplet bursts a total length ~400 ps and ~600 ps, respectively. In both cases depicted in Figs. 5.3.2 (a) & (b), the first input perturbation is a single super-threshold pulse. This is used as a control to indicate the system is suitably close the spiking threshold and that inputs of sufficient strength can successfully activate spiking responses. Similarly, the second pulse in Figs. 5.3.2 (a) & (b) is created with a sub-threhsold amplitude, failing to activate an output spiking response. In this situation, we therefore expect to observe a consistent spiking response at the beginning of the VCSEL neuron output, followed by a gap of no spiking activity. The pulse amplitude of individual inputs within the following doublet and triplet input bursts were set to match that of the previous sub-threshold

control pulse. In both cases (Figs. 5.3.2 (a) & (b)) the injected input sequences are the same, however, each plot is configured with a different spike threshold level for the VCSEL neuron. These different spiking threshold levels were set by altering the frequency detuning between the optically injected signal and the VCSEL's resonance. An injection power of 183 μW into the orthogonal mode of the VCSEL was used for both the far from threshold (-6.0 GHz) and close to threshold (-6.35 GHz) measurements.

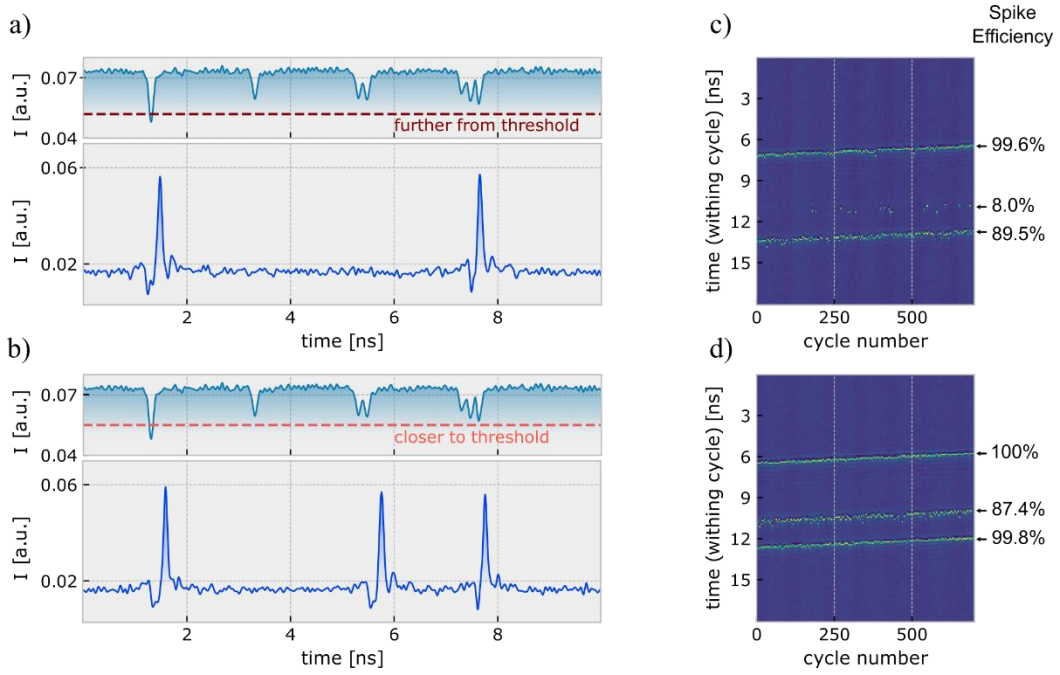

Figure 5.3.2. - Investigation of optical integration in a VCSEL neuron using multiple input pulse patterns. Optically injected input (top) and recorded optical response from the VCSEL neuron (bottom) when using (a) far from & (b) close to threshold operation points. The injected input contains first large and small control pulses, before a doublet and a triplet pulse input burst. Temporal maps (c) & (d) plot the continuous time traces of (a) & (b). Spike intensity is represented using colour, with yellow and blue colours showing respectively spike crests and stable output intensities. The spiking efficiency of the VCSEL neuron's response is given as a percentage of the total number of recorded injections (750 consecutive cycles). Experimental parameters: I = 5.0 mA, T = 298 K, Orthogonal (XP) mode injection, P_{inj} = 183 μW, Δf = (a) -6.0 GHz (b) -6.35 GHz. Figure reproduced from [193].

In both cases (Figs. 5.3.2 (a) & (b)), initially the VCSEL neuron produces a stable injection locked output. Then, upon the arrival of the large super-threshold control pulse at (~1.5 ns), exceeding the activation threshold of the VCSEL neuron, a spike is ellicited (with a 99.6% and 100% efficiency). At ~3.5 ns in both cases, as expected, the arrival of the second sub-threshold input pulse does not trigger a spiking event from the system. After the arrival of the two control pulses, the doublet and triplet bursts enter the VCSEL neuron. For the case of the higher spike firing threshold level, Fig. 5.3.2 (a) shows the activation of a single spike event at ~7.5 ns. The spike is activated by the successful integration of the individual sub-threshold pulses within the triplet input burst, whose combined energy exceeds the spike activation threshold of the system (with an efficiency of 89.5%) as in the LIF neuron model. In Fig. 5.3.2 (a) the doublet input does not trigger a consistent spiking response from the VCSEL neuron as their combined energy falls below the threshold level. For this first case of analysis, the temporal map of Fig. 5.3.2 (c) shows the response of the system for 750 consecutive injections of the input perturbation sequence. From the map we see that the spiking response from the intial control pulse and the triplet each produce consistent responses (99.6 % and 100% efficient), conversely, the doublet does not ellict a regular response over all input cycles, with a poor spike efficiency of 8%.

The response of the system does however change when we consider the case closer to threshold. Individual time series and the temporal map (measured for 750 consecutive input sequences) for this second case of analysis are shown in Fig. 5.3.2 (b) & (d), respectively. The reduction in spike firing threshold level lowers the overall total energy requirement for spike activation, allowing for more reliable responses from integrated input bursts. Thus, the integration of the doublet bursts observed in Figs. 5.3.2 (b) & (d) now shows a reliable spiking response at the output of the VCSEL neuron with a higher spike efficiency of 87.4%. Similarly the response of the triplet burst is improved further with activations across 99.8% of cycles. These experimental results demonstrate that optical input integration is possible within our VCSEL neurons given responses occur within a short time window, similar to the LIF model of a neuron. It also demonstrates that we can tune the spiking response of the system by controlling either the weights of incoming inputs or by altering the threshold level via experimental parameters. The demonstration of optical input

integration is paramount to the neuromorphic capabilitites of VCSEL neurons as input integration is key for network interconnectivity functionalities and the development of decision making processing systems.

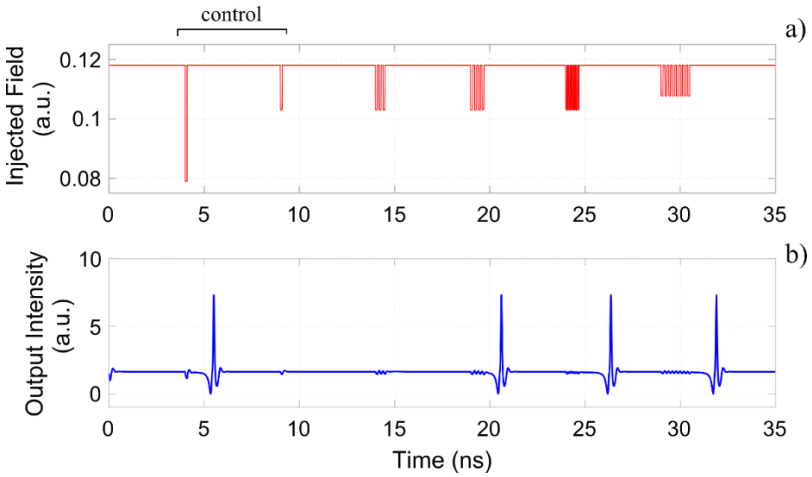

Figure 5.3.3. - Simulated optical integration in a spiking VCSEL neuron using the Spin-Flip Model. (a) Optically injected inputs and (b) simulated optical responses from the VCSEL neuron. The input injection contains first a large and a small control pulse before a series of pulse bursts. The input bursts entering the VCSEL are pulse sets of 3, 4, 8 (narrow width) and 8 (regular) pulses, respectively. Simulation parameters: I = 2.5I_{th}, λ = 1300 nm, Orthogonal (XP) mode injection, Δf = -4.0 GHz, $k = 185ns^{-1}$, $\gamma_a = 2ns^{-1}$, $\gamma_p = 128ns^{-1}$, $\alpha = 2$, $\gamma_N = 0.5ns^{-1}$, $\gamma_s = 110ns^{-1}$, $\beta_{sp} = 10^{-6}$ and $k_{inj} = 125ns^{-1}$.

Using the Spin-Flip Model (SFM) (see Chapter 2.3), we confirm the experimental findings on the input integration capability of VCSEL neurons. In the simulations developed, input pulses are optically injected into the simulated VCSEL neuron. The simulation parameters used were the same as those described in Chapter 2.3. Similar to the experiment (Fig. 5.3.2), a pair of control pulses, one of super-threshold and sub-threshold input strength, are injected into the VCSEL neuron as shown in Fig. 5.3.3 (a). Input bursts of 3, 4 and 8 pulses are then injected into the device. Pulse widths of 100 ps with inter-pulse-intervals of 100 ps are used in each burst with the exception of the third burst which features narrow 50 ps pulses with inter-pulse intervals of 50 ps. The simulated response of the VCSEL to the injected inputs is plotted in Fig. 5.3.3 (b).

Figure 5.3.3 shows that initially the VCSEL neuron output remains stable as the system is injection locked to the external constant signal. The simulated VCSEL neuron responds to the incoming super- and sub-threshold control inputs with a single activation of a spike event at ~5.0 ns. This indicates that the injection level configured yields an injection locking output, and that the spike activation threshold is between the amplitudes of the large and small input pulses (perturbations). After the control pulses, the first input burst of 3 sub-threshold pulses, at ~14 ns, enters the simulated VCSEL neuron. Here however, the total energy of the input burst is not sufficient to activate a spike at the output of the VCSEL neuron. In the second burst (at ~19 ns) an additional pulse is added, creating a burst of four pulses. Now, the VCSEL neuron fires a spike indicating that pulse integration across the burst has enough energy to cross the activation threshold of the system. The integration of multiple temporally-delayed inputs is also successfully simulated in the third and fourth bursts of eight pulses. In these demonstrations, eight pulses (both equal and shorter in duration than the bursts before) are used to successfully trigger excitable responses. The narrow burst demonstrates that theoretically, given the capability to generate signals at higher rates, we could experimentally combine more inputs within the integration window, keeping the duration of input bursts short. This is possible as the total energy of both the four pulse, and narrow 8 pulse bursts are similar. The same effect is true for the fourth burst of input pulses. In this case the 8 pulses are forced to integrate over a larger time but due to the increased pulse width, a lower overall pulse amplitude is required to trigger the VCSEL response. This effect further demonstrates that pulse integration is indeed possible within VCSEL neurons, but also highlights that given the appropriate input rate and amplitude, the width of the window of integration can be controlled. Overall, the simulations in Fig. 5.3.3 confirm the experimental findings of Fig. 5.3.2 regarding the integration capability of the VCSEL neuron, similar to the LIF model.

In a functional application of the optical input integration in VCSEL neurons, we demonstrate a decision making process referred to as temporal coincidence detection. Used in biological neurons to combat timing jitter [267], coincidence detection is the recognition of two temporally-close sub-threshold inputs that activate a spiking

output when their arrival times fall within a short time window, remaining quiescent otherwise. Coincidence detection is exemplified for our VCSEL neuron in Fig. 5.3.4.

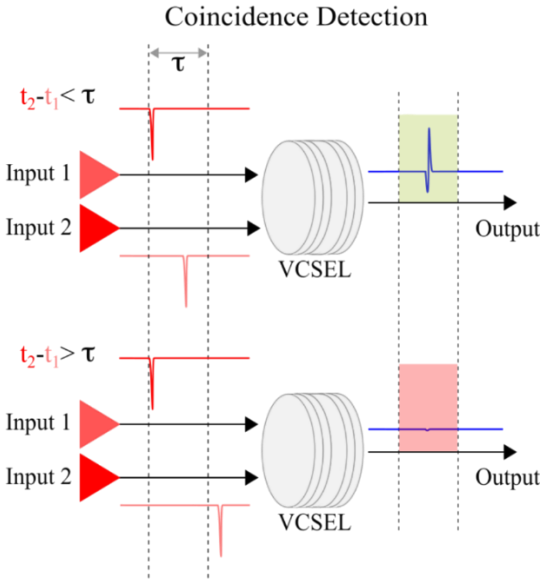

Figure 5.3.4. - Coincidence Detection Schematic. Two inputs that arrive within a coincidence time window, τ, activate a spike at the output of VCSEL neuron. The system operates as a temporal 'AND' gate, requiring the sychronised injection of two separate inputs. Figure reproduced from [193].

In Fig. 5.3.4 two input sources each injecting a perturbation (pulse) are incident on a VCSEL neuron. Input 1 injects a pulse at t_1, and Input 2 injects a pulse at t_2. In the (top) case that t_2-t_1 is less than the coincidence time window, τ, the inputs are deemed coincident, and the VCSEL neuron fires a spike. In the (bottom) case that t_2-t_1 > τ, the inputs are not coincident and the system does not fire. Coincidence detection therefore performs a temporally-resolved AND logic operation. We investigate experimentally this functionality in a VCSEL neuron using the setup in Fig. 3.1.3, where a single optical injection line is encoded with two temporally-resolved (virtual) inputs via the time-division multiplexing (TDM) of pulse pairs. This arrangement therefore demonstrates the processing functionality of a system of 3 neurons in a 2-into-1 fan-in architecture. Here the presynaptic neurons and their

inputs are virtual as they are encoded in different time instants and are generated directly with the AWG in the setup. The experimental results demonstrating the achievement of coincident detection functionality at ultrafast rates using a single VCSEL neuron are provided in Fig. 5.3.5.

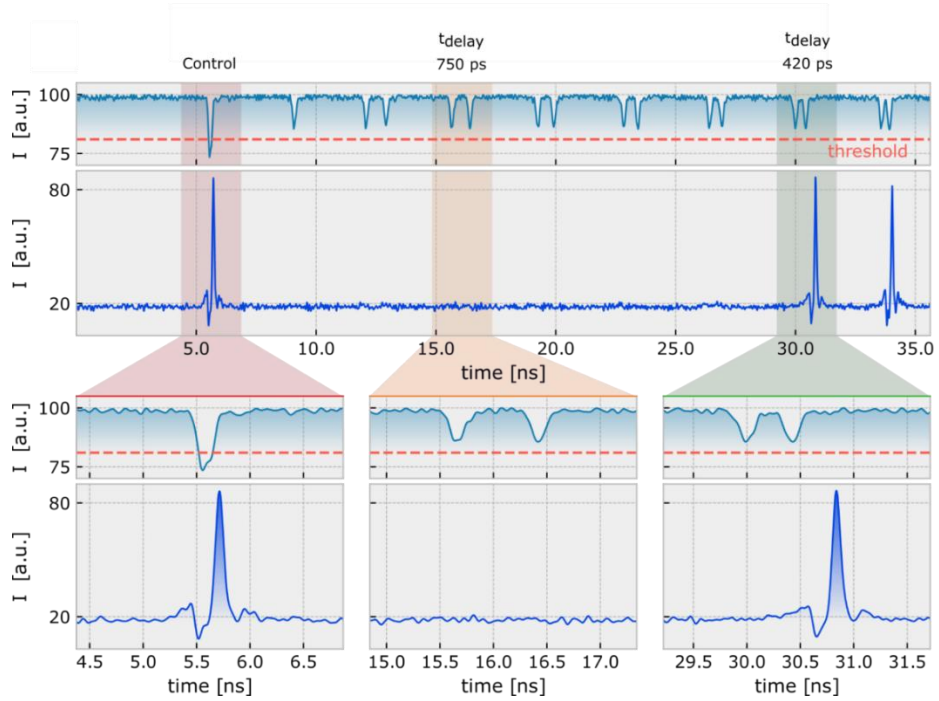

Figure 5.3.5. - Experimental coincidence detection using optical input integration. Inputs are optically injected (top) into a VCSEL neuron which fires spikes (middle) when inputs are sufficiently coincident in time. Selected corresponding insets are expanded below. 7 sets of two input pulses with separations (t_{delay}) decreasing from ~820 ps to ~340 ps are injected alongside a set of control pulses. The threshold is indicated by the dotted red line. Experimental parameters: I = 5.0 mA, T = 298 K, Orthogonal (XP) mode injection, P_{inj} = 244.2 μW, Δf = -9.18 GHz. Figure reproduced from [193].

The optical inputs injected into the VCSEL neuron are shown in the top plot of Fig. 5.3.5, with the measured time series response of the system shown below. Again, a pair of control pulses, super-threshold and sub-threhsold respectively, are used to ensure the system is operating with the correct spike activation threshold. The optical inputs incident on the VCSEL neuron are pairs of temporally-uncorrelated pulses

with time separations (t_{delay}) decreasing gradually from ~820 ps to ~340 ps. The input pulses were programmed to have the same amplitude as the sub-threshold control pulse, each with ~170 ps pulse widths. Optical injection was made such that the VCSEL neuron was initially injection locked, generating a stable output. Figure. 5.3.5 shows that the control pulses, as expected, activate a single spike from the system at ~6 ns (inset left). At ~13 ns and ~15 ns the first a second pulse pairs, of t_{delay} ~ 820 ps and ~750 ps (inset middle) respectively, enter the VCSEL neuron. Both these pulses pairs fail to activate a spike response from the system indicating that their integrated pulse energies do not exceed the spiking threshold given their large temporal separations (t_{delay}). Since the latter is larger than the coincidence temporal window τ, the system deems them as not coincident, remaining quiescent. It is not until the sixth input pulse pair, with t_{delay} ~420 ps, that we find the case of coincident pulses. Similarly, the seventh pulse pair, t_{delay} ~340 ps, elicits a spike at output of the VCSEL neuron. The integration of these pulse pairs successfully creates a total input that is capable of crossing the activation threshold of the system given their short pulse separations below the value of the coincident time window τ. The system deems these inputs as coincident producing a spike firing response.

Figure 5.3.6 plots the temporal map of the VCSEL neuron's response to 172 consecutive cycles of the optical input sequence. In the temporal map the first consistent response (at approx. 4 ns), indicated by a yelow line, is that of the strong input control pulse (with a 100% spike efficiency). The map then shows that as the input pulse separation t_{delay} decreases, the number of consistent spiking responses elicited at the output of the device increases, becoming increasingly consistent (33.1 % and 73.2% efficient) at approx. 28 ns and 35 ns (for pulse separations of ~420 ps and ~340 ps). This result points to the VCSEL neuron acting, as anticipated, like a leaky system where any resultant integrated amplitude degrades or decays over time. This effect produces the coincidence detection operation we expect as pulses that are more temporally correlated integrate more efficiently, hence activating spiking outputs in the system. The results in the temporal map show the system deems input pulse pairs occuring within ~340 ps as coincident as there the system activates 73.2% of the time. Unlike the result shown in Fig. 5.3.5, pulse pairs with t_{delay} ~420 ps a

lower efficiency (33.1%) than would be desired in the impementation of a decision making system.

The coincidence window in the VCSEL neuron, can be altered by varying the amplitude (weight) of inputs or through the control of experimental parameters. A selective integration window such as this is a simple pathway to programmable coincidence detection, a feature commonly applied in alarm triggering systems, where sets of input values, occuring sychronously, elicit a specific output alert. In the case of the VCSEL neuron system demonstrated here, this functionality can be achieved in the optical domain using input integration and fast 100 ps spiking responses, compatible with SNNs for decision making circuits at telecom wavelengths.

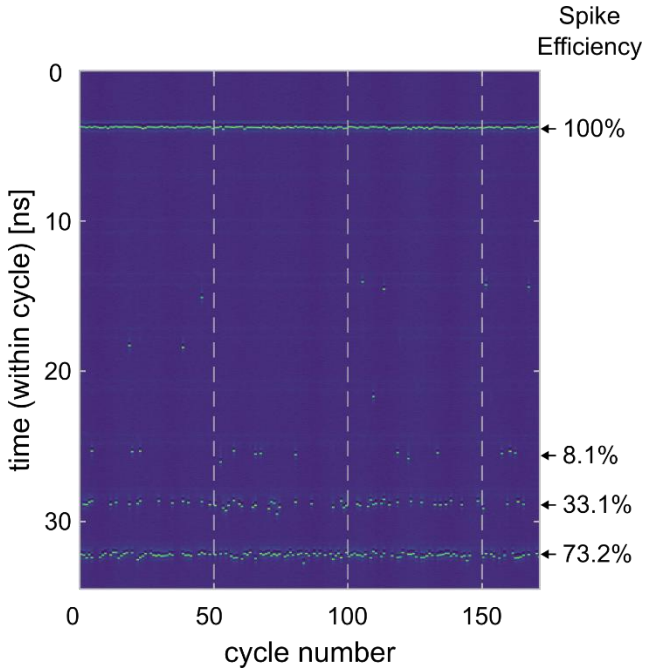

Figure 5.3.6. - Temporal map of the coincidence detection responses from the VCSEL neuron. Results are produced from 172 cycles of data corresponding to Fig. 5.3.5. Seven sets of two input pulses with separations (t_{delay}) decreasing from ~820 ps to ~340 ps are injected alongside a set of control pulses. The spike efficiencies for the control pulse as well as the pulse pairs of ~340 ps, ~420 ps, and ~490 ps are given as percentages of the 172 total cycles. Experimental parameters: I = 5.0 mA, T = 298 K, Orthogonal (XP) mode injection, P_{inj} = 244.2 μW, Δf = -9.18 GHz. Figure reproduced from [193].

In summary, we probed the VCSEL neuron to investigate its ability to perform the integration of multiple optical inputs. We found that, as in the LIF neuronal model, the VCSEL neuron has the ability to integrate bursts of inputs that occur within a short (sub-ns) temporal window. Through experiment and simulation we observed that input amplitude (weight), input separation (input rate) and spiking threshold level, each play interconnected roles that allow us to selectively control the integration window of inputs. This revelation of the integration functionality in the VCSEL neuron is very imporant for neuromorphic functionalities. This result helps propel the functionality of VCSEL-neurons beyond single input threshold-and-activate applications such as Digital-to-Spiking (DTS) conversion, and into integrate-and-fire inteconnected network applications. In a basic demonstration of this new integrate-and-fire functionality we approached the decision making task of temporal coincidence detection. In this experiment two virtual neurons feed inputs into a single VCSEL neuron with the system operating similar to a temporally-resolved AND logic gate, activating only when the inputs are coincident. We demonstrated that the integration of optical inputs can implement an optical AND gate and discussed that by programming the selective integration window of the system, the coincidence window can be controlled. This experimental system gives a simple pathway to optical alarm triggering systems with rapid decision windows (sub-nanosecond long) that utlise optical input signals at high speed (100 ps-long input pulses) and produce 100 ps-long spikes, compatible with SNNs and other telecomunication wavelength platforms.

5.4 Pattern Recognition and Learning with Photonic Neuron Architectures

In this Chapter we build upon the optical input integration functionality of VCSEL neurons and apply this system to a functional pattern recognition task. We again utlise time-division multiplexing to incorporate multiple (virtual) inputs into

the injection line of the VCSEL neuron for the recognition of high-speed 4-bit data patterns via the firing of fast optical spikes.

One of the large motivators for ANNs and neuromorphic computing systems is the ability to efficiently process large data volumes and perform complex tasks. One such complex task, where ANNs excel is pattern recognition. In pattern recognition systems, inputs are tested for regularitites or patterns to enable classification operations, that attempt to give each set of inputs a predetermined distinctive label. In order to perform this task, recognition systems are trained using inputs that have known labels, allowing the weights of the system to be calculated. When the data or pattern arrives at the input, it is mulitplied by the weights (mask) of the system and depending on its result, is or is not identified by the system as the target label. This complex task is efficiently implemented in neural networks using the reconfigurable weights of synaptic connections. These connections allow the weights of different inputs to be controlled independently, granting the capablity to enhance or reject different input contributions to indicate the true label.

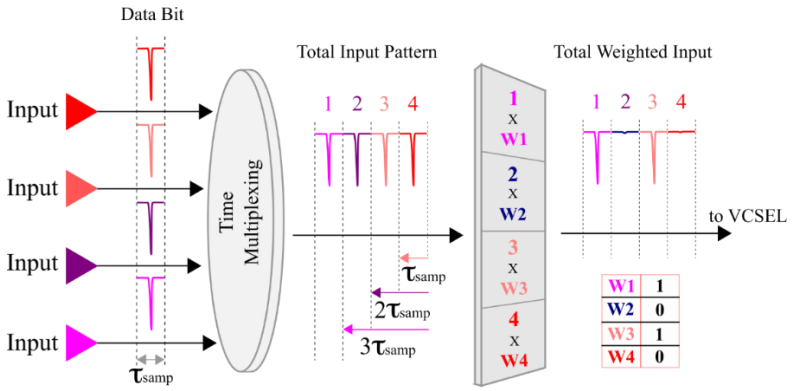

Figure 5.4.1. - Time-division multiplexing (TDM) and 4-bit input weighting scheme utilised for the pattern recognition task with the VCSEL neuron. Four virtual inputs are sampled (τ_{samp}) and staggered into a single injection line, creating 4-bit data patterns. These are weighted using a customisable weight array before injection into the VCSEL neuron for processing. Input multiplexing and weighting is performed offline after which the weighted input is generated in an AWG and injected into the VCSEL neuron. Figure reproduced from [193].

Here, we demonstrate experimentally, using a single VCSEL neuron, a 4-bit input pattern recognition system able to operate at very high speeds. Similar to the demonstration of the LIF functionality (Chapter 5.3), we will make use of virtual (time multiplexed) inputs to place our VCSEL neuron in a virtual fan-in network. We use 4 virtual inputs incident on a single VCSEL neuron to test the pattern recognition capability of our system while keeping the hardware complexity low. Time-division multiplexing (TDM) is used to combine the 4 virtual inputs into a single optical injection line as shown in Fig. 5.4.1.

In TDM, each of the four utilised inputs is sampled for a short duration (τ_{samp}), before being sequencially staggered into a four input temporal pattern. In this experiment we generate inputs where pulses have a bit value of '1' and pulse absenses (stable outputs) have a bit value of '0'. Four virtual inputs are therefore combined to produce 4-bit input patterns. As discussed above, pattern recognition requires the application of weight to each input bit. In this system we multiply the bit value of each input by a weight, determined by a customisable weighting array. The application of weight is completed offline, prior to the generation of the modulation signal and the injection of the VCSEL neuron. Here we focus on the recognition of an individual target pattern, applying a unique set of weights to the input data. Input 4-bit patterns that are successfully detected activate a spiking response at the output of the system with non-target patterns remaining silent.

Sequences of input patterns were used to test the recognition efficiency of different target patterns. The input data sequences were created with bit value intensities ('1' or '0') and sample steps of 83.3 ps (at a rate of 12 GSa/s). Each virtual input was assigned 2 samples, the first one corresponds to the 'true value' of the input bit and the second a return to zero value. Using this process we create 4-bit input patterns with a total duration of ~650 ps. The patterns were then grouped according to the number of active input bits. This created 3 sets of sequences (data, input patterns) with 1 active '1' bit, 2 active '1' bits and 3 active '1' bits. All input data sequences, encoded in optical injection without weighting, are shown below in Fig. 5.4.2.

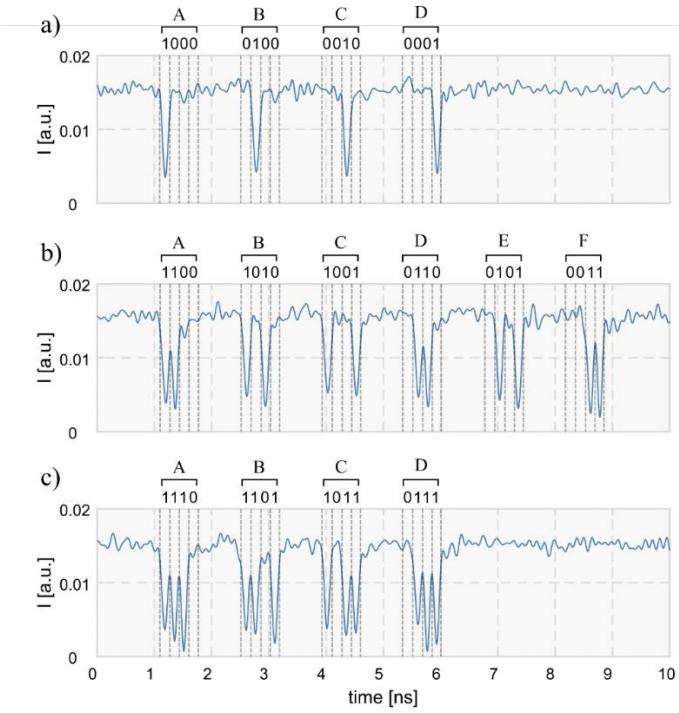

Figure 5.4.2. - Time series of 4-bit input data patterns (Pre-weighting) with (a) 1 active '1' bit, (b) 2 active '1' bits and (c) 3 active '1' bits. A total of 14 patterns are generated. Active '1' bits are encoded as drops in optical intensity and '0' bits as stable intensity. Figure reproduced from [193].

The 4-bit input patterns are referred to as patterns A-F within their active bit number sets. A total of 14 unique patterns are created using the 4-bit scheme, 4 in set 1, 6 in set 2, and 4 in set 3. The testing of 4-bit patterns 1111 and 0000 are excluded due to their unique classification. Each pattern within an input sequence or set is separated by 10 samples (~830 ps). The separation helps distinguish neighbouring patterns while extending the input timing to match better the system's refractory period to provide successful pattern detections.

The weighting step within our pattern recognition system sees each individual bit within the 4-bit patterns multiplied by a weighting value. The same 4 weighting values are applied across all patterns in an input sequence. The weighting is used to eliminate, or reduce, the contributions of incorrect bits to the spike firing response of a target detection. Each value in the weighting array corresponds to a sample point in the data sequence and holds a weighting value between -1 and 1. Weighting values

W1, W2, W3 and W4 were applied to the first, second, third and fourth bits of each input pattern respectively. The product of the input data and weighting array produces the weighted data which will be generated with the AWG for injection into the VCSEL neuron. Using unique weight combinations allows us to detect target patterns individually. The weighting tables for all 4-bit patterns and examples of weighted data inputs for some 1, 2 and 3 active '1' bit patterns are shown in Fig. 5.4.3. The weighing values were selected through a supervised learning approach. The bit weights were varied and tested experimentally to improve the recognition efficiency of target patterns or decrease the number of false recognitions.

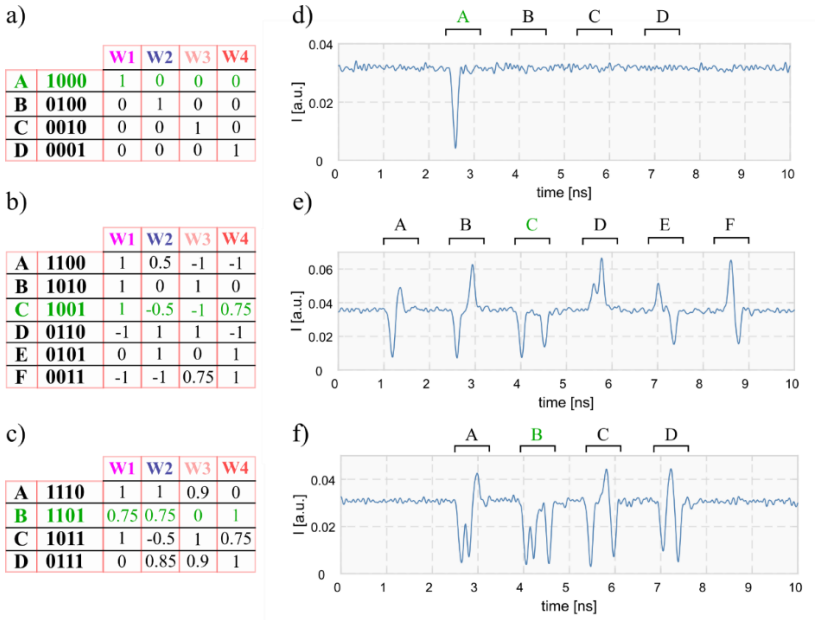

		W1	W2	W3	W4
A	1000	1	0	0	0
B	0100	0	1	0	0
C	0010	0	0	1	0
D	0001	0	0	0	1

		W1	W2	W3	W4
A	1100	1	0.5	-1	-1
B	1010	1	0	1	0
C	1001	1	-0.5	-1	0.75
D	0110	-1	1	1	-1
E	0101	0	1	0	1
F	0011	-1	-1	0.75	1

		W1	W2	W3	W4
A	1110	1	1	0.9	0
B	1101	0.75	0.75	0	1
C	1011	1	-0.5	1	0.75
D	0111	0	0.85	0.9	1

Figure 5.4.3. - Weight tables and weighted 4-bit input data sequences. Bit weights applied to detect each 4-bit pattern in (a) 1, (b) 2 and (c) 3 active '1' bit pattern classes. Weighted input time series (d-f) are shown for the highlighted (green) patterns of each set. Figure reproduced from [193].

The recognition of a target 4-bit pattern using our neuromorphic VCSEL-based spiking system is demonstrated in Fig 5.4.4. This shows the data inputs, the weighting values, the weighted data and the VCSEL neuron's response for four patterns from the 2 active '1' bits data set. The target for recognition is the 4-bit pattern C (1001). The time series at the top of Fig. 5.4.4 show four 4-bit patterns, namely A (1100), B (1010), C (1001) and D (0011), before weighting. Below the data inputs, the weights

that are applied offline to the input data sequences are shown. In this case the weights applied are 1, -0.5, -1 and 0.75, respectively. Time series of the weighted data are shown in the third row of Fig. 5.4.4. These weighted inputs are then optically injected into the VCSEL neuron producing the output time series at the bottom row of Fig. 5.4.4. In the case of the 4 injected patterns shown in Fig. 5.4.4, only the target pattern C (1001) elicits a spike from the VCSEL neuron, which remains quiescent for all other non-target patterns. In this specific case, after weighting, only target pattern C has the combined contribution of 2 input bits. These two input bits, that occur within ~650 ps, integrate together towards the threshold of spiking, successfully activating a response where other patterns do not, highlighting a positive recognition.

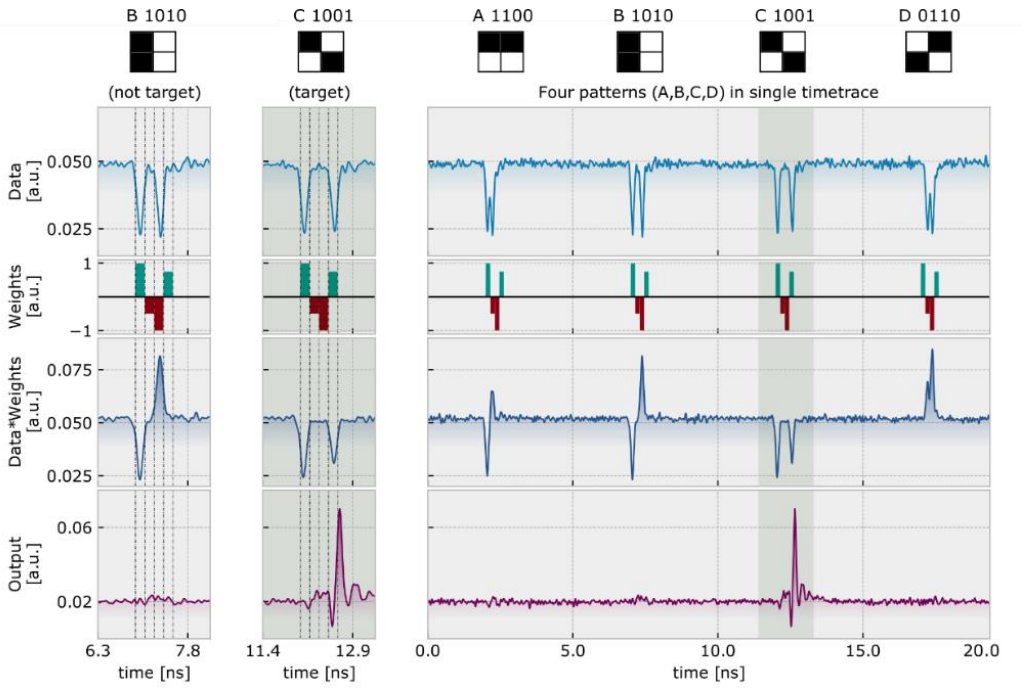

Figure 5.4.4. - Pattern recognition task with a VCSEL neuron. Measured time series (top) show the pre-weighting optical inputs (Data) for various target and non-target 4-bit patterns. The weighting values (Weights) and the resulting post-weighting optical inputs (Data*Weights) are plotted in the middle rows. The VCSEL neuron's optical output (Output) is plotted at the bottom showing successful detection of the target pattern. 4 patterns are shown with 2 active '1' bits: A (1100), B (1010), C (1001) and D (0110), with pattern C (1001) being the target. Figure reproduced from [193].

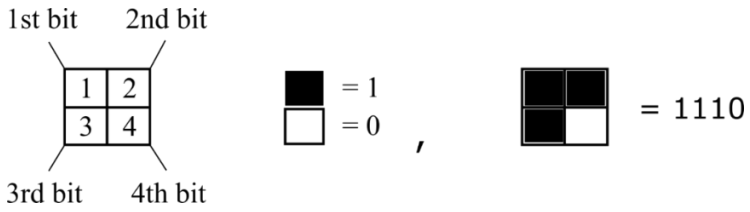

Figure 5.4.5. - 4-bit pattern representation using 2x2 grids. Figure reproduced from [193].

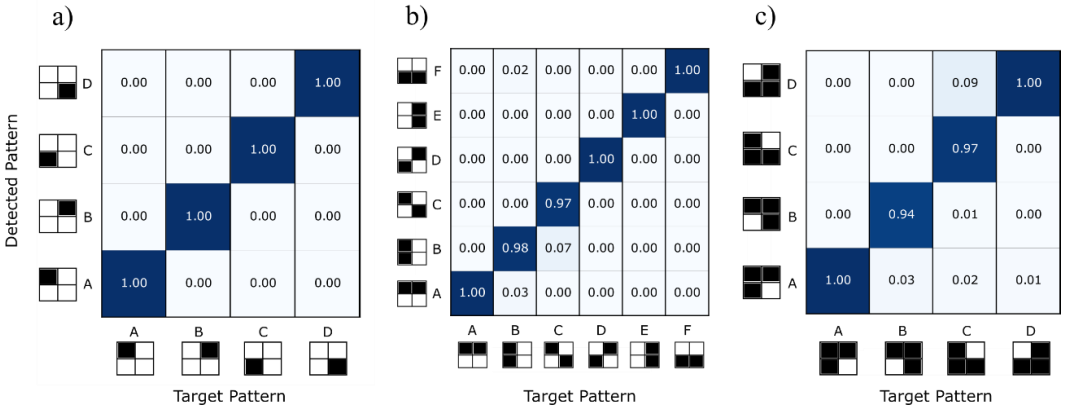

Figure 5.4.6. - 4-bit pattern recognition confusion matrices of the VCSEL neuron system. The measured recognition/detection efficiencies for all 4-bit data patterns of each set (a) 1 active '1' bit, (b) 2 active '1' bits and (c) 3 active '1' bits. The blue colour depth indicates the efficiency measured over 130 consecutive test cycles. Experimental parameters: I = 5 mA, T = 298K, Orthogonal (XP) mode injection, Δf = -7.41 GHz, P_{inj} = 140.5 μW. Figure reproduced from [193].

Using the VCSEL neuron we tested the recognition efficiency of all 14 4-bit patterns. For each target pattern we investigated the response of the system to 130 consecutive recognition tests, comparing the expected and measured spiking responses. In each of the experimental runs optical injection was made at a frequency detuning of Δf = -7.41 GHz from the XP mode of the VCSEL with an injection power of P_{inj} = 140.5 μW. To improve the presentation of recognition efficiencies we implement a simple graphical representation for each 4-bit pattern as shown in Fig. 5.4.5. 2x2 grids, where black (1) and white (0) pixels denote bit value, are read (by row) from left to right, to give the complete 4-bit pattern value. The recognition efficiency of each pattern is shown in the confusion matrices of Fig. 5.4.6. Three confusion matrices

are given, one for each set of input patterns: 1 active (Fig. 5.4.6 (a)), 2 active (Fig. 5.4.6 (b)) and 3 active '1' bits (Fig. 5.4.6 (c)).

The confusion matrices represent the detection accuracy of the 4-bit input patterns. The horizontal axis represents the target patterns and the vertical axis represents the patterns detected by the VCSEL neuron. The recognition efficiency is given within the matrix, which represents the ratio of observed-to-expected pattern detections. In an ideal case, the confusion matrix would show '1.0' values on the diagonals and '0.0' elsewhere, meaning the system returned no false negatives or false positives. False positives (false detections) appear as non-zero recognition efficiencies for non-matched target and detected patterns. The sum of each column can be larger than unity as spiking detections may be triggered by multiple weighted input patterns in a single input sequence. Fig. 5.4.6 (a) shows the recognition efficiencies for patterns containing 1 active '1' bit. In this data set, the weights applied to the inputs are trivial as shown in Fig. 5.4.3 (a). As each input pattern contains only 1 bit, after weighting, only the target pattern has an input. The '1' bits from all non-target patterns are eliminated. Therefore, no false detections occur in 130 cycles and the confusion matrix shows the ideal results. In the case of 1 bit inputs no input integration is required as only one of four virtual inputs is active. The VCSEL neuron is therefore demonstrating the threshold and activation of a single input, hence we therefore expect the ideal performance demonstrated by the system. The recognition efficiency of the 2 active '1' bit set is shown in Fig. 5.4.6 (b). In this data set we see very high recognition efficiencies with the best performance being achieved for patterns A (1100), D (0110) and F (0011). These patterns can be characterised as having two consecutive '1' bits. This means upon injection into the VCSEL neuron these inputs occur within the shortest possible integration window, reducing the effects of the leaky system and achieving a stronger overall contribution towards the spiking activation threshold of the VCSEL neuron. As previously observed (Chapter 5.3), this creates a more consistent response from the system, improving recognition efficiency. The recognition of patterns B (1010), C (1001) and E (0101) also show high consistency but with increasing number of false positives. In these patterns we see an increased separation of input bits within the pattern which requires larger integration times. This inevitably creates a weaker, leakier, integration which

requires a reduced activation threshold when compared to other patterns. The reduced activation requirement gives rise to the higher number of false positives with pattern C (1001) having the largest possible separation between active '1' bits, giving the highest number of false positives. In Fig. 5.4.6 (c) we see the recognition efficiencies of the set of inputs with 3 active '1' bit patterns. The recognition efficiencies of patterns A (1110) and D (0111) showed the highest values due to their consecutive active '1' bits. The patterns of increased bit separation, B (1101) and C (1011), also showed high recognition efficiencies but produced higher numbers of false positives.

These results show that a single VCSEL neuron can successfully implement a high-speed 4-bit pattern recognition system. We must note that in spite of the very good performance and accuracy shown by the system, the results of the pattern recognition task could still be further improved via the selection of optimal weight values (that might decrease the number of false recognitions) and the reduction of the length of the integration window. Here, a minimum bit separation of 2 samples (~160 ps) had to be selected because it reached the maximum available bandwidth provided by our experimental equipment (AWG). This enabled us to integrate sub-nanosecond pulse bursts however, faster modulation speeds would reduce the integration window further, improving the input bit rate and the total integration contribution of our optical inputs. Similarly, with improved input bit rate our system could investigate larger patterns (e.g. 8-bit or higher), expanding the usefulness and applicability of the system.

To advance this pattern recognition system in the future we could implement automatic supervised or unsupervised learning schemes. These would remove the need to train the system weights manually by incorporating an external feedback loop, potentially improving system performance. Unsupervised learning schemes for pattern recognition systems have been implemented in other reports [82], [83], showing the final weighting solution can provide excellent recognition efficiencies.

Finally, these results provide a first proof-of-concept demonstration of a successful neuromorphic processing system based upon VCSEL neurons, capable of performing a complex pattern recognition task. Our report here shows specifically how we implement 4-bit pattern recognition with fast spiking optical components. Initially

we implement TDM to create 4-bit input patterns from 4 virtual inputs and perform the weighting of input bits offline. Applying the optical integrate-and-fire functionality of the VCSEL neuron, we perform pattern recognition of each sub-nanosecond 4-bit pattern, triggering fast ~100 ps spiking responses for positive detections. The optical signals that we utilise demonstrate that we can perform the recognition of sub-nanosecond pulse bursts at near GHz rates with very high recognition efficiencies. The current system, created using commercially-available, hardware-friendly and telecom compatible components, utilises a supervised learning scheme, granting yet further room for system performance improvement. Motivated by these results we believe that multi-VCSEL functionality, with the capability to perform multistep classification in parallel, could be achieved with these devices, as well as the ability to recognise longer (e.g. 8-bit) patterns given improvements to experimental equipment. There is therefore significant potential for VCSEL neurons to be implemented in new developments of light-enabled intelligent neuromorphic processing systems, given the inherent advantageous attributes of VCSELs e.g. compactness, low cost, ease of use, etc. Neuromorphic systems based upon VCSEL neurons, therefore have great prospects to be implemented in complex architectures for future avenues of ultrafast systems that apply brain-inspired functionalities towards pattern recognition processing applications.

5.5 Image Processing and Feature Detection

In this Chapter we apply the neuromorphic functionalities of VCSEL neurons to image processing, achieving edge-feature detection in digital images with neural-like spiking responses at very high speeds. We utilise time-division multiplexing (TDM) to realise complex image processing with hardware friendly systems using a single VCSEL neuron for operation. We will introduce first our approach to spike-based convolution and edge-feature detection with a threshold-and-fire demonstration, moving to an all-optical binary convolution realisation, and finally an all-optical integrate-and-fire approach. We will also demonstrate the performance of the integrate-and-fire VCSEL neuron when working with a large number of complex images from the popular MNIST-handwritten digit database and share theoretical

results showcasing spike-based convolution operation with higher dimensional kernels for enhanced performance.

Training computers to interpret and recognise images as humans do, more commonly known as computer vision, is a complex task being undertaken using a combination of image processing and machine learning techniques [268]. Branching from artificial intelligence (AI), computer vision is now seeing a surge in interest as the goal to automate traditionally human tasks becomes more prevalent with the rapid development of fields such as medical image analysis [269] and autonomous vehicles [270]. Image classification and interpretation is one of the characteristic tasks frequently performed by ANNs, and within these one of the essential steps for computer vision and image processing is the collection of edge-feature information. This is usually extracted by applying kernel operators (masks) to the source image in a traditional image processing task referred to as convolution [271]. The kernel operators multiply the intensity values of the source image pixels, creating a product that identifies the successful or unsuccessful detection of key image features such as interest points, lines, edges and corners. Using a large number of parallel nodes in a convolutional neural network (CNN), edge information can be generated and compared such that a recognition can be performed by assembling many smaller features [272]. CNN-based systems however, suffer from increased power and computational resource requirements, due to the complicated interconnected architectures and computationally expensive convolution operations. This problem leads to the requirement of dedicated hardware, such as multicore-CPUs or GPUs [8], [273], [274], restricting the footprint and application of many electronic CNN systems. However, like neuromorphic spiking systems, the investigation of CNNs with photonic technologies has seen a rise in recent years [54], [81]–[83], [275], [276]. In the move to a light-based approach the computationally intensive convolution task can benefit from the speed, energy efficiency, bandwidth and parallelism offered by photonic technologies. A number of complete approaches to photonic CNNs have been proposed with devices such as Mach-Zehnder interferometers [54], [276], ring resonators and photodiodes [81], [275], and phase change materials (PCMs) [82], [83] providing the core neuronal functionalities required for image convolution. Recent experimental and numerical reports suggest

that these state-of-the-art photonic systems can help improve convolution operation speed by up to 5 orders of magnitude, making them highly desirable for novel photonic processing applications [81]. We have focused our attention on this challenging research aspect. Specifically, we provide here experimental demonstrators of photonic spike-based convolution system based upon a single VCSEL neuron for image processing and edge-feature detection tasks.

5.5.1 Threshold-and-Fire Image Feature Detection

In a first experimental demonstration, we implement a photonic spike-based convolution system based upon a single VCSEL neuron, which elicits spiking responses upon the injection of pre-convolved optical inputs. In this configuration the neuromorphic system performs a threshold-and-fire functionality, outputting edge-feature information in the form of ultrafast sub-nanosecond optical spikes. Unlike conventional photonic implementations of CNNs, we utilise time-division multiplexing (TDM) to achieve image edge detection using a single VCSEL neuron, helping reduce dramatically hardware complexity. Experimental results for the edge detection of multiple digital images are reported here alongside the predicted theoretical (SFM-modelled) response to the pre-processed image input [194]. The pre-processing stage that implements the image convolution and input generation for this initial threshold-and-fire demonstration is described in Fig. 5.5.1.

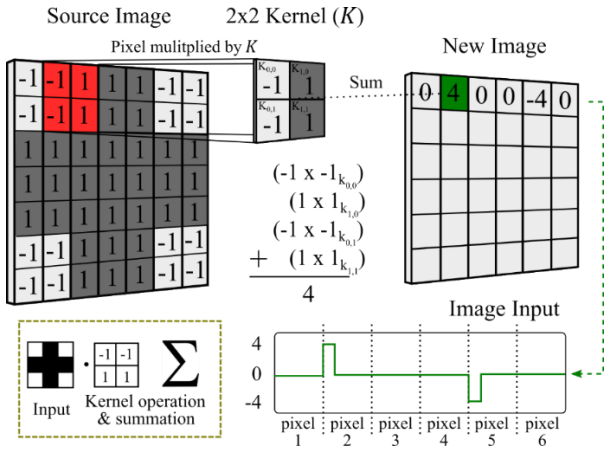

Figure 5.5.1. - Pre-processing stage for threshold-and-fire edge detection by a VCSEL neuron. Figure reproduced from [194].

Firstly, in the preprocessing stage matrices of positive (black) and negative (white) integer pixels are formed from digital greyscale or colour images. Three source images were selected, each with different directional features as shown in Fig. 5.5.2. These were 28x28 pixel images of a cross (Fig. 5.5.2 (a)) and a Saltire (Scotland's national flag, Fig. 5.5.2 (b)) which have vertical, horizontal and diagonal features present. The third larger 50x50 pixel image of the University of Strathclyde's Institute of Photonics (IOP) logo (Fig. 5.5.2 (c)) contains additional curved features. To extract the edge-feature information from these images we perform spiking convolution with a 2x2 kernel operator. The kernel operator applies a set of weights to a 2x2 neighbourhood of pixels within the image. After weighting, the 2x2 set of weighted values are summated into a single value called the destination pixel. By repeating the kernel operation, scanning across every pixel in each row of the source image, the destination pixels can be reconstructed into the final convolved image. The selection of the kernel is key in this operation as different kerenel operators target different features for recognition. The comparison of pixels within the kernel neighbourhood to the kernel itself is what creates positive recognitions in this process. The value of the destination pixel for the pixel neighbourhood used in this work is described in the following equation (Eq. 5.5.1):

$$g_{p,q} = \sum_{m=0}^{M} \sum_{n=0}^{N} f_{p+m,q+n} \cdot K_{m,n} \qquad \text{(Eq. 5.5.1)}$$

Here the destination pixel value is given by $g_{p,q}$, when anchor-pixel $f_{p,q}$ is operated on by customisable kernel K. A pixel neighbourhood (local pattern descriptor) of $(M+1)$ x $(N+1)$, with $M = N = 1$ is used to match the 2x2 operator. Applying the 2x2 kernel in this way means pixels on either the far right-hand side or the bottom of the image cannot be operated on as they contain half the required neighbouring pixels. It is possible to compensate for the missing pixels by padding the image with additional redundant pixels, however this is not required and may alter the detection of features near the edge of the image. When performed without padding (as done here), the dimensions of the resulting convolved image are reduced by 1, due to the dropping of a single row and column of pixels.

As is shown in Fig. 5.5.1, once the new convolved image is calculated, we create an image input suitable for injection into our threshold-and-fire VCSEL neuron. This image input will be used to identify target edge-features through the activation of sub-nanosecond optical spikes at the output of the VCSEL neuron. Similar to Chapter 5.4, TDM is used to sequentially inject each destination pixel from the convolved image into the VCSEL neuron. The input signal is generated with each pixel allocated the same configurable pixel duration. In this demonstration a pixel duration of 1.5 ns was selected, slightly higher than the refractory period of the VCSEL neuron (see Chapter 3.3). A return-to-zero (RZ) coding scheme is employed to generate each input, with the initial 0.25 ns of each sequence holding the destination pixel value and the remainder set to 0. The RZ encoding scheme and the 1.5 ns pixel duration are selected to ensure only a single spike output can be activated in the VCSEL neuron by a target detection, and that neighbouring pixels each have the capability to trigger their own specific spiking response. In the example in Fig. 5.5.1, pixel 2 triggers a positive recognition with a total destination pixel value of 4. Hence, in the image input it holds a value of 4 for a short time at the beginning of the 1.5 ns segment before returning to zero, where the next TDM pixel is then encoded. This input encoding is repeated for all the pixels in the convolved image, and the resulting signal was generated using an AWG.

Overall, the pre-processing stage utilised in this demonstration is responsible for the application of the kernel to the image and the summation of the resultant pixels into the destination pixel value. This process, often referred to as the multiply-and-accumulate (MAC) process is therefore performed offline, outside the photonic VCSEL neuron system. This MAC process, inspired by the synaptic weighting and integration of inputs in biological neural networks, is responsible for the convolution operation in CNN demonstrations. In this demonstration our photonic VCSEL neuron is acting as a threshold-and-fire neuron, responsible for the thresholding and conversion of the convolved image into high-speed temporal spiking regimes with the detected edge-feature information of the image.

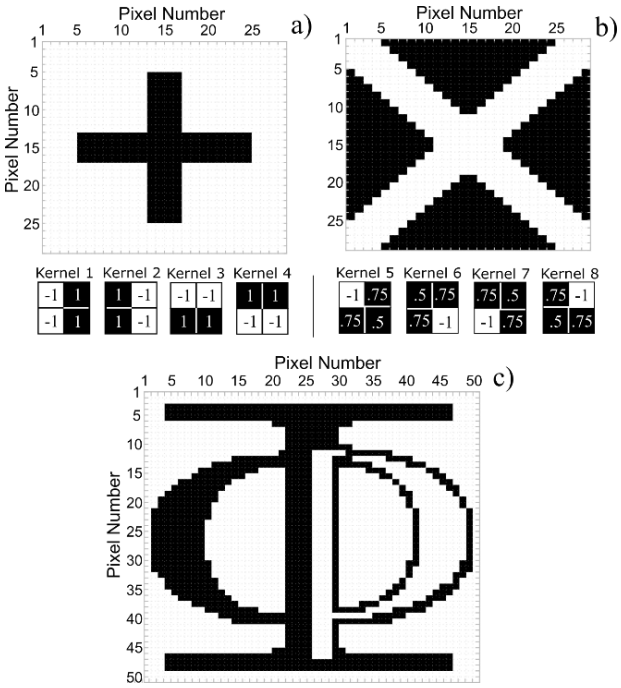

Figure 5.5.2. - Black and white source images of a cross (a), a saltire (Scotland's national flag) (b) and the logo of Strathclyde's Institute of Photonics (c). Vertical (Kernels 1-2), horizontal (Kernels 3-4) and diagonal (Kernels 5-8) operators are used to detect specific edge-features in the images. (a) and (b) have a resolution of 28x28 pixels whereas (c) has a larger resolution of 50x50 pixels. Figure reproduced from [194].

The experimental setup used to realise the threshold-and-fire edge detection is shown in Fig. 5.5.3. Experimentally the system is identical to the modulated optical injection setup used in the previous realisation of multi-pulse integration and earlier demonstrations of controlled spike activation (see Chapter 5.3). A single tuneable laser is used as a source of optical injection (encoding the image information via TDM) for our VCSEL neuron. The optical injection is passed through an optical isolator, a variable optical attenuator and a polarisation controller before entering a 10 GHz MZ amplitude modulator. The optical intensity is encoded with the TDM image input created in the pre-processing stage, with positive input values creating intensity drops in the optical injection. The optical injection is passed through a second polarisation controller before entering the VCSEL neuron via an optical circulator. Amplified fast photodetectors were used to collect the output of the VCSEL neuron before the signal was analysed using a high-speed real-time

oscilloscope. Throughout this experimental demonstration of threshold-and-fire edge detection, the (fibre-pigtailed) VCSEL neuron was driven at a bias current of 6.5 mA and temperature stabilised at 298 K. Under these operating conditions the VCSEL neuron produced single mode emission with a dominant parallel (YP) polarisation. In this demonstration optical injection was made at -4.58 GHz frequency detuning from the subsidiary, attenuated, orthogonal (XP) polarisation mode, inducing polarisation switching upon injection locking to the external signal. An injection power of 152.7 μW was used. Here, when inputs of sufficient intensity enter the VCSEL neuron, we expect the injection locking to breakdown triggering a fast neuromorphic spike. By configuring the threshold for all input pulse amplitudes equal to 4, as in pixel 2 of the example given in Fig. 5.5.1, the system should activate spiking responses correctly revealing target edge-features.

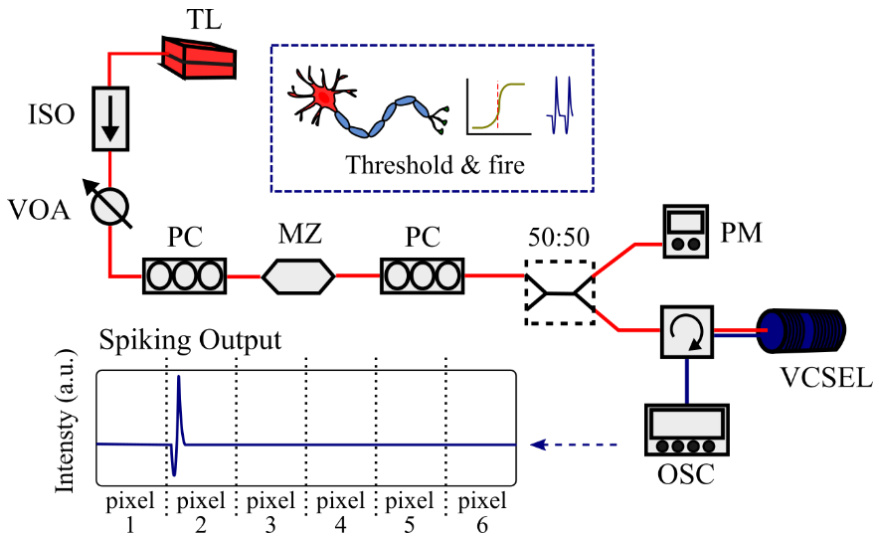

Figure 5.5.3. - Experimental setup used for threshold-and-fire image edge detection with a VCSEL neuron. TDM inputs generated in the pre-processing stage are encoded into optical injection through the use of an optical modulator. Only pre-processed inputs relating to target featuers have sufficient intensity to activate spiking responses. TL – tuneable master laser, ISO – optical isolator, VOA – variable optical attenuator, PC- polarisation controller, MZ – Mach Zehnder intensity modulator, PM – power meter, OSC – oscilloscope. Figure reproduced from [194].

Alongside the experimental demonstration of the threshold-and-fire image edge-feature detection with a VCSEL neuron, we also numerically modelled (using the SFM described in Chapter 2.3) the response of the system to the TDM image input generated in the pre-processing stage. The modified SFM includes additional terms for the injection of an optical signal (encoding the image information) and was solved using the fourth order Runge-Kutta method. The SFM simulations allow us to compare the experimentally achieved spiking responses to those predicted by theory.

In the first demonstration of threshold-and-fire image edge detection, four kernel operators were scanned across the 'cross' image shown in Fig. 5.5.2. Kernels 1-4 (also shown in Fig. 5.5.2) were applied to the source image in sequence with the resulting image input being injected into the VCSEL neuron. In this demonstration Kernels 1-2 are responsible for detecting vertical lines, with Kernel 1 detecting transitions from white-to-black pixels and Kernel 2 detecting black-to-white transitions. Kernels 3-4 were used to target horizontal features, with Kernel 3 detecting edges with white-to-black transitions and Kernel 4 detecting black-to-white transitions. Once injected into the VCSEL neuron its output was captured, demultiplexed and reconstructed to form (M-1) x (N-1) pixel maps. Experimental results for Kernels 1-4 are plotted in Fig. 5.5.4. The image reconstruction maps shown in Figs. 5.5.4 (a)-(b) & (e)-(f) depict the time series captured at the output of the VCSEL neuron as intesity colourmaps. In these maps yellow pixels reveal the firing of a spiking event by the VCSEL neuron; hence marking the presence of a target edge-feature in the source image. In the case of Figs. 5.5.4 (a) & (b) the colourmaps reveal the vertical edges of the 'cross' image indicating the vertical features were successfully identified by Kernels 1 and 2. In Fig. 5.5.4 (c)-(d) the pre-processed image input and the corresponding VCSEL neuron's response for pixel row 10 in (a) are plotted. Figure 5.5.4 (c) shows the image input contains a positive input of 4 and a negative input of 4, corresponding to each vertical edge of the cross pattern for that specific row of the image. Upon injection into the VCSEL neuron, the system activates a single spiking response for the positive pulse only. This indicates that the system is operating correctly and that only positive inputs can activate the spiking machanism in our neuromorphic system.

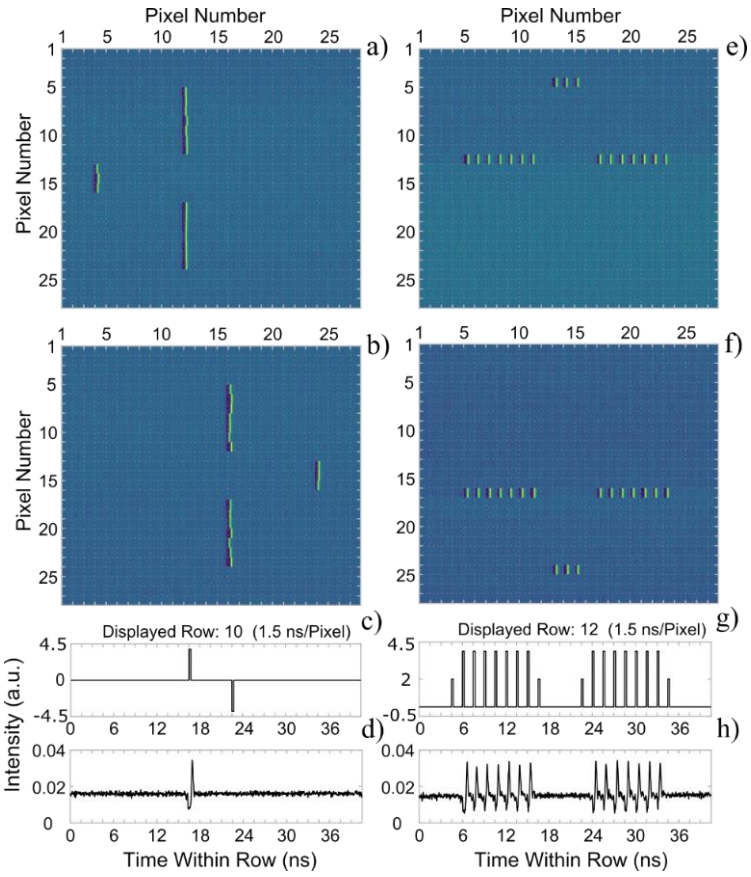

Figure 5.5.4. - Threhsold-and-fire responses from the VCSEL neuron when Kernels 1 (a), 2 (b), 3 (e) and 4 (f) are applied to the 'cross' source image. The pre-processed image input and recorded time series corresponding to the selected rows in (a) and (e), are plotted at the bottom of the figure. Input (c) and output (d) correspond to row 10 of (a). Input (g) and output (h) correspond to row 12 of (e). The pixel duration is set to 1.5 ns. Experimental parameters: I = 6.5 mA, T = 298 K, Orthogonal (XP) mode injection, P_{inj} = 152.7 μW, Δf = -4.58 GHz. Figure reproduced from [194].

Horizontal edge detection is also performed in Figs. 5.5.4 (e) & (f) using Kernel operators 3-4. Again in the reconstructed image maps, we see the successful activation of fast spiking events along both the rising and falling horizontal features. Unlike the vertical activations, the colourmaps do not form neat lines along the edges but instead appear as dotted/broken lines. This is a simple visual effect caused by the the short duration of the spikes (~100 ps) compared to the length of the pixel (1.5 ns), meaning the yellow spike does not fill the entire pixel. As before, Figs. 5.5.4 (g) & (h) plot the image input injected into the VCSEL neuron and the response from the

system for row 12 of Fig. 5.5.4 (e). In this example, as Kernel 3 is scanned horizontally across the 'cross' image, an input of multiple positive pulses is generated. Upon its injection into the VCSEL we find the system successfully activates for all the positive inputs of value 4, identifying the target features. The system correctly remains silent during the injection of half-amplitude inputs of value 2 (corner features). This result demonstrates that the system is effectively thresholding the different input values, allowing only inputs of value 4 to cross the activation threshold of the device. These results show that our experimental system is capable of performing a threshold-and-fire functionality when horizontal and vertical kernels (Kernels 1-4) are applied to a black and white digital image.

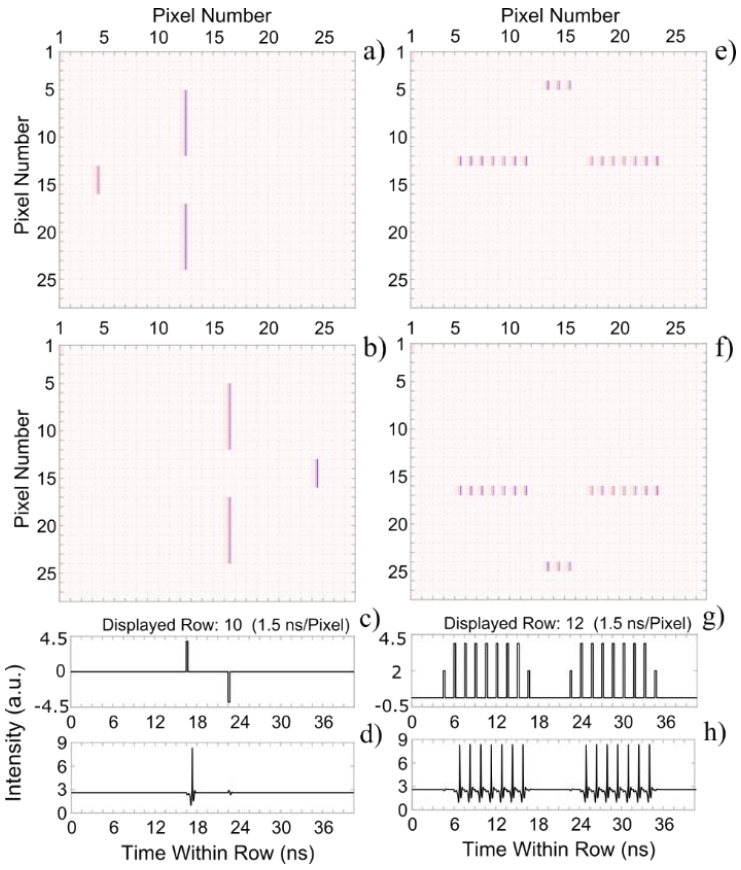

Figure 5.5.5. - Simulated response of the VCSEL neuron when Kernels 1 (a), 2 (b), 3 (e) and 4 (f) are applied to the 'cross' image using the SFM. Similar to Fig. 5.5.4, inputs and outputs are plotted for row 10 of (a) and row 12 of (e). Simulation parameters: γ_p =128 ns^{-1}, γ_a =2 ns^{-1}, γ_N =0.5 ns^{-1}, γ_s =110 ns^{-1}, α =2, k =185 ns^{-1}, k_{inj} =15 ns^{-1} and β_{sp} =10^{-5}. Figure reproduced from [194].

Using SFM-based simulations, the theoretical response of the VCSEL neuron to the injection of the same 'cross' source image was calculated. The theoretical results, plotted in Fig. 5.5.5, calculated using the same Kernels 1-4 as in the experiments, have white and blue colourmaps to help destinguish simulations from experimental measurements. The reconstructed numerical colourmaps (Figs. 5.5.4 (a)-(b) & (e)-(f)) show excellent agreement with the experimental findings, with the same number of spiking responses being activated when each individual kernel is applied. The simulated results present a similar spiking threshold to the experimental measurements avoiding the activation of corner pixels.

Additionally, the spiking frequency achieved by the numerical model showed good consistency with the experiment, enabling the edge-detection system to operate at 1.5 ns/pixel, allowing ~910,000 28x28 pixel images to be processed every second. Overall, a comparison of activated pixels in the simulated results to those measured experimentally gives a total pixel error of 0, with no false or absent detections present. The theoretical and experimental results therefore show a high level of consistency. These results demonstrate the VCSEL neuron can be used as a threshold-and-fire device, in tandem with convolution, for the generation of vertical and horizontal edge information in a fast spiking respresentation.

The application of individual kernels for complete image edge detection necessitates the running of multiple experimental inputs. However, it is possible to reduce the number of experimental runs required to reveal all edge information by performing gradient edge detection. The gradient of the source image, which reveals information about the rate of change of pixel intensity, can be used to detect features regardless of their directionality. By specifically calculating the magnitude of the gradient, we can create an input for our VCSEL neuron that identifies all pixel features that sufficiently cross the activation threshold of the device. The gradient magnitude can be calculated using Eq. 5.5.2:

$$\left|G\left(x,y\right)\right| = \sqrt{G_x^2 + G_y^2} \qquad \text{(Eq. 5.5.2)}$$

Where $|G(x,y)|$ is the gradient magnitude and G_x and G_y are the resulting convolutions of the source image with a horizontal and vertical kernel. Here the horizontal and vertical kernels are required to be 90º rotations of one another. The gradient magnitude of an image can therefore be calculated by combining two of the kernels used in the previous 'cross' image demonstration. By combining the results of Kernel 1 and 3 according to Eq. 5.5.2, we create the gradient magnitude to replace the destination pixel value in our pre-processed image inputs. This allows us to perform edge detection with gradient magnitudes in combination with our neuromorphic threshold-and-fire VCSEL system. In Fig. 5.5.6 the results for the gradient magnitude edge detection of the 'saltire' and 'IOP' images are plotted.

The experimental gradient magnitude edge detection of the 'saltire' (Fig. 5.5.2 (b)) source image is plotted in Fig. 5.5.6 (a). The results show that the VCSEL neuron triggered fast spiking responses for pixels containing diagonal features. The system is therefore capable of activating spiking outputs to detect different directionalities (in addition to vertical and horizontal features) as well as both black-to-white and white-to-black pixel transisitons without the requirement for multiple kernels, as shown in the experimental time series (Fig. 5.5.6 (c)). This indicates that the gradient magnitiude works correctly for the collection of all-edge information as no diagonal kernels were utilised, only Kernels 1 and 3 (vertical and horizontal operators) were combined according to Eq. 5.5.2. The theoretical response for the edge detection of the 'saltire' source image with gradient magnitude (Fig. 5.5.6 (b)) shows excellent agreement with the result obtained experimentally. The modelling detected all of the same diagonal features in the source image with experimental results proving 99.86% accurate to the theoretical findings. To further test the image gradient magnitude technique in tandem with our threshold-and-fire VCSEL neuron, the larger 50x50 pixel 'IOP' logo source image (Fig. 5.5.2 (c)) was run experimentally and simulated theoretically. Despite using this larger image containing curved and straight line features, the VCSEL neuron demonstrated (Fig. 5.5.6 (e) & (g)) its ability to identify every edge-feature in the image, regardless of directionality or shape. The larger 50x50 image only required the extension of the image input and a longer time series measurement to process the image, with pixel duration (1.5 ns/pixel) remaining consistent. Again, the numerically predicted VCSEL response (Fig. 5.5.6 (f)) showed

excellent agreement with the experimental results, yielding an accuracy of 99.67% when compared to the modelled result. The gradient magnitude edge detection technique can therefore be used in tandem with our threshold-and-fire VCSEL neuron to reveal all edge information in a source image, irrespective of its shape or directionality, within a single experimental run.

Overall these results show that our VCSEL neuron is capable of performing a neuronal threshold-and-fire functionality which we capitalise on to yield image edge-feature detection operation. Using TDM inputs and an offline pre-processing stage we are able to detect all edge-features in source images with kernel operators, activating sub-nanosecond optical spikes for positive target edge-feature recognitions. Our single VCSEL neuron system also demonstrated its capability to detect all image edge information using inputs pre-processed with image gradient magnitude. This allowed our system to threshold pulsed inputs and fire fast optical spikes for all edges in a single experimental run, removing the requirement for multiple kernels to achieve a complete detection. In both cases, pre-processing with individual kernels or pre-processing with gradient magnitude, experimental results showed excellent agreement with our numerical findings. The theoretical results confirmed both the successful edge detection capability and fast spiking rates achievable from our devices. In these results our system demonstrated operation at 1.5 ns/pixel, allowing the photonic edge detection of a 50x50 pixel images in 3.75 μs. We believe that this speed could be increased to achieved operation at 1 ns/pixel, in-line with the refractory period of these devices, however, even faster operation could be achieved by VCSELs with further increased spiking rates. Additonally, in our work a single VCSEL neuron is employed to perform the image processing task, helping reduce hardware complexity. It would however be possible to have multiple devices perform their neuronal functionalities in parallel, potentially peforming edge detection with different kernel operators, or even processing different sections or pixels of an image simultaneously. Such a system architecture would resemble more those of traditional CNNs, helping further improve processing speed.

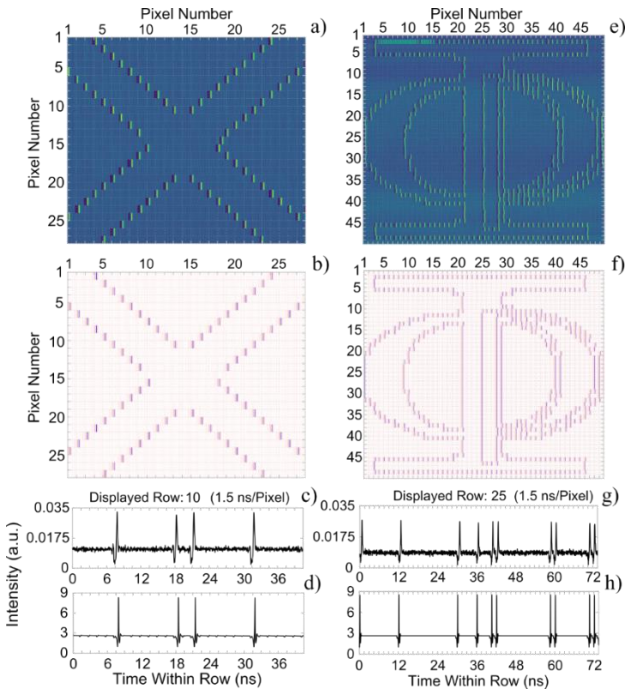

Figure 5.5.6. - Gradient magnitude edge detection results for 'saltire' (a-d) and 'IOP' logo (e-h) source images. Experimental (blue) and theoretical (white) responses are plotted in reconstructed image temporal maps (a,e) and (b,f), using the spiking responses at the VCSEL neuron's output. The experimental and theoretical time series of row 10 in (a) and (b) are plotted in (c) and (d). The experimental and theoretical time series of row 25 in (e) and (f) are plotted in (g) and (h). Experimental and theoretical parameters match those used in Figs. 5.5.4 and 5.5.5. Figure reproduced from [194].

The system in its current state does not perform in-system MAC operations (required for in-system convolution) and is the implementation of a single layer, capable of edge detection. We will explore and demonstrate the implementation of our VCSEL neuron system for traditional CNN tasks, such as image classification, in later chapters of this work. Finally, in this demonstration we use a 2x2 kernel operator, however, in this threshold-and-fire system the size of the kernel is flexible. Larger kernel sizes could be used in the pre-processing stage without issue as only the destination pixel value is encoded in the image input. This means the VCSEL sees no significant change of input when the size of the kernel is altered. These results therefore show that traditional image convolution tasks can be implemented alongside a threshold-and-fire VCSEL neuron to achieve edge-feature detection in a

fast optical spiking representation. This system is therefore a promising first step towards implementing VCSEL neurons in future photonic neuromorphic image processing systems for novel computer vision applications.

5.5.2 Binary Convolution for Image Gradient Magnitude

In our second demonstrator of a VCSEL neuron system for neuromorphic image processing, we apply what is known as binary convolution to reveal edge-feature information through image gradient magnitude. As mentioned previously, the traditional implementation of CNNs in electronic-based systems often requires the use of dedicated hardware such as mulitcore processors and graphical processing units [8], [273], [274]. This requirement is caused by the large number of convolution operations performed by CNNs, often imposing a vast computational expense on the system. This requirement might make CNNs unsuitable for implemetation into smaller platforms where power and speed may be limited. This is one of the reasons to investigate photonics for future CNN technology however, there are yet further changes we can make to remedy the computational expense of these systems. By altering the weights applied to each of the inputs in the CNN such that it holds a binary value, we can optimise and approximate traditional CNN operation. This process, that creates a binary CNN, has shown to provide a reduction in the memory requirements and a boost to operation speed (up x58 performance) when compared to traditional CNN operation [277]. There have been a number of optimised binary CNNs proposed for training processes and image classification tasks in literature [277]–[279]. Here, we propose and demonstrate an all-optical binary convolution system based on a spiking photonic VCSEL neuron. We also utilise a single VCSEL and TDM to realise an extremely hardware-friendly image processing system. The experimental setup used to implement the all-optical binary convolution is shown in Fig. 5.5.7. The all-optical binary convolution results shown here have been adapted from our recent publication [201].

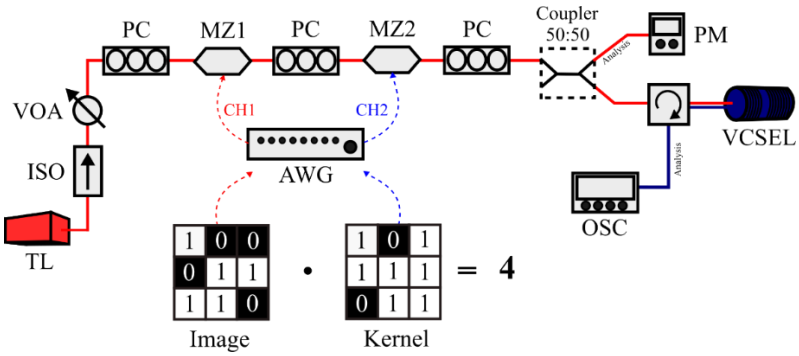

Figure 5.5.7. - Experimental setup used for all-optical binary convolution with a spiking VCSEL neuron. The system implements in series modulators (MZ1 & MZ2) to perform the kernel operation on the selected source image. The number of resulting spiking dynamics reveals the convolution outcome. TL – tuneable master laser, ISO – optical isolator, VOA – variable optical attenuator, PC- polarisation controller, MZ – Mach Zehnder intensity modulator, PM – power meter, OSC – oscilloscope.

The experimental all-optical binary convolution system implemented with a VCSEL neuron is fed information through two inputs. The two inputs pass respectively the information regarding the source image and the kernel operator to two Mach Zehnder intensity modulators (MZ1 & MZ2). The kernel operators hold weighting values of 0 and 1 only for this binary convolution system. The two MZs are connected in series within the optical injection setup, as shown in Fig. 5.5.7. The inputs representing the source image and kernel are generated using a 12 GSa/s AWG, amplified using electrical amplifiers, and fed to each MZ where they are encoded into the optical injection. Here, the MZ modulators are used in series within a single optical injection line to create a multi-level optical signal. This multi-level injection is required for the in-system convolution, responsible for the image edge detection process described graphically in Fig. 5.5.8. The use of a single optical injection line is also beneficial to the system as it enables simple optical injection locking (required for spike activation) and reduced hardware requirements, lowering setup complexity and cost. As in previous experimental arrangements, light from a tuneable laser is optically injected into our VCSEL neuron via a fibre-coupled optical isolator, attenuator, polarisation controllers and circulator. In this arrangement an additional polarisation controller was added to the setup to control the polarisation of the light entering the

second MZ (MZ2), maximising performance. The VCSEL used in this work was driven with a bias current of I = 6.5 mA at a stabilised temperature of T = 293 K. The device displayed parallel polarisation (YP) mode dominance when in solitary operation however, optical injection was made into the orthogonal (XP) mode of the device with a detuning of Δf = -5.64 GHz and power of P_{inj} = 127 µW.

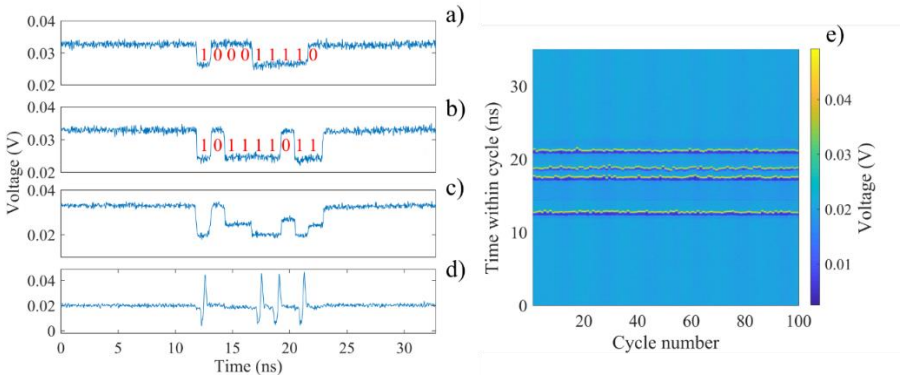

Figure 5.5.8. - An example of all-optical binary convolution with a spiking VCSEL neuron. A 3x3 image sub matrix (a) and a 3x3 kernel operator (b), are encoded in a single injection line creating a 3-level injection signal (c). Upon injection into the VCSEL neuron the spiking binary convolution (d) is produced, with the number of spikes totalling the final result. The temporal map for 100 consecutive responses (e) indicates the result reproduceability. Figure reproduced from [201].

Two-dimensional (2D) binary convolution calculations are now performed by the VCSEL neuron to reveal the edge-feature information of complex digital images. To do so an M x N kernel is element-wise multiplied with an M x N pixel neighbourhood from the source image, subsequently producing a weighted set of values. In our experiments, pixels and kernels are temporally encoded using rectangular pulses, with pulses of value '1' being encoded as intensity drops in the optical injection, and pulses of value '0' producing no modulation. An experimental illustration showing how the encoding of image and kernel data inputs is performed in this arrangement, is shown in Figs. 5.5.8 (a) & (b). The rectangular pulses used to encode image data and kernel inputs were set to a duration of 1.5 ns to align with the refractory period of the spiking dynamics of the VCSEL neuron. In the example of Fig. 5.5.8, 9 pulses are present in the time series to reproduce a 3 x 3 image sub matrix and kernel

operator inputs. In order to achieve the in-system binary convolution, both the image modulation and kernel modulation are required to overlap. As both signals were generated synchronously, we had to delay the generation of the kernel signal such that the image encoded signal had sufficient time to reach MZ2. The delay was introduced via the AWG and was equal to the time required for light to travel from MZ1 to MZ2. The resulting combined signal is shown in Fig. 5.5.8 (c). This three-level signal (low, medium and high) was injected into our VCSEL neuron. The experimental conditions are set for the system to remain injection-locked for the medium and high input intensity levels and to trigger fast optical spike outputs for the lowest intensity level. The VCSEL neuron would then fire a single fast spiking response for each pulse in the low level state as shown in Fig. 5.5.8 (d). Importantly, the number of fast spiking responses for every M x N set of input values, reveals directly the result of the all-optical binary convolution operation. In the example in Fig. 5.5.8, the result of the binary convolution is therefore 4. The VCSEL response to 100 consecutive three-level inputs is shown in the temporal map of Fig. 5.5.8 (e). The appearance of four straight lines indicates that the VCSEL can consistently activate the same spiking pattern, making the optical binary convolution results obtained with the VCSEL neuron reproducible. By sequentially injecting at different time instants all the pixels in a source image (using TDM), we can recreate a complete (binary) convolved image hereby revealing its target edge-feature information. This technique allows us to perform the binary convolution operation directly in the optical domain without pre-processing stages. Additionally, in this system, a spike does not directly indicate the detection of a target feature, instead, the number of spikes hold the result of the convolution operation. Hence, directly counting the number of spikes completes the MAC convolution operation. In this work we achieve this during software analysis of the time series collected at the output of the VCSEL neuron (post-experiment). It might in the future be possible to achieve this spike counting experimentally using spike/photon counting hardware.

In Fig. 5.5.8 a single kernel operator is applied. For the detection of all edge-features in a source image we can again calculate the gradient magnitude $G(x)$ of the image. Like the demonstration given in Fig. 5.5.6, the extraction of gradient magnitude can be achieved by combining the results of multiple binary kernel operations. In our

all-optical binary convolution system the following equations describes this process in more detail [280]:

$$G(x) = \sqrt{G_X(x)^2 + G_Y(x)^2} \quad \text{(Eq. 5.5.3)}$$

$$G_X(x) = (B(x) \otimes B_X^+) - (B(x) \otimes B_X^-) \quad \text{(Eq. 5.5.4)}$$

$$G_Y(x) = (B(x) \otimes B_Y^+) - (B(x) \otimes B_Y^-) \quad \text{(Eq. 5.5.5)}$$

$$B(x) = \sum_{p=0}^{N-1} s(i_p, i_x) \cdot 2^p \quad \text{(Eq. 5.5.6)}$$

Here $G_X(x)$ and $G_Y(x)$ are made up of a total of four binary convolutions, $B(x) \otimes B_{X,Y}^{\pm}$, according to Fig. 5.5.9. These four binary convolutions can be combined according to Eq. 5.5.3 to reveal the gradient magnitude information $G(x)$ of the image. $B(x)$ represents the 5x5 pixel neighbourhood (see Fig. 5.5.9 (b)) of pixel x in the 'square' source image (Fig. 5.5.9 (a)). Due to binary weighting, a kernel operation can be thought of as a sampling of $B(x)$ with a local pattern descriptor. Within this local pattern descriptor (Fig. 5.5.9 (c)) 4 smaller segments, $B_X^+, B_Y^+, B_X^-, B_Y^-$, correspond to the 4 kernel operations required for gradient magnitude calculation. Each individual kernel operator therefore only requires a small 2x5 range of the pixels sampled from the 5x5 pixel neighbourhood. The local pattern descriptor is set using i_x, i_p (the intensity of pixel x and the intensity of its pth neighbour respectively) and a comparison function $s(i_p, i_x)$.

$$s(i_p, i_x) = \begin{cases} 1 & if \left| i_p - i_x \right| > T_x \\ 0 & otherwise \end{cases} \quad \text{(Eq. 5.5.7)}$$

The comparison function uses the pixel intensity threshold $T_x = 0.25i_x + 20$ to convert the image intensity values into N binary values (N = 5 x 5 -1). Of the N pixels within

range of the pattern descriptor, only 16 pixels in total require sampling as 8 pixels are given descriptor values of 0. This reduces the number of pixels that require sampling, improving speed and efficiency. The 24x24 pixel source image used in this experimental demonstration is that of a black square on a white background (Fig. 5.5.9 (a)). The intensities of the white and black pixels in the greyscale 'square' image are 255 and 0, respectively.

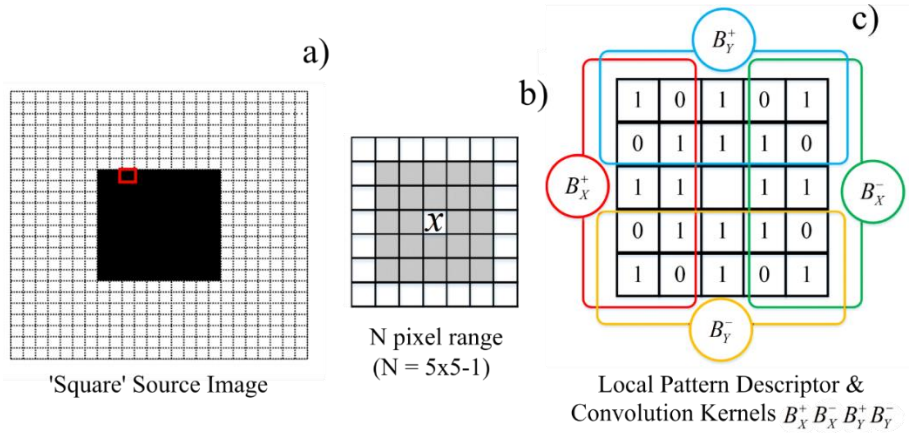

Figure 5.5.9. - The 'square' source image and the local binary pattern descriptor applied to the image. The 'square' source image (a) is 24x24 pixel white background with a 10x10 pixel black square. The local pattern descriptor (c) indicates the weights and hence pixels sampled. The highlighted sections are used to calculate each kernel operator, $B_X^+, B_Y^+, B_X^-, B_Y^-$. *N* pixels (grey) fall within the range of the local pattern descriptor (b), when centred around pixel *x*. Figure reproduced from [201].

Selecting the red-highlighted black pixel in the 'square' source image, we get an intensity of $i_x = 0$. Serialising neighbouring pixels in columns, for the 1st neighbour we get an intensity of $i_p = i_1 = 255$, hence $s(i_1, i_x) = 1$. However, for the 3rd neighbour we get an intensity of $i_p = i_3 = 0$, hence $s(i_3, i_x) = 0$. If we sample all *N* pixels in the range of the local pattern descriptor for red-highlighted pixel *x* we get:

$$B(x) = \begin{bmatrix} s(i_1,i_x) & - & - & - & s(i_{20},i_x) \\ s(i_2,i_x) & - & - & - & s(i_{21},i_x) \\ s(i_3,i_x) & - & x & - & s(i_{22},i_x) \\ s(i_4,i_x) & - & - & - & s(i_{23},i_x) \\ s(i_5,i_x) & - & - & - & s(i_{24},i_x) \end{bmatrix} = \begin{bmatrix} 1 & 1 & 1 & 1 & 1 \\ 1 & 1 & 1 & 1 & 1 \\ 0 & 0 & x & 0 & 0 \\ 0 & 0 & 0 & 0 & 0 \\ 0 & 0 & 0 & 0 & 0 \end{bmatrix}$$

In the case of $B(x)$, white pixels have a value of 1 and black pixels have a value of 0. The kernel operators adopted in this work are highlighted in Fig. 5.5.9 (c). $B(x)$ here corresponds directly to a thresholded pixel neighbourhood of the image. The kernel operators are then applied to $B(x)$ with any pixels falling outside the kernel given a value of 0. The kernel operator B_X^+, when operating on N sampled pixels is also shown.

$$B_X^+ = \begin{bmatrix} 1 & 0 & 0 & 0 & 0 \\ 0 & 1 & 0 & 0 & 0 \\ 1 & 1 & 0 & 0 & 0 \\ 0 & 1 & 0 & 0 & 0 \\ 1 & 0 & 0 & 0 & 0 \end{bmatrix}$$

Serialising both the kernel and the sampled image in columns we can obtain N value strings for $B(x) = (1,1,0,0,0,1,1,0,0,0\ldots)$ and $B_X^+ = (1,0,1,0,1,0,1,1,1,0\ldots)$. However, many of the N values within these strings are redundant, as their value will always be zero. For this reason, we shorten each string and select the 10 values in which the kernel operator was applied. The shortened strings were then used to generate pulsed inputs similar to Figs. 5.5.8 (a) & (b). Each pulse had a 1.5 ns duration, creating a 15 ns long input for every time-division multiplexed pixel in the edge detection task. The calculation of the gradient magnitude $G(x)$ requires four binary convolutions therefore four sets of image submatrices and kernel operators were created to each be injected into the all-optical system. The dimensions of the final image were reduced following the binary convolution. This is the result of edge and corner pixels not having sufficient neighbours to apply all the kernels effectively [281].

It should be noted here that if, as mentioned briefly, only 16 pixels are sampled from the original image (as opposed to sampling N) then each kernel, $B_X^+, B_Y^+, B_X^-, B_Y^-$, will have only 6 values to operate on. This would in turn reduce the length of each string to 6, making it possible to perform the same convolution in 9 ns as opposed to 15 ns. For demonstrational purposes, in the following we show experimental results that use 10-value strings and inputs. The experimental binary convolution results for the red-highlighted pixel are plotted in Fig. 5.5.10. For the example case of the B_X^+ kernel operator we find the result of the binary convolution is 2, with both the first and seventh inputs generating a sub-nanosecond spiking response (Fig. 5.5.10 (a)). This

result is as expected and is consistent with $B(x) \otimes B_X^+$. The results for the remaining kernel operators (B_Y^+, B_X^-, B_Y^-) produce binary convolution results of 6, 2 and 0 respectively. Using the experimental results for the red highlighted pixel we find that $G(x)$, $G_X(x)$ and $G_Y(x)$ calculate as 6, 0 and 6 respectively, using Eqs. 5.5.3-5.5.5.

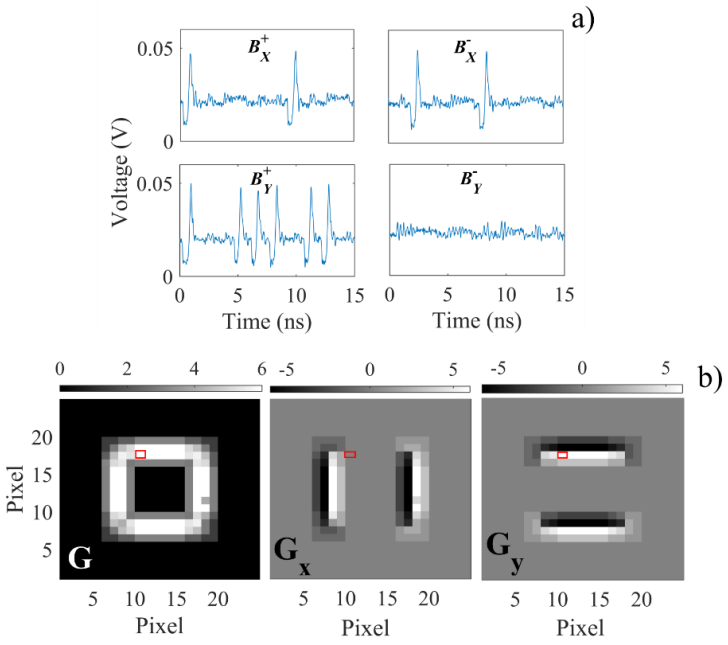

Figure 5.5.10. - Experimental binary convolution results for the red-highlighted pixel in the 'square' image for each kernel operator $(B_X^+, B_Y^+, B_X^-, B_Y^-)$ and the complete gradient map reconstructions. Experimental parameters: I = 6.5 mA, T = 293 K, Orthogonal (XP) mode injection, P_{inj} = 127 μW, Δf = -5.64 GHz. Figure reproduced from [201].

Experimentally repeating the process for all the pixels in the 'square' image, by means of TDM, we measure and calculate the gradient magnitude of each pixel and plot the final results in gradient maps (see Fig. 5.5.10 (b)). These reconstruct the source image, using the gradient magnitude to plot and reveal changes in pixel intensity and highlight edge information. We can see in the $G(x)$ plot (Fig. 5.5.10 (b)) the 'square' appears hollow, indicating the four edges of the square were successfully detected. The resolution of the edge information in the gradient maps can be further enhanced by filtering $G(x) > 3$. This helps by thinning white lines to better reveal the locations of true edges where large pixel intensity changes occur. Additionally, the gradient maps of $G_X(x)$ and $G_Y(x)$, calculated from the experimentally measured

response of the VCSEL neuron are plotted in Fig. 5.5.10 (b). These gradient maps reveal that the horizontal and vertical features of the 'square' source image can also be individually detected, meaning specific kernel operators can still be used to search for target edge-features. Running the four binary convolutions in our all-optical experimental setup has therefore demonstrated it can successfully identify edge information in a digital image via gradient magnitude calculations.

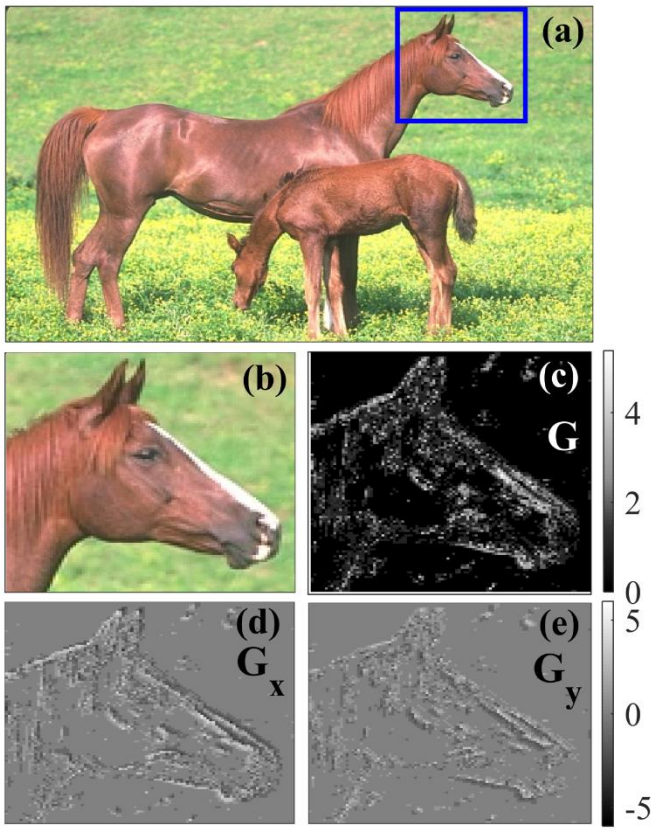

Figure 5.5.11. - The 'Horse' source image and resulting experimentally measured gradient maps. The original 'horse' image (a) was sampled to create a smaller 100x105 pixel 'Horse head' image (b). The experimentally obtained gradient maps plot the final gradient magnitude $G(x)$ (c) as well as the vertical $G_X(x)$ (d) and horizontal $G_Y(x)$ (e) components. Experimental parameters were identical to those used previously in Fig. 5.5.10. Figure reproduced from [201].

To further test the capability of our experimental system we selected a more complex source image (Fig. 5.5.11 (a)) from the Berkeley Segmentation Dataset [56]. A 100x105 pixel portion of the 'horse' image was selected (Fig. 5.5.11 (b)) for binary

convolution with our VCSEL-based all-optical photonic spiking system. This smaller portion was selected to help keep the experimental demonstration within the useable memory of the oscilloscope. The 'horse head' image was converted from RGB to greyscale before the same experimental procedure, used previously in the 'square' image experiment, was applied. The four sets of image and kernel operators were encoded into the optical injection and the temporal response of the VCSEL neuron was recorded. The number of fast spikes from the VCSEL neuron was counted for each pixel and the resultant gradient maps were plotted (Fig. 5.5.11 (c)-(e)). The gradient maps reveal that even in the larger, more complex image, the optical binary convolution system still successfully reveals the outline and shape of the horse head. The system also reveals it can detect some smaller detail in the image including; the stripe along the nose of the horse, parts of the mane and the cheek bone. The gradient map does however reveal the detection of background features within the image, such as the darker spots of grass behind the horse. This level of detail indicates that the current all-optical binary convolution system, based on a spiking VCSEL neuron, is capable of performing image gradient magnitude. The tuning of the activation threshold would permit to reduce low gradient magnitude activations, if desired.

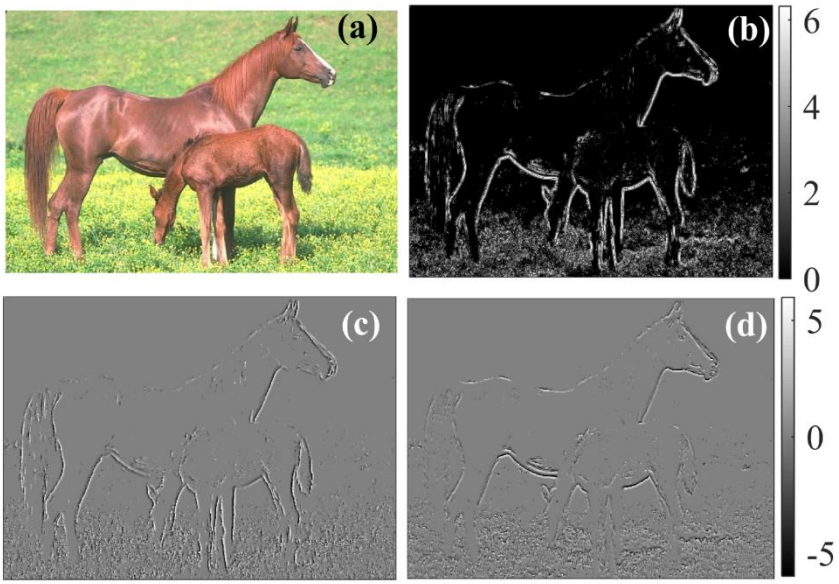

Figure 5.5.12. - Horse source image (a) from the Berkeley Segmentation Dataset and numerically simulated gradient maps for $G(x)$ (b), $G_X(x)$ (c), $G_Y(x)$ (d). Theoretical parameters: γ_p =128 ns^{-1}, γ_a =2 ns^{-1}, γ_N =0.5 ns^{-1}, γ_s =110 ns^{-1}, α =2, k =185 ns^{-1}, k_{inj} =125 ns^{-1} and β_{sp} =10^{-6}. Figure reproduced from [201].

To further reinforce the experimental all-optical binary convolution results, the SFM was used to numerically simulate the response of the VCSEL neuron. Using the same theoretical model described previously in Chapter 2.3, the predicted all-optical binary convolution of the full 'horse' image by the VCSEL neuron was computed. The simulated input remained consistent with the experimental system, using 10 pulsed inputs of 1.5 ns duration per pixel. The theoretical response of the VCSEL neuron to the four sets of inputs was then used to calculate the gradient magnitude, resulting in the gradient maps presented in Fig. 5.5.12. The gradient maps show that edge information is successfully revealed in the theoretical simulations, and that a good level of agreement is found between experimental and theoretical responses.

We also tested numerically the performance of the proposed binary convolution system to noisy inputs. The response of the VCSEL-based system to the example image and kernel inputs demonstrated in Fig. 5.5.8, were calculated using the SFM. The results in Fig. 5.5.13 show that in the case of no input noise (left row in Fig. 5.5.13), the simulated system responds with the expected result, i.e. 4 fast spike activations (as it was found experimentally in Fig. 5.5.8). After this, we tested numerically the response of the system to image and kernel inputs with a signal to noise ratio (SNR) of 20 dB, as seen in the right row plots in Fig. 5.5.13 (a) & (b)). For the case of noisy inputs, the simulated results also show that the result of the convolution remains the same, with 4 spikes activated. The proposed all-optical binary convolution system is therefore resilient to noisy inputs suggesting that in the experimental system, the exposure to electrical or optical noise should not significantly affect the activation of target features.

Overall, the all-optical binary convolution system demonstrated experimentally in this work, is capable of revealing gradient magnitude and edge information in both simple and complex images. Additionally, we have provided the theoretical modelling of the system using the SFM, revealing a good level of agreement with experimental findings.

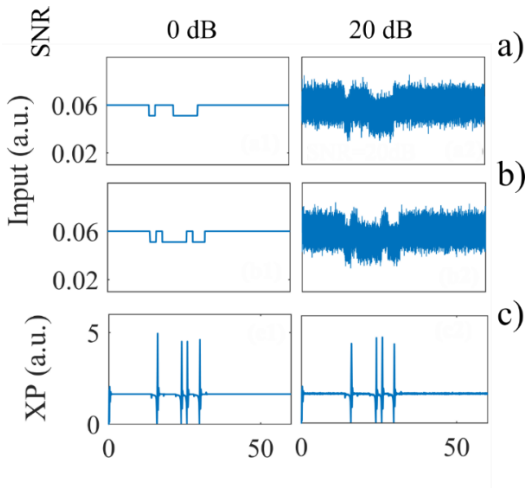

Figure 5.5.13. - Theoretical binary convolutions with noisy inputs. The image inputs (a) and kernels (b) with no noise (left) and 20 dB SNR (right) produce the same VCSEL output (c). Figure reproduced from [201].

In these experimental and theoretical demonstrations, a time of 15 ns is required to perform the optical binary convolution operation of one pixel. With four binary convolution operations required to reveal the image gradient magnitude, a total of 60 ns is needed to process one pixel completely. Considering that the VCSEL used in the experiments may deliver approximately 0.5 mW of optical power, we can deduce that the energy consumption for the calculation of gradient magnitude with a VCSEL neuron could be as low as 30 pJ (0.5 mW x 60 ns) per pixel, using commercially-sourced devices without any additional optimisation stage. Furthermore, given the local pattern descriptor, if we sampled the minimum 16 pixels, we could perform each binary convolution in 9 ns, further reducing the energy consumption to 18 pJ per pixel. Alongside the encouraging energy consumption levels, the reduced number of convolution operations in comparison to traditional convolution helps improve system's performance. Where traditional convolution would require the sampling of all 25 pixels in the 5x5 range of the kernel, we need only 16, with 6 pixels being used for each of the 4 kernel operations. A recent report in literature [280], where binary convolution was compared to the Canny implementation of convolution [282] when producing image gradient maps, showed the improvement in speed that can be gained. The binary convolution was able to perform the image processing task at 4.7

Hz with the Canny technique producing an operation speed of 0.5 Hz. This report also made use of a intel i7 mobile processor that operates with several watts of power (15 W in the case of the i7 [283]). This indicates that the binary convolution technique can be faster than alternative convolution methods and that our photonic all-optical system has the potential to increase binary convolution energy efficiency significantly. Overall, we demonstrate here a simple, hardware friendly system capable of image edge detection via image gradient magnitudes with a single VCSEL neuron. In this, our second implementation of image processing and edge detection, we perform the kernel operation, thresholding and spike firing within the optical system with our VCSEL neuron. In this work the counting of spiking responses is completed offline, but we believe this could be achieved using the appropriate hardware in the future. Unlike other impressive, but complex, photonic binary CNNs [284], our experimental setup is easily approachable, containing only off-the-shelf commercial components, delivering a fast, spiking output directly at the telecommunication's wavelength of 1300 nm. We have also demonstrated that the system can be resilient to noisy inputs and that this binary convolution system holds key advantages in terms of energy consumption and operation speed. We believe this method of implementing VCSEL neurons as image processing devices demonstrates the high prospects for VCSEL-based platforms for novel application in edge detection and computer vision systems.

5.5.3 Integrate-and-Fire Image Feature Detection

In our third and final implementation of VCSEL-based neuromorphic image processing systems, we look to make use of the multiple input integration functionality present within VCSEL neurons for all-optical operation. In this configuration, referred to here as the integrate-and-fire method, we build upon the initial threshold-and-fire technique by incorporating bursts of consecutive input pulses. This method allows for the complete embedding of the convolution operation into the photonic system as we reported in [202]. Again, unlike alternative reports of photonic CNNs [81]–[83], [275], [276] we make use of a system built with only a

single VCSEL neuron, using time-multiplexed kernel operators to perform complete image edge detection with reduced hardware complexity and expense.

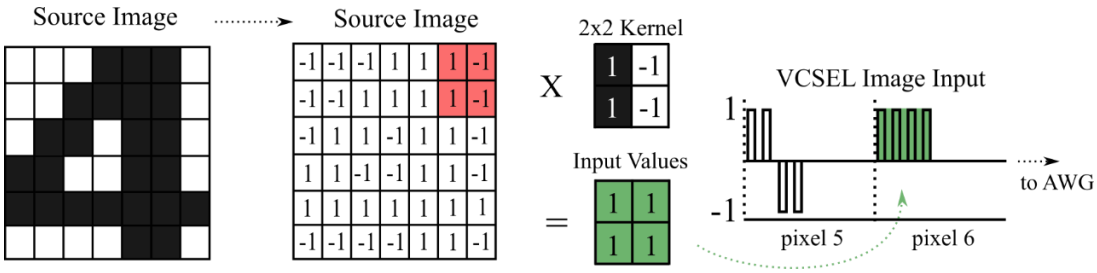

Figure 5.5.14. - Integrate-and-fire image processing technique applied to images in the VCSEL neuron system. A source image is converted into binary values and multiplied by a 2x2 kernel, creating a Hadamard (elementwise) product. The resulting 2x2 product is used as a set of values for the generation of a return-to-zero (RZ) image input, where each value dictates the amplitude of a pulse within a configurable pixel duration. The process is repeated, scanning the kernel operator across the entire image, time-multiplexing the input for each pixel. Figure reproduced from [202].

The technique applied to achieve integrate-and-fire image edge detection draws a number of similarities to that described in Fig. 5.5.3. Source images are selected and converted into black and white integers, and 2x2 kernel operators are applied to the source images using the same scanning window method as in previous realisations to produce Hadamard products for each image pixel. In this work, as shown in Fig. 5.5.14, we demonstrate for the first time the in-system integration ability of a VCSEL neuron to perform the pooling of the Hadamard product. To achieve this, we encode the weighted pixel values into a (return-to-zero) RZ signal, where each value is assigned an individual pulse. Each encoded input pulse has an amplitude corresponding to its Hadamard product value and a duration of ~100 ps FWHM. A peak-to-peak separation of ~150 ps is used between input pulses with zero padding also added to fill the total pixel time duration up to a configurable value. In this work a pixel duration of 3.0 ns was selected. This value, well over the spiking refractory period of the VCSEL neuron, allowed each pixel to independently activate spiking outputs. This encoding scheme effectively makes use of TDM to encode the Hadamard product into a burst of input pulses, while also encoding multiple

convolution operations sequentially into a single device, making the VCSEL neuron act in effect as a full neuronal layer able to directly perform complex operations, such as image-feature detection. The encoded image input is then generated in the AWG and fed via optical injection into the VCSEL neuron, using the same experimental setup described previously in Fig. 5.5.3. We highlight here that the pre-processing of the encoded image input incorporates the matrix multiplication operations of pixels values and kernel operators. In this demonstration the optically-injected VCSEL is incorporated as an integrate-and-fire neuron which accumulates the results of these matrix multiplications via time-multiplexed input pulses.

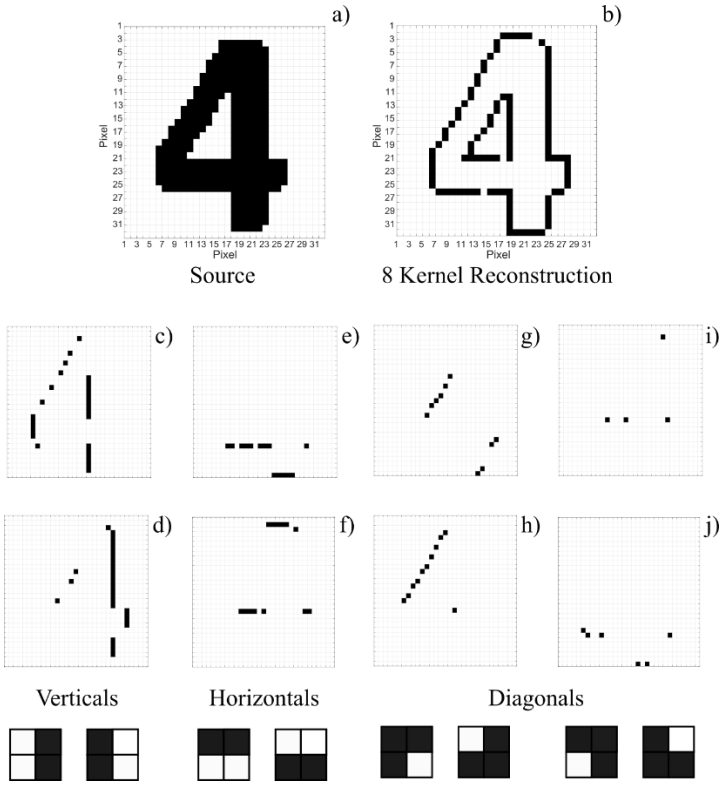

Figure 5.5.15. - Experimental edge detection with an integrate-and-fire VCSEL neuron. The 32x32 pixel image of a printed “Digit 4” (a) is operated on by 8 different 2x2 kernels (c)-(j). Two vertical (c)-(d) and horizontal (e)-(f), as well as four diagonal (g)-(j) kernels are shown. The final 8 kernel reconstruction (b) reveals all edges in the image. Each plot is created by de-multiplexing the time series of the VCSEL neuron, plotting pixels with a positive spike activation (recognition) in black. Experimental parameters: I = 4.0 mA, T = 293 K, Parallel (YP) mode injection, Pinj = 112.6 μW, Δf = -7.6 GHz. Figure reproduced from [202].

For the first demonstration of integrate-and-fire edge-feature detection with a VCSEL neuron, we run multiple kernel operators on the 32x32 pixel image of a printed “Digit 4”. The source image pixel data, plotted in Fig. 5.5.15 (a), is first converted into integer values before applying the kernel operators. Due to the 2x2 kernel dimension, two kernels were required to activate each side of the vertical and horizontal features. Similarly, no padding was used on the source image, resulting in the reduction of the final image dimension by 1. The kernel operators used on the “Digit 4” image applied integer, 1 (black) and -1 (white), weights. The operation with each kernel produced a bursting image input which was subsequently generated by the AWG, optically encoded with a MZ modulator into the optical input line, and injected into the VCSEL neuron. The optical spiking responses of the VCSEL neuron were captured with a fast real-time oscilloscope and analysed using temporal maps. These de-multiplexed the captured time series into the appropriate number of image rows and columns. Finally, 3.0 ns segments (the configured pixel duration) were sampled from the temporal maps to reveal which pixel inputs had activated spiking responses. If a spiking response was present (not present), a black (white) pixel was plotted in a final image reconstruction. The convolution results for vertical and horizontal kernel operations are plotted in the 31x31 pixel reconstructions shown in Figs. 5.5.15 (c)-(f). The latter clearly show the identification of both the vertical and horizontal edges of the “Digit 4”. This means each kernel operator correctly produced a Hadamard product corresponding to a burst of 4 positive input pulses for each target feature. When integrated by the VCSEL neuron, the bursts overall input contribution has sufficient strength to cross the activation threshold of the device, producing a spiking response for each target feature. Similarly, additional kernel operators were used to reveal the diagonal edges of the four. The diagonal kernel operators had non-integer weights with values 0.5, 0.75, 0.75 and -1 (and the three rotations) respectively. The results of the diagonal integrate-and-fire convolutions, shown in Figs. 5.5.15 (g)-(j), clearly show the diagonal edges, as well as additional features such as corners, of the “Digit 4” are successfully identified. Therefore, using all eight experimental runs, we can combine the convolutions into a single 8 kernel reconstruction (Fig. 5.5.15 (b)), revealing all edge information present in the source image. The optical technique presented here, with our integrating VCSEL neuron, is

therefore capable of providing edge detection functionality, where the photonic system performs the summation or pooling of convolved values with optical hardware.

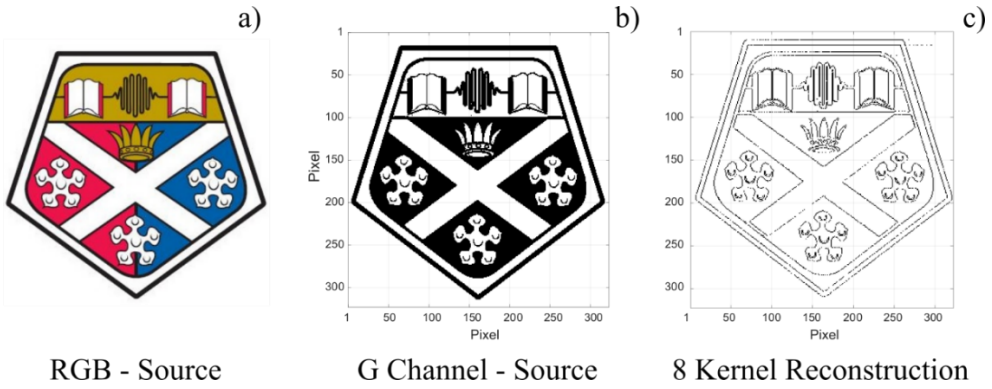

Figure 5.5.16. - All-optical edge-feature detection of the RGB 323x323 pixel "University of Strathclyde (UoS) crest" by the VCSEL neuron (a). The green (G) colour channel of the image was selected (b). Experimental results from 8 2x2 kernel operators combined to produce the final reconstruction (c), revealing all edges in the image. Experimental parameters: I = 4.0 mA, T = 293 K, Parallel (YP) mode injection, Pinj = 147.2 μW, Δf = -6.88 GHz. Figure reproduced from [202].

To continue testing the capability of our all-optical VCSEL neuron system we selected a higher resolution 323x323 pixel RGB image of the University of Strathclyde's (UoS's) crest (Fig. 5.5.16 (a)). This image, containing more complex features, has three colour channels, red, green and blue (RGB). Typically, the conversion of an RGB image to greyscale can be completed by averaging over the pixel intensity of each channel, however, by selecting a specific channel we can enhance the contrast of the black and white image, simplifying the edge detection. For this reason, the green channel was selected before conversion to greyscale, and subsequent conversion into black and white pixels (Fig. 5.5.16 (b)). Using the same 8 kernel operators as in the previous demonstration (Fig. 5.5.15), 8 unique image inputs were calculated and generated for injection into the VCSEL neuron. The results of the 8 experimental convolutions are combined into the kernel reconstruction plotted in Fig. 5.5.16 (c).

From Fig. 5.5.16 (c) we can see that the edge detection of the "UoS's crest" image successfully revealed edge-features of every directionality. Horizontal, vertical and diagonal lines were all recognised by their respective kernel operators, each successfully creating and integrating burst of input pulses, producing fast spiking responses. From this result we can deduce that the size and complexity of the image does not impede the operation of the photonic spiking edge detection system. In this demonstration the configurable pixel duration remained 3.0 ns per pixel. For this reason, the larger image only required a longer processing time and a larger time series measurement to successful complete each experimental convolution (3.0 ns x 322 x 322 = 311.1 µs per convolution). This result means that complete edge detection of this larger image can be accomplished in 2.5 ms, with up to 400 images of this resolution possible every second, despite the utilization of a very simple and highly hardware friendly approach using a single commercially-available VCSEL.

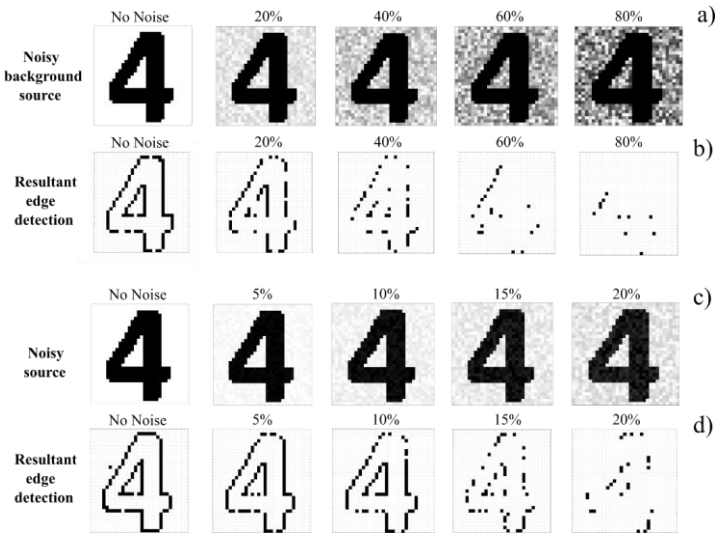

Figure 5.5.17. - Spiking edge-feature detection with the VCSEL neuron with noisy source images. Noise was introduced to the "Digit 4" image using random variations of background-pixel (a)-(b), and global-pixel intensity (c)-(d), where 100% noise represents a random intensity variation from white (-1) to black (1). 8 2x2 kernels are run sequentially for complete edge detection. Experimental parameters are identical to those used in Fig. 5.5.15. Figure reproduced from [202].

The all-optical edge-feature detection performance of the integrate-and-fire VCSEL neuron was next tested with noisy source images. Noise was added to the printed "Digit 4" source image in two ways:

1) In the first method, noise was added into the intensity of the white background pixels, varying each white pixel randomly between its current value (-1) and a percentage (%) of the maximum intensity value (1). For a background noise of 100% we therefore expect white pixels to vary randomly between white (-1) and black (1). Background noise levels of 0%, 20%, 40%, 60% and 80% were implemented into the source images as shown in Fig. 5.5.17 (a).
2) In the second method, the global pixel intensity was varied according to the configurable noise percentage (%). In this case, 100% noise would cause white pixels to vary randomly varied between white (-1) and black (1), and black pixels to randomly vary between black (1) and white (-1). Global noise was varied from 0% to 5%, 10%, 15% and 20%, as shown in Fig. 5.5.17 (c).

In both cases investigated, 8 (2x2) kernels were applied to each source image with each convolution operation sequentially generated into a single temporal input. This allowed us to perform complete edge-feature detection with just one VCSEL neuron, acting in fact as a full neuronal layer, in a single experimental run. Therefore, the weights of the kernel operators had to be altered such that the activation threshold was consistent for all integrating bursts. This is required as the maximum integrated input for a diagonal kernel is 3 (1+0.75+0.75+0.5) and the maximum integrated input for vertical and horizontal kernels is 4 (1+1+1+1). The maximum integrated input was therefore normalised by adjusting the vertical and horizontal kernel weights to the non-integer value of 0.75, such that 0.75+0.75+0.75+0.75 = 3. This allowed all integrated bursts throughout the 8 convolutions (for all kernels used) to activate the desired spiking outputs with the same activation threshold of the VCSEL neuron. Finally, the convolutions of all 5 noisy images were combined into a single image input, using TDM. This meant that the activation threshold for spiking edge detection was consistent across all tested images and that all could be tested in one

experimental run. The spiking responses of the system were measured and analysed, producing the 8 kernel reconstructions shown in Figs. 5.5.17 (b) & (d).

Looking at the case of increasing image background noise (Figs. 5.5.17 (a) & (b)), we find that initially the system responds as expected, revealing all edges in the noiseless image. This result highlights that the normalisation of all kernel weights used correctly allows each target feature to integrate inputs bursts and activate spiking responses when all data is fed in a single experimental run. When the background noise in the image is increased to 20%, we see that most diagonal and vertical activations remain intact, with the number of horizontal detections dropping (25.9% less activations overall). This indicates that input bursts, generated by horizontal kernels, are integrating less effectively than of others and are therefore not activating as frequently. This discrepancy is likely caused by the horizontal scanning of the kernel operator during the convolution, which creates positive detections in consecutive pixels. The constant activation of excitable spikes may slightly reduce the influence of pulsed inputs in the following pixel, resulting in a small drop in integration efficiency compared to other kernel operators. Nevertheless, the 'four' shape can still be recognised as horizontal, vertical and diagonal features remain detected. Increasing the background noise to 40%, we see the number of detections reduce overall (57.7% less activations), however, sufficient horizontal, vertical and diagonal features still remain, allowing the digit to be recognizable. Yet further increasing the background noise of the image to 60%, we see that the detection of almost all vertical and horizontal edges are lost, with a total 79.8% reduction in spike activations. The detection of mostly diagonal features is achieved in this result, but this is not unexpected. The diagonal kernels are built with 3 black-pixel and 1 white-pixel detecting value. This means that the changes to background noise only apply to 1 of 4 values present during the kernel operation, compared to 2 of 4 in the vertical and horizontal operation, making the diagonal kernel more resilient to background noise. Despite this, the image becomes unrecognisable, and performance further decreases as background noise reaches 80%. These results in any case show that without altering the activation threshold of the spiking system (VCSEL neuron), recognition of target features can still be achieved up to levels as high as 40% background noise.

The results for globally increasing pixel noise are shown in Fig. 5.5.17 (d). Again, as expected, when an image without noise is injected, the experimental results show successful spike-firing detection for all edge-features of the "Digit 4". Increasing the global noise to 5% and 10%, reveals a good level of performance overall, with the number of horizontal detections reducing by 11% and 20.1%, similar to the previous case of growing background noise. Increasing the global noise further to 15% causes the number of detections for vertical, horizontal and diagonal edges to all drop overall (52.2% less activations). The image however, contains enough feature information to recognise the image as a "Digit 4". Finally, increasing global image noise to 20% removes almost all feature detection (76.1% less activations) as now varying pixel intensities fail to match the kernel operator, creating input bursts incapable of spike activation. Unlike the background noise case, diagonal kernels do not show additional resilience as they are equally affected by the global noise. These results show that source images can be influenced by a pixel intensity variation of at least 15% before kernel operators (set for noiseless images) fail to recognise target features.

Overall, this all-optical spike-based approach to image processing with an integrate-and-fire VCSEL neuron has demonstrated that it can successfully perform edge-feature detection tasks on large complex images at high speed rates, and with high noise robust operation. It has also demonstrated that despite utilizing a highly hardware-friendly approach using a single spiking VCSEL neuron and TDM, it can perform distinct kernel operations on multiple complex images.

Additionally, we have further tested the integrate-and-fire VCSEL neuron system using large numbers of images from the MNIST handwritten digit database [285]. The latter's significance is that no two of the images are the same, making it more challenging for classification systems to identify which of the 10 classes (0-9) an image belongs to. For this study, a total of 5000 28x28 pixel images of digits 0-9 (500 per digit) were tested in our system, with each image subject to convolution operation by 6 symmetrical kernel operators. TDM was used to sequentially perform each kernel operation on all 500 images (per digit) in a single experimental run.

An example of the experimental results obtained with a (digit 4) MNIST image and its 6-kernel reconstruction are shown in Figs. 5.5.18 (a) & (b). Additional results for different digits are also plotted in Fig. 5.5.18 (c). These results show that the spiking VCSEL neuron system can successfully generate edge-feature image information with the MNIST input data. The use of symmetrical kernel operators and binary weights allow all integrating bursts to successfully activate for all 500 consecutive images that were injected in a single experimental run. Utilising TDM to compute different kernel operators sequentially over consecutive source images, permitted the single VCSEL neuron system to perform complete edge-feature detection of 500 MNIST images in 6.56 ms (3 ns x 27 x 27 x 6 kernels x 500 images). This speed, 13.12 μs per MNIST image, achieved with commercially-sourced VCSELs, without any additional device optimization, is theoretically limited by the refractory period of the spiking dynamics in the VCSEL neuron (approx. 1 ns in our case). Hence, further speed operation improvements are possible simply by reducing the total pixel time duration, currently set at 3 ns to values closer to the spiking refractory period (approx. 1 ns). Also, additional optimization of VCSEL design and fabrication might permit to increase the spiking rate of VCSEL neurons, beyond those currently reported here, and hence allow higher speed spiking edge detection operation.

In addition, we combined our VCSEL neuron spiking edge detection system with a software implemented spiking neural network (SNN), in order to perform digit classification with the processed images of MNIST handwritten digits. The software SNN was fed directly the temporal spiking edge-feature information produced by the VCSEL neuron, which in fact acted as a full neuronal layer implemented in photonic hardware. The software SNN then performed further spiking convolution and pooling operations to provide a classification for each tested MNIST source image. The structure and operation of the software SNN is detailed in our recent literature report [202] and was designed and operated by colleagues in Dr Gaetano di Caterina's group in Strathclyde's Electronic and Electrical Engineering (EEE) department. This architecture, combining photonic (VCSEL-based) hardware and a software-implemented SNN, revealed successful image classification, with a very high mean 'handwritten digit' recognition efficiency of 96.1%. This exciting result indicates the feasibility for hybrid photonic/software SNN systems for spike-based

image processing applications including both edge detection and image recognition tasks with high accuracy and at high rates. Further, this positive result highlights that VCSEL neurons have the capability to perform spiking edge detection to the standard required for such complex tasks and that their spike-based output is compatible with larger SNN architectures.

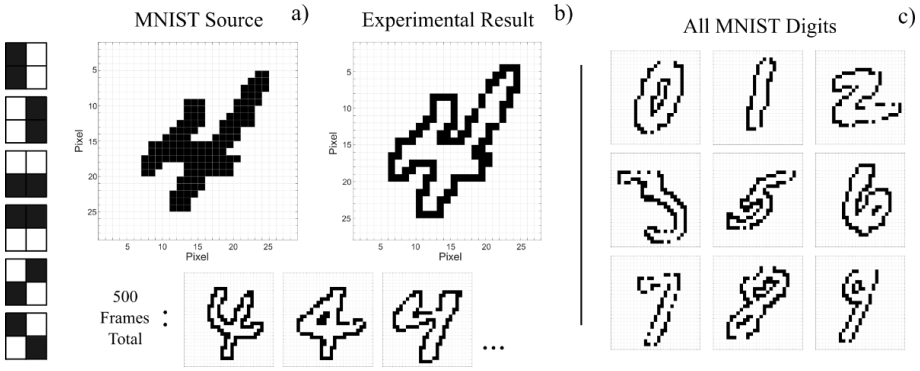

Figure 5.5.18. - MNIST handwritten-digit edge detection with an integrate-and-fire VCSEL neuron. Six 2x2 symmetrical kernels (2 vertical, 2 horizontal, 2 diagonal) were applied to 500 images of each digit from the MNIST dataset. All kernels are sequentially applied to the source image (a) which, when analysed and combined, produce reconstructions (b) that reveal all edge information. Each set of MNIST digits (c) were processed separately. Experimental parameters: I = 4.0 mA, T = 293 K, Parallel (YP) mode injection, Pinj = 159.1 μW, Δf = -5.79 GHz. Figure reproduced from [202].

Finally, we also investigated the potential for VCSEL neurons to perform spike-based convolution operations with larger kernel operators for enhanced system performance. Using the SFM, we simulated the operation of a VCSEL neuron with 3x3 kernel operators. We calculated the response of the VCSEL neuron to incoming image data inputs, generated using the technique described in Fig. 5.5.14, implementing bursts of 9 input pulses, one for each Hadamard product value (3x3 kernel). The input pulses were configured with pulse widths of 100 ps and pulse separations of 10 ps, creating 1 ns-long bursts of 9 input pulses within the configurable 3 ns pixel duration. Using an image of a ‘handwritten digit 3’ from the MNIST database (Fig. 5.5.19 (a)), the simulated VCSEL neuron performed spike-

based convolution operations with 8 (2 horizontal, 2 vertical and 4 diagonal) 3x3 kernel operators (Fig. 5.5.19 (c)-(j)). The following simulation parameters were used: γ_p =128 ns^{-1}, γ_a =2 ns^{-1}, γ_N =0.5 ns^{-1}, γ_s =110 ns^{-1}, α =2, k =185 ns^{-1}, k_{inj} =125 ns^{-1} and β_{sp} =10^{-6}.

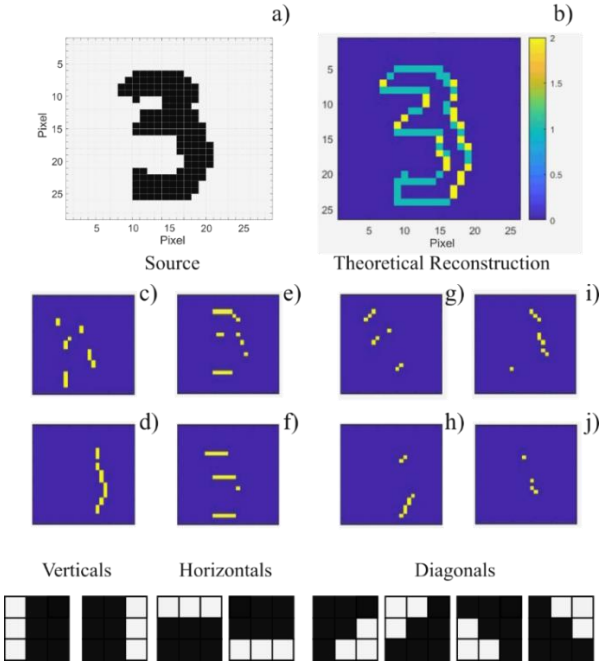

Figure 5.5.19. - SFM simulation of VCSEL neuron-based MNIST edge detection with 3x3 kernels. The MNIST source image (a) is operated on by 8 different 3x3 kernels (c)-(j). Two vertical (c)-(d), two horizontal (e)-(f), and four diagonal (g)-(j) kernels are shown. The final 8 kernel reconstruction (b) reveals all edges in the image. Figure reproduced from [202].

The numerically calculated results in Fig. 5.5.19 reveal that successful detection of target features without the activation of false positives is possible for higher (3x3) dimensional kernels, indicating the effective integration of bursts of 9 pulses (producing a Hadamard product) within the VCSEL neuron. This result, beyond the current capabilities of our experimental setup, reveals the integration of the VCSEL neuron can be utilised for larger bursts of input pulses. Overall, the 8-kernel reconstruction, shown in Fig. 5.5.19 (b), reveals that complete edge detection can theoretically be performed with an integrate-and-fire VCSEL neuron. It could therefore be possible to implement VCSEL neurons for feature detection layers in

photonic hardware SNNs using higher dimensionality kernels for operation (as those applied in the software-implemented SNN [202]), towards advanced spiking VCSEL-based photonic image processing platforms.

In this Chapter we have demonstrated three methods of implementing the image processing task of edge detection with a photonic spiking VCSEL neuron. In the first method we demonstrated a threshold-and-fire approach that utilised pre-convolved inputs for the edge detection of digital images. These results showcased that the thresholding of destination pixel values could be performed to output target edge information in a fast-optical spiking representation. Experimentally measured time series showed excellent agreement with theoretical modelling and gradient based edge detection was demonstrated, revealing all the edge information present in one image in a single experimental run. Secondly, we provided results showcasing image edge detection via a VCSEL-based all-optical binary convolution system. In this method the result of the convolution was given in the number of spiking responses produced by the VCSEL neuron. Using a sparse local pattern descriptor and kernel operator, gradient maps were calculated revealing all edge information in digital images. The binary convolution technique helped reduce the number of convolution operations performed and improved the energy efficiency and speed of the image processing task. Finally, in the third approach to VCSEL-based image processing and edge detection, we exploited the integrate-and-fire functionality of VCSEL neurons. This technique, implementing further the convolution operation into the photonic system, demonstrated the edge detection of complex images with various resolutions. Images from the MNIST handwritten digit database were processed using this method, with complete edge detection performed at a rate of 13.12 μs per image. Additionally, the experimental edge detection results from this experiment were fed directly into a SNN for the further classification of MNIST digits, achieving a final mean recognition efficiency of 96.1%. Finally, theoretical modelling of the integrate-and-fire technique showed its successful operation with larger 3x3 kernel operators, revealing the ability of VCSEL neurons to develop further convolution application, such as feature detection, in the future.

Overall, these results have revealed that VCSEL neurons have a potential future in the realisation of image processing and computer vision systems. They have

demonstrated the ability to apply neuromorphic functionalities to achieve convolution and edge detection with optical systems, through integrating, thresholding and activating fast spiking information directly in the optical domain. Despite employing a single VCSEL neuron these methods have shown pathways to fast (13.12 μs per MNIST image) and efficient edge detection and have demonstrated their ability to interface with other spike-based SNNs for complex image processing tasks. We believe for these reasons that VCSEL neurons have great prospects for image processing systems, in both their hardware-friendly single device architectures, or in larger networks for spike-based neuromorphic systems.

Chapter 6

Conclusions and Future work

6.1 Conclusions

VCSELs are an exciting photonic technology with regards to their capability to generate a range of fast (sub-nanosecond) dynamical behaviours alongside their technology maturity, low cost, wide availability, compactness and low power requirements. In this thesis we experimentally exploit the behavioural similarities of VCSELs to biological neurons in order to assess their suitability for artificial optical spiking neurons for future photonic neuromorphic brain-inspired platforms for beyond Von Neumann information processing.

In Chapter 3 we first investigated the controllable neuron-like spiking dynamics generated by VCSEL neurons under optical injection. By exploiting a bifurcation point around the injection locking/unlocking boundary we activated fast spiking dynamics at the output of the VCSEL neuron using short input perturbations (stimuli) in both the power of the optical injection, and the bias current of the VCSEL. The neuron-like excitable responses (spikes) activated had short ~100 ps pulse widths and sub-nanosecond rates, making the spiking responses multiple orders of magnitude faster than the MHz-rate of electronic systems [72]. We revealed the spiking responses of the VCSEL neuron were reproducible and that by increasing the length of the input stimuli we could achieve continuous tonic spike firing like that produced by neurons. Further, we showed the injection locking mechanism could be used inversely to suppress the spiking output of the VCSEL neuron, realising a neuronal inhibitory response. Our experimental investigation also revealed that the controllable excitable spiking responses in VCSEL neurons were governed by activation thresholds, like those of threshold-and-fire neuronal models, and that this could be easily controlled by varying the position of the system in parameter space. These results additionally revealed a neuron-like data rate encoding mechanism in photonic VCSEL neurons, which showed increasingly strong input stimuli would

reduce the activation delay of spiking dynamics. Similarly, the maximum encoding rate, which like in biological neurons is governed by the refractory period of the spiking responses, was measured here to be as low as 0.84 ns. This means the photonic artificial VCSEL neuron can be operated at rates >1 GHz (given strong enough inputs) for ultrafast spiking-based information encoding. Photonic VCSEL neurons therefore possess multiple neuromorphic functionalities in-line with those of neurons and importantly are capable of producing fast optical spiking responses, at multiple orders of magnitude faster than electronic implementations [72].

In Chapter 4 we investigated the interconnection of artificial VCSEL neurons in different neural network-inspired architectures. We first demonstrated the communication of excitable neuron-like spiking dynamics in a feedforward 1-to-1 configuration of two similar telecom wavelength, commercially-available VCSELs. We revealed VCSEL neurons connected in this 1-to-1 manner could exhibit cascadable spiking/inhibitory behaviour, providing sufficient output to influence downstream devices, effectively realising the communication of spiking information between two layers of artificial neurons in a neuromorphic system. We then demonstrated the propagation of spiking signals in a diverging 1-to-2 feedforward architecture with a single VCSEL neuron triggering simultaneous responses in two downstream VCSEL neurons. This result revealed that a single VCSEL neuron could provide information (spikes) to many neurons in a network, more easily facilitating the additional neural connections required for complex neural network architectures capable of information processing. We next created a real biological-inspired retinal neural circuit using three cascaded (1-to-1-to-1) VCSEL neurons. Both spiking and non-spiking signals were used to investigate the conversion of bipolar and retinal ganglion cell signals. We showed two ON-type-inspired circuits (increasing and decreasing light stimuli) and that an input layer of modulated VCSEL neurons could successfully inject signals into the network. We demonstrated here that VCSELs can be used to create and communicate non-spiking signals as well as perform the conversion of non-spiking signal into fast sub-nanosecond spikes without additional signal manipulation steps. The successful demonstration of the all-VCSEL system provides the addition benefit of simplifying hardware requirements, reducing system

footprint, and increasing the energy efficiency of potential future implementations of artificial networks of VCSEL neurons.

In Chapter 5 we demonstrated different potential applications of systems based on spiking VCSEL neurons for functional neuro-inspired information processing. In our first demonstration we revealed that VCSEL neurons could be used to bridge the gap between existing digital-binary technologies and spike-based optical systems by performing digital-to-spike conversion. We demonstrated that modulated optical injection could be used to convert NRZ and RZ signals at high rates, up to 1 Gb/s, into output trains of fast 100 ps-long optical spikes. The VCSEL neuron-based system enables a hardware-friendly off-the-shelf solution for integrating neuromorphic spike-based systems with conventional technologies, directly at the wavelength of telecommunications networks. We next demonstrated the use of VCSEL neurons in feedback architectures, through the use of artificial autaptic connections, to create neuromorphic photonic spiking memory systems. We showed that a single VCSEL neuron, subject to optical feedback (autapse), could be made to activate and store spiking signals in τ-long memory cycles. Using optical pertubations we demonstrated the writing of spikes within memory at will. Similarly, we demonstrated the formation of stable spiking memory sequences in mutually coupled VCSEL neurons. In both cases we deduce that the storage capacity of the memory is dictated by the refractory period of the VCSEL neuron and the length of the feedback delay. These VCSEL-based implementations could therefore be applicable in neuromorphic systems where the creation of spiking memories is required via off-the-shelf, hardware-friendly optical components. We next demonstrated the exciting capability of the VCSEL neuron to integrate temporally separated inputs, effectively realising the integrate-and-fire operation of neuronal models. We showed both experimentally and theoretically that a VCSEL neuron, subject to time multiplexed inputs, could be made to integrate bursts within a short temporal window and respond accordingly with a fast (100 ps-long) spiking response. This revelation of integrate-and-fire functionality allowed the VCSEL neurons to move towards neural network operation. In our first demonstration, we performed the coincidence detection of two optical inputs incident on the VCSEL neuron, showing that the latter sucessfully activated when the two inputs were close

in time effectively realising a time-resolved AND logic gate. This VCSEL-based coincidence detection system could provide a simple pathway to optical alarm triggering systems where rapid decision making (sub-nanosecond-long windows) is required with fast optical inputs, compatible with spiking neural networks.

Our next functional VCSEL neuron processing circuit demonstrated a pattern recognition task that identified 4-bit input sequences with the triggering of fast spiking responses. We employed time-division multiplexing (TDM) and the integrate-and-fire functionality of the VCSEL neuron, to identify (at high-speeds) target 4-bit patterns by injecting sub-nanosecond bursts of weighted inputs (at 80 ps/bit). We demonstrated experimentally that by weighting the input pattern effectively, the VCSEL neuron could trigger spikes for the correct pattern with overall high average recognition efficiencies and inputs rates of near 1 GHz. These proof-of-concept results yet still utilised a supervised learning scheme and a single VCSEL neuron, but nevertheless highlight the significant potential these devices have for the implemention of off-the-shelf, ultrafast, spike-based classification systems towards pattern recognition processing applications.

Our final experimental demonstrations of VCSEL neurons for functional applications tackled the field of image processing and feature detection. We first demonstrated that by combining a VCSEL neuron with the image processing technique convolution, we could perform the edge-feature detection of digital images, outputting fast spiking responses for positive recognitions. By scanning 2x2 kernel operators over images in an offline pre-processing stage, we generated destination pixel values which were injected into the VCSEL neuron for processing. We showed that the threshold-and-fire neuronal behaviour of the VCSEL neuron could be used to detect the appropriate target and respond accordingly with fast 100 ps-long spikes. We revealed a single VCSEL neuron was capable of detecting all the edge-feature information in an image (through the use of multiple kernels or in a single run using gradient magnitude) at rates of up to 1.5 ns per pixel, matching SFM simulated results. We next showed an alternative all-optical binary convolution method for extracting image gradient magnitudes using a single spiking VCSEL neuron. In this image processing method we applied kernel operators within the photonic system by generating and overlapping the kernel weights and pixel data in two interconnected

modulators. The subsequent multilevel signal was injected into the VCSEL neuron, creating a train of fast optical spiking responses containing the image's gradient magnitude information. We revealed that VCSEL neuron-based binary convolution system also holds key advantages in terms of efficiency and speed, despite the hardware-friendly system using solely a single VCSEL neuron. The experimental findings were found to closely match those simulated using the SFM and the theoretical system showed good resilience to noisy inputs. Our last demonstration of a functional image processing system exploited the neuronal integrate-and-fire functionality of the VCSEL neuron to perform the 2x2 high-speed spike-enabled image convolution. We used TDM to inject the hadamard products of each kernel operation into the VCSEL neuron, futher implementing convolution within the optical system, and sucessfully detected edge-feature information in images of various resolutions with fast optical spikes. We processed images from the MNIST handwritten digit database and achieved a VCSEL neuron processing rate of 13.12 μs per image, and further demonstrated the classification of the MNIST images by directly feeding our edge information into a software-implemented SNN, achieving a high mean reconigition efficiency of 96.1%. Using the SFM we again demonstrated in theory that edge-feature detection could also be performed with larger (3x3) kernel operators. The results achieved here highlight the prospects of the image processing functionality of VCSEL-based neuromorphic systems built with just a single VCSEL performing the operation of an entire network layer of artificial neurons. This hardware system, operating at a telecom wavelengths, hence realises a hardware-friendly photonic spike-based processing system towards image processing applications and computer vision for AI.

To conclude, we have investigated VCSELs as potential candidates for future neuromorphic systems amidst rising demands for increasing information processing speeds and AI. We have demonstrated that VCSELs have the capability to emulate biological neurons, presenting many of the features of neuronal models (tonic spike-firing, thresholding, integration, refractoriness, etc.) but at speeds >6 order of magnitude faster (sub-nanosecond rates). Our investigations have focused on VCSEL neurons for neuromorphic processing applications, and through such have experimentally and theoretically demonstrated sucessful pattern recognition and

image processing tasks all with commercially-sourced, telecom wavelength VCSELs and hardware-friendly designs. The possibility for the use of VCSEL neurons in future neuromorphic systems is therefore exciting and with the room for further developments and research, VCSEL-based systems could help realise brain-inspired spike-based computing on an ultrafast, low power requirement, photonic platform.

6.2 Future Work

In this thesis we have obtained a diverse range of interesting results during our investigation of VCSELs as artificial spiking neurons, however, there are avenues of this research that present opportunities for further study. Here I will briefly highlight a few areas of potential future investigation.

In future studies of VCSELs as artificial spiking neurons I believe it is of key interest to more closely investigate, experimentally and theoretically, the behaviour of the neuronal integrate-and-fire functionality of the VCSEL neurons. Investigation into the use of higher numbers of temporally separated inputs could diversify the uses of the integrate-and-fire functionality, allowing VCSEL neurons to break into image feature recognition with the processing of larger kernel operators (as demonstrated theoretically in Fig. 5.3.19). This could be done by generating inputs at a higher rate (>12 GSa/s), allowing for smaller input pulse widths and separations to be used, similar to the theoretical demonstration shown in Fig. 5.3.3. Alternatively, attempts could be made to integrate temporally-correlated inputs from different sources in a single VCSEL neuron, realising a true fan-in (many to one) architecture. This result would nullify the temporal leakage of the activation energy in integrate-and-fire VCSEL neurons, allowing for improved input weighting schemes and more efficient integration operations. An investigation of this type would be necessary for the development of artificial neural networks of VCSELs where the connectivity between different layers is high. Further, studying the effect of inhibitory pulses during input integration would improve the understanding of the system, potentially opening doors to schemes with negatives weights for unique processing operations

such as the XOR classification task. Finally, investigating the potential for integrate-and-fire operation with electrically-triggered spiking responses could provide a gateway to optical-electrical-optical (OEO) connections between VCSEL neurons. In this scheme the strict wavelength requirement of upstream signals/neurons to match the integrating neuron could be circumvented, allowing for simplier neural network implementations.

The expansion and scalability of VCSEL neurons into larger networks of devices is another research area of key interest to the development of future VCSEL-based photonic neuromorphic systems. Increasing the scale of the VCSEL neuron systems would help improve their processing speed, by enabling access to in-parallel operations with multiple VCSEL neurons, and their applicability, by achieving different artificial neural network architectures for different processing tasks. One interesting approach that could be investigated is the scaling VCSEL neurons via the use of VCSEL arrays, specifically arrays grown for the purpose of network connectivity, with each VCSEL device exhibiting a similar operational wavelength. Such arrays of VCSEL neurons would allow for the investigation of all-VCSEL networks, as shown in Chapter 3.3, that could propagate spiking signals at a single wavelength without the requirement for signal manipulation. The experimental implementation of such an array system (and its interconnects) would be highly interesting, and could potentially be achieved using technologies such as microlens arrays or digital micromirror devices. Alternatively, the scaling of VCSEL neuron systems could be studied with OEO inter-neuron connections, which would remove the requirement for single wavelength operation, enabling the possibility of wavelength-division multiplexing inputs at the potential cost of operation speed and energy efficiency. Finally, the investigation of suitable optical weighting elements, for photonic synaptic connections, is also required when considering the scaling of VCSEL neurons in larger neural networks. The weighting operation of synaptic connections is key to the processing capability of neuronal models and should therefore be studied before the implementation of multiple VCSEL neurons. Several approaches to optical weighting could be considered as synaptic elements including optical modulators, microring resonators and Vertical Cavity Semiconductor Optical Amplifiers (VCSOAs).

Finally, the use of commercially-available VCSELs has proven effective at implementing off-the-shelf, hardware-friendly photonic spiking systems. However, as discussed throughout this thesis, the maximum processing rate of a VCSEL neuron is frequently dictacted by the refractory period of the excitable spiking dynamics (approximately 1 ns). Hence an interesting research avenue would be the investigation of different VCSEL fabrication designs towards the realisation of ultrafast >1 GHz excitable spiking responses. Given improvements in the spiking refractory period could be achieved, the processing rate of the spike-based platform would directly benefit, allowing DTS, pattern recognition and image processing to each be completed at higher maximum speeds.

In conclusion, we have demonstrated the exciting functionality and flexibility of VCSELs to operate as ultrafast (GHz rates) artificial spiking neurons. We have reported functional processing applications, such as pattern recognition and image edge-feature detection and classification, that were implemented using only a single off-the-shelf, telecom VCSEL (acting as an artificial photonic neuron). However, given the potential for further research and the development of faster neural networks of VCSEL neurons, we anticipate further interest in VCSELs for future spike-based photonic information processing systems and light-enabled AI platforms.

References

[1] Intel, “The Story of the Intel 4004,” 2022. https://www.intel.co.uk/content/www/uk/en/history/museum-story-of-intel-4004.html (accessed Mar. 18, 2022).

[2] G. E. Moore, “Cramming more components onto integrated circuits, Reprinted from Electronics, volume 38, number 8, April 19, 1965, pp.114 ff.,” *IEEE Solid-State Circuits Soc. Newsl.*, vol. 11, no. 3, pp. 33–35, Sep. 2006, doi: 10.1109/N-SSC.2006.4785860.

[3] R. H. Dennard, F. H. Gaensslen, H.-N. Yu, V. L. Rideout, E. Bassous, and A. R. LeBlanc, “Design of ion-implanted MOSFET’s with very small physical dimensions,” *IEEE J. Solid-State Circuits*, vol. 9, no. 5, pp. 256–268, Oct. 1974, doi: 10.1109/JSSC.1974.1050511.

[4] D. A. B. Miller, “Attojoule Optoelectronics for Low-Energy Information Processing and Communications,” *J. Light. Technol.*, vol. 35, no. 3, pp. 346–396, Feb. 2017, doi: 10.1109/JLT.2017.2647779.

[5] J. Koomey, S. Berard, M. Sanchez, and H. Wong, “Implications of Historical Trends in the Electrical Efficiency of Computing,” *IEEE Ann. Hist. Comput.*, vol. 33, no. 3, pp. 46–54, Mar. 2011, doi: 10.1109/MAHC.2010.28.

[6] K. Rupp, “42 Years of Microprocessor Trend Data,” 2018. https://www.karlrupp.net/2018/02/42-years-of-microprocessor-trend-data/ (accessed Mar. 18, 2022).

[7] A. Krizhevsky, I. Sutskever, and G. E. Hinton, “ImageNet Classification with Deep Convolutional Neural Networks,” in *Advances in Neural Information Processing Systems*, 2012, vol. 25, [Online]. Available: https://proceedings.neurips.cc/paper/2012/file/c399862d3b9d6b76c8436e924a68c45b-Paper.pdf.

[8] P.-S. Wang, Y. Liu, Y.-X. Guo, C.-Y. Sun, and X. Tong, “O-CNN: octree-based convolutional neural networks for 3D shape analysis,” *ACM Trans.*

Graph., vol. 36, no. 4, pp. 1–11, Jul. 2017, doi: 10.1145/3072959.3073608.

[9] C. Zhang, P. Li, G. Sun, Y. Guan, B. Xiao, and J. Cong, "Optimizing FPGA-based Accelerator Design for Deep Convolutional Neural Networks," in *Proceedings of the 2015 ACM/SIGDA International Symposium on Field-Programmable Gate Arrays*, Feb. 2015, pp. 161–170, doi: 10.1145/2684746.2689060.

[10] Y. LeCun, Y. Bengio, and G. Hinton, "Deep learning," *Nature*, vol. 521, no. 7553, pp. 436–444, May 2015, doi: 10.1038/nature14539.

[11] K. Simonyan and A. Zisserman, "Very Deep Convolutional Networks for Large-Scale Image Recognition," *CoRR*, vol. abs/1409.1, 2015.

[12] K. He, X. Zhang, S. Ren, and J. Sun, "Deep Residual Learning for Image Recognition," in *2016 IEEE Conference on Computer Vision and Pattern Recognition (CVPR)*, Jun. 2016, pp. 770–778, doi: 10.1109/CVPR.2016.90.

[13] Y. Leviathan, "Google duplex: An AI system for accomplishing real-world tasks over the phone.," 2018. .

[14] D. Silver *et al.*, "Mastering the game of Go with deep neural networks and tree search," *Nature*, vol. 529, no. 7587, pp. 484–489, Jan. 2016, doi: 10.1038/nature16961.

[15] Kenneth Saladin, *Human Anatomy*, 6th ed. McGraw-Hill Higher Education, 2020.

[16] S. Thorpe, A. Delorme, and R. Van Rullen, "Spike-based strategies for rapid processing," *Neural Networks*, vol. 14, no. 6–7, pp. 715–725, Jul. 2001, doi: 10.1016/S0893-6080(01)00083-1.

[17] W. S. McCulloch and W. Pitts, "A logical calculus of the ideas immanent in nervous activity," *Bull. Math. Biophys.*, vol. 5, no. 4, pp. 115–133, Dec. 1943, doi: 10.1007/BF02478259.

[18] E. M. Izhikevich, "Which Model to Use for Cortical Spiking Neurons?," *IEEE Trans. Neural Networks*, vol. 15, no. 5, pp. 1063–1070, Sep. 2004, doi:

10.1109/TNN.2004.832719.

[19] W. Gerstner and W. M. Kistler, *Spiking Neuron Models: Single Neurons, Populations, Plasticity*. Cambridge university Press, 2002.

[20] L. Alzubaidi *et al.*, "Review of deep learning: concepts, CNN architectures, challenges, applications, future directions," *J. Big Data*, vol. 8, no. 1, p. 53, Dec. 2021, doi: 10.1186/s40537-021-00444-8.

[21] Y. Yu, X. Si, C. Hu, and J. Zhang, "A Review of Recurrent Neural Networks: LSTM Cells and Network Architectures," *Neural Comput.*, vol. 31, no. 7, pp. 1235–1270, Jul. 2019, doi: 10.1162/neco_a_01199.

[22] D. A. Drachman, "Do we have brain to spare?," *Neurology*, vol. 64, no. 12, pp. 2004–2005, Jun. 2005, doi: 10.1212/01.WNL.0000166914.38327.BB.

[23] B. Farley and W. Clark, "Simulation of self-organizing systems by digital computer," *Trans. IRE Prof. Gr. Inf. Theory*, vol. 4, no. 4, pp. 76–84, Sep. 1954, doi: 10.1109/TIT.1954.1057468.

[24] D. E. Rumelhart, G. E. Hinton, and R. J. Williams, "Learning representations by back-propagating errors," *Nature*, vol. 323, no. 6088, pp. 533–536, Oct. 1986, doi: 10.1038/323533a0.

[25] S. O. Haykin, *Neural Networks and Learning Machines*, 3rd ed. Pearson, 2009.

[26] R. FitzHugh, "Mathematical models of threshold phenomena in the nerve membrane," *Bull. Math. Biophys.*, vol. 17, no. 4, pp. 257–278, Dec. 1955, doi: 10.1007/BF02477753.

[27] A. N. Burkitt, "A Review of the Integrate-and-fire Neuron Model: I. Homogeneous Synaptic Input," *Biol. Cybern.*, vol. 95, no. 1, pp. 1–19, Jul. 2006, doi: 10.1007/s00422-006-0068-6.

[28] L. . Abbott, "Lapicque's introduction of the integrate-and-fire model neuron (1907)," *Brain Res. Bull.*, vol. 50, no. 5–6, pp. 303–304, Nov. 1999, doi: 10.1016/S0361-9230(99)00161-6.

[29] J. Gautrais and S. Thorpe, “Rate coding versus temporal order coding: a theoretical approach,” *Biosystems*, vol. 48, no. 1–3, pp. 57–65, Nov. 1998, doi: 10.1016/S0303-2647(98)00050-1.

[30] R. Sarpeshkar, “Analog Versus Digital: Extrapolating from Electronics to Neurobiology,” *Neural Comput.*, vol. 10, no. 7, pp. 1601–1638, Oct. 1998, doi: 10.1162/089976698300017052.

[31] J. Hasler and B. Marr, “Finding a roadmap to achieve large neuromorphic hardware systems,” *Front. Neurosci.*, vol. 7, 2013, doi: 10.3389/fnins.2013.00118.

[32] J. Vreeken, “Spiking Neural Networks, An Introduction,” *Tech. Rep. UU-CS*, pp. 1–5, 2003.

[33] W. Maass, “Networks of spiking neurons: The third generation of neural network models,” *Neural Networks*, vol. 10, no. 9, pp. 1659–1671, Dec. 1997, doi: 10.1016/S0893-6080(97)00011-7.

[34] S. J. Verzi *et al.*, “Computing with Spikes: The Advantage of Fine-Grained Timing,” *Neural Comput.*, vol. 30, no. 10, pp. 2660–2690, Oct. 2018, doi: 10.1162/neco_a_01113.

[35] B. V. Benjamin *et al.*, “Neurogrid: A Mixed-Analog-Digital Multichip System for Large-Scale Neural Simulations,” *Proc. IEEE*, vol. 102, no. 5, pp. 699–716, May 2014, doi: 10.1109/JPROC.2014.2313565.

[36] C. Pehle *et al.*, “The BrainScaleS-2 accelerated neuromorphic system with hybrid plasticity,” Jan. 2022, [Online]. Available: http://arxiv.org/abs/2201.11063.

[37] S. B. Furber, F. Galluppi, S. Temple, and L. A. Plana, “The SpiNNaker Project,” *Proc. IEEE*, vol. 102, no. 5, pp. 652–665, May 2014, doi: 10.1109/JPROC.2014.2304638.

[38] C. Mead, *Analog VLSI Implementation of Neural Systems*, vol. 80. Boston, MA: Springer US, 1989.

[39] B. V. Benjamin, N. A. Steinmetz, N. N. Oza, J. J. Aguayo, and K. Boahen, “Neurogrid simulates cortical cell-types, active dendrites, and top-down attention,” *Neuromorphic Comput. Eng.*, vol. 1, no. 1, p. 013001, Sep. 2021, doi: 10.1088/2634-4386/ac0a5a.

[40] P. A. Merolla *et al.*, “A million spiking-neuron integrated circuit with a scalable communication network and interface,” *Science (80-.).*, vol. 345, no. 6197, pp. 668–673, Aug. 2014, doi: 10.1126/science.1254642.

[41] M. V. DeBole *et al.*, “TrueNorth: Accelerating From Zero to 64 Million Neurons in 10 Years,” *Computer (Long. Beach. Calif).*, vol. 52, no. 5, pp. 20–29, May 2019, doi: 10.1109/MC.2019.2903009.

[42] J. Schemmel, D. Briiderle, A. Griibl, M. Hock, K. Meier, and S. Millner, “A wafer-scale neuromorphic hardware system for large-scale neural modeling,” in *Proceedings of 2010 IEEE International Symposium on Circuits and Systems*, May 2010, pp. 1947–1950, doi: 10.1109/ISCAS.2010.5536970.

[43] M. Davies *et al.*, “Loihi: A Neuromorphic Manycore Processor with On-Chip Learning,” *IEEE Micro*, vol. 38, no. 1, pp. 82–99, Jan. 2018, doi: 10.1109/MM.2018.112130359.

[44] C. A. Brackett, “Dense wavelength division multiplexing networks: principles and applications,” *IEEE J. Sel. Areas Commun.*, vol. 8, no. 6, pp. 948–964, 1990, doi: 10.1109/49.57798.

[45] T. Sharma *et al.*, “Review of Recent Progress on Silicon Nitride-Based Photonic Integrated Circuits,” *IEEE Access*, vol. 8, pp. 195436–195446, 2020, doi: 10.1109/ACCESS.2020.3032186.

[46] P. R. Prucnal, B. J. Shastri, and M. C. Teich, *Neuromorphic Photonics*. CRC Press, 2017.

[47] E. C. Mos, J. J. L. Hoppenbrouwers, M. T. Hill, M. W. Blum, J. J. H. B. Schleipen, and H. de waardt, “Optical neuron by use of a laser diode with injection seeding and external optical feedback,” *IEEE Trans. Neural Networks*, vol. 11, no. 4, pp. 988–996, Jul. 2000, doi: 10.1109/72.857778.

[48] A. M. Yacomotti *et al.*, “Fast Thermo-Optical Excitability in a Two-Dimensional Photonic Crystal,” *Phys. Rev. Lett.*, vol. 97, no. 14, p. 143904, Oct. 2006, doi: 10.1103/PhysRevLett.97.143904.

[49] M. Brunstein, A. M. Yacomotti, I. Sagnes, F. Raineri, L. Bigot, and A. Levenson, “Excitability and self-pulsing in a photonic crystal nanocavity,” *Phys. Rev. A*, vol. 85, no. 3, p. 031803, Mar. 2012, doi: 10.1103/PhysRevA.85.031803.

[50] B. J. Shastri, M. A. Nahmias, A. N. Tait, B. Wu, and P. R. Prucnal, “SIMPEL: Circuit model for photonic spike processing laser neurons,” *Opt. Express*, vol. 23, no. 6, p. 8029, Mar. 2015, doi: 10.1364/OE.23.008029.

[51] B. J. Shastri, M. A. Nahmias, A. N. Tait, A. W. Rodriguez, B. Wu, and P. R. Prucnal, “Spike processing with a graphene excitable laser,” *Sci. Rep.*, vol. 6, no. 1, p. 19126, May 2016, doi: 10.1038/srep19126.

[52] K. S. Kravtsov, M. P. Fok, P. R. Prucnal, and D. Rosenbluth, “Ultrafast All-Optical Implementation of a Leaky Integrate-and-Fire Neuron,” *Opt. Express*, vol. 19, no. 3, p. 2133, Jan. 2011, doi: 10.1364/OE.19.002133.

[53] R. Toole *et al.*, “Photonic Implementation of Spike-Timing-Dependent Plasticity and Learning Algorithms of Biological Neural Systems,” *J. Light. Technol.*, vol. 34, no. 2, pp. 470–476, Jan. 2016, doi: 10.1109/JLT.2015.2475275.

[54] S. Xu, J. Wang, R. Wang, J. Chen, and W. Zou, “High-accuracy optical convolution unit architecture for convolutional neural networks by cascaded acousto-optical modulator arrays,” *Opt. Express*, vol. 27, no. 14, p. 19778, Jul. 2019, doi: 10.1364/OE.27.019778.

[55] M. P. Fok, Y. Tian, D. Rosenbluth, and P. R. Prucnal, “Asynchronous spiking photonic neuron for lightwave neuromorphic signal processing,” *Opt. Lett.*, vol. 37, no. 16, p. 3309, Aug. 2012, doi: 10.1364/OL.37.003309.

[56] J. M. Shainline, S. M. Buckley, R. P. Mirin, and S. W. Nam, “Superconducting Optoelectronic Circuits for Neuromorphic Computing,”

Phys. Rev. Appl., vol. 7, no. 3, p. 034013, Mar. 2017, doi: 10.1103/PhysRevApplied.7.034013.

[57] M. Hejda *et al.*, "Resonant Tunneling Diode Nano-Optoelectronic Excitable Nodes for Neuromorphic Spike-Based Information Processing," *Phys. Rev. Appl.*, vol. 17, no. 2, p. 024072, Feb. 2022, doi: 10.1103/PhysRevApplied.17.024072.

[58] M. Feiginov, "Frequency Limitations of Resonant-Tunnelling Diodes in Sub-THz and THz Oscillators and Detectors," *J. Infrared, Millimeter, Terahertz Waves*, vol. 40, no. 4, pp. 365–394, Apr. 2019, doi: 10.1007/s10762-019-00573-5.

[59] R. Izumi, S. Suzuki, and M. Asada, "1.98 THz resonant-tunneling-diode oscillator with reduced conduction loss by thick antenna electrode," in *2017 42nd International Conference on Infrared, Millimeter, and Terahertz Waves (IRMMW-THz)*, Aug. 2017, pp. 1–2, doi: 10.1109/IRMMW-THz.2017.8066877.

[60] I. Ortega-Piwonka, O. Piro, J. Figueiredo, B. Romeira, and J. Javaloyes, "Bursting and Excitability in Neuromorphic Resonant Tunneling Diodes," *Phys. Rev. Appl.*, vol. 15, no. 3, p. 034017, Mar. 2021, doi: 10.1103/PhysRevApplied.15.034017.

[61] B. Romeira, J. Javaloyes, C. N. Ironside, J. M. L. Figueiredo, S. Balle, and O. Piro, "Excitability and optical pulse generation in semiconductor lasers driven by resonant tunneling diode photo-detectors," *Opt. Express*, vol. 21, no. 18, p. 20931, Sep. 2013, doi: 10.1364/OE.21.020931.

[62] B. Romeira, R. Avó, J. Javaloyes, S. Balle, C. N. Ironside, and J. M. L. Figueiredo, "Stochastic induced dynamics in neuromorphic optoelectronic oscillators," *Opt. Quantum Electron.*, vol. 46, no. 10, pp. 1391–1396, Oct. 2014, doi: 10.1007/s11082-014-9905-3.

[63] B. Romeira, J. M. L. Figueiredo, and J. Javaloyes, "Delay dynamics of neuromorphic optoelectronic nanoscale resonators: Perspectives and applications," *Chaos An Interdiscip. J. Nonlinear Sci.*, vol. 27, no. 11, p.

114323, Nov. 2017, doi: 10.1063/1.5008888.

[64] K. Alexander, T. Van Vaerenbergh, M. Fiers, P. Mechet, J. Dambre, and P. Bienstman, “Excitability in optically injected microdisk lasers with phase controlled excitatory and inhibitory response,” *Opt. Express*, vol. 21, no. 22, p. 26182, Nov. 2013, doi: 10.1364/OE.21.026182.

[65] R. Mirek *et al.*, “Neuromorphic Binarized Polariton Networks,” *Nano Lett.*, vol. 21, no. 9, pp. 3715–3720, May 2021, doi: 10.1021/acs.nanolett.0c04696.

[66] W. Coomans, L. Gelens, S. Beri, J. Danckaert, and G. Van der Sande, “Solitary and coupled semiconductor ring lasers as optical spiking neurons,” *Phys. Rev. E*, vol. 84, no. 3, p. 036209, Sep. 2011, doi: 10.1103/PhysRevE.84.036209.

[67] L. Gelens *et al.*, “Excitability in semiconductor microring lasers: Experimental and theoretical pulse characterization,” *Phys. Rev. A*, vol. 82, no. 6, p. 063841, Dec. 2010, doi: 10.1103/PhysRevA.82.063841.

[68] C. Mesaritakis, A. Kapsalis, A. Bogris, and D. Syvridis, “Artificial Neuron Based on Integrated Semiconductor Quantum Dot Mode-Locked Lasers,” *Sci. Rep.*, vol. 6, no. 1, p. 39317, Dec. 2016, doi: 10.1038/srep39317.

[69] M. Dillane, J. Robertson, M. Peters, A. Hurtado, and B. Kelleher, “Neuromorphic dynamics with optically injected quantum dot lasers,” *Eur. Phys. J. B*, vol. 92, no. 9, p. 197, Sep. 2019, doi: 10.1140/epjb/e2019-90733-6.

[70] B. Kelleher, C. Bonatto, G. Huyet, and S. P. Hegarty, “Excitability in optically injected semiconductor lasers: Contrasting quantum- well- and quantum-dot-based devices,” *Phys. Rev. E*, vol. 83, no. 2, p. 026207, Feb. 2011, doi: 10.1103/PhysRevE.83.026207.

[71] H. J. Wünsche, O. Brox, M. Radziunas, and F. Henneberger, “Excitability of a Semiconductor Laser by a Two-Mode Homoclinic Bifurcation,” *Phys. Rev. Lett.*, vol. 88, no. 2, p. 023901, Dec. 2001, doi: 10.1103/PhysRevLett.88.023901.

[72] P. R. Prucnal, B. J. Shastri, T. Ferreira de Lima, M. A. Nahmias, and A. N.

Tait, “Recent progress in semiconductor excitable lasers for photonic spike processing,” *Adv. Opt. Photonics*, vol. 8, no. 2, p. 228, Jun. 2016, doi: 10.1364/AOP.8.000228.

[73] B. J. Shastri, A. N. Tait, T. Ferreira de Lima, M. A. Nahmias, H.-T. Peng, and P. R. Prucnal, “Neuromorphic Photonics, Principles of,” in *Encyclopedia of Complexity and Systems Science*, Berlin, Heidelberg: Springer Berlin Heidelberg, 2018, pp. 1–37.

[74] B. J. Shastri *et al.*, “Photonics for artificial intelligence and neuromorphic computing,” *Nat. Photonics*, vol. 15, no. 2, pp. 102–114, Feb. 2021, doi: 10.1038/s41566-020-00754-y.

[75] A. N. Tait *et al.*, “Microring Weight Banks,” *IEEE J. Sel. Top. Quantum Electron.*, vol. 22, no. 6, pp. 312–325, Nov. 2016, doi: 10.1109/JSTQE.2016.2573583.

[76] A. N. Tait *et al.*, “Neuromorphic photonic networks using silicon photonic weight banks,” *Sci. Rep.*, vol. 7, no. 1, p. 7430, Dec. 2017, doi: 10.1038/s41598-017-07754-z.

[77] A. N. Tait *et al.*, “Silicon Photonic Modulator Neuron,” *Phys. Rev. Appl.*, vol. 11, no. 6, p. 064043, Jun. 2019, doi: 10.1103/PhysRevApplied.11.064043.

[78] T. F. de Lima *et al.*, “Noise Analysis of Photonic Modulator Neurons,” *IEEE J. Sel. Top. Quantum Electron.*, vol. 26, no. 1, pp. 1–9, Jan. 2020, doi: 10.1109/JSTQE.2019.2931252.

[79] A. N. Tait, M. A. Nahmias, B. J. Shastri, and P. R. Prucnal, “Broadcast and Weight: An Integrated Network For Scalable Photonic Spike Processing,” *J. Light. Technol.*, vol. 32, no. 21, pp. 4029–4041, Nov. 2014, doi: 10.1109/JLT.2014.2345652.

[80] T. F. de Lima *et al.*, “Machine Learning With Neuromorphic Photonics,” *J. Light. Technol.*, vol. 37, no. 5, pp. 1515–1534, Mar. 2019, doi: 10.1109/JLT.2019.2903474.

[81] A. Mehrabian, Y. Al-Kabani, V. J. Sorger, and T. El-Ghazawi, “PCNNA: A

Photonic Convolutional Neural Network Accelerator," in *2018 31st IEEE International System-on-Chip Conference (SOCC)*, Sep. 2018, pp. 169–173, doi: 10.1109/SOCC.2018.8618542.

[82] J. Feldmann, N. Youngblood, C. D. Wright, H. Bhaskaran, and W. H. P. Pernice, "All-optical spiking neurosynaptic networks with self-learning capabilities," *Nature*, vol. 569, no. 7755, pp. 208–214, May 2019, doi: 10.1038/s41586-019-1157-8.

[83] J. Feldmann *et al.*, "Parallel convolutional processing using an integrated photonic tensor core," *Nature*, vol. 589, no. 7840, pp. 52–58, Jan. 2021, doi: 10.1038/s41586-020-03070-1.

[84] H. Jaeger, "The" echo state" approach to analysing and training recurrent neural networks-with an erratum note'," *Bonn, Ger. Ger. Natl. Res. Cent. Inf. Technol. GMD Tech. Rep.*, vol. 148, 2001.

[85] W. Maass, T. Natschläger, and H. Markram, "Real-Time Computing Without Stable States: A New Framework for Neural Computation Based on Perturbations," *Neural Comput.*, vol. 14, no. 11, pp. 2531–2560, Nov. 2002, doi: 10.1162/089976602760407955.

[86] J. J. Steil, "Backpropagation-decorrelation: online recurrent learning with O(N) complexity," in *2004 IEEE International Joint Conference on Neural Networks (IEEE Cat. No.04CH37541)*, vol. 2, pp. 843–848, doi: 10.1109/IJCNN.2004.1380039.

[87] D. Verstraeten, B. Schrauwen, M. D'Haene, and D. Stroobandt, "An experimental unification of reservoir computing methods," *Neural Networks*, vol. 20, no. 3, pp. 391–403, Apr. 2007, doi: 10.1016/j.neunet.2007.04.003.

[88] J. B. Butcher, D. Verstraeten, B. Schrauwen, C. R. Day, and P. W. Haycock, "Reservoir computing and extreme learning machines for non-linear time-series data analysis," *Neural Networks*, vol. 38, pp. 76–89, Feb. 2013, doi: 10.1016/j.neunet.2012.11.011.

[89] K. Vandoorne *et al.*, "Experimental demonstration of reservoir computing on a

silicon photonics chip," *Nat. Commun.*, vol. 5, no. 1, p. 3541, May 2014, doi: 10.1038/ncomms4541.

[90] D. Brunner, M. C. Soriano, C. R. Mirasso, and I. Fischer, "Parallel photonic information processing at gigabyte per second data rates using transient states," *Nat. Commun.*, vol. 4, no. 1, p. 1364, Jun. 2013, doi: 10.1038/ncomms2368.

[91] Q. Vinckier *et al.*, "High-performance photonic reservoir computer based on a coherently driven passive cavity," *Optica*, vol. 2, no. 5, p. 438, May 2015, doi: 10.1364/OPTICA.2.000438.

[92] A. Argyris, J. Bueno, and I. Fischer, "PAM-4 Transmission at 1550 nm Using Photonic Reservoir Computing Post-Processing," *IEEE Access*, vol. 7, pp. 37017–37025, 2019, doi: 10.1109/ACCESS.2019.2905422.

[93] P. Kirkland, G. Di Caterina, J. Soraghan, Y. Andreopoulos, and G. Matich, "UAV Detection: A STDP Trained Deep Convolutional Spiking Neural Network Retina-Neuromorphic Approach," 2019, pp. 724–736.

[94] P. Kirkland, G. Di Caterina, J. Soraghan, and G. Matich, "SpikeSEG: Spiking Segmentation via STDP Saliency Mapping," in *2020 International Joint Conference on Neural Networks (IJCNN)*, Jul. 2020, pp. 1–8, doi: 10.1109/IJCNN48605.2020.9207075.

[95] P. Kirkland *et al.*, "Imaging from temporal data via spiking convolutional neural networks," in *Emerging Imaging and Sensing Technologies for Security and Defence V; and Advanced Manufacturing Technologies for Micro- and Nanosystems in Security and Defence III*, Sep. 2020, p. 15, doi: 10.1117/12.2573484.

[96] H. Soda, K. Iga, C. Kitahara, and Y. Suematsu, "{GaInAsP}/{InP} Surface Emitting Injection Lasers," *Jpn. J. Appl. Phys.*, vol. 18, no. 12, pp. 2329–2330, Dec. 1979, doi: 10.1143/jjap.18.2329.

[97] O. Svelto, *Principles of Lasers*. Boston, MA: Springer US, 2010.

[98] A. Donges and R. Noll, *Laser Measurement Technology*, vol. 188. Berlin,

Heidelberg: Springer Berlin Heidelberg, 2015.

[99] S. Royo and M. Ballesta-Garcia, “An Overview of Lidar Imaging Systems for Autonomous Vehicles,” *Appl. Sci.*, vol. 9, no. 19, p. 4093, Sep. 2019, doi: 10.3390/app9194093.

[100] P. J. Winzer, D. T. Neilson, and A. R. Chraplyvy, “Fiber-optic transmission and networking: the previous 20 and the next 20 years [Invited],” *Opt. Express*, vol. 26, no. 18, p. 24190, Sep. 2018, doi: 10.1364/OE.26.024190.

[101] W. W. Chow and S. W. Koch, *Semiconductor-Laser Fundamentals*. Berlin, Heidelberg: Springer Berlin Heidelberg, 1999.

[102] R. N. Hall, G. E. Fenner, J. D. Kingsley, T. J. Soltys, and R. O. Carlson, “Coherent Light Emission From GaAs Junctions,” *Phys. Rev. Lett.*, vol. 9, no. 9, pp. 366–368, Nov. 1962, doi: 10.1103/PhysRevLett.9.366.

[103] M. I. Nathan, W. P. Dumke, G. Burns, F. H. Dill, and G. Lasher, “STIMULATED EMISSION OF RADIATION FROM GaAs p-n JUNCTIONS,” *Appl. Phys. Lett.*, vol. 1, no. 3, pp. 62–64, Nov. 1962, doi: 10.1063/1.1777371.

[104] J. Ohtsubo, *Semiconductor Lasers*, vol. 111. Berlin, Heidelberg: Springer Berlin Heidelberg, 2013.

[105] S. W. Koch and M. R. Hofmann, “Semiconductor Lasers,” in *Encyclopedia of Modern Optics*, Elsevier, 2018, pp. 462–468.

[106] D. A. B. Miller, “Optical physics of quantum wells,” in *Quantum Dynamics of Simple Systems*, 1st, Ed. CRC Press, 1996.

[107] R. H. Wang *et al.*, “Room-temperature operation of InAs quantum-dash lasers on InP [001],” *IEEE Photonics Technol. Lett.*, vol. 13, no. 8, pp. 767–769, Aug. 2001, doi: 10.1109/68.935797.

[108] D. L. Huffaker, G. Park, Z. Zou, O. B. Shchekin, and D. G. Deppe, “1.3 μm room-temperature GaAs-based quantum-dot laser,” *Appl. Phys. Lett.*, vol. 73, no. 18, pp. 2564–2566, Nov. 1998, doi: 10.1063/1.122534.

[109] C. H. Henry, “Theory of the Linewidth of Semiconductor Lasers,” *IEEE J. Quantum Electron.*, vol. 18, no. 2, pp. 259–264, 1982, doi: 10.1109/JQE.1982.1071522.

[110] R. Michalzik, *VCSELs*, vol. 166. Berlin, Heidelberg: Springer Berlin Heidelberg, 2013.

[111] A. Y. Cho and W. C. Ballamy, “GaAs planar technology by molecular beam epitaxy (MBE),” *J. Appl. Phys.*, vol. 46, no. 2, pp. 783–785, Feb. 1975, doi: 10.1063/1.321645.

[112] J. L. Jewell *et al.*, “Low-threshold electrically pumped vertical-cavity surface-emitting microlasers,” *Electron. Lett.*, vol. 25, no. 17, p. 1123, 1989, doi: 10.1049/el:19890754.

[113] F. Koyama, “Recent Advances of VCSEL Photonics,” *J. Light. Technol.*, vol. 24, no. 12, pp. 4502–4513, Dec. 2006, doi: 10.1109/JLT.2006.886064.

[114] M. San Miguel, Q. Feng, and J. V. Moloney, “Light-polarization dynamics in surface-emitting semiconductor lasers,” *Phys. Rev. A*, vol. 52, no. 2, pp. 1728–1739, Aug. 1995, doi: 10.1103/PhysRevA.52.1728.

[115] K. Iga, S. Kinoshita, and F. Koyama, “Microcavity GalaAs/GaAs surface-emitting laser with Ith = 6 mA,” *Electron. Lett.*, vol. 23, no. 3, p. 134, 1987, doi: 10.1049/el:19870095.

[116] F. Koyama, S. Kinoshita, and K. Iga, “Room-temperature continuous wave lasing characteristics of a GaAs vertical cavity surface-emitting laser,” *Appl. Phys. Lett.*, vol. 55, no. 3, pp. 221–222, Jul. 1989, doi: 10.1063/1.101913.

[117] H. E. Li and K. Iga, *Vertical-Cavity Surface-Emitting Laser Devices*, vol. 6. Berlin, Heidelberg: Springer Berlin Heidelberg, 2003.

[118] K. Iga, “Surface-emitting laser-its birth and generation of new optoelectronics field,” *IEEE J. Sel. Top. Quantum Electron.*, vol. 6, no. 6, pp. 1201–1215, Nov. 2000, doi: 10.1109/2944.902168.

[119] K. D. Choquette and H. Q. Hou, “Vertical-cavity surface emitting lasers:

moving from research to manufacturing," *Proc. IEEE*, vol. 85, no. 11, pp. 1730–1739, 1997, doi: 10.1109/5.649649.

[120] T. Baba, Y. Yogo, K. Suzuki, F. Koyama, and K. Iga, "Near room temperature continuous wave lasing characteristics of GaInAsP/InP surface emitting laser," *Electron. Lett.*, vol. 29, no. 10, pp. 913–914, May 1993, doi: 10.1049/el:19930609.

[121] Keun Ho Rhew, Su Chang Jeon, O-Kyun Kwon, Dae Hee Lee, Byung Soo Yoo, and Ilgu Yun, "Reliability Assessment of 1.55-μM Vertical Cavity Surface Emitting Lasers for Optical Communication Systems," in *2007 IEEE International Reliability Physics Symposium Proceedings. 45th Annual*, Apr. 2007, pp. 476–479, doi: 10.1109/RELPHY.2007.369937.

[122] VERTILAS GmbH, "Near-IR Gas Analysis, VCSEL Product Catalog," 2018. https://www.vertilas.com/sites/default/files/Downloads/vertilas_vcsel_gas_analysis_v10_0_0.pdf (accessed Mar. 18, 2022).

[123] Alight Technologies ApS, "Alight Technologies." https://www.alight.dk/ (accessed Mar. 18, 2022).

[124] C.-H. Cheng, W.-C. Lo, B. Su, C.-H. Wu, and G.-R. Lin, "Review of VCSELs for Complex Data-Format Transmission Beyond 100-Gbit/s," *IEEE Photonics J.*, vol. 13, no. 5, pp. 1–13, Oct. 2021, doi: 10.1109/JPHOT.2021.3104647.

[125] L. Chorchos *et al.*, "Energy Efficient 850 nm VCSEL Based Optical Transmitter and Receiver Link Capable of 80 Gbit/s NRZ Multi-Mode Fiber Data Transmission," *J. Light. Technol.*, vol. 38, no. 7, pp. 1747–1752, Apr. 2020, doi: 10.1109/JLT.2020.2970299.

[126] N. Ledentsov *et al.*, "Serial data transmission at 224 Gbit/s applying directly modulated 850 and 910 nm VCSELs," *Electron. Lett.*, vol. 57, no. 19, pp. 735–737, Sep. 2021, doi: 10.1049/ell2.12236.

[127] S. Wieczorek, B. Krauskopf, T. B. Simpson, and D. Lenstra, "The dynamical complexity of optically injected semiconductor lasers," *Phys. Rep.*, vol. 416, no. 1–2, pp. 1–128, Sep. 2005, doi: 10.1016/j.physrep.2005.06.003.

[128] G. H. M. van Tartwijk and D. Lenstra, “Semiconductor lasers with optical injection and feedback,” *Quantum Semiclassical Opt. J. Eur. Opt. Soc. Part B*, vol. 7, no. 2, pp. 87–143, Apr. 1995, doi: 10.1088/1355-5111/7/2/003.

[129] R. Lang, “Injection locking properties of a semiconductor laser,” *IEEE J. Quantum Electron.*, vol. 18, no. 6, pp. 976–983, Jun. 1982, doi: 10.1109/JQE.1982.1071632.

[130] S. Eriksson and Å. M. Lindberg, “Periodic oscillation within the chaotic region in a semiconductor laser subjected to external optical injection,” *Opt. Lett.*, vol. 26, no. 3, p. 142, Feb. 2001, doi: 10.1364/OL.26.000142.

[131] E.-K. Lee, H.-S. Pang, J.-D. Park, and H. Lee, “Bistability and chaos in an injection-locked semiconductor laser,” *Phys. Rev. A*, vol. 47, no. 1, pp. 736–739, Jan. 1993, doi: 10.1103/PhysRevA.47.736.

[132] K. Schires, A. Hurtado, I. D. Henning, and M. J. Adams, “Comprehensive experimental analysis of nonlinear dynamics in an optically-injected semiconductor laser,” *AIP Adv.*, vol. 1, no. 3, p. 032131, Sep. 2011, doi: 10.1063/1.3625868.

[133] Jia-Ming Liu and T. B. Simpson, “Four-wave mixing and optical modulation in a semiconductor laser,” *IEEE J. Quantum Electron.*, vol. 30, no. 4, pp. 957–965, Apr. 1994, doi: 10.1109/3.291366.

[134] J. I. Nishizawa and K. Ishida, “Injection-Induced Modulation of Laser Light by the Interaction of Laser Diodes,” *IEEE J. Quantum Electron.*, vol. 11, no. 7, pp. 515–519, 1975, doi: 10.1109/JQE.1975.1068656.

[135] S. Kobayashi and T. Kimura, “Coherence of injection phase-locked AlGaAs semiconductor laser,” *Electron. Lett.*, vol. 16, no. 17, p. 668, 1980, doi: 10.1049/el:19800474.

[136] S. Kobayashi, J. Yamada, S. Machida, and T. Kimura, “Single-mode operation of 500 Mbit/s modulated AlGaAs semiconductor laser by injection locking,” *Electron. Lett.*, vol. 16, no. 19, p. 746, 1980, doi: 10.1049/el:19800530.

[137] N. Schunk and K. Petermann, “Noise analysis of injection-locked

semiconductor injection lasers," *IEEE J. Quantum Electron.*, vol. 22, no. 5, pp. 642–650, May 1986, doi: 10.1109/JQE.1986.1073018.

[138] A. Furusawa, "Amplitude squeezing of a semiconductor laser with light injection," *Opt. Lett.*, vol. 21, no. 24, p. 2014, Dec. 1996, doi: 10.1364/OL.21.002014.

[139] G. M. Stéphan, "Spectral properties of an injected laser," *Phys. Rev. A*, vol. 58, no. 3, pp. 2467–2471, Sep. 1998, doi: 10.1103/PhysRevA.58.2467.

[140] Z. Liu and R. Slavik, "Optical Injection Locking: From Principle to Applications," *J. Light. Technol.*, vol. 38, no. 1, pp. 43–59, Jan. 2020, doi: 10.1109/JLT.2019.2945718.

[141] T. B. Simpson, J. M. Liu, K. F. Huang, and K. Tai, "Nonlinear dynamics induced by external optical injection in semiconductor lasers," *Quantum Semiclassical Opt. J. Eur. Opt. Soc. Part B*, vol. 9, no. 5, pp. 765–784, Oct. 1997, doi: 10.1088/1355-5111/9/5/009.

[142] F. Mogensen, H. Olesen, and G. Jacobsen, "Locking conditions and stability properties for a semiconductor laser with external light injection," *IEEE J. Quantum Electron.*, vol. 21, no. 7, pp. 784–793, Jul. 1985, doi: 10.1109/JQE.1985.1072760.

[143] Z. G. Pan *et al.*, "Optical injection induced polarization bistability in vertical-cavity surface-emitting lasers," *Appl. Phys. Lett.*, vol. 63, no. 22, pp. 2999–3001, Nov. 1993, doi: 10.1063/1.110264.

[144] I. Gatare, J. Buesa, H. Thienpont, K. Panajotov, and M. Sciamanna, "Polarization Switching Bistability and Dynamics in Vertical-Cavity Surface-Emitting Laser under Orthogonal Optical Injection," *Opt. Quantum Electron.*, vol. 38, no. 4–6, pp. 429–443, Mar. 2006, doi: 10.1007/s11082-006-0041-6.

[145] B. S. Ryvkin, K. Panajotov, E. A. Avrutin, I. Veretennicoff, and H. Thienpont, "Optical-injection-induced polarization switching in polarization-bistable vertical-cavity surface-emitting lasers," *J. Appl. Phys.*, vol. 96, no. 11, pp. 6002–6007, Dec. 2004, doi: 10.1063/1.1807519.

[146] A. Hurtado, I. D. Henning, and M. J. Adams, “Two-Wavelength Switching With a 1550 nm VCSEL Under Single Orthogonal Optical Injection,” *IEEE J. Sel. Top. Quantum Electron.*, vol. 14, no. 3, pp. 911–917, 2008, doi: 10.1109/JSTQE.2008.918312.

[147] P. Guo, W. Yang, D. Parekh, C. J. Chang-Hasnain, A. Xu, and Z. Chen, “Experimental and theoretical study of wide hysteresis cycles in 1550 nm VCSELs under optical injection,” *Opt. Express*, vol. 21, no. 3, p. 3125, Feb. 2013, doi: 10.1364/OE.21.003125.

[148] Y. Hong, P. S. Spencer, and K. A. Shore, “Power and frequency dependence of hysteresis in optically bistable injection-locked VCSELs,” *Electron. Lett.*, vol. 37, no. 9, p. 569, 2001, doi: 10.1049/el:20010386.

[149] Y. Hong, P. S. Spencer, P. Rees, and K. A. Shore, “Optical injection dynamics of two-mode vertical cavity surface-emitting semiconductor lasers,” *IEEE J. Quantum Electron.*, vol. 38, no. 3, pp. 274–278, Mar. 2002, doi: 10.1109/3.985568.

[150] H. Kawaguchi, *Bistabilities and Nonlinearities in Laser Diodes*. Norwood, MA: Artech House, 1994.

[151] J. BuesaAltes, I. Gatare, K. Panajotov, H. Thienpont, and M. Sciamanna, “Mapping of the Dynamics Induced by Orthogonal Optical Injection in Vertical-Cavity Surface-Emitting Lasers,” *IEEE J. Quantum Electron.*, vol. 42, no. 2, pp. 198–207, Feb. 2006, doi: 10.1109/JQE.2005.862025.

[152] A. Hurtado, A. Quirce, A. Valle, L. Pesquera, and M. J. Adams, “Nonlinear dynamics induced by parallel and orthogonal optical injection in 1550 nm Vertical-Cavity Surface-Emitting Lasers (VCSELs),” *Opt. Express*, vol. 18, no. 9, pp. 9423–9428, Apr. 2010, doi: 10.1364/OE.18.009423.

[153] R. Al-Seyab, K. Schires, N. Ali Khan, A. Hurtado, I. D. Henning, and M. J. Adams, “Dynamics of Polarized Optical Injection in 1550-nm VCSELs: Theory and Experiments,” *IEEE J. Sel. Top. Quantum Electron.*, vol. 17, no. 5, pp. 1242–1249, Sep. 2011, doi: 10.1109/JSTQE.2011.2138683.

[154] J. P. Toomey *et al.*, “Stability of the nonlinear dynamics of an optically injected VCSEL,” *Opt. Express*, vol. 20, no. 9, p. 10256, Apr. 2012, doi: 10.1364/OE.20.010256.

[155] M. Ghisoni, J. Halonen, K. A. Shore, A. Larsson, and Y. Hong, “Polarisation switching in a vertical cavity surface emitting semiconductor laser by frequency detuning,” *IEE Proc. - Optoelectron.*, vol. 148, no. 1, pp. 31–34, Feb. 2001, doi: 10.1049/ip-opt:20010246.

[156] Y. Hong, P. S. Spencer, S. Bandyopadhyay, P. Rees, and K. A. Shore, “Polarisation-resolved chaos and instabilities in a vertical cavity surface emitting laser subject to optical injection,” *Opt. Commun.*, vol. 216, no. 1–3, pp. 185–189, Feb. 2003, doi: 10.1016/S0030-4018(02)02296-4.

[157] F. Denis-le Coarer *et al.*, “Polarization dynamics induced by parallel optical injection in a single-mode VCSEL,” *Opt. Lett.*, vol. 42, no. 11, p. 2130, Jun. 2017, doi: 10.1364/OL.42.002130.

[158] P. Pérez, A. Quirce, L. Pesquera, and A. Valle, “Polarization-resolved nonlinear dynamics in long-wavelength single-mode VCSELs subject to orthogonal optical injection,” Feb. 2011, p. 79330B, doi: 10.1117/12.875191.

[159] S. Barbay, R. Kuszelewicz, and A. M. Yacomotti, “Excitability in a semiconductor laser with saturable absorber,” *Opt. Lett.*, vol. 36, no. 23, p. 4476, Dec. 2011, doi: 10.1364/OL.36.004476.

[160] A. Hurtado and J. Javaloyes, “Controllable spiking patterns in long-wavelength vertical cavity surface emitting lasers for neuromorphic photonics systems,” *Appl. Phys. Lett.*, vol. 107, no. 24, p. 241103, Dec. 2015, doi: 10.1063/1.4937730.

[161] E. M. IZHIKEVICH, “NEURAL EXCITABILITY, SPIKING AND BURSTING,” *Int. J. Bifurc. Chaos*, vol. 10, no. 06, pp. 1171–1266, Jun. 2000, doi: 10.1142/S0218127400000840.

[162] E. M. Izhikevich, “Class 1 neural excitability, conventional synapses, weakly connected networks, and mathematical foundations of pulse-coupled models,”

IEEE Trans. Neural Networks, vol. 10, no. 3, pp. 499–507, May 1999, doi: 10.1109/72.761707.

[163] A. Hurtado, K. Schires, I. D. Henning, and M. J. Adams, "Investigation of vertical cavity surface emitting laser dynamics for neuromorphic photonic systems," *Appl. Phys. Lett.*, vol. 100, no. 10, p. 103703, 2012, doi: 10.1063/1.3692726.

[164] R. Al-Seyab, I. D. Henning, M. J. Adams, and A. Hurtado, "Controlled single- and multiple-pulse excitability in vcsels for novel spiking photonic neurons," *Conf. Dig. - IEEE Int. Semicond. Laser Conf.*, pp. 165–166, 2014, doi: 10.1109/ISLC.2014.215.

[165] M. Turconi, B. Garbin, M. R. Feyereisen, M. Giudici, and S. Barland, "Control of excitable pulses in an injection-locked semiconductor laser.," *Phys. Rev. E. Stat. Nonlin. Soft Matter Phys.*, vol. 88 2, p. 22923, 2013.

[166] B. Garbin, G. Tissoni, and S. Barland, "Excitable pulses and diffusion of localized states in a driven semiconductor laser with delay," *Cybern. Phys.*, no. Volume 7, 2018, Number 3, pp. 96–101, Nov. 2018, doi: 10.35470/2226-4116-2018-7-3-96-101.

[167] A. Dolcemascolo, B. Garbin, B. Peyce, R. Veltz, and S. Barland, "Resonator neuron and triggering multipulse excitability in laser with injected signal," *Phys. Rev. E*, vol. 98, no. 6, p. 062211, Dec. 2018, doi: 10.1103/PhysRevE.98.062211.

[168] F. Selmi *et al.*, "Spike latency and response properties of an excitable micropillar laser," *Phys. Rev. E*, vol. 94, no. 4, p. 42219, Oct. 2016, doi: 10.1103/PhysRevE.94.042219.

[169] F. Selmi, R. Braive, G. Beaudoin, I. Sagnes, R. Kuszelewicz, and S. Barbay, "Relative Refractory Period in an Excitable Semiconductor Laser," *Phys. Rev. Lett.*, vol. 112, no. 18, p. 183902, May 2014, doi: 10.1103/PhysRevLett.112.183902.

[170] F. Selmi, R. Braive, G. Beaudoin, I. Sagnes, R. Kuszelewicz, and S. Barbay,

"Temporal summation in a neuromimetic micropillar laser," *Opt. Lett.*, vol. 40, no. 23, pp. 5690–5693, 2015, doi: 10.1364/OL.40.005690.

[171] J. L. A. Dubbeldam, B. Krauskopf, and D. Lenstra, "Excitability and coherence resonance in lasers with saturable absorber," *Phys. Rev. E*, vol. 60, no. 6, pp. 6580–6588, Dec. 1999, doi: 10.1103/PhysRevE.60.6580.

[172] M. Yamada, "A theoretical analysis of self-sustained pulsation phenomena in narrow-stripe semiconductor lasers," *IEEE J. Quantum Electron.*, vol. 29, no. 5, pp. 1330–1336, 1993, doi: 10.1109/3.236146.

[173] V. A. Pammi, K. Alfaro-Bittner, M. G. Clerc, and S. Barbay, "Photonic Computing With Single and Coupled Spiking Micropillar Lasers," *IEEE J. Sel. Top. Quantum Electron.*, vol. 26, no. 1, pp. 1–7, Jan. 2020, doi: 10.1109/JSTQE.2019.2929187.

[174] S. Terrien *et al.*, "Pulse train interaction and control in a microcavity laser with delayed optical feedback," *Opt. Lett.*, vol. 43, no. 13, p. 3013, Jul. 2018, doi: 10.1364/OL.43.003013.

[175] S. Terrien *et al.*, "Equalization of pulse timings in an excitable microlaser system with delay," *Phys. Rev. Res.*, vol. 2, no. 2, p. 023012, Apr. 2020, doi: 10.1103/PhysRevResearch.2.023012.

[176] J. M. Bekkers and C. F. Stevens, "Excitatory and inhibitory autaptic currents in isolated hippocampal neurons maintained in cell culture.," *Proc. Natl. Acad. Sci.*, vol. 88, no. 17, pp. 7834–7838, Sep. 1991, doi: 10.1073/pnas.88.17.7834.

[177] M. A. Nahmias, B. J. Shastri, A. N. Tait, and P. R. Prucnal, "A Leaky Integrate-and-Fire Laser Neuron for Ultrafast Cognitive Computing," *IEEE J. Sel. Top. Quantum Electron.*, vol. 19, no. 5, pp. 1–12, 2013, doi: 10.1109/JSTQE.2013.2257700.

[178] S. Xiang, A. Wen, and W. Pan, "Emulation of Spiking Response and Spiking Frequency Property in VCSEL-Based Photonic Neuron," *IEEE Photonics J.*, vol. 8, no. 5, 2016, doi: 10.1109/JPHOT.2016.2614104.

[179] S. Y. Xiang *et al.*, "Cascadable Neuron-Like Spiking Dynamics in Coupled

VCSELs Subject to Orthogonally Polarized Optical Pulse Injection," *IEEE J. Sel. Top. Quantum Electron.*, vol. 23, no. 6, 2017, doi: 10.1109/JSTQE.2017.2678170.

[180] Y. Zhang, S. Xiang, X. Guo, A. Wen, and Y. Hao, "All-optical inhibitory dynamics in photonic neuron based on polarization mode competition in a VCSEL with an embedded saturable absorber," *Opt. Lett.*, vol. 44, no. 7, p. 1548, Apr. 2019, doi: 10.1364/OL.44.001548.

[181] M. Skontranis, G. Sarantoglou, S. Deligiannidis, A. Bogris, and C. Mesaritakis, "Time-Multiplexed Spiking Convolutional Neural Network Based on VCSELs for Unsupervised Image Classification," *Appl. Sci.*, vol. 11, no. 4, 2021, doi: 10.3390/app11041383.

[182] Y. Zhang, S. Xiang, J. Gong, X. Guo, A. Wen, and Y. Hao, "Spike encoding and storage properties in mutually coupled vertical-cavity surface-emitting lasers subject to optical pulse injection," *Appl. Opt.*, vol. 57, no. 7, p. 1731, Mar. 2018, doi: 10.1364/AO.57.001731.

[183] S. Xiang, Y. Zhang, X. Guo, A. Wen, and Y. Hao, "Photonic Generation of Neuron-Like Dynamics Using VCSELs Subject to Double Polarized Optical Injection," *J. Light. Technol.*, vol. 36, no. 19, 2018, doi: 10.1109/JLT.2018.2818195.

[184] Y. Zhang, S. Xiang, X. Guo, A. Wen, and Y. Hao, "Polarization-resolved and polarization- multiplexed spike encoding properties in photonic neuron based on VCSEL-SA," *Sci. Reports 2018 81*, vol. 8, no. 1, pp. 1–9, 2018, doi: 10.1038/s41598-018-34537-x.

[185] Z. Zhang, Z. Wu, D. Lu, G. Xia, and T. Deng, "Controllable spiking dynamics in cascaded VCSEL-SA photonic neurons," *Nonlinear Dyn.*, vol. 99, no. 2, 2020, doi: 10.1007/s11071-019-05339-1.

[186] Y. Zhang, S. Xiang, X. Guo, A. Wen, and Y. Hao, "The Winner-Take-All Mechanism for All-Optical Systems of Pattern Recognition and Max-Pooling Operation," *J. Light. Technol.*, vol. 38, no. 18, pp. 5071–5077, 2020, doi: 10.1109/JLT.2020.3000670.

[187] S. Xiang *et al.*, “Computing Primitive of Fully VCSEL-Based All-Optical Spiking Neural Network for Supervised Learning and Pattern Classification,” *IEEE Trans. Neural Networks Learn. Syst.*, vol. 32, no. 6, pp. 2494–2505, 2021, doi: 10.1109/TNNLS.2020.3006263.

[188] S. Xiang *et al.*, “Numerical Implementation of Wavelength-Dependent Photonic Spike Timing Dependent Plasticity Based on VCSOA,” *IEEE J. Quantum Electron.*, vol. 54, no. 6, pp. 1–7, Dec. 2018, doi: 10.1109/JQE.2018.2879484.

[189] S. Xiang, Y. Zhang, J. Gong, X. Guo, L. Lin, and Y. Hao, “STDP-Based Unsupervised Spike Pattern Learning in a Photonic Spiking Neural Network With VCSELs and VCSOAs,” *IEEE J. Sel. Top. Quantum Electron.*, vol. 25, no. 6, 2019, doi: 10.1109/JSTQE.2019.2911565.

[190] Z. Song, S. Xiang, Z. Ren, G. Han, and Y. Hao, “Spike Sequence Learning in a Photonic Spiking Neural Network Consisting of VCSELs-SA With Supervised Training,” *IEEE J. Sel. Top. Quantum Electron.*, vol. 26, no. 5, 2020, doi: 10.1109/JSTQE.2020.2975564.

[191] S. Gao, S. Xiang, Z. Song, Y. Han, and Y. Hao, “All-optical Sudoku solver with photonic spiking neural network,” *Opt. Commun.*, vol. 495, p. 127068, Sep. 2021, doi: 10.1016/j.optcom.2021.127068.

[192] S. Xiang, Z. Ren, Y. Zhang, Z. Song, and Y. Hao, “All-optical neuromorphic XOR operation with inhibitory dynamics of a single photonic spiking neuron based on a VCSEL-SA,” *Opt. Lett.*, vol. 45, no. 5, pp. 1104–1107, 2020, doi: 10.1364/OL.383942.

[193] J. Robertson, M. Hejda, J. Bueno, and A. Hurtado, “Ultrafast optical integration and pattern classification for neuromorphic photonics based on spiking VCSEL neurons,” *Sci. Rep.*, vol. 10, no. 1, p. 6098, Dec. 2020, doi: 10.1038/s41598-020-62945-5.

[194] J. Robertson, Y. Zhang, M. Hejda, J. Bueno, S. Xiang, and A. Hurtado, “Image edge detection with a photonic spiking VCSEL-neuron,” *Opt. Express*, vol. 28, no. 25, pp. 37526–37537, Dec. 2020, doi: 10.1364/OE.408747.

[195] M. Hejda, J. Robertson, J. Bueno, J. A. Alanis, and A. Hurtado, "Neuromorphic encoding of image pixel data into rate-coded optical spike trains with a photonic VCSEL-neuron," *APL Photonics*, vol. 6, no. 6, p. 60802, 2021, doi: 10.1063/5.0048674.

[196] J. Robertson, E. Wade, and A. Hurtado, "Electrically Controlled Neuron-Like Spiking Regimes in Vertical-Cavity Surface-Emitting Lasers at Ultrafast Rates," *IEEE J. Sel. Top. Quantum Electron.*, vol. 25, no. 6, 2019, doi: 10.1109/JSTQE.2019.2899040.

[197] J. Robertson, T. Deng, J. Javaloyes, and A. Hurtado, "Controlled inhibition of spiking dynamics in VCSELs for neuromorphic photonics: Theory and experiments," *Opt. Lett.*, vol. 42, no. 8, pp. 1560–1563, 2017, doi: 10.1364/OL.42.001560.

[198] T. Deng, J. Robertson, and A. Hurtado, "Controlled Propagation of Spiking Dynamics in Vertical-Cavity Surface-Emitting Lasers: Towards Neuromorphic Photonic Networks," *IEEE J. Sel. Top. Quantum Electron.*, vol. 23, no. 6, 2017, doi: 10.1109/JSTQE.2017.2685140.

[199] T. Deng *et al.*, "Stable Propagation of Inhibited Spiking Dynamics in Vertical-Cavity Surface-Emitting Lasers for Neuromorphic Photonic Networks," *IEEE Access*, vol. 6, 2018, doi: 10.1109/ACCESS.2018.2878940.

[200] J. Robertson, E. Wade, Y. Kopp, J. Bueno, and A. Hurtado, "Towards Neuromorphic Photonic Networks of Ultrafast Spiking Laser Neurons," *IEEE J. Sel. Top. Quantum Electron.*, 2019, doi: 10.1109/JSTQE.2019.2931215.

[201] Y. Zhang, J. Robertson, S. Xiang, M. Hejda, J. Bueno, and A. Hurtado, "All-optical neuromorphic binary convolution with a spiking VCSEL neuron for image gradient magnitudes," *Photon. Res.*, vol. 9, no. 5, pp. B201–B209, 2021, doi: 10.1364/PRJ.412141.

[202] J. Robertson *et al.*, "Ultrafast neuromorphic photonic image processing with a VCSEL neuron," *Sci. Rep.*, vol. 12, no. 1, p. 4874, Dec. 2022, doi: 10.1038/s41598-022-08703-1.

[203] M. Hejda, J. Robertson, J. Bueno, and A. Hurtado, “Spike-based information encoding in vertical cavity surface emitting lasers for neuromorphic photonic systems,” *JPhys Photonics*, vol. 2, no. 4, p. 44001, 2020, doi: 10.1088/2515-7647/aba670.

[204] Y. Zhang *et al.*, “Experimental demonstration of pyramidal neuron-like dynamics dominated by dendritic action potentials based on a VCSEL for all-optical XOR classification task,” *Photonics Res.*, vol. 9, no. 6, p. 1055, Jun. 2021, doi: 10.1364/PRJ.422628.

[205] J. Bueno, J. Robertson, M. Hejda, and A. Hurtado, “Comprehensive Performance Analysis of a VCSEL-Based Photonic Reservoir Computer,” *IEEE Photonics Technol. Lett.*, vol. 33, no. 16, pp. 920–923, Aug. 2021, doi: 10.1109/LPT.2021.3075095.

[206] L. Appeltant *et al.*, “Information processing using a single dynamical node as complex system,” *Nat. Commun.*, vol. 2, no. 1, p. 468, Sep. 2011, doi: 10.1038/ncomms1476.

[207] J. Vatin, D. Rontani, and M. Sciamanna, “Enhanced performance of a reservoir computer using polarization dynamics in VCSELs,” *Opt. Lett.*, vol. 43, no. 18, p. 4497, Sep. 2018, doi: 10.1364/OL.43.004497.

[208] J. Vatin, D. Rontani, and M. Sciamanna, “Experimental reservoir computing using VCSEL polarization dynamics,” *Opt. Express*, vol. 27, no. 13, p. 18579, Jun. 2019, doi: 10.1364/OE.27.018579.

[209] X. Porte, A. Skalli, N. Haghighi, S. Reitzenstein, J. A. Lott, and D. Brunner, “A complete, parallel and autonomous photonic neural network in a semiconductor multimode laser,” *J. Phys. Photonics*, vol. 3, no. 2, p. 024017, Apr. 2021, doi: 10.1088/2515-7647/abf6bd.

[210] A. Skalli, X. Porte, N. Haghighi, S. Reitzenstein, J. A. Lott, and D. Brunner, “Computational metrics and parameters of an injection-locked large area semiconductor laser for neural network computing,” Dec. 2021, [Online]. Available: http://arxiv.org/abs/2112.08947.

[211] A. Hurtado, I. D. Henning, and M. J. Adams, “Effects of parallel and orthogonal polarization on nonlinear optical characteristics of a 1550 nm VCSOA,” *Opt. Express*, vol. 15, no. 14, p. 9084, 2007, doi: 10.1364/OE.15.009084.

[212] J. A. Alanis, J. Robertson, M. Hejda, and A. Hurtado, “Weight adjustable photonic synapse by nonlinear gain in a vertical cavity semiconductor optical amplifier,” *Appl. Phys. Lett.*, vol. 119, no. 20, p. 201104, 2021, doi: 10.1063/5.0064374.

[213] A. N. Tait, T. Ferreira de Lima, M. A. Nahmias, B. J. Shastri, and P. R. Prucnal, “Continuous Calibration of Microring Weights for Analog Optical Networks,” *IEEE Photonics Technol. Lett.*, vol. 28, no. 8, pp. 887–890, Apr. 2016, doi: 10.1109/LPT.2016.2516440.

[214] Z. Cheng, C. Ríos, W. H. P. Pernice, C. D. Wright, and H. Bhaskaran, “On-chip photonic synapse,” *Sci. Adv.*, vol. 3, no. 9, Sep. 2017, doi: 10.1126/sciadv.1700160.

[215] J. Robertson, J. A. Alanis, M. Hejda, and A. Hurtado, “Photonic synaptic system for MAC operations by interconnected vertical cavity surface emitting lasers,” *Opt. Mater. Express*, vol. 12, no. 4, p. 1417, Apr. 2022, doi: 10.1364/OME.450923.

[216] F. T. Arecchi, G. Giacomelli, A. Lapucci, and R. Meucci, “Two-dimensional representation of a delayed dynamical system,” *Phys. Rev. A*, vol. 45, no. 7, pp. R4225–R4228, Apr. 1992, doi: 10.1103/PhysRevA.45.R4225.

[217] P. Perez, A. Valle, L. Pesquera, and A. Quirce, “All-Optical Inverter Based on Polarization Switching in VCSELs Subject to Single and Dual Optical Injection,” *IEEE J. Sel. Top. Quantum Electron.*, vol. 19, no. 4, pp. 1700408–1700408, Jul. 2013, doi: 10.1109/JSTQE.2012.2235823.

[218] F. V Salinas, K. Malik, and H. T. Benzon, “Chapter 44 - Local Anesthetics for Regional Anesthesia and Pain Management,” in *Raj’s Practical Management of Pain (Fourth Edition)*, Fourth Edi., H. T. Benzon, J. P. Rathmell, C. L. Wu, D. C. Turk, and C. E. Argoff, Eds. Philadelphia: Mosby, 2008, pp. 811–838.

[219] OpenStax, *Anatomy & Physiology*. OpenStax CNX, 2015.

[220] E. D. Adrian and Y. Zotterman, “The impulses produced by sensory nerve-endings,” *J. Physiol.*, vol. 61, no. 2, pp. 151–171, Apr. 1926, doi: 10.1113/jphysiol.1926.sp002281.

[221] S. Panzeri, N. Brunel, N. K. Logothetis, and C. Kayser, “Sensory neural codes using multiplexed temporal scales,” *Trends Neurosci.*, vol. 33, no. 3, pp. 111–120, Mar. 2010, doi: 10.1016/j.tins.2009.12.001.

[222] D. A. Butts *et al.*, “Temporal precision in the neural code and the timescales of natural vision,” *Nature*, vol. 449, no. 7158, pp. 92–95, Sep. 2007, doi: 10.1038/nature06105.

[223] D. S. Reich, F. Mechler, and J. D. Victor, “Temporal Coding of Contrast in Primary Visual Cortex: When, What, and Why,” *J. Neurophysiol.*, vol. 85, no. 3, pp. 1039–1050, Mar. 2001, doi: 10.1152/jn.2001.85.3.1039.

[224] S. Furukawa and J. C. Middlebrooks, “Cortical Representation of Auditory Space: Information-Bearing Features of Spike Patterns,” *J. Neurophysiol.*, vol. 87, no. 4, pp. 1749–1762, Apr. 2002, doi: 10.1152/jn.00491.2001.

[225] O. K. Swanson and A. Maffei, “From Hiring to Firing: Activation of Inhibitory Neurons and Their Recruitment in Behavior,” *Front. Mol. Neurosci.*, vol. 12, Jul. 2019, doi: 10.3389/fnmol.2019.00168.

[226] T. P. Vogels *et al.*, “Inhibitory synaptic plasticity: spike timing-dependence and putative network function,” *Front. Neural Circuits*, vol. 7, 2013, doi: 10.3389/fncir.2013.00119.

[227] B. Garbin, A. Dolcemascolo, F. Prati, J. Javaloyes, G. Tissoni, and S. Barland, “Refractory period of an excitable semiconductor laser with optical injection,” *Phys. Rev. E*, vol. 95, no. 1, p. 012214, Jan. 2017, doi: 10.1103/PhysRevE.95.012214.

[228] K. Koizumi, M. Yoshida, and M. Nakazawa, “10-GHz 11.5-ps Pulse Generation From a Single-Mode Gain-Switched InGaAs VCSEL at 1.1 μm,” *IEEE Photonics Technol. Lett.*, vol. 21, no. 22, pp. 1704–1706,

Nov. 2009, doi: 10.1109/LPT.2009.2031920.

[229] D. Tauber, G. Wang, R. S. Geels, J. E. Bowers, and L. A. Coldren, “Large and small signal dynamics of vertical cavity surface emitting lasers,” *Appl. Phys. Lett.*, vol. 62, no. 4, pp. 325–327, Jan. 1993, doi: 10.1063/1.108947.

[230] J. von Neumann, *The Computer and the Brain*. USA: Yale University Press, 1958.

[231] T. Van Vaerenbergh *et al.*, “Cascadable excitability in microrings,” *Opt. Express*, vol. 20, no. 18, p. 20292, Aug. 2012, doi: 10.1364/OE.20.020292.

[232] T. Van Vaerenbergh, K. Alexander, J. Dambre, and P. Bienstman, “Excitation transfer between optically injected microdisk lasers,” *Opt. Express*, vol. 21, no. 23, p. 28922, Nov. 2013, doi: 10.1364/OE.21.028922.

[233] C. F. Marki, S. Moro, D. R. Jorgesen, P. Wen, and S. C. Esener, “Cascadable optical inversion using 1550 nm VCSEL,” *Electron. Lett.*, vol. 44, no. 4, p. 292, 2008, doi: 10.1049/el:20082539.

[234] T. Deng *et al.*, “Stable propagation of inhibited spiking dynamics in vertical-cavity surface-emitting lasers for neuromorphic photonic networks,” *IEEE Access*, vol. 6, pp. 67951–67958, 2018, doi: 10.1109/ACCESS.2018.2878940.

[235] T. Euler, S. Haverkamp, T. Schubert, and T. Baden, “Retinal bipolar cells: elementary building blocks of vision,” *Nat. Rev. Neurosci.*, vol. 15, no. 8, pp. 507–519, Aug. 2014, doi: 10.1038/nrn3783.

[236] R. H. Masland, “The Neuronal Organization of the Retina,” *Neuron*, vol. 76, no. 2, pp. 266–280, Oct. 2012, doi: 10.1016/j.neuron.2012.10.002.

[237] E. R. Kandel, S. Mack, T. M. Jessell, J. H. Schwartz, S. A. Siegelbaum, and A. J. Hudspeth, *Principles of Neural Science, Fifth Edition*. McGraw-Hill Education, 2013.

[238] C. A. Mead and M. A. Mahowald, “A silicon model of early visual processing,” *Neural Networks*, vol. 1, no. 1, pp. 91–97, Jan. 1988, doi: 10.1016/0893-6080(88)90024-X.

[239] C. Mead, “Neuromorphic electronic systems,” *Proc. IEEE*, vol. 78, no. 10, pp. 1629–1636, 1990, doi: 10.1109/5.58356.

[240] M. A. Mahowald and C. Mead, “The Silicon Retina,” *Sci. Am.*, vol. 264, no. 5, pp. 76–82, May 1991, doi: 10.1038/scientificamerican0591-76.

[241] C. Posch, T. Serrano-Gotarredona, B. Linares-Barranco, and T. Delbruck, “Retinomorphic Event-Based Vision Sensors: Bioinspired Cameras With Spiking Output,” *Proc. IEEE*, vol. 102, no. 10, pp. 1470–1484, Oct. 2014, doi: 10.1109/JPROC.2014.2346153.

[242] T. Serrano-Gotarredona and B. Linares-Barranco, “A 128 x 128 1.5% Contrast Sensitivity 0.9% FPN 3 µs Latency 4 mW Asynchronous Frame-Free Dynamic Vision Sensor Using Transimpedance Preamplifiers,” *IEEE J. Solid-State Circuits*, vol. 48, no. 3, pp. 827–838, Mar. 2013, doi: 10.1109/JSSC.2012.2230553.

[243] A. Hurtado, I. D. Henning, and M. J. Adams, “Optical neuron using polarisation switching in a 1550nm-VCSEL,” *Opt. Express*, vol. 18, no. 24, p. 25170, Nov. 2010, doi: 10.1364/OE.18.025170.

[244] J. Dong, X. Zhang, J. Xu, D. Huang, S. Fu, and P. Shum, “40 Gb/s all-optical NRZ to RZ format conversion using single SOA assisted by optical bandpass filter,” *Opt. Express*, vol. 15, no. 6, p. 2907, 2007, doi: 10.1364/OE.15.002907.

[245] Lei Xu, B. C. Wang, V. Baby, I. Glesk, and P. R. Prucnal, “All-optical data format conversion between RZ and NRZ based on a Mach-Zehnder interferometric wavelength converter,” *IEEE Photonics Technol. Lett.*, vol. 15, no. 2, pp. 308–310, Feb. 2003, doi: 10.1109/LPT.2002.806105.

[246] P. Y. Ma, B. J. Shastri, T. F. de Lima, A. N. Tait, M. A. Nahmias, and P. R. Prucnal, “All-optical digital-to-spike conversion using a graphene excitable laser,” *Opt. Express*, vol. 25, no. 26, p. 33504, Dec. 2017, doi: 10.1364/OE.25.033504.

[247] C. Pouzat and A. Marty, “Autaptic inhibitory currents recorded from

interneurones in rat cerebellar slices," *J. Physiol.*, vol. 509, no. 3, pp. 777–783, Jun. 1998, doi: 10.1111/j.1469-7793.1998.777bm.x.

[248] J. Lübke, H. Markram, M. Frotscher, and B. Sakmann, "Frequency and Dendritic Distribution of Autapses Established by Layer 5 Pyramidal Neurons in the Developing Rat Neocortex: Comparison with Synaptic Innervation of Adjacent Neurons of the Same Class," *J. Neurosci.*, vol. 16, no. 10, pp. 3209–3218, May 1996, doi: 10.1523/JNEUROSCI.16-10-03209.1996.

[249] R. Saada, N. Miller, I. Hurwitz, and A. J. Susswein, "Autaptic Excitation Elicits Persistent Activity and a Plateau Potential in a Neuron of Known Behavioral Function," *Curr. Biol.*, vol. 19, no. 6, pp. 479–484, Mar. 2009, doi: 10.1016/j.cub.2009.01.060.

[250] A. Bacci and J. R. Huguenard, "Enhancement of Spike-Timing Precision by Autaptic Transmission in Neocortical Inhibitory Interneurons," *Neuron*, vol. 49, no. 1, pp. 119–130, Jan. 2006, doi: 10.1016/j.neuron.2005.12.014.

[251] C. G. Rusin, S. E. Johnson, J. Kapur, and J. L. Hudson, "Engineering the synchronization of neuron action potentials using global time-delayed feedback stimulation," *Phys. Rev. E*, vol. 84, no. 6, p. 066202, Dec. 2011, doi: 10.1103/PhysRevE.84.066202.

[252] F. Kimura, Y. Otsu, and T. Tsumoto, "Presynaptically Silent Synapses: Spontaneously Active Terminals Without Stimulus-Evoked Release Demonstrated in Cortical Autapses," *J. Neurophysiol.*, vol. 77, no. 5, pp. 2805–2815, May 1997, doi: 10.1152/jn.1997.77.5.2805.

[253] H. Wang, J. Ma, Y. Chen, and Y. Chen, "Effect of an autapse on the firing pattern transition in a bursting neuron," *Commun. Nonlinear Sci. Numer. Simul.*, vol. 19, no. 9, pp. 3242–3254, Sep. 2014, doi: 10.1016/j.cnsns.2014.02.018.

[254] H.-T. Wang and Y. Chen, "Firing dynamics of an autaptic neuron," *Chinese Phys. B*, vol. 24, no. 12, p. 128709, Dec. 2015, doi: 10.1088/1674-1056/24/12/128709.

[255] K. Kikuchi and T. Okoshi, “Simple formula giving spectrum-narrowing ratio of semiconductor-laser output obtained by optical feedback,” *Electron. Lett.*, vol. 18, no. 1, p. 10, 1982, doi: 10.1049/el:19820008.

[256] L. Goldberg, H. F. Taylor, A. Dandridge, J. F. Weller, and R. O. Miles, “Spectral Characteristics of Semiconductor Lasers with Optical Feedback,” *IEEE Trans. Microw. Theory Tech.*, vol. 30, no. 4, pp. 401–410, 1982, doi: 10.1109/TMTT.1982.1131081.

[257] T. Heil, I. Fischer, and W. Elsäßer, “Coexistence of low-frequency fluctuations and stable emission on a single high-gain mode in semiconductor lasers with external optical feedback,” *Phys. Rev. A*, vol. 58, no. 4, pp. R2672–R2675, Oct. 1998, doi: 10.1103/PhysRevA.58.R2672.

[258] I. Fischer, G. H. M. van Tartwijk, A. M. Levine, W. Elsässer, E. Göbel, and D. Lenstra, “Fast Pulsing and Chaotic Itinerancy with a Drift in the Coherence Collapse of Semiconductor Lasers,” *Phys. Rev. Lett.*, vol. 76, no. 2, pp. 220–223, Jan. 1996, doi: 10.1103/PhysRevLett.76.220.

[259] T. Suzuki, T. Endo, T. Iwana, and O. Sasaki, “A Tunable External Cavity Laser Diode Possessing a Stable Wavelength,” *Opt. Rev.*, vol. 14, no. 1, pp. 23–28, Jan. 2007, doi: 10.1007/s10043-007-0023-3.

[260] J.-G. Wu *et al.*, “Time delay signature concealment of optical feedback induced chaos in an external cavity semiconductor laser,” *Opt. Express*, vol. 18, no. 7, p. 6661, Mar. 2010, doi: 10.1364/OE.18.006661.

[261] I. Kanter, Y. Aviad, I. Reidler, E. Cohen, and M. Rosenbluh, “An optical ultrafast random bit generator,” *Nat. Photonics*, vol. 4, no. 1, pp. 58–61, Jan. 2010, doi: 10.1038/nphoton.2009.235.

[262] J. Bueno, D. Brunner, M. C. Soriano, and I. Fischer, “Conditions for reservoir computing performance using semiconductor lasers with delayed optical feedback,” *Opt. Express*, vol. 25, no. 3, p. 2401, Feb. 2017, doi: 10.1364/OE.25.002401.

[263] F. Marino and G. Giacomelli, “Pseudo-spatial coherence resonance in an

excitable laser with long delayed feedback," *Chaos An Interdiscip. J. Nonlinear Sci.*, vol. 27, no. 11, p. 114302, Nov. 2017, doi: 10.1063/1.5006744.

[264] B. Kelleher, C. Bonatto, P. Skoda, S. P. Hegarty, and G. Huyet, "Excitation regeneration in delay-coupled oscillators," *Phys. Rev. E*, vol. 81, no. 3, p. 036204, Mar. 2010, doi: 10.1103/PhysRevE.81.036204.

[265] Y.-S. Hou, G.-Q. Xia, E. Jayaprasath, D.-Z. Yue, W.-Y. Yang, and Z.-M. Wu, "Prediction and classification performance of reservoir computing system using mutually delay-coupled semiconductor lasers," *Opt. Commun.*, vol. 433, pp. 215–220, Feb. 2019, doi: 10.1016/j.optcom.2018.10.014.

[266] W. Gerstner, W. M. Kistler, R. Naud, and L. Paninski, *Neuronal Dynamics: From Single Neurons to Networks and Models of Cognition*, 1st ed. Cambridge: Cambridge university Press, 2014.

[267] P. Maršálek, C. Koch, and J. Maunsell, "On the relationship between synaptic input and spike output jitter in individual neurons," *Proc. Natl. Acad. Sci.*, vol. 94, no. 2, pp. 735–740, Jan. 1997, doi: 10.1073/pnas.94.2.735.

[268] N. Sebe, I. Cohen, A. Garg, and T. S. Huang, *Machine Learning in Computer Vision*, vol. 29. Berlin/Heidelberg: Springer-Verlag, 2005.

[269] G. Litjens *et al.*, "A survey on deep learning in medical image analysis," *Med. Image Anal.*, vol. 42, pp. 60–88, Dec. 2017, doi: 10.1016/j.media.2017.07.005.

[270] J. Janai, F. Güney, A. Behl, and A. Geiger, "Computer Vision for Autonomous Vehicles: Problems, Datasets and State of the Art," Apr. 2017, [Online]. Available: http://arxiv.org/abs/1704.05519.

[271] D. Marr and H. Hildreth, "Theory of edge detection," *Proc. R. Soc. London. Ser. B. Biol. Sci.*, vol. 207, no. 1167, pp. 187–217, Feb. 1980, doi: 10.1098/rspb.1980.0020.

[272] M. A. El-Sayed, Y. A. Estaitia, and M. A. Khafagy, "Automated Edge Detection Using Convolutional Neural Network," *Int. J. Adv. Comput. Sci. Appl.*, vol. 4, no. 10, 2013, doi: 10.14569/IJACSA.2013.041003.

[273] C. Farabet, C. Couprie, L. Najman, and Y. LeCun, “Learning Hierarchical Features for Scene Labeling,” *IEEE Trans. Pattern Anal. Mach. Intell.*, vol. 35, no. 8, pp. 1915–1929, Aug. 2013, doi: 10.1109/TPAMI.2012.231.

[274] L. Cavigelli, M. Magno, and L. Benini, “Accelerating real-time embedded scene labeling with convolutional networks,” in *Proceedings of the 52nd Annual Design Automation Conference*, Jun. 2015, pp. 1–6, doi: 10.1145/2744769.2744788.

[275] V. Bangari *et al.*, “Digital Electronics and Analog Photonics for Convolutional Neural Networks (DEAP-CNNs),” *IEEE J. Sel. Top. Quantum Electron.*, vol. 26, no. 1, pp. 1–13, Jan. 2020, doi: 10.1109/JSTQE.2019.2945540.

[276] Y. Shen *et al.*, “Deep learning with coherent nanophotonic circuits,” *Nat. Photonics*, vol. 11, no. 7, pp. 441–446, Jul. 2017, doi: 10.1038/nphoton.2017.93.

[277] M. Rastegari, V. Ordonez, J. Redmon, and A. Farhadi, “XNOR-Net: ImageNet Classification Using Binary Convolutional Neural Networks,” 2016, pp. 525–542.

[278] M. Courbariaux, I. Hubara, D. Soudry, R. El-Yaniv, and Y. Bengio, “Binarized Neural Networks: Training Deep Neural Networks with Weights and Activations Constrained to +1 or -1,” Feb. 2016, [Online]. Available: http://arxiv.org/abs/1602.02830.

[279] M. Courbariaux, Y. Bengio, and J.-P. David, “BinaryConnect: Training Deep Neural Networks with binary weights during propagations,” Nov. 2015, [Online]. Available: http://arxiv.org/abs/1511.00363.

[280] P.-L. St-Charles, G.-A. Bilodeau, and R. Bergevin, “Fast Image Gradients Using Binary Feature Convolutions,” in *2016 IEEE Conference on Computer Vision and Pattern Recognition Workshops (CVPRW)*, Jun. 2016, pp. 1074–1082, doi: 10.1109/CVPRW.2016.138.

[281] E. Nadernejad, S. Sharifzadeh, and H. Hassanpour, “Edge Detection Techniques: Evaluations and Comparison,” *Appl. Math. Sci.*, vol. 2, no. 31,

pp. 1507–1520, 2008.

[282] J. Canny, “A Computational Approach to Edge Detection,” *IEEE Trans. Pattern Anal. Mach. Intell.*, vol. PAMI-8, no. 6, pp. 679–698, Nov. 1986, doi: 10.1109/TPAMI.1986.4767851.

[283] G. Spiliopoulos, V., Keramidas, S. Kaxiras, and K. Efstathiou, “Power-performance adaptation in Intel core i7,” in *Proc. 2nd Workshop on Computer Architecture and Operating System Co-Design*, 2011, p. 10.

[284] R. Hamerly, L. Bernstein, A. Sludds, M. Soljačić, and D. Englund, “Large-Scale Optical Neural Networks Based on Photoelectric Multiplication,” *Phys. Rev. X*, vol. 9, no. 2, p. 021032, May 2019, doi: 10.1103/PhysRevX.9.021032.

[285] Y. Lecun, L. Bottou, Y. Bengio, and P. Haffner, “Gradient-based learning applied to document recognition,” *Proc. IEEE*, vol. 86, no. 11, pp. 2278–2324, 1998, doi: 10.1109/5.726791.